Spatial variation of the non-linear interactions between estuarine flooding drivers in Aotearoa New Zealand

A thesis

submitted in fulfilment

of the requirements for the Degree

of

PhD in Earth Sciences

at

The University of Waikato

by

WAGNER LUIZ LANGER COSTA

THE UNIVERSITY OF
WAIKATO
Te Whare Wānanga o Waikato

2023

Abstract

Coastal flooding is one of the main concerns worldwide associated with climate change. Historically, coastal cities have regularly experienced hazardous flooding across the globe, contributing to coastal population vulnerability. In Aotearoa New Zealand, an island nation, the outlook of rising sea levels is especially concerning due to the number of people that live in the coastal zone. Predicting extreme water levels is challenging and depends on properly identifying the main physical processes. Swells, wind waves, storm surges, and astronomical tides are transformed when propagating inside shallow coastal lagoons, bays and estuaries, mainly because of their mutual interaction (e.g., phase alteration) but also because of the effects of constrictions and friction imposed by the estuarine morphology (e.g., amplification and asymmetry). Furthermore, the compound action of different drivers and extreme events in close succession can exacerbate flooding. The understanding of non-linear interactions between flooding drivers can substantially improve the power of prediction of flooding in coastal areas with complex morphology such as estuaries. For that, proper bathymetry and topography data are fundamental for assessing flooding risk, which can be challenging because some of the current acquision methods are economically expensive or not applicable to remote and shallow areas exposed during low tide. Satellite-derived bathymetry and topography are a recent approach which are increasingly used to tackle this issue.

Although flooding drivers have already been identified and studied around the coast of Aotearoa New Zealand, few studies have focused on their interaction inside estuaries. Similarly, very little has been undertaken on the applicability of satellite-derived elevation data for hydrodynamic modelling. This thesis regionally assesses the non-linear interactions between storm surges, waves, astronomical tides and estuarine morphology and the suitability of satellite-derived data to represent these complex interactions in hydrodynamic models.

The main findings are that tide-surge interactions are a major contributor to the water level inside estuaries and cannot be neglected when simulating flooding events. Tide-surge interactions can represent variations in the water level ranging from -16 cm (below mean sea level) to +27 cm (above mean sea level). In addition, non-linear interactions induced by the estuarine morphology — especially the coverage of the intertidal zone related to the total

surface area of the estuary — modulate the co-occurrence rate between events outside and inside an estuary. It was found that co-occurrence rates can vary largely according to the estuary (20–86%). Furthermore, storm-surge and wave interactions have shown strong potential for compound and clustering effects in estuaries on the North Island, linked to severe south and southwesterly winds generated by local weather patterns. Wave height and storm surges corresponding to extreme water levels are significantly correlated, especially inside estuaries in locations close to the estuarine entrance. Wind waves are more strongly correlated to storm surges on the west coast while swell waves show a stronger correlation on the east coast of the North Island. However, when wind and swell waves are combined (i.e., integrated wave hindcast data) the correlation between wave heights and storm surges is stronger than when analysed separately. Furthermore, independent and clustered extreme events of waves and storm surges follow similar seasonality, can co-occur and can be composed of up to 12 extreme events occurring within 15 days. Finally, based on existing techniques, a framework was applied to obtain satellite-derived topo-bathymetric data. Although the applied method is sensitive to several factors (e.g., the complexity of the relief, number of processed images, bottom reflection), the derived topographic data showed good approximation to LiDAR data validation — showing similar accuracy of ~20 cm, in an elevation range of approximately 2m. The elevation estimates were used in hydrodynamic modelling to assess extreme water levels in a complex estuarine system, considering non-linear interactions. Simulation scenarios using only satellite-derived elevations could represent extreme water levels inside an estuary with complex morphology with comparable accuracy of the scenarios using topo-bathymetric data acquired using *in-situ* methods (< 0.1 m difference). The results show that satellite-derived data can be a good replacement when data originating from traditional methods are scarce or unavailable.

In conclusion, the thesis shows the regional patterns of non-linear interactions between different flooding drivers around Aotearoa New Zealand, showing where and when these interactions are important. Furthermore, it shows how satellite-derived techniques can improve the power of predicting flooding in remote areas with data scarcity. These findings are crucial for enhancing the prediction of flooding in morphologically complex areas such as estuaries, where a great part of the coastal community and civil infrastructure are based and have major social-economic importance. A better understanding of estuarine flooding would make coastal adaptation policies more effective by making the current models more accurate.

Acknowledgements

After three and half years pursuing my doctorate in Earth Sciences at The University of Waikato, New Zealand, I would describe the Ph.D. journey as quite a paradox: while it feels like a lonely road sometimes, it is only possible to be completed because the people you meet on the way. Firstly, I would like to acknowledge my supervisors. My main supervisor, prof. Karin Bryan, for choosing me for this Ph.D. position, for all the patience with my learning process, especially for all guidance in scientific writing. Co-supervisors Scott Stephens and Giovanni Coco for showing interest in my research and for all insightful contributions. In addition, I acknowledge all the staff of The University of Waikato for showing support in all matters when requested. A special acknowledgement to the National Resilience Challenge Program for having financed my PhD and the many helpful staff from different institutions that have helped me by providing information and data (e.g., NIWA, Regional Councils of Waikato, Bay of Plenty, Auckland, Northand, Southland regions).

A huge thanks to all my office colleagues and friends from Coastal Marine Research Group, especially Beréngère for (but not only!) always providing awesome brownies and making our office days sweeter and Amin for sharing delicious Persian food and being such a barbecue master. After all, PhD candidates must eat well! Cheers to Zhanchao, who, like his energy drinks, always brought some extra good vibrations and a happy atmosphere to the office! Also, huge thanks to Saeed and Danche, for the friendship and all the chats in the tearoom and by the lake. Thanks for all the amazing moments and delicious food to Christian and Ting. To Maria, Maria, Alex, and Zac, living in Hamilton would not be the same without you guys. Our climbing gatherings and jams were so important to me and lay in my best memories! To all the climbing crew, thanks for all the time spent together, especially for showing me K-bay! A huge thanks to Johnno, Alex and John for introducing me to this awesome sport! Thanks Mariana, Ben, Ted, and MetOcean community for sharing great times in Raglan.

During this journey, I had the unexpected but happy event of spending precious time in Wellington, where I could meet some awesome people I am grateful for. For all them, I am so happy to have met you all and I will always remember the legendary surf-camping trips to Cape Palliser, awesome waves, burnfires and stargazing! A huge hug to Marco and Isabela; you guys

are such special friends that I could write an entire page just about our time; thank you so much for everything! A special thanks to Anna and the Chilka pack.

My journey has been built between different countries, institutions, and people. I want to thank my former supervisors, Antonio Klein, Omar Gutierrez, Mauricio, Deborah Idier, and Jeremy Rohmer, for teaching me so much. You certainly inspired me to do a PhD. Thanks for showing interest in my pathway and for keeping in contact. Equally, I would like to acknowledge some friends who also happen to be awesome scientists and are true inspirations for me: Ana Paula, Maurizio, Paula, Charline, and Eduardo.

Finally, I am grateful to my family to have always supported me. Even far away, we always found a way to be connected. Our video-calls and their presence always warm my soul. I am happy and proud to say that my family are my friends too. I dedicate this thesis to you. A special mention to my grandmas, who are always in my heart and my best memories!

Table of contents

List of figures

List of tables

Chapter 1

General introduction

Coastal flooding has become one of the bigger climate change concerns worldwide due to the observation that flooding events have grown in frequency and strength in the last century (Sobel et al., 2016; Taherkhani et al., 2020; Kirezci et al., 2020). Historically, coastal cities have constantly experienced hazardous flooding across the globe, which has contributed to the vulnerability of coastal populations. In Europe, the great flood of 1953 impacted extensive areas of the Netherlands, and other examples are Cyclone Xynthia in 2010 in France (Chadenas et al., 2014), and the North Sea flood in 2013 in northern Europe (Dangendorf et al., 2016). At low latitudes, tropical cyclones (hurricanes and typhoons) have caused devastating economic and life losses—Hurricanes Katrina in 2005 and Sandy in 2012 in the United States. In Asia, the Bhola Cyclone (1970) may be one of the most notorious because it caused 300,000 fatalities along the coasts of Pakistan and India (Karim and Mimura, 2008). In 2008, Cyclone Nargis impacted Myanmar. Extratropical storms can also generate strong flooding events, such as the 1993 storm that affected the east coast of the United States (Thompson et al., 2013). The increased storminess combined with sea-level rise has caused significant stress to coastal communities associated with projected economic and ecosystem impacts (Oppenheimer et al., 2019). Without adaptation, up to 4.6% of the world population is expected to be flooded annually in 2100, with estimated annual losses of up to 9.3% on the global gross domestic product (Hinkel et al., 2014). For coastal ecosystems, sea-level rise is expected to be an increasing threat over the century (Nerem et al., 2018; Oppenheimer et al., 2019). For instance, 24% of the world's sandy beaches erode at rates exceeding 0.5 m/yr (Luijendijk et al., 2018). Up to 78% of the world's salt marsh areas could be submerged by 2100 (Spencer et al., 2016). Tidal flats worldwide have already lost 16% of total area between 1984 and 2016 (Murray et al., 2019). In addition, mangrove forests which grow on tidal flats, may not be able to adapt by accumulating sediment (by vertical accretion) in some regions of the world under future projections of sea-level rise (Saintilan et al., 2020). Moreover, mean sea-level changes can modify the hydrodynamics (e.g., current magnitude, tidal amplitude, sediment transport) in

coastal environments, especially in estuaries, where fundamental biological and ecosystem services can be highly impacted (Khojasteh, 2021).

Coastal inundation is also a major hazard to New Zealand, with 15,000 km of coastline where around 150,000 people live in low-lying coastal areas (Ministry of the Environment, 2022) — i.e., geographical regions situated at relatively lower elevations compared to surrounding terrain, often prone to flooding or inundation. Currently, the sea level rises at an average rate of 1.7 mm/yr without considering the strong land subsidence of some areas due to tectonic activities (Beavan and Litchfield, 2012; Bell et al., 2022). It has been estimated that sea-level rise could severely compromise critical national structures (e.g., airports, roads) and urban areas (i.e., residential buildings), with a total cost of building replacement around $40 billion (Paulik et al., 2020). Although the storm surges around New Zealand are low if compared to equatorial and high latitudes — Heath (1979) has found a maxima storm surge of 0.8 m, and Stephens et al. (2020) have found rare occurrences that are >1m above the mean sea level — they can still cause coastal flooding and strong coastal erosion (Bell et al., 2000). Historically, New Zealand has an extensive list of hazardous storm events that date back to the first half of the 20th century. However, the extent of damage of these historical storms is poorly documented since not many sea-level gauges operated at those times (Stephens et al., 2020). For example, notable events are the great cyclone of 1936 (Brenstrum, 2000), the great flood in the Hauraki Plains (May 1938) (Stephens et al., 2020), the storm Gisele in 1968 (de Lange and Gibb, 2000), and the great flooding event in the Thames Region (1995), which caused severe economic damage (~3–4 million dollars). In the last decade, several large storms, including ex-tropical cyclones Fehi, Gita, and Hola, impacted New Zealand — during the spring and summer of 2017 and 2018 —; most of them were potentialised by high perigean-spring tides, flooding homes and damaging infrastructure. More recently, Cyclone Gabrielle (2023) caused the inundation of vast urban and agricultural areas (e.g., Northland, Auckland, Coromandel, Gisborne).

Aotearoa New Zealand's complex coastline geometry contemplates estuaries with large intertidal areas and deep fjords. Such a diverse coast implies big challenges in predicting flooding. One of them is the non-linear processes between the different flooding drivers, which are boosted in extensive shallow areas and constricted geometries. Moreover, properly representing the compound effect of different drivers (e.g., waves and storm surges) is still challenging for different model techniques, which is fundamental for flooding prediction once

the combined effect of different drivers can represent a threat much greater than when these drivers are considered individually, exacerbating flooding risk. Ultimately, accurate and updated topo-bathymetry data is fundamental for modelling the estuaries' physical processes and determining the extension of the flooding area. The thesis is focused on the interactions between different flooding drivers and estuarine morphology.

1.1 Thesis aims and structure

The format of the present document is thesis by publication. The overarching objective of this thesis is **to identify and explain the spatial variation of the interaction between tide, storm surge, waves, and estuarine morphology in order to improve the prediction of these events in New Zealand**. This was accomplished by answering the following questions:

1. **How does estuarine morphology affect tide and surge in NZ?** Does it amplify the effect, or does frictional dissipation in shallow water remove energy and dimmish the effect?

2. **What are the main drivers of spatial variation in storm surges?** Can the co-occurrence of different drivers and the storm surge be used as a way to measure whether they are related?

3. **How well can we predict estuarine flooding events in areas where we do not have good topo-bathymetric data?** Can we use remote sensing techniques as an alternative to traditional surveying techniques for generating topo-bathymetric data?

Figure 1.1 shows a conceptual diagram of the thesis structure and how the chapters are connected; in the centre are shown the main process that influence estuarine flooding that I have focused on (i.e., estuarine morphology, astronomical tides, non-linear interactions, storm surge, and waves). Chapter 2 is a revision of the main concepts that the thesis is focused on, thus it is not shown in Figure 1.1. Chapters 3 and 4 show a region analysis investigating interactions between different drivers: estuarine morphology, tide-surge and wave-surge interactions. Chapter 3 also brings a detailed numerical modelling for Manukau Harbour — an estuary in Aotearoa New Zealand — where tide-surge interactions were further investigated.

Ultimately, in Chapter 5, satellite-derived topo-bathymetric data were tested in hydrodynamic modelling of extreme water levels inside a complex estuarine system, where the non-linear interactions investigated in Chapters 3 and 4 have a high impact on physical processes involving flooding events.

This thesis will add to the literature by investigating the non-linear interactions of different estuarine flooding drivers (e.g., storm surge, astronomical tides, waves, estuarine morphology) and evaluate how well satellite-derived topo-bathymetry can replace surveyed elevation data for predicting floodings in estuarine systems. I hypothesise that estuarine morphology strongly affects tide and surge interactions and that waves can potentially exacerbate storm surges. Moreover, although accurate topo-bathymetry data is fundamental for modelling flooding events, satellite-derived elevation data could replace surveyed bathymetry to predict extreme water levels in remote and economically deprived areas where survey techniques are not applicable.

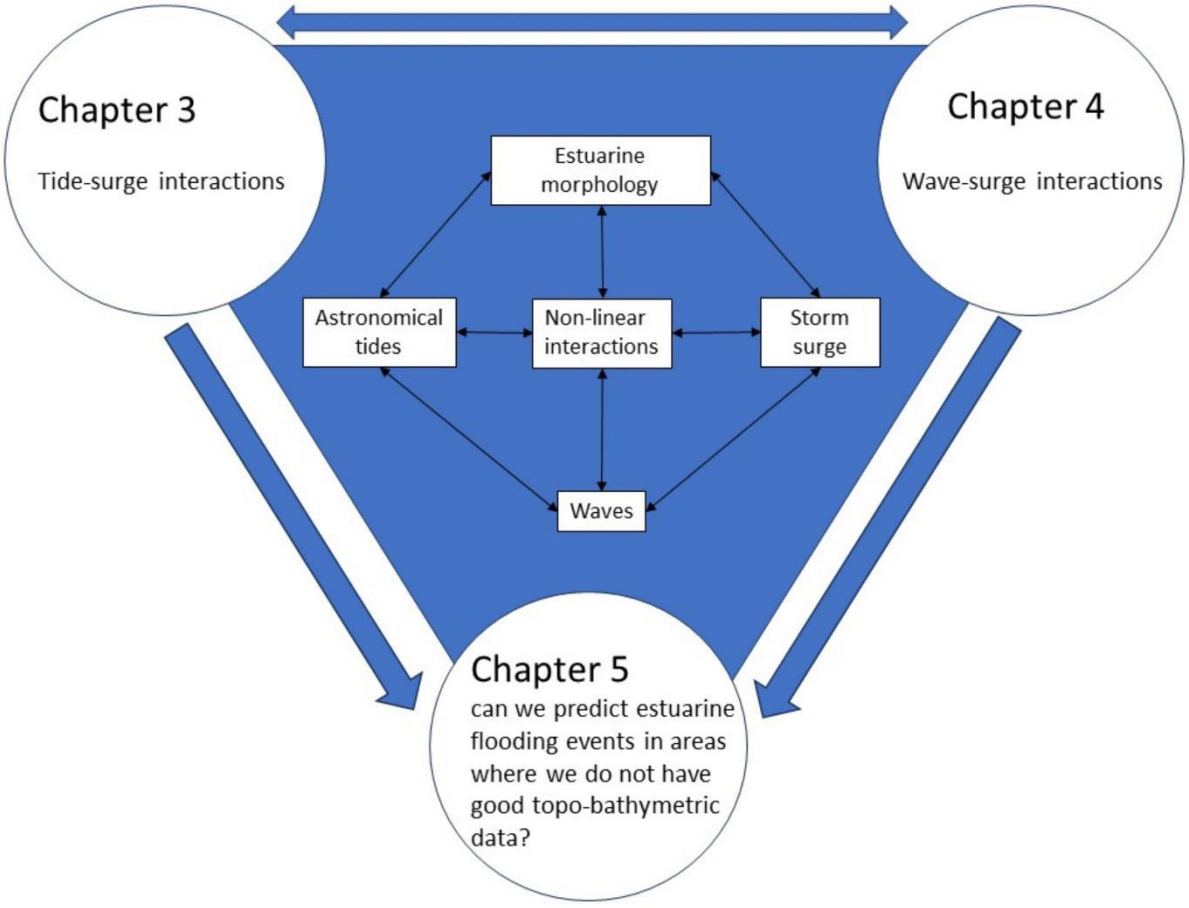

Figure 1.1. Conceptual diagram demonstrating the connection between chapters.

Chapter 2

Problem background

2.1 Modelling coastal flooding

Flooding occurs when the total water level equals or exceeds the topographic level where a coastal urban area or environment (e.g., coastal dunes, estuarine harbours) is located (Pugh, 1987). The total water level (TWL) components (also called drivers) are shown in Figure 2.1. Because of the complexity in determining each of these terms and accounting for their mutual physical interactions — which often requires numerical modelling to consider the conservation of momentum equation — TWL is often conceptually simplified (Equation 2.1.) as a sum of the contributions of different flooding drivers. The mean sea-level variation (MSL) is mainly caused by eustatic sea-level changes, controlled by the volume of glacial ice on land. Astronomical tide (AT) is the variation of the sea level because of the effect of gravitational pull of moon and sun. The storm surge (SS) is the change in the sea level caused by the atmospheric effect of the horizontal gradient pressure and wind stress at the sea-surface. Often, astronomical tide and storm surge are represented as a combined term called storm-tide (Stephens et al. 2020). Waves (W) can also contribute to the TWL at the coast by processes related to the wave break at the surfing zone, known as wave run-up. Other components can also be fundamental when computing TWL. For instance, the geological component represented by the vertical land motion due to the tectonic activity (VLM). In estuaries, the fluvial component (FLU), the rainfall component (RA), and the wind-generated waves can be essential for fully describing flooding processes at the interface sea and land. Fluvial discharge/level can locally alter the water level, whereas the pluviosity in a hydrological basin controls the volume of water in the rivers. The volume of rain can also contribute to the saturation of the soil, which makes water penetrate less in naturally flooding zones by rivers and estuaries, thus exacerbating flooding.

$$TWL = MSL + AT + SS + W + VLM + FLU + RA + \ldots \qquad (2.1)$$

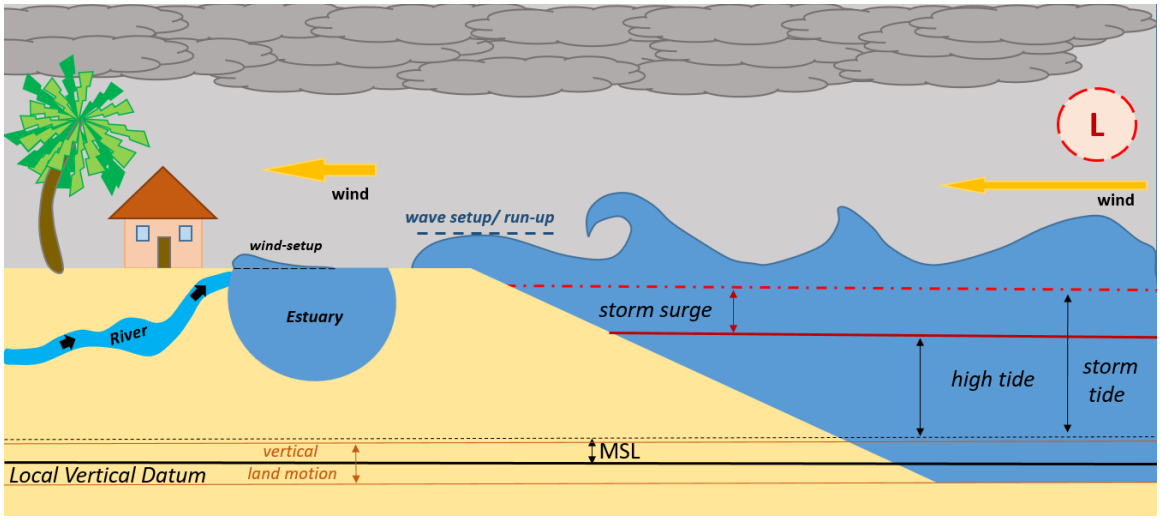

Figure 2.1. Estuarine flooding drivers.

The contribution of each flooding driver is site specific. For instance, in enclosed bays and estuaries, the action of waves is often not considered. Fluvial discharge is neglected if there is no large inflow of riverine waters. Wind set-up is relatively low in wind-fetch-restricted areas. Vertical land motion is also not considered if tectonic activities are rare. The mean sea-level changes are important in long-term projections; however, MSL is less important for mid to short-term predictions. Because the astronomical tide is a deterministic variable that can easily be predicted for any horizon (short-, mid-, and long-term) (Pugh, 1987), predicting SS and W is key for properly predicting flooding levels at the coast. In estuaries, flooding modelling becomes more complex because it needs to account for other physical processes like fluvial and pluvial discharge and non-linear interactions between the different flooding drivers induced by the morphology changes. These non-linear processes are neglected when assuming conceptual approaches as the one shown by Equation 2.1. and are the focus of this thesis.

Studies have shown that the combined action of different drivers —called compound flooding — poses a threat much greater than what each in isolation is capable of due to non-linear processes (Bevacqua et al., 2021; Zscheischler et al., 2020). By 2100, the concurrence probability between storm surges, waves, and precipitation is expected to increase globally by more than 25% compared to the present (Bevacqua et al., 2020a). Considering storm surges, riverine, and precipitation forcings, compound flooding has four main mechanisms (Wahl et al., 2015; Bevacqua et al., 2020b). First, the co-occurrence of high river discharge and storm surge raises water levels in an estuary, causing flooding or exacerbating its impacts. Second, a severe storm surge event that already causes widespread flooding is followed by rainfall, which

can cause additional or prolonged flooding. Third, an average storm surge increases the water level to a point where it cannot directly cause flooding but fully blocks or slows down gravity-fed stormwater drainage. Consequently, precipitation causes flooding. Fourth, an initial storm surge saturates the soil, which makes the next rainfall flood the wet ground.

In summary, modelling coastal flooding needs to apply different modelling techniques to represent the flooding drivers and estimate the water level; thus, the water level information is combined with elevation data to produce flooding maps. In a recent review of compound flooding, Jafarzadegan (2023) highlighted the main challenges for improving coastal flooding assessment: representing the interdependence and spatiotemporal correlation between different flooding drivers, representing non-stationarity of coastal flooding dynamics due to mean-sea level rise, and data constraints.

The existing methods to model coastal flooding can be categorised into dynamic and data-driven approaches. The former integrates the governing shallow water equations explaining the physical processes inducing flooding, which makes it a robust tool for assessing flooding risk (Barnard et al., 2019). However, it requires high-quality topo-bathymetric data and a comprehensive observation record to validate numerical models. Furthermore, the high computational cost of numerical models and their assumptions in the formulation and parametrisation of physical processes limit their performance (Schwanenberg et al., 2018; Santiago-Collazo et al., 2019; Abbaszadeh et al., 2022).

Data-driven approaches use statistical models or machine learning to establish the relationship between predictors and predictands. It is a relatively simple and fast way to simulate compound flooding. The need for spatiotemporal coverage of records limits data-driven methods. Long overlapping records (decades) are required to characterise the interdependencies of the flood drivers properly. In addition, data-driven methods often consider a stationary assumption and cannot fully capture anthropogenic effects such as climate change and land cover change (Jafarzadegan et al., 2023).

To properly assess the flooding exposure of a given coastal area under different water level scenarios, the combination of statistical and hydrodynamic models (also called surrogate, hybrid, or meta-models) is applied. They can be univariate or multivariate. The former implicit considers the interdependence between the flood drivers by using the observed water level (which is the ultimate response variable, being composed by storm, wave contribution, and

astronomical tides). However, observations of water level are often data restricted. Moreover, methods using only one variable (univariate), ignore the joint probability of flooding drivers, ultimately underestimating flooding risk (Moftakhari et al., 2019). The multivariate models can be divided into structure variable, impact-based, and joint density approaches. The structure variable approaches rely on numerically simulating several scenarios using as input different flooding drivers, which can be time-prohibitive and depends on having sufficiently long records of different variables. The impact-based approach reduces the number of numerical simulation scenarios by only considering values of a water level above a threshold and then taking the coincident values of the flooding drivers as input in the model. Approaches using join density of multivariate distributions investigate the dependence structure of multiple variables to extrapolate the input data to extreme values. For instance, copulas and multivariate parametric distributions are commonly applied on this approach. Copulas have the advantage over multivariate parametric distributions for capturing non-linear dependence between the flooding drivers (Salvadori & De Michele, 2007; Durante & Sempi, 2015; Kyprioti et al., 2023).

Compounding flooding studies have investigated a broad combination of drivers such as water level and river discharge (e.g., Bevacqua et al., 2017; Gori et al., 2020a; Gori et al., 2020b), water level and waves (e.g., Wahl et al., 2016; Serafin et al., 2017), storm surge and river flow (e.g., Bass & Bedient, 2018; Bilskie et al., 2022a; Bilskie et al., 2022b), storm surge and river flow with rainfall (e.g., Svensson & Jones, 2004), storm surge and rainfall (e.g., van den Hurk et al., 2015; Wahl et al., 2015; Zheng et al., 2014), wave/surge parameters (e.g., Corbella & Stretch, 2013; Salvadori et al., 2015; Shope et al., 2022), rainfall, surge, and waves (e.g., Bilskie & Hagen, 2018) and storm surge, wave, river flow and rainfall (e.g., Camus et al., 2021; Nasr et al., 2021).

The mean-sea level rise imposes non-stationary changes on every coastal flooding driver: storm surges (Vousdouskas et al., 2016; Calafat et al., 2022), waves (Morim et al., 2019), tides (e.g., Idier et al., 2017), and coastline position (d'Anna et al. 2021). In coasts and estuaries, these impacts are reflected primarily in the tidal regime (amplitude and asymmetry) (Haigh et al., 2019; Talke and Jay, 2019), consequently impacting the ecology and biogeochemical cycles. Studies have shown that estuarine morphology modulates the response of the tidal range and asymmetry to sea level rise (Du et al., 2018; Khojasteh et al., 2020; Khojasteh et al., 2021). For instance, the tidal range is more likely to decrease in short estuaries with broad intertidal zones (Du et al. 2018), and the smaller the cross-sectional area of the estuary mouth, the smaller the

tidal range within the estuary (Khojasteh et al., 2020). Ultimately, in estuaries with preserved intertidal zones and flood plains, the effects of sea level rise can be mitigated through landward migration of these environments; in contrast, in estuaries with fixed structures (e.g., sea walls), the tidal range is more likely to increase (Khojasteh et al., 2021).

Although the astronomical tide is the main driver for coastal flooding in Aotearoa New Zealand (Rueda et al. 2019, Stephens et al. 2020), the combination of multiple flooding drivers has yet to be assessed. Aotearoa New Zealand possesses a relatively extensive tidal gauge and weather station network. However, they often do not overlap in sufficient long observation periods, restricting compound flooding assessment. In addition, Land Information New Zealand has been measuring topography nationwide through LiDAR equipment; however, this method is expensive (which limits updating this data), and extensive areas of the country are still without any elevation data. The present thesis is focused on non-linear effects between astronomical tides, non-tidal residuals (which compromise storm surge and wave forcing), estuarine geometry and topo-bathymetry.

2.2 Shallow water non-linear processes for tides, storm surges, and waves

Storm surges are defined as the changes in sea level caused by only atmospheric forcings, specifically the stress caused by the wind on the sea surface and the gradient of sea level pressure associated with storms. The largest storm surges are associated with mid-latitude storms and tropical cyclones (hurricanes and typhoons). Storm surges have a period from a few hours to 2 or 3 days, and like the tides, they have large wavelengths when compared with the water depth. Storm surges and tides are superimposed and generate storm tides. Pugh (1987) and Flather (2001) described tides and storm surges using depth-averaged hydrodynamic equations, which include non-linear terms responsible for their interaction, which is given by Equations 2.2 and 2.3, where the conservation of volume is assumed, and the viscosity term is neglected assuming that the convective acceleration term dominates over the viscous term:

$$\frac{\partial U}{\partial t} + U\frac{\partial U}{\partial x} + V\frac{\partial U}{\partial y} = -\frac{1}{\rho}\frac{\partial P}{\partial x} + \frac{\tau_{sx}-\tau_{bx}}{\rho(d+\zeta)} + f \qquad (2.2)$$

$$\frac{\partial V}{\partial t} + U\frac{\partial V}{\partial x} + V\frac{\partial V}{\partial y} = -\frac{1}{\rho}\frac{\partial P}{\partial y} + \frac{\tau_{sy}-\tau_{by}}{\rho(d+\zeta)} + f \qquad (2.3)$$

Equations 2 .2 and 2.3 equate the advection term (left side) to the horizontal sea level pressure gradient and friction terms (right side). *U* and *V* are the vector components of the current, ρ is the seawater density, *P* is the surface pressure; ζ is sea surface elevation and *d* is water depth; τ_s and τ_b are the surface and bottom stress, respectively. Both can be represented by applying the quadratic law as follows. The bottom stress is given in *x* and *y* components, described by Equations 2.4 and 2.5:

$$\tau_{bx} = k\rho U\sqrt{U^2 + V^2} \quad (2.4)$$

$$\tau_{by} = k\rho V\sqrt{U^2 + V^2} \quad (2.5)$$

where *k* is a friction parameter. Surface stress can be defined as Equation 2.6:

$$\tau_s = c_D\rho_a W|W| \qquad (2.6)$$

where c_D is a drag coefficient, ρ_a is the air density, and *W* is the wind magnitude at 10 m height above sea level. *f* is the Coriolis parameter.

Equations 2.2–2.6 show that the current magnitude, pressure gradient, and friction terms drive the storm surges. The pressure gradient term does not depend on the water depth $(d + \zeta)$. However, the frictional and advection terms are affected by it. The bottom stress (linked to the currents) and the surface stress (linked to the wind) are divided by the water depth. Thus, the shallower the water column, the higher the effect of the frictional term. Consequently, considering a constant pressure gradient, if the frictional term increases, the advection term must also increase to balance the conservation mass equation. In summary, in deep water, the storm surge results mainly from the sea surface pressure gradient, where non-linear terms can be neglected. In shallow water, the frictional term contributes more to the storm surge, enhancing non-linear interactions.

Effects of wind on storm surges are enhanced in shallow waters, as shown in Equations 2.2 and 2.3 by the friction terms. This is especially important for extensive shallow estuaries, where surface stress increases storm surges (e.g., Smith et al., 2001). Moreover, on a regional scale, strong winds can increase the sea level by the Ekman transport (e.g., Shen and Gong,

2009; Kennedy et al., 2011; Bertin et al., 2012) — when the wind direction is parallel to the coast — and by wind set-up — when the wind is blowing towards the coast (e.g., Wolf, 2009; Dietrich et al., 2010; Brown et al., 2011). In addition, when a storm moves, it can generate free waves propagating alongshore as trapped waves (Edge or Kelvin waves). Wind can also generate waves, ultimately affecting storm surges through three main mechanisms (Flather, 2001; Dodet et al., 2019). First, wind waves can enhance sea surface stress. Second, wave orbital velocities in shallow waters reach the seabed and increase bottom stress. Third, at the beach, non-linear interactions can induce changes in the mean water depth (wave set-up and set-down), causing a surplus momentum flux called radiation stress (Longuet-Higgins and Stewart,1964). Although waves are expected to be constrained by coastal and mouth geometry in enclosed estuaries and tidal lagoons, papers have shown their influence on sea levels within such environments (e.g., Thompson and Hamon, 1980; Bertin et al., 2015; Rahbani et al., 2022). Wave set-up can also occur in estuaries and harbours through radiation stress. When waves enter a harbour from a narrow entrance, their amplitude decreases, causing the mean water level inside the harbour to be higher than at the mouth (at distances greater than a few times the entrance width) (Thompson and Hamon, 1980). Moreover, other processes as infragravity waves and meteo-tsunamis can also be specially important in semi-enclosed bodies of water. Ultimately storm waves can also occur in close succession to storm surges, exacerbating flooding risks by coastal erosion, wave run-up and overtopping (Dodet et al., 2019). Moreover, Marcos et al. (2019) have shown that approximately 55% of the world's coastlines can have underestimated extreme water levels if the compound effects of storm surges and wave extremes are not accounted for.

When a storm tide (storm surge + astronomical tide) propagates inside estuaries, it can be amplified, damped, reflected, and phase changed (Khojasteh et al., 2021). Amplification occurs more commonly because of the effects of funnelling (when the coastline converges) or shoaling (when the depth gradually decreases) (van Rijn, 2011). However, reflection and resonance can also amplify the tidal wave. When a tidal wave encounters an obstacle imposed by the morphology of the estuary (e.g., rigid wall, abrupt shallowing), it can be amplified by reflection. Tidal resonance occurs when the tidal frequency is synchronised with the natural frequency of the estuary — which is the frequency at which the estuary's water body naturally oscillates or resonates in response to external forces, such as tidal forcing. (Khojasteh et al., 2021). Estuaries can have multiple natural frequencies or resonant modes mainly depending on their shape, size, bathymetry (depth variations).. The friction of the estuarine bed causes

dampening. In addition, the bed friction can cause tide phase modification, changing the duration of the ebb and flood tides, a process called tidal asymmetry.

When astronomical tides propagate inside an estuary or shallow areas, the finite amplitude of the tide relative to the water depth, bed friction, and morphology can cause the development of overtides or so-called shallow water harmonics (e.g., M_4, S_4). Speer and Aubrey (1985) have proposed a method to evaluate whether shallow-water harmonics are important using the ratio between the amplitude (a) and phase (g) of the principal lunar harmonic (M_2) and the fourthly principal lunar harmonic (M_4). Consider a situation where the tide amplifies between two observation points — one outside the estuary, the other in the upper estuarine area) — the greater the amplitude ratio (aM_4/aM_2), the stronger the effects of friction or geometry (e.g., funnelling) on the tide amplification. Thus, for estuarine or shallow areas, the amplitude ratio is expected to be higher than in open coast or deep areas. The phase ratio ($2gM_2/gM_4$) indicates whether the tidal regime is ebb or flood dominant. For instance, a phase ratio between 0^o–180^o means that the tidal regime is flood dominated; conversely, 180^o–360^o implies that the regime the ebb dominated. Values ~ 0^o or 360^o mean the regime is quasi-symmetric: flood and ebb tides have similar durations.

When tides and surges propagate inside an estuary, not only do the geometry, topography and bed friction act in tides and surges, they mutually interact. Pioneering studies on tide-surge interactions have shown this effect on the Thames River, United Kingdom (Proudman, 1957a,b; Rossiter, 1961; Wolf, 1981). The tide is a long wave (periods of 12 to 24 h) that propagates as a shallow wave, meaning that its celerity depends on the depth. Once the storm surge can rise or decrease the sea level for long periods (scale of days), they modify the phase of the astronomical tide. Similarly, the tides can modify the storm surges celerity (if we consider that storm surges are shallow water waves) and magnitude (considering that friction terms depend on the depth). Extensive shallow areas or coasts with complex geometry and strong tidal currents are well-known for experiencing strong tide-surge interactions. For instance, the Gulf of Mexico (Rego and Li, 2010), the Bay of Bengal (Antony et al. 2020), the English Channel (Idier et al., 2012), and the South China Sea (Zhang et al., 2017). All these studies have shown that tide-surge interactions are important for modelling storm surges at coasts and estuaries on a local scale.

Representing non-linear processes is one of the main challenges in modelling water levels in complex estuaries. Studies using dynamical methods have tried to solve as many processes as possible, coupling different models and forcings. For instance, Fernández-Montblanc et al. (2019) have shown that numerically modelling storm surges and tides in combination improves a pan-European storm surge forecast. Models that are forced combining waves, storm surge, and astronomical tides were developed specifically for solving extreme water levels during tropical cyclones in two (Ding et al., 2020) and three (Sheng et al., 2010) dimensions. Although robust, these models fall under the limitations mentioned earlier (Section 2.1) of computational and time costs when applied on larger scales (i.e., regional, global).

In the domain of data-driven methods, Arns et al. (2020) have developed a statistical model to quantify tide-surge interactions, which has shown that if non-linear processes are not accounted for, extreme water levels can be overestimated by 0.7 m globally. That happens because when non-tidal residuals are calculated, they do not consider the phase alteration in tides and surges that happens in shallow waters. The skew surge parameter has been created to account for tide-surge interactions and make statistical methods, such as join probabilities, more robust to analyse extreme water level values for shallow areas (Batstone et al., 2013). The skew-surge is the vertical difference between the peak of the water level and the peak of the tide within the same tide cycle in which the surge occurs (Figure 2.2). Moreover, Artificial Neural networks have been widely implemented to predict storm surges at the coast (e.g., Tadesse et al., 2020, Bruneau et al., 2020; Tiggeloven et al., 2021) and in estuaries (e.g., French et al., 2017; Guillou and Chapalain, 2021), because deep learning techniques can improve predictions of water level where non-linear processes are strong. However, a disadvantage of machine-learning algorithms is that they do not physically interpret the problem. To tackle this issue, hybrid models have been implemented (e.g., Anderson et al., 2021), and physics-based machine learning algorithms are yet to be implemented in coastal flooding (Brunton et al., 2016; Willard et al., 2020; Kashinath et al., 2021).

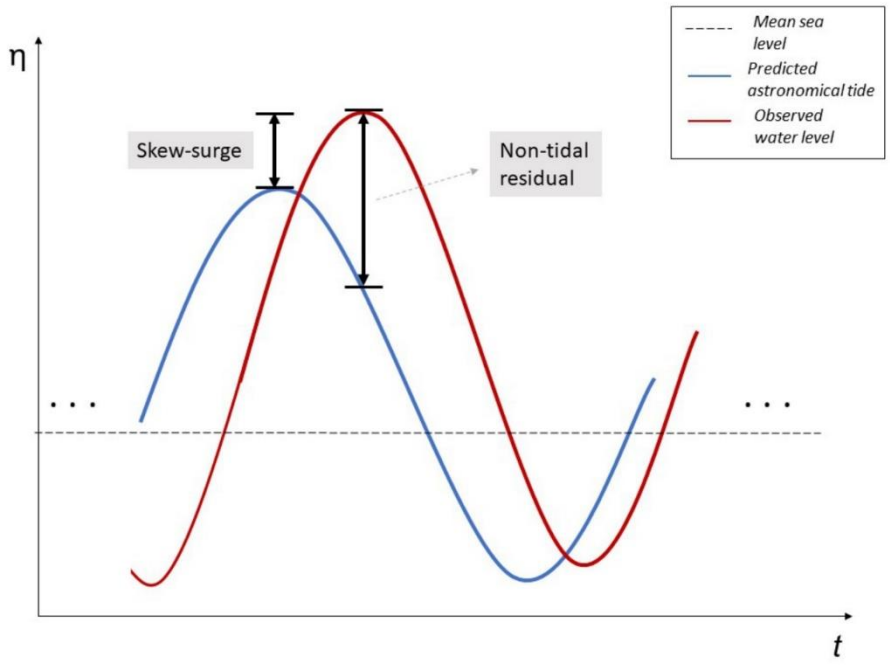

Figure 2.2. Skew-surge conceptualization.

2.3 Monitoring the coastal and estuarine morphology of Aotearoa New Zealand from space.

In Section 2.2, bathymetry was shown to be extremely important to surge propagation into enclosed areas through the friction term causing non-linear transfers. Therefore, a good understanding of the spatial variability of topography and bathymetry are important to understanding storm surges.

Aotearoa New Zealand comprises two main islands (North and South) with a narrow continental shelf. The coastline is 18,000 km in extent (including estuarine shores) of complex geometry, which has been shown to affect extreme sea level observations (Tausía et al., 2023). Moreover, Aotearoa New Zealand has a diverse coastal environment, from pristine fjords on South Island to large estuaries with extensive tidal flats, mangrove forests, and intense human activity on the North Island. Hume et al. (2016) have counted approximately 500 coastal hydrosystems in Aotearoa New Zealand and classified them into 11 geomorphologic classes. Only five classes are estuarine: tidal river mouths, tidal lagoons, shallow drowned valleys, deep drowned valleys, and fjords. The first three are characterised by shallow

bathymetry/topography, where intertidal zones were developed. Intertidal zones are coastal areas exposed and flooded at low and high tide. Some estuaries in Aotearoa New Zealand can have an intertidal area representing more than 80% of the total surface area. Deep drowned valleys and fjords have deeper bathymetry, preventing intertidal flats formation. Tidal river mouths are elongated, narrow, shallow basins that permanently connect to the sea. The hydrodynamics is dominated by the river flows. Tidal lagoons are characterised by shallow bathymetry (mean depth 1–3 m), with simple geometry (circular to elongated basins) and narrow entrance to the sea, constricted by a spit or sand barrier, which can be permanently or intermittently connected. The tides dominate the hydrodynamics, where much water leaves the estuary on the outgoing tide. Shallow drowned valleys have a complex geometry — numerous narrow arms (with dendritic form) connected to a main central basin or channel and extensive tidal flats. The entrance to the sea is always open and constricted by hard headlands or substantial barriers. The hydrodynamic is tidally dominated.

The present thesis is focused on tidal lagoons and shallow and deep drowned valleys, which correspond to the estuarine systems that are usually associated with human installations (Ports, wharves) where observation systems are more commonly established (e.g., tidal gauges). Shallow drowned valleys and tidal lagoons have being impacted by sediment infilling caused by the development of human activities such as agriculture, which contributes to higher sediment loads into riverine systems that ultimately end in estuaries. The sediment infilling has caused the expansion of mangrove forests in estuaries of Aotearoa New Zealand (Horstman et al., 2018).

In estuarine environments, topo-bathymetric data are fundamental to assessing the estuarine hydrodynamic in the short- and long term. Topographic changes — whether caused by human activities (e.g., dredging) or sediment flux (e.g., infilling) — directly affect the non-linear interactions with tides, storm surges, and waves, also modify tidal range (Ralston et al. 2019; Haigh et al. 2019; Talke and Jay, 2020). In the long term, geometry features such as the mouth width, slope and extension of intertidal zones will modulate the capability of adjustment of the estuary to future projections of sea level rise. Moreover, the lack of updated topographic data has been shown as one of the main sources of uncertainty regarding the costs of coastal flooding due to sea-level rise because flooding map models need highly accurate elevation data to efficiently calculate vulnerable flooding areas (Gesch, 2018; Schuman and Bates, 2018; Sheng et al., 2022).

Surveys and remote sensing are the most applicable techniques to measure elevation in coastal areas. Survey methods use sonar accoupled to a ship — when measuring bathymetry — and are highly accurate; however, they are economically expensive, time prohibitive to cover large areas, and specifically in estuaries, their coverage is limited because they cannot navigate in intertidal zones due to the ebb and flood tides. To remedy this issue, remote sensing has been widely applied in coastal sciences because of the low economic cost and the large area coverage. Remote sensing covers a wide range of techniques, like LiDAR (Light Detection and Ranging), stereo-video, multispectral satellite images, synthetic aperture radar (SAR). Moreover, its use has been increasing recently (Turner et al., 2021; Vitousek et al., 2022) because cloud computing and large datasets have become easier to access (Gorelick et al., 2017). Several efforts have been put into monitoring coastline changes (e.g., Vos et al., 2019; Almeida et al., 2021) and coastal bathymetry through empirical (e.g., Lyzenga 1985; Stumpf, 2003; Caballero and Stumpf, 2020) and physic-based algorithms (e.g., Almar et al. 2019). Specifically for estuaries, there were developments in monitoring estuarine geometry (e.g., mouth width and channel length) (Heimhuber et al., 2021) and measuring area and topography of intertidal zones (e.g., Bishop et al., 2019; Murray et al., 2019; Bué et al. 2020, Salameh et al., 2020)

Chapter 3

A regional analysis of tide-surge interactions during extreme water levels in complex coastal systems of Aotearoa New Zealand.

Wagner L.L. Costa[1*], Karin R. Bryan[1], Scott A. Stephens [2], Giovanni Coco [3] (published in *Frontiers of Marine Science* (2023) 10:1170756. DOI 10.3389/fmars.2023.1170756)

[1]Coastal Marine Group, School of Science, The University of Waikato, Hamilton, New Zealand

[2] National Institute for Water and Atmospheric Research Ltd, Hamilton, New Zealand.

[3] School of Environment, University of Auckland, Auckland, New Zealand.

Contribution of Authors: The main conception and design of the study were given by Wagner L.L. Costa with important contributions given by Karin Bryan, Scott Stephens, and Giovanni Coco. The statistical analysis and numerical modelling were performed by Wagner L.L. Costa and supervised by Karin Bryan and Scott Stephens. The hydrodynamic modelling was elaborated and performed by Wagner L.L. Costa under supervision of Karin Bryan. The database was organised by Scott Stephens and Wagner L.L. Costa. The first draft of the manuscript was written by Wagner Costa. All authors contributed to manuscript revision, read, and approved the published version.

Code availability: the main codes used in this chapter are available at https://github.com/CostaAndCoasts/

Conference presentation and scientific promotion: the developments of this chapter were presented in the International Conference of Coastal Engineering, Sydney, December, 2022.

Abstract

Tide-surge interaction (TSI) is a critical factor in assessing flooding in shallow coastal systems, particularly in estuaries and harbours. Non-linear interactions between tides and surges can occur due to the water depth and bed friction. Global investigations have been conducted to examine TSI, but its occurrence and impact on water levels in Aotearoa New Zealand (NZ) have not been extensively studied. Water level observations from 36 tide gauges across the diverse coast of NZ were analysed to determine the occurrence and location of TSI. Statistical analysis and numerical modelling were conducted on data from both inside and outside estuaries, focusing on one estuary (Manukau Harbour) to determine the impact of TSI and estuarine morphology on the co-occurrence rate of extreme events. TSI was found to occur at most sites in NZ and primarily affects the timing of the largest surges relative to high tide. There were no regional patterns associated with the tide, non-tidal residual, or skew-surge regimes. The strongest TSI occurred in inner estuarine locations and was correlated with the intertidal zone area. The magnitude of the TSI varied depending on the method used, ranging from -16 cm to +27 cm. Co-occurrence rates of extreme water levels outside and inside the same estuary varied from 20% to 84%, with TSI modulating the rate by affecting tidal amplification. The results highlight the importance of investing in a more extensive tide gauge network to provide longer observations in highly populated estuarine coastlines. The incorporation of TSI in flooding hazard projections would benefit from more accurate and detailed observations, particularly in estuaries with high morphological complexity. TSI occurs in most sites along the coast of NZ and has a significant impact on water levels in inner estuarine locations. TSI modulates the co-occurrence rate of extreme water levels in estuaries of NZ by affecting tidal amplification. Therefore, further investment in the tide gauge network is needed to provide more accurate observations to incorporate TSI in flooding hazard projections.

3.1 Introduction

Coastal flooding has threatened coastal communities worldwide, causing economic and human losses (Oppenheimer et al., 2019). Climate change and the consequent sea-level rise are likely to increase the exposure of coastal zones to flooding risk. Recent studies have focused on improving models and methods to predict extreme sea levels and storm surges (e.g. Fernández-Montblanc et al., 2019). The assessment of extreme coastal flooding events is generally based on the total water level which is the sum of: sea level rise, astronomical tide, vertical land motion, and non-tidal residual (NTR). The NTR includes storm surges and other physical contributors (e.g., surf beat, set up and set-down). The storm surge is the change in the water level caused by sea level pressure gradients and wind stress at the sea surface associated with storms (Pugh and Woodworth, 2014).

When the storm surge originates in the ocean, arrives at the coast, and propagates inside an estuary, its characteristics can be substantially modified by local physical processes. For instance, fluvial discharge, rainfall, wind set-up, and local-generated wind waves can contribute to the NTR (e.g., Plüß et al., 2001; Rego and Li, 2010; Orton et al., 2012). The statistical dependence of these variables can be used as a basis for compound-flooding risk assessment (Nasr et al., 2021; Santos et al., 2021; Jane et al., 2022). Ideally, such analysis should also incorporate the influence of tides in shallow water.

The tides are a deterministic variable, which makes them relatively easy to predict (Pugh and Woodworth, 2014). However, when tidal waves propagate into an estuary, they can be strongly affected by the local morphology, a process which can be modified by the NTR (Proudman, 1955a, 1955b; Rossiter, 1961). The morphology can cause tidal transformations (e.g., amplification, dampening, tidal asymmetry) (Khojasteh et al., 2021) and enhance non-linear interactions between tides and surges (Wolf, 1981). A tidal wave can be amplified because of the gradual decrease of the width or depth of the estuary — processes called funnelling and shoaling, respectively (van Rijn, 2011). Also, tidal waves can be amplified due to reflection and resonance effects. Tidal reflection occurs when a tidal wave encounters an obstacle on the bed or banks of the estuary (e.g., rigid wall, abrupt shallowing). Friction at the estuarine bed causes the dampening of a tidal wave. Tidal asymmetry occurs when extensive tidal flats exist

within an estuary. These slow the tidal wave celerity and cause changes in the tide phase that consequently induce ebb or flood dominance in the tidal regime. To investigate the effects of bed friction on the magnitude and phase of the tides, the differences between principal lunar (M_2) and fourth-order lunar (M_4) are often analysed (Speer and Aubrey, 1985). M_4 is a shallow-water harmonic constituent generated by the tide's interaction with the bed friction and morphology. In addition to the M_4, the amplification of other shallow-water harmonics can be used for the same purpose.

Tide-surge interaction (TSI) is significant and occurs to varying degrees in shallow seas and estuaries (Wolf, 1981). The main mechanism for TSI is mutual phase alteration. For instance, a positive surge increases the speed of the tidal propagation, whereas a negative surge decreases the speed of the tidal wave (Proudman, 1955a, 1955b; Rossiter, 1961). This mechanism causes the maximum surges to occur on the rising or falling tide, depending on whether the tide is progressive or standing (Doodson, 1929; Wolf, 1981; Horsburgh and Wilson, 2007). Some studies have analysed the shallow-water equations in detail and have identified that the non-linear terms (the shallow-water effect (water depth), advective term, and bottom friction term) are the main contributors to the TSI (Flather, 2001; Zhang et al., 2010). These are also the terms that cause tidal distortions leading to shallow water harmonics or overtides.

Numerical techniques to study TSI often consist of first modelling the astronomical tides and surges together and comparing the model outputs with a modelling scenario where astronomical tides and surges are simulated independently (e.g., Idier et al., 2012; Fernández-Montblanc et al., 2019). Several studies have numerically modelled TSI and show their impact on water levels around the world. For example, in the English Channel (e.g., Idier et al., 2012; Fernández-Montblanc et al., 2019) and in the Northern Sea (Fernández-Montblanc et al., 2019), the water level predictions can be underestimated if TSI is not included in the numerical simulations. Antony et al. (2020) have shown that TSI reduces the peak water level during extreme events in the Bay of Bengal. Other studies in the Gulf of Mexico (Rego and Li, 2010), the Taiwan Strait (Liu et al., 2016), the Gulf of St. Lawrence (Bernier and Thompson, 2007), the South China Sea (Zhang et al., 2017), the Australian coasts (Tang et al., 1996), and the South Korean (Park and Suh, 2012) show global interest in TSI and that it can range from few centimetres to more than a metre.

Statistical approaches have also been used to investigate the TSI. Pioneering studies were focused on the United Kingdom and the North Sea coasts (Dixon and Tawn, 1994; Haigh et al., 2010). Firstly, Dixon and Tawn (1994) proposed a statistical framework to identify whether tide and surge are independent based on hourly observations. This method selects the highest 1% of the NTRs and determines the tidal level at which they occur. Later, Haigh et al. (2010) modified Dixon and Tawn (1994) and proposed a method based on clustering extreme NTRs according to their time of occurrence relative to the closest high tide. Recently, Arns et al. (2020) investigated the TSI by analysing the statistical dependence of tides and surges during extreme water levels rather than analysing the extreme NTRs and the corresponding astronomical tide independently. In the same work, Arns et al. developed a statistical model to estimate the TSI globally, by applying copula methods to a dataset comprising more than 150 tide gauges worldwide. However, the authors validated the statistical model only for the German Bight and only with numerical modelling output. Ultimately, Arns et al (2020) showed that the extreme water level can be overestimated by up to 70 cm worldwide if interactions between astronomical tide and NTR are not considered in the extreme value analysis.

The statistical assessment of extreme water levels applies block maxima or peaks over threshold (POT) methods. Usually, the term still water level (SWL) is used to assess local water level maxima. Here, SWL is defined as the water level obtained after the historical sea level and surface wave signal are removed from the total water level, therefore isolating fluctuations associated with the tide and NTR. The blocking maxima method is not affected by TSI because it calculates the extreme events by using the maximum SWL over a period of time (e.g., annual maximums). However, the method requires long time-period records to capture a representative number of extreme events to fit a maximum extreme value function (e.g., the Generalized Extreme Value (GEV)). The POT method is applied where only short-period records are available because it provides a greater number of extreme events for analysis. The POT method selects the extreme events of a specific variable (e.g., tide, NTR, water level) over a threshold (e.g., 99th quantile). Thus, this method is sensitive to uncertainties in the determination of the threshold (e.g., Scarrott and MacDonald, 2012; Naderi and Siadatmousavi, 2023). Several joint probability techniques have been applied to make the fit of extreme SWLs to an extreme-value analysis function more robust. One is the skew-surge joint probability method (SSJPM) (Batstone et al., 2013).

The SSJPM first calculates the corresponding skew-surge for each SWL peak and tide in a time series. The skew-surge is the difference between the peak of SWL and the peak of the tide within the same tide cycle in which the surge occurs. This means that the effects of the change in the phase of a tidal wave (i.e., tidal wave deformation) induced by the changing water depth as well as TSI would be considered when calculating the extreme water levels. The last step in the SSJPM is the convolution between the skew-surge and tide, which results in several synthetic water levels. These synthetic SWLs are fit to an extreme value function, overcoming the limit of block maxima techniques when applied to shorter records and providing robust results.

However, the SSJPM assumes that skew-surges and astronomical tides are independent. This assumption has been applied widely on global (Tadesse and Wahl, 2021), regional (Rueda et al.., 2019), and local (Stephens et al., 2020) scales. Williams (2016) has proven that the assumption of statistical independence between tides and skew-surges is valid for the North Atlantic. Given the number of global studies that show TSI is important, such assumptions need further investigation. Indeed, several studies have shown that skew-surges and tide are more likely to be dependent in shallow areas (Santamaria-Aguilar and Vafeidis, 2018; Arns et al.., 2020) (e.g., estuaries, bays, coasts with shallow continental shelves) where the shallow water effects, the bottom friction, and advection term can be intensified by the morphology. The highly variable Aotearoa New Zealand open coast and estuaries provide an excellent case study to explore the importance of TSI (Aotearoa is the Maōri name for New Zealand, and the dual name is now in common usage; hereafter shortened to NZ). The continental shelf of NZ is narrow and deep; consequently, the tides and surges are expected to be independent. However, water level gauges are often within complex estuarine and bay systems, and therefore TSI may play a stronger role than expected. Here the water level observations from 36 tide gauges around NZ were analysed to:

- Identify whether TSI occurs in NZ and how the regional pattern is linked with tide, surges, water level and coastal morphology setting of NZ. Are the skew-surge, NTR and tides independent in NZ?

- Understand whether interactions between surge and tides affect the magnitude of the extreme water levels.

- Determine whether and how TSI and estuarine morphology impact the rate of co-occurrence of extreme events outside and inside the same estuary.

The manuscript is organised as follows. Section 3.2 details the regime of tides, surges, extreme water levels, and sea level rise in NZ. Section 3.3 explains the main methods applied in five subsections, which can be divided into the data (Sec. 3.3.1–3.3.4) and the numerical (Section 3.3.5) analysis. Section 3.4 is the results. Section 3.5 is the discussion part, which focuses on how the magnitude and frequency of extreme water levels are affected by the interactions between tides, surges, and estuarine morphology. Section 3.6 is the conclusions.

3.2 Aotearoa New Zealand tide and NTR characteristics

NZ has a complex morphological setting and is exposed to diverse meteo-oceanographic conditions during coastal flooding events. The main driver for extreme water levels in NZ is the perigean spring tide combined with moderate atmospheric-response surges (Stephens et al., 2020). This means that NZ's coastal flood hazard climate is tide-dominant, where the tidal range dominates the water level height rather than the storm surge and wave setup (Rueda et al., 2019).

Figure 3.1 shows the general geographical setting of NZ and the main study locations. The tidal regime is mixed semi-diurnal and mostly meso-tidal (2–4 m tidal range), although with some micro-tidal (< 2m range) locations (e.g., Wellington). Tides flow in the west-east orientation through the constricted Cook Strait (which separates the North Island and the South Island, Figure 3.1). The constriction causes the largest tides to occur near Nelson (Site 28, Figure 3.1) and the smallest tides at Wellington (Site 18, Figure 3.1). The largest tides occur in the west coast due in part to the larger amplitude of the S2 constituent. Hume et al. (2016) have classified all hydro systems of Aotearoa New Zealand; most estuaries in NZ are permanently connected to the ocean through one or more entrances. These systems have a complex morphology, with various geometries and extensive intertidal zones — which in some cases, can be more than 90% of the estuary's total area.

NZ does not experience large NTRs relative to other places in the world because of its deep and narrow continental shelf. NTRs are limited to mostly < 0.5 m, approximately 25 % of the average tidal range (Stephens et al., 2020). However, Stephens et al. 2020 showed that larger NTRs and skew-surges can occur — the maximum NTR ever observed was 2.26 m at Jackson Bay on 1st February 2018; the largest skew-surge was 1.15 m and occurred at Raglan on the 6th of May 2013. The seasonality of extreme water levels and NTR in NZ closely follows the seasonal mean sea-level anomaly (MSLA) pattern. Consequently, even small sea-level rise (SLR) will potentially increase the frequency of presently rare extreme sea levels. This is a particular issue for NZ because the SLR trend is 1.88 ± 0.1 mm yr−1 (Bell et al., 2022), and most parts of the country are subsiding due to tectonic activity (Beavan and Litchfield, 2012). The SLR, vertical land motion and extreme water levels threaten the NZ's estuaries and harbours due to their ecological importance or because coastal communities and maritime trade are concentrated in these regions (e.g., Auckland, Tauranga, Wellington, Dunedin).

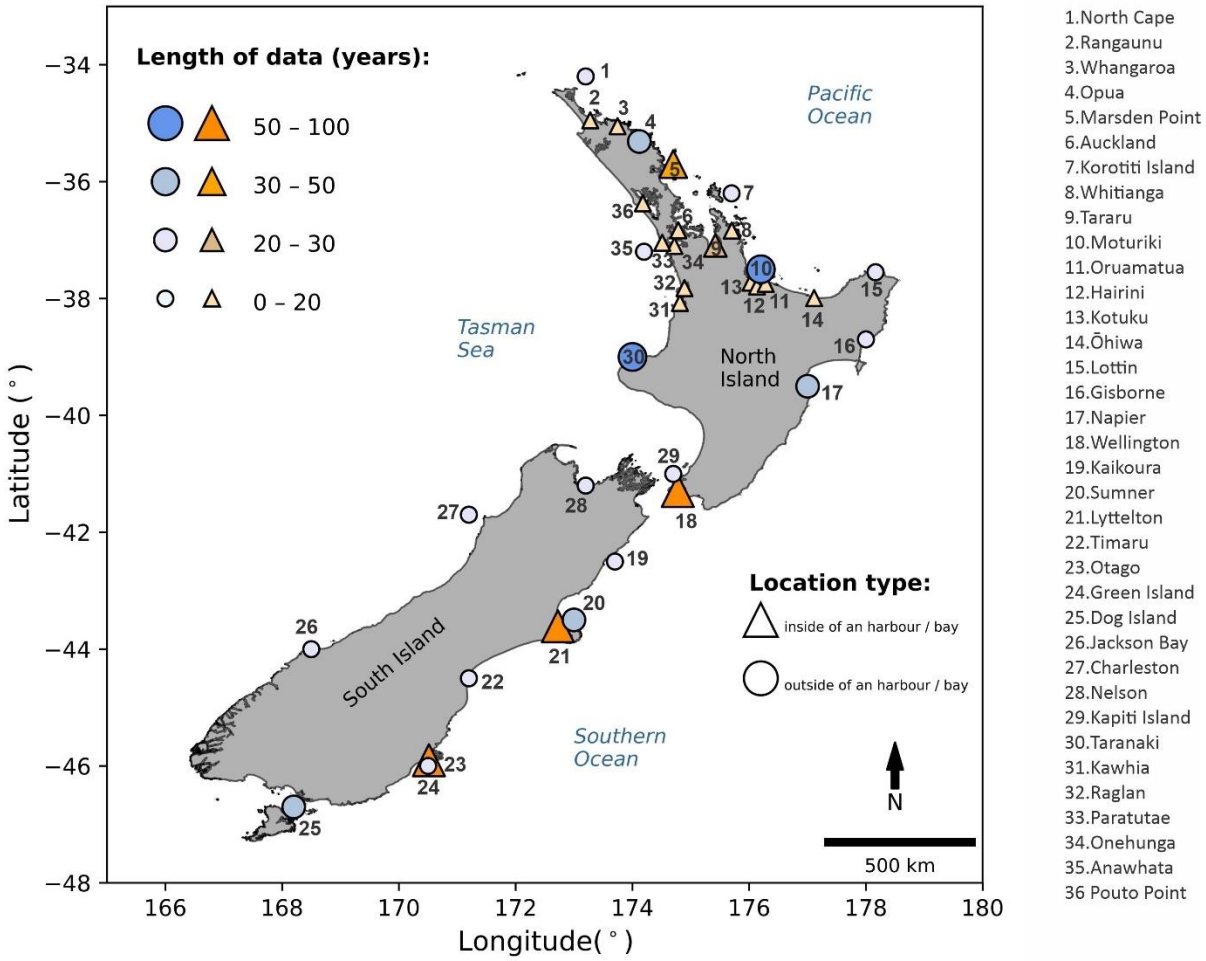

Figure 3.1. Location of the tide gauges used in the data analysis.

3.3 Methods

The methods applied in the manuscript can be divided into two parts: a regional analysis, based on observed data, and the analysis of the TSI and morphological effects, based on data and a numerical modelling investigation. Figure 3.2 shows a general flow chart of the methods. Firstly, the database is described (Section 3.3.1) as well as the processing of the water levels observed with 36 tide gauges (Section 3.3.2). After, in Section 3.3.3–3.3.4, the methods that were applied in the regional assessment of the TSI (which includes NTR, skew-surge, and astronomical tide) are described. In Section 3.3.5, the methods for analysing the effects of the interaction between the estuarine morphology, tide, and surges (i.e., NTR and skew-surge) on the magnitude and co-occurrence of extreme water levels within an estuary are shown.

3.3.1 Study Site and database

The present study analysed the observed water level of 36 different tide gauges around NZ (Figure 3.1). The period of observations ranges from 6 to 87 years. A complete list of tide stations and associated metadata are shown in Table A.1. The NZ sea-level records analysed here are from various locations, including wave-exposed open coasts, inside port breakwaters, or mounted on wharves inside estuaries, so they have different levels of wave exposure, which requires specific data pre-processing, which is described in Section 3.3.2. All observations were used for the regional analysis in the first part of the study.

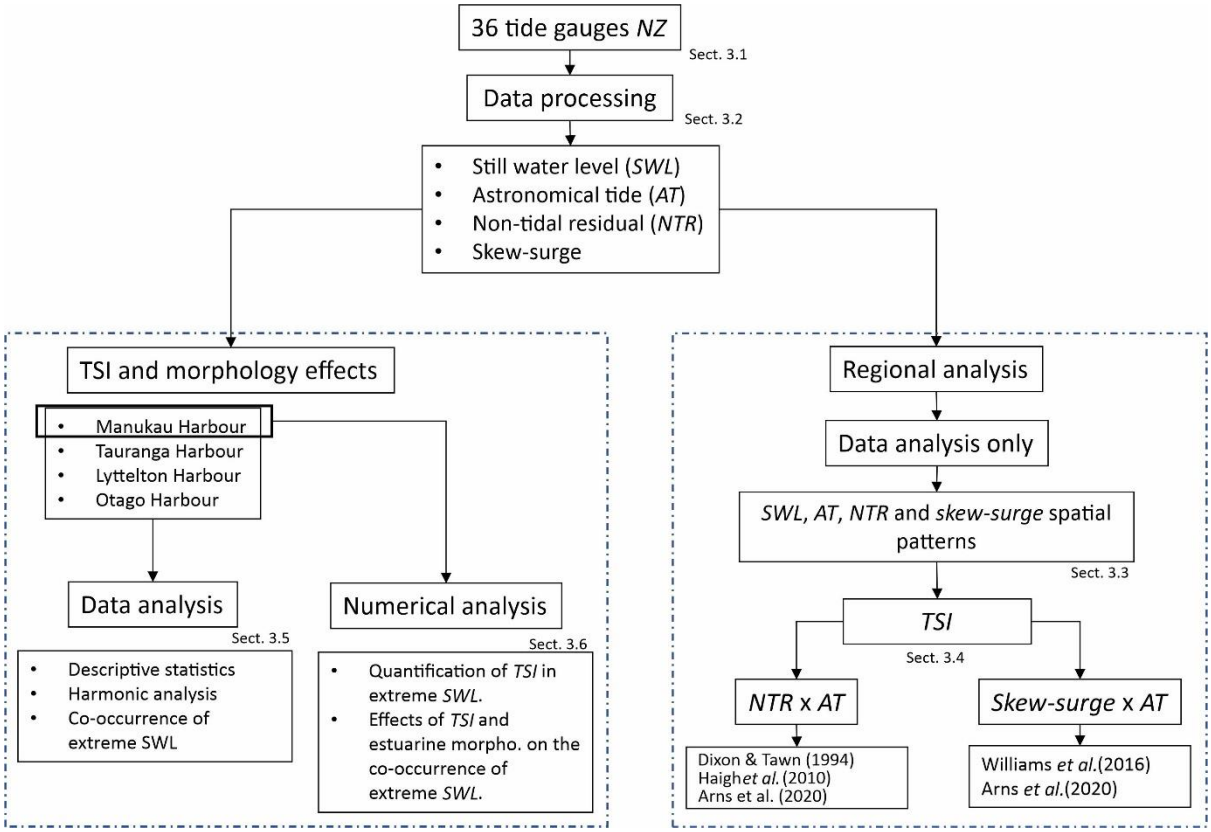

Figure 3.2. Flow chart of the methods.

Four different locations were selected for the second part of the study, which was to analyse the combined effect of the estuarine morphology (i.e., bathymetry and geometry), tide, surges and their interactions: (1) Tauranga Harbour, with Moturiki and Hairini tide gauges; (2) Manukau Harbour, with Anawhata and Onehunga tide gauges; (3) Lyttelton Harbour, with Sumner and Port Lyttelton tide gauges; (4) Otago Harbour, with Green Island and Port Dunedin tide gauges. The reason for choosing these estuaries is that they had at least one tide gauge record inside and outside the estuary with an overlap duration of ≥ 10-year.

The four estuaries have different morphology and dynamical characteristics. Manukau and Tauranga harbours have constricted mouths, extensive total areas (~365 km2 and ~200 km2, respectively), and vast intertidal zones in proportion to the entire surface area of the estuary (60% and 77%, respectively). However, Manukau Harbour is more extensive and has a deeper main channel (up to 30 m close to the mouth) than Tauranga Harbour (15 m at the Port of Tauranga). Tauranga Harbour also has estuarine subsystems (e.g. Hairini and Oruamatua) caused by the underlying volcanic geology of the region. Otago and Lyttelton harbours are

smaller in their total area and have less than half of their estuary area covered by tidal flats (45% and 16%, respectively).

To further study the effects of the estuarine morphology on the tides, NTR, and TSI, a numerical modelling study was set up for Manukau Harbour, detailed in the Section 3.3.5. For the model, topo-bathymetric and hydrodynamic data were needed. For the coastal and estuarine areas of the model grid, the depth data used were obtained from digital nautical charts (no 4314 and 4315) surveyed by New Zealand Navy and topography data from LiDAR aero surveys executed by Land Information New Zealand (LINZ). The LiDAR data were taken between 2016–2017 with a spatial resolution of 1m×1m and accuracy of 20 cm (vertical) and 60 cm (horizontal). Both bathymetry and topography data for the Manukau coast and Harbour are freely and publicly available from the LINZ data portal (https://data.linz.govt.nz/). For the oceanic part of the numerical grid, bathymetry data (250 m spatial resolution) from the National Institute for Water and Atmospheric Research (NIWA) was used (https://niwa.co.nz/). The hydrodynamic data used in the model's boundary conditions are the still water level (SWL) derived from the data pre-processing described in Section 3.3.2.

3.3.2 Data pre-processing

The data pre-processing for the water level records follows Stephens et al. (2020) and consisted of five steps applied for each of the 36 tide gauges. Firstly, a 15 min running average filter was used to reduce the effect of infragravity and tsunami waves; secondly, all the water level data were subsampled to 1 h intervals to homogenize all the time series to the same time resolution; thirdly, the effects of historical SLR were filtered out from the water level records by subtracting the 1-year-running average of the water level record. The third step results in a filtered water level record (SWL), where water level variations are relative to MSL=0 m. Fourthly, the SWL was separated into its main components (i.e. astronomical tide and NTR) by predicting the 67 standard astronomical components of the tide using the Unified Tidal Analysis package (Codiga, 2011) and subtracting the astronomical tide from the SWL to obtain the NTR. In addition, the skew-surge was estimated by calculating the height difference between the peak of the SWL and the closest high tide.

3.3.3 Regional distribution of extreme SWL, astronomical tide, NTR, and skew-surge

To analyse the regional distribution of SWL, astronomical tide, NTR, and skew-surge, the 98th, 99th, and 99.8th percentiles of these four variables were calculated. The percentiles were chosen to focus on extreme values of the SWL, astronomical tide, NTR, and skew-surges records at each of the 36 tide gauges. The 99.8th percentile was chosen for the analysis because it represents the extreme SWL for NZ well, according to Stephens et al. (2020), which is further explained in Section 3.3.4.

3.3.4 Tide-surge interaction (TSI)

The techniques used to analyse the degree of tide and surge interactions can be divided into two categories. The first considers a null hypothesis that the extremes of NTR or skew-surge and their corresponding astronomical tide are independent, which means that any surge (i.e., NTR or skew-surge) could happen at any tidal level (Dixon and Tawn, 1994; Haigh et al., 2010; Williams 2016). In the second category, the statistical dependence between astronomical tides and surges is analysed (i.e., NTR or skew-surges) during extreme SWLs. The null hypothesis is that tides and surges are dependent, which means that TSI occurs, and the highest surges will not necessarily coincide with the highest tides (Arns et al., 2020).

The tide-surge statistical dependence was tested in each one of the 36 tide gauges using four different techniques: Dixon and Tawn (1994), Haigh et al. (2010), Williams et al. (2016), and Arns et al. (2020). The first two techniques aim to detect the degree of the TSI by analysing the differences in distributions of the extreme NTR at different tidal heights or at different times of occurrence relative to the high tide, respectively. The third method assumes independence between surges and astronomical tides and calculates the correlation between the extreme skew-surges and the corresponding astronomical tide. The fourth method assesses the dependence between astronomical tides and surges (i.e., NTR or skew-surge) in the extreme SWL.

The Dixon and Tawn (1994) method splits the tidal range into five bins between low astronomic tide and high astronomic tide. The highest 1% of hourly NTR are placed in each range based on the tide height associated with the time of their occurrence. To establish the statistical significance, a chi-squared (χ^2) test is performed:

$$\chi^2 = \sum_{n=1}^{5} (N_i - e)^2 / e \qquad (3.1)$$

Where N_i is the number of NTR heights in bin i and e is the expected number if there were no TSI:

$$e = \sum_{i=1}^{5} N_i / 5 \qquad (3.2)$$

The expected number of events for the null hypothesis (no interaction) — at the 95% significance level — from the chi-squared distribution is $\chi^2_{4,0.95} \leq 9.5$, where the number of degrees of freedom is 4 (1 less than the number of bins). Therefore, if χ^2 from Equation (3.1) is less than 9.5, there is a 95% probability of no interaction, but a value greater than 9.5 is indicative of an interaction.

The Haigh et al. (2010) method selects the 1% highest NTRs and clusters them in hourly bins for 6 hours before and after the time of the high tide. The method assesses whether there is a significant relationship between NTR and tides, similarly to Dixon and Tawn (1994), using the chi-squared test (Equation 3.1). However, the null hypothesis, which is no interaction, is considered as $\chi^2_{12,0.95} \leq 21$ — since there 13 values, there are more degrees of freedom —. Thus, if $\chi^2 \geq 21$, interactions between astronomical tides and storm surges are more likely to occur.

The Williams et al. (2016) and the Arns et al. (2020) methods test whether skew-surges and tides are independent using different statistical tests. Both establish statistical dependence between these variables by calculating Kendall's rank correlation (τ) (Kendall, 1938). The coefficient can have values between -1 and 1, where 0 indicates no correlation and 1 (-1) a perfect relationship (disagreement). There is no interaction if the correlation is insignificant ($\rho \geq 0.05$). Conversely, when the correlation is significant ($\rho \leq 0.05$), TSI occurs. Rank-ordered methods have been widely applied to study non-linear statistical relationships in coastal science because they are less sensitive to outliers and skewed distribution than Pearson's correlation and do not depend on assumptions of linearity between the variables.

Williams et al. (2016) assume that astronomical tides and skew-surges are independent during extreme skew-surges. The method selects the largest 1% of the skew-surges and the corresponding astronomical tide and calculates the coefficient between the variables. Here, the skew-surge was calculated for every SWL peak by subtracting it from the closest high-tide

level within ± 6 h. Then, the Kendall coefficient was calculated by selecting skew-surges over a threshold of the 98th, 99th, and 99.8th percentiles and the corresponding astronomical tide.

The Arns et al. (2020) method assumes that NTR (and skew-surges) depend on the astronomical tides at the largest SWL. The method first selects the extreme SWLs in a time series. In this study, the Stephens et al. (2020) approach was used in which extreme events of SWL were selected by applying peaks over threshold (POT) using the 99.8th percentile with a declustering scheme of 3 days between events (to ensure that events are independent from each other). This is required for a statistically robust calculation of extreme values using maxima techniques like POT (Coles, 2001). According to Stephens et al. (2020), these are the threshold and periods that are ideal for selecting SWL extreme events in NZ, and which results in an average of 5 events per year for NZ's tide gauges. Extreme events were also selected by using the 98th and 99th percentiles of the SWL to check how the TSI affects different percentiles of SWL and vice versa.

Furthermore, the Arns et al. (2020) method can statistically quantify the TSI effect in the extreme SWL. The statistical model was built based on global analyses of tidal gauges. It uses a copula-based method to generate extreme synthetic SWL considering a scenario where the astronomical tides and NTR are dependent (i.e., $\tau \neq 0$) and another where these two variables are independent (i.e., $\tau = 0$). The difference in the simulated SWL between the scenarios is fitted to a multiple regression model as a function of the rank correlation between the observed NTR and astronomical tide (τ) in a specific quantile. Thus, the average difference in centimetres for a given percentile of the SWL can be expressed by the following:

$$TSI \sim a + b * \tau + c * \tau^2 + d * \tau^3 \quad (3.3)$$

With the coefficients a =-21, b = -151, c = -419, and d= -463 for the percentile 98th; and a =-21, b = -164, c = -461, d= -517, for the percentile 99th. To calculate the TSI for the percentile 99.8th, which was not calculated in Arns et al. (2020), the coefficients were assumed to be the same as for the 99th percentile. Each tide gauge was treated independently, considering the whole time range.

Past work has suggested that TSI is larger in shallow areas. In this section the focus is on the enclosed shallow areas of the database, to test whether they are more likely to have TSI, what is the likely effect of that, and why might that occur (friction, morphology…).

3.3.4.1 Estuarine morphologic attributes and TSI

The correlation between the TSI found by applying the Arns et al. (2020) statistical model and the morphologic attributes of estuaries was analysed. For this analysis, only tide gauges located within estuaries were considered, which resulted in 14 tide gauges. We choose four morphologic attributes: the coverage of the intertidal zone relative to the surface area of the estuary; the average depth of the estuary; the surface area of the estuary; and the mouth width of the estuary. The attributes were obtained from the Hume et al. (2016) database.

3.3.4.2 Transformations in tides, NTR, and skew-surges in shallow enclosed areas.

The goal of this Section was to determine whether the TSI is generated within or just outside the estuaries. For this analysis only the harbours with one tide gauge record inside and outside the estuary with observation periods that overlap for at least ten years were selected, as described in Section 3.3.1. This selection resulted in four different estuaries: Manukau, Tauranga, Lyttelton, and Otago Harbour. This analysis was aimed at observing the attenuation/enhancement of the extreme events that occur in areas outside and propagate within the estuary, and the role that morphology of the estuary and other local physical processes may play in that process. The effects of the estuary's morphology in the SWL were identified by performing two different analyses.

Firstly, the probability distribution and the quantiles of the SWL, astronomical tide, NTR, and skew-surge of the tide gauges inside and outside the harbour were compared. The probability distribution comparison was used to identify tidal asymmetry (measured by the skewness of the distribution) and the quantile comparison to identify amplification/dampening of the SWL, astronomical tide, and increase/decrease of the NTR within the harbour. To quantify the quantile comparison, the differences between the 99.8th quantile of the gauges located both inside and outside were calculated.

Secondly, the rate of co-occurrence between extreme SWLs outside and inside the harbours was determined. This analysis shows the practical implications of TSI within estuaries; for

example, understanding how useful sensors outside estuaries are for determining extremes inside estuaries. For each of the four estuaries, the extreme SWL events were extracted in two ways. First, similar to Section 3.3.4 — by applying POT (99.8th percentile) and a declustering scheme of three days — but only considering the period when the records from the tide gauges located inside and outside the harbour coincide. Second, the co-occurrence of the SWL annual maximum between the tidal gauges was considered. For the POT selection, time windows of 6h before and after each extreme event were applied to ensure that the distances between tide gauges and storm durations were considered. For the maxima selection, the number of SWL annual maxima that co-occur within 12 h prior or later to each maxima event were counted.

3.3.4.3 Harmonic analysis

One indicator that TSI is likely to be important is if nonlinear transfer of tidal energy between different tidal harmonics occurs. This is because TSI is caused by the same terms in the shallow water equations as tidal distortions. For instance, the non-linear interactions between the principal astronomical constituents (e.g., M_2, S_2, and N_2), bed friction, and morphology can generate shallow-water constituents (e.g., M_4, MS_4, MN_4). The approach of Speer and Aubrey (1985) was applied to calculate the degree of interaction between M_2 and M_4 amplitudes (aM_4/aM_2) and phases ($2gM_2/gM_4$) for all 36 tide gauges in this study. The Kendall ranked coefficient was then calculated between the aM_4/aM_2 and the τ coefficient calculated following Arns et al (2020), where τ is calculated using the skew-surge and astronomical tide associated with the extreme SWLs (Section 3.3.4). The aim of this analysis is to test whether TSI and aM_4/aM_2 are correlated. In addition, the differences of aM_4/aM_2 and $2gM_2/gM_4$ were analysed between tide gauges located inside and outside our four focus estuaries: Tauranga, Manukau, Lyttelton, and Otago Harbour. The simple amplification of the M_4 component inside an estuary can indicate that the non-linear interactions are an important process. The phase relation between the M_2 and the M_4 indicates the flood and/or the ebb dominance. The relation between amplitudes of M_2 and M_4 can indicate if there is spectral energy transfer in the tidal wave between these two harmonics.

3.3.5 Hydrodynamic modelling

To further investigate the interactions between tide, surges and morphology within estuaries, a hydrodynamic model was constructed for Manukau Harbour to address two objectives. First, to quantify the TSI occurring at the coast and inside the harbour. Second, to elucidate the

physical mechanism of how the estuarine morphology affects the TSI and potentially contributes to the co-occurrence of extreme SWLs inside and outside the harbour. This estuary was chosen because tidal amplification is known to occur there and it has already been studied (Bell et al., 1998). In addition, Manukau Harbour is located in Auckland, the most populated city in NZ, with the biggest international airport. These factors give Manukau Harbour remarkable social-economic importance. The software DELFT3D-FLOW was used for the hydrodynamic model and 8 scenarios (SC1–SC8 detailed in Table 3.1). The model solves the hydrodynamic equations in two dimensions by averaging the depth velocity. Since Manukau Harbour does not receive large fluvial discharges and summer stratification is unlikely to happen because of the strong tidal currents and shallow domain (Bell et al., 1998), using a two-dimension model can be considered appropriate for this case (a test with a 5-layer 3D domain made < 1 cm difference in water levels within the domain).

Table 3.1 Simulation scenarios for modelling the effects of TSI and estuarine morphology on the co-occurrence of extreme SWLs.

Simulation scenarios	Changes in comparison to control scenario
SC1	Control scenario. Forced with SWL.
SC2	Astronomical forcing. Forced with astronomical tide only
SC3	Surge forcing. Forced with NTR only
SC4	Bed Roughness. Homogeneous Chézy coefficient (65 m1/2s-1)
SC5	Depth of the channel. We made the areas of the channel with depth ≥ 15m shallower by 10m
C6	Elevation of the intertidal zone. We increase the elevation of the intertidal zone by +1m
SC7	Positive storm surge. We forced the model with astronomical constituents and a constant increase in the mean sea level equal to the 99.8th percentile NTR

For the boundary conditions, topo-bathymetric and hydrodynamic data were acquired as described in Section 3.3.1. Figure 3.3 shows the topo-bathymetric data interpolated in the model domain and the location of Paratutae (33), Onehunga (34) and Anawhata (35). In addition, Cornwallis, Weymouth and Clarks Beach locations are also shown in the Figure 3.3 to help describe results according to the region of Manukau Harbour. The model was forced at the northern boundary with the astronomical tidal constituents, SWL, and NTR (depending on the scenario) calculated for the Anawhata tide gauge, as described in Section 3.3.2. The northern boundary was chosen because the tide on the west coast propagates from north to

south. Open boundaries were set using Neuman conditions at the western and the southern boundaries at the coast. The direct effects of local wind were not considered (e.g., wind-setup, currents, and vertical flows), because the focus is to isolate the effect of morphology on TSI and, moreover, there are insufficient observations to warrant an increase in model complexity (e.g., no in-situ current measurements exist).

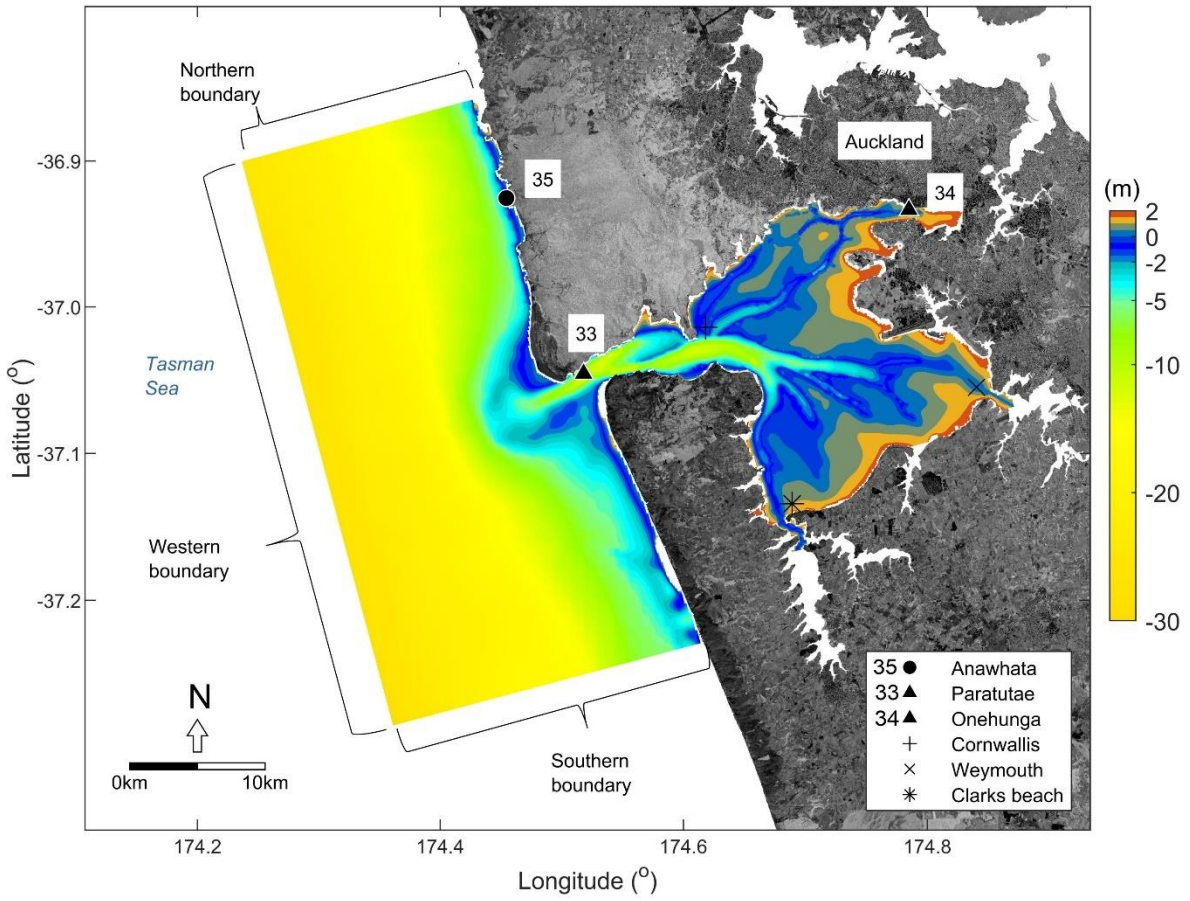

Figure 3.3. Hydrodynamical model setup. Interpolated topo-bathymetric data in the model domain. Positive (negative) values are used for areas above (below) the mean-sea level. The location of Paratutae (33), Onehunga (34), and Anawhata (35) tide gauges is also shown. Note that the numbering is used based on Figure 3.1. Cornwallis, Weymouth and Clarks Beach are reference sites used to help describe the results. Background image: aerial photos from Land Information New Zealand (LINZ). Projection: WGS84.

Although the model was used in an exploratory sense to understand the relevant physical drivers, it was still calibrated against available data to ensure simulations were realistic. Model calibration was performed by testing a range of bed roughness values by modifying the Chézy coefficient = 40–80 $m^{1/2}s^{-1}$ (see Figure A.1). The optimum Chézy was selected by comparing the modelled and observed differences in amplification between Anawhata and Onehunga tidal

gauges at the maximum SWL, and by calculating the root mean squared error over the entire simulation period. The result was a homogeneous bed roughness of Chézy coefficient = 50 $m^{1/2}s^{-1}$ through the model domain, which showed the best match to the observed data. Note that although the Chézy coefficient = 45 $m^{1/2}s^{-1}$ showed the best amplification, it was less accurate in terms of root mean squared error. See Figure A.1, A.2, and Table A.2 for the detailed model setup and calibration.

3.3.5.1 Numerical quantification of TSI on extreme SWL

To determine the magnitude of the TSI, the method of Idier et al. (2012) was used, in which three different simulation scenarios were set up. In the first scenario (SC1), the model was forced by the SWL observed at the Anawhata tide gauge. The SC1 was the control scenario, aimed at simulating a condition where tide and surge are dependent, and TSI occurs. The second scenario (SC2) was forced with the astronomical tidal constituents only. In the third scenario (SC3), the model was forced using the NTR only. The SC2 and SC3 outputs are summed to represent the SWL case in which tide and surge interactions do not occur. Finally, to estimate the magnitude of TSI, the difference between SC1 and (SC2+SC3) was calculated at the locations of the Anawhata, Paratutae and Onehunga tide gauges.

3.3.5.2 Modelling the effects of estuarine morphology and bed friction on the TSI.

As described in Section 3.1, the shallow-water effect and bottom friction are likely some of the main contributors to TSI. To assess the importance of each of these elements, and how they impact the TSI throughout the Harbour domain, the scenarios SC4, SC5, and SC6 were set up. SC4 explores the effects of bed friction, by homogenously increasing the Chézy coefficient to 65 $m^{1/2}s^{-1}$ over the entire model domain. SC5 and SC6 explores how changes in morphology can affect TSI, by making the main channel shallower (+10 m, close to the entrance) and the intertidal zones shallower (+1m), respectively as described in Table 3.1. For each one of the scenarios, the TSI was calculated for the model domain, considering the maximum TSI at each grid cell over the entire simulation period. Additionally, TSI on the peaks of SWL over the 99.8^{th} percentile was calculated for Onehunga.

3.3.5.3 Modelling the effects of TSI on the tidal amplification

To further investigate the effect of the surges on tidal amplification, the astronomical tide at a constant positive surge of NTR = 99.8th percentile (SC7) and a constant negative surge of NTR = 5th percentile (SC8) were simulated. To compare the results of these scenarios, the maximum water level at each grid cell of each simulation scenario was calculated (i.e., control scenario and SC7 and SC8) through the entire simulation period. Then, the amplification factor of each simulation scenario was calculated independently, using Equation 3.4:

$$Amp.Fac. = \frac{peak\ tide\ inside}{peak\ tide\ outside} - 1 \qquad (3.4)$$

where the peak tide inside is anywhere inside the estuary (location of a tide gauge or model grid cell) and peak tide outside is the model boundary condition or observed data at Anawhata tide gauge. Finally, for each simulation scenario (i.e., SC7 and SC8), the amplification factor of a given scenario was subtracted from the control scenario (SC1), to infer if the amplification increased (positive difference) or decreased (negative difference). Additionally, the non-linear terms (i.e., shallow-water effects, and bed friction) are assessed for their impact the NTR by calculating the amplification factor (Equation 3.4) for the SC3, which simulates only NTR over the model domain.

3.4 Results

3.4.1 Regional patterns of SWL, NTR, skew-surge, astronomical tide, and TSI occurrence.

Figure 3.4 shows the regional patterns of SWL, astronomical tide, NTR and skew-surge for the 99.8th percentile of each variable. The patterns of extremes in SWL follow the extremes of astronomical tide (Figure 3.4 A, B). The largest values of SWL and AT were found on the west coast, because the tidal range is larger. On the east coast, where the tidal range is smaller, the percentiles of SWL and AT are the smallest. Regarding the NTR, the highest values occur in the tide gauges located inside estuaries, for instance, in Raglan and Kawhia (Figure 3.4 C). The values of the skew-surge are similar to the NTR. Of the 36 tide gauges, differences between skew-surges and NTR of ≅ 0 cm occurred at 18 of them. A small difference between 1 cm and

4 cm occurred at the remaining 18 sites. The maximum difference occurs at the location of the Onehunga and Hairini tide gauges. The Table A.3 the 99.8th percentile for each variable and the difference between NTR and skew-surge for each tide gauge.

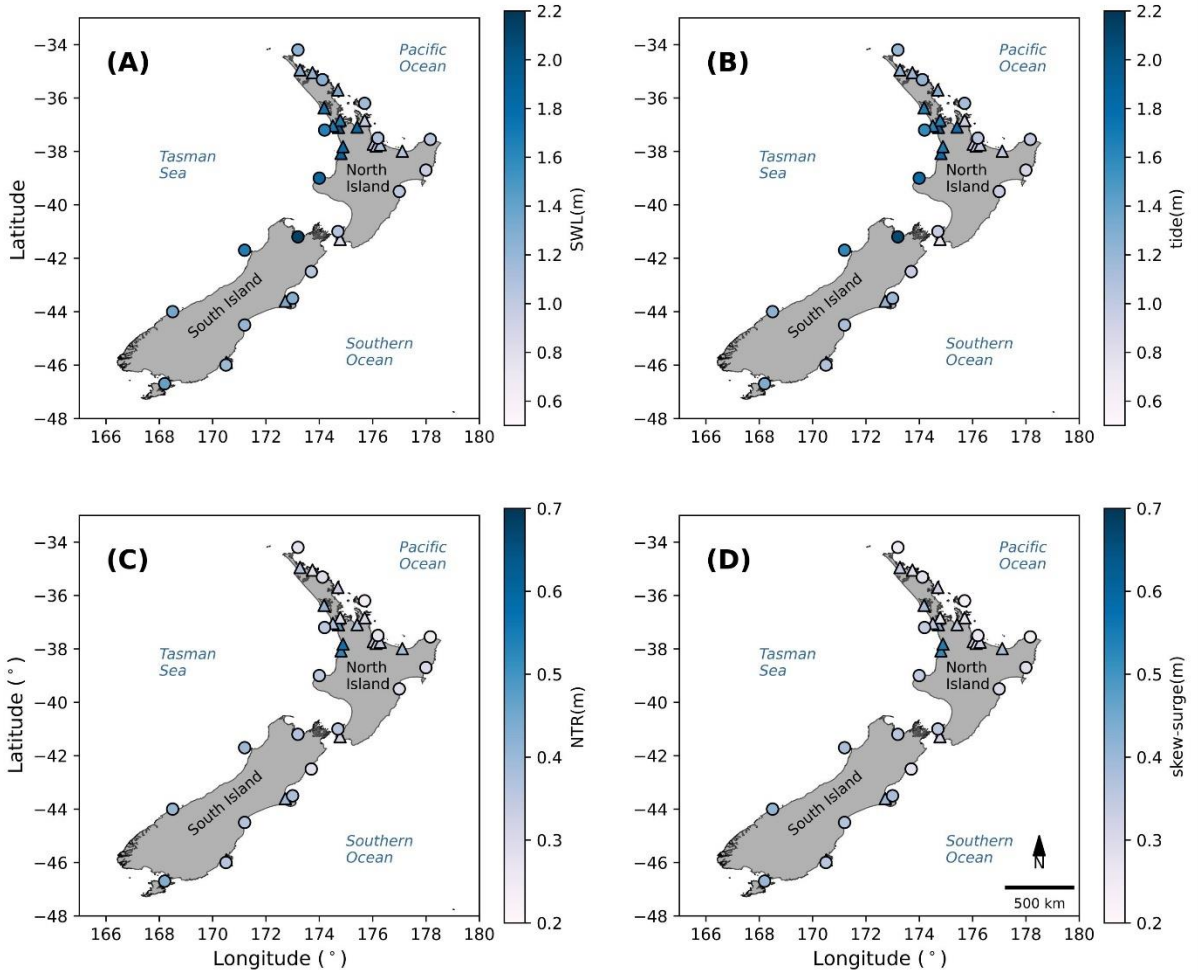

Figure 3.4 Quantile of 99.8% for SWL (A), astronomical tide (B), NTR (C), and skew-surge (D) for tide gauges around NZ. Triangles (circles) mark tide gauges located within estuaries (outside estuaries).

The highest 1% of the NTR and the corresponding astronomical tide were dependent in most of the tide gauge records located in estuaries, ports and bays, assessed using both the Dixon and Tawn (1994) ($\chi^2 \geq 9.5$), and Haigh et al (2010) ($\chi^2 \geq 21$) approaches (Figure 3.5 A and B, respectively), which means that TSI generally occurs at these sites. However, Dixon and Tawn (1994) showed that TSI does not occur at most of the exposed coastal locations (of these, TSI was only observed at Anawhata, Charleston, Dog Island, and Timaru). Conversely, the Haigh et al. (2010) approach showed dependence ($\chi^2 \geq 21$) at most of the tide gauges, even at the exposed coastal locations (NTRs are independent (i.e., TSI does not occur) at only North Cape,

Sumner, Whangaroa, and Lottin (Figure 3.5 B), and only for the largest 1%). All values of χ^2 found for both methods (Haigh et al. and Dixon and Tawn) are provided in Table A.4.

At inner estuarine locations, the largest NTRs usually occur 4 – 6 h after (+) the peak of the tide, close to the low tide. For instance, Figure 3.6 compares the Haigh et al. (2010) (I) and the Dixon and Tawn (1994) (II) analysis for Anawhata (A), Onehunga (B), Otago (C), Green Island (D), and (E) Gisborne. The Onehunga tide gauge is generally representative of inner estuarine locations (B I and II). The only location that shows similar evidence of TSI, although occurring 2–3h before (-) the peak of the tide, is in Otago Harbour (C.I). For locations outside estuaries, the effects of TSI are smaller (i.e., lower value of χ^2), which is illustrated for Anawhata, Green Island, and Gisborne in Figure 3.6 A, D, and E, respectively.

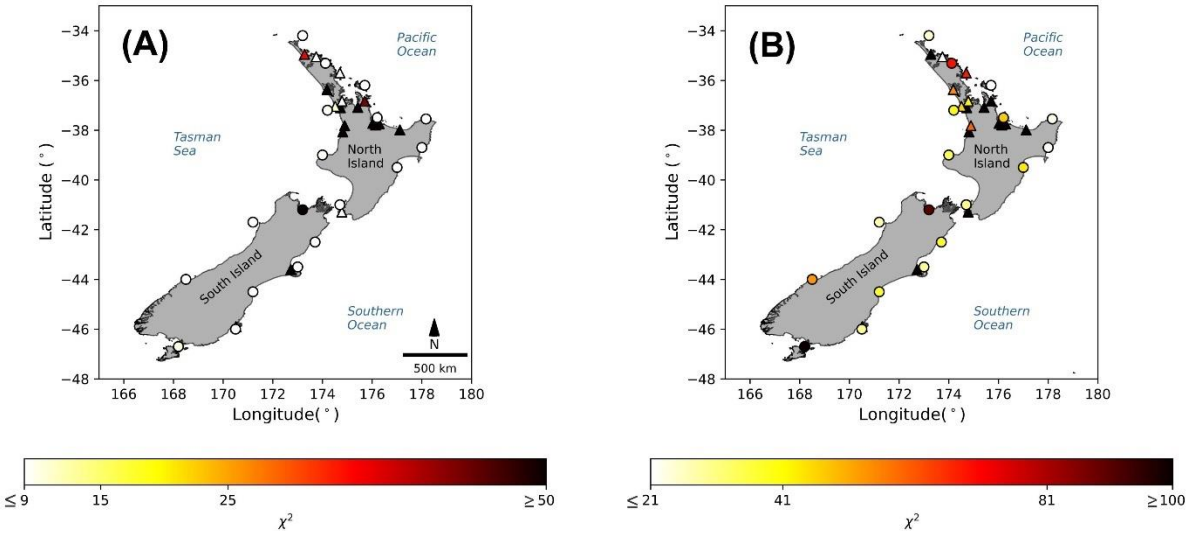

Figure 3.5. Tide and surge χ2 in different tide gauges according to Dixon and Tawn (1994) (A) and Haigh et al. (2010) (B). In (A) values ≤ (≥)9 indicate that NTR and tide are independents (dependents). Similarly, in (B) values ≤ (≥)21 indicate that NTR and tide are independents (dependents). Triangles (circles) mark tide gauges located within estuaries (outside estuaries).

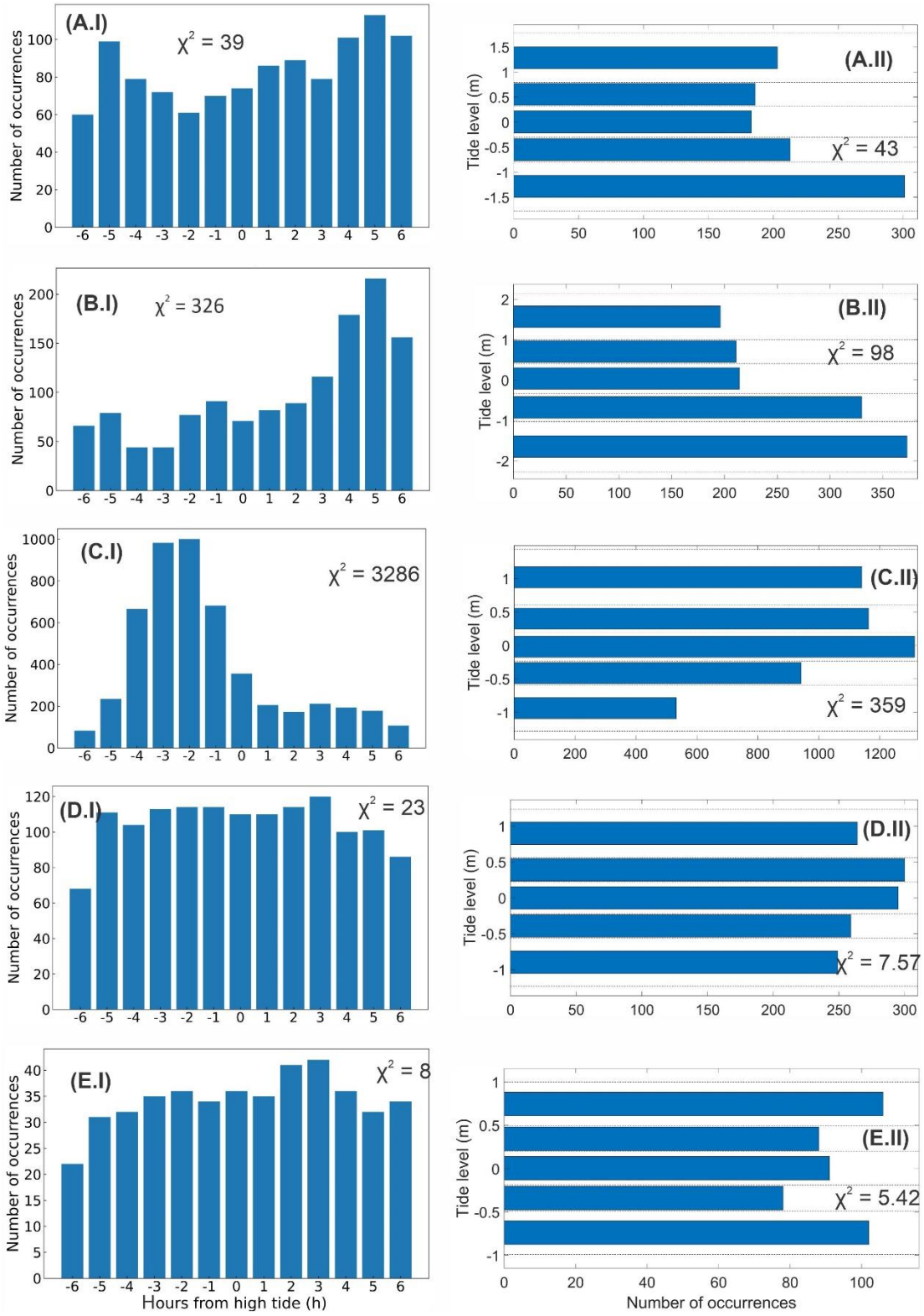

Figure 3.6. Bar plots show the resulting analysis from Haigh et al. (I) and Dixon and Tawn (II) approaches. The Haigh et al. approach shows the time difference between the largest 1% NTRs and the high tide. Dixon and Tawn's approach shows the tidal interval where the highest 1% of the NTR occurs. The panels show the resulting analysis for (A) Anawhata, (B) Onehunga, (C) Otago, (D) Green Island, (E) Gisborne. The χ2 of each analysis is also shown.

The Arns et al. (2020) approach shows a significant correlation between the NTRs and tides at all tide gauge locations during extreme SWLs (98th, 99th, and 99.8th percentiles; Figure 3.7 A I–III, respectively). The Kendall coefficient (τ) varies between -0.35 and -0.60 over all the tide gauges, meaning that the higher is the tide, the lower will be the NTR and vice-versa. The relationship is stronger (more negative) for the percentile 99.8th (III) and becomes weaker for the percentiles 99th (II), and 98th (I), in this order. Tide gauges in the inner estuarine locations (e.g., Raglan, Kawhia, Rangaunu, Whangaroa, Ohiwa) and ports (Gisborne, Napier) have the strongest τ. This analysis was performed for the relationship between skew-surge and astronomical tides, showing similar dependence of the extreme SWLs (see Table A.5).

The Arns et al. (2020) statistical model showed that the TSI is positive at most of the tide gauge locations for the different percentiles of SWL. Again, the largest TSI was found for tide gauges located inside estuaries. For instance, Figure 3.7 B.I–III shows that most of the TSI ranges between 0 to 10 cm and show small variations through all gauges locations for the 98th (I) and 99th (II) percentiles, reaching up to 12 cm at Ōhiwa. In the 99.8th percentile of SWL (B.III), the values of TSI increase at most of the tide gauges, reaching up to 27 cm at Hairini. The number of locations showing no interaction between tides and NTR (i.e., TSI values ~0 cm) is greater for the 98th and 99th percentiles than for the 99.8th percentile. At the sites where TSI $\cong$ 0, the associated τ is $\geq$ -0.35. See Table A.5 for the values of TSI at each tide gauge location.

The last method trialed, the Williams et al. (2016), was specifically designed to analyse the dependence between the skew-surges and tides. Note that skew-surge accounts for TSI by calculating the difference between peak of the SWL and the peak of the high tide, which should not be affected by phase difference caused by distortions in tide and NTR within the harbour. Ultimately, evaluating tide and skew-surge dependence is fundamental for the validation of SSJPM for use in prediction (see Section 3.1). According to the method, the highest skew-surges and the corresponding astronomical tides are independent at most locations of NZ. Significant correlations were only found between the highest skew-surges (over the 99.8th percentile) and astronomical tides at the Hairini tide gauge location. However, the correlation is low, with τ = -0.16 (see Table A.6). Surprisingly, the number of sites showing significant correlation increased as the threshold applied in the POT selection (99th and 98th percentiles) decreased. For instance, for the extreme skew-surges selected over the threshold of the 98th percentile, a total of six sites showed a significant correlation ($p \leq 0.05$). Although most sites show negative and low coefficients (range between -0.05 to -0.16).

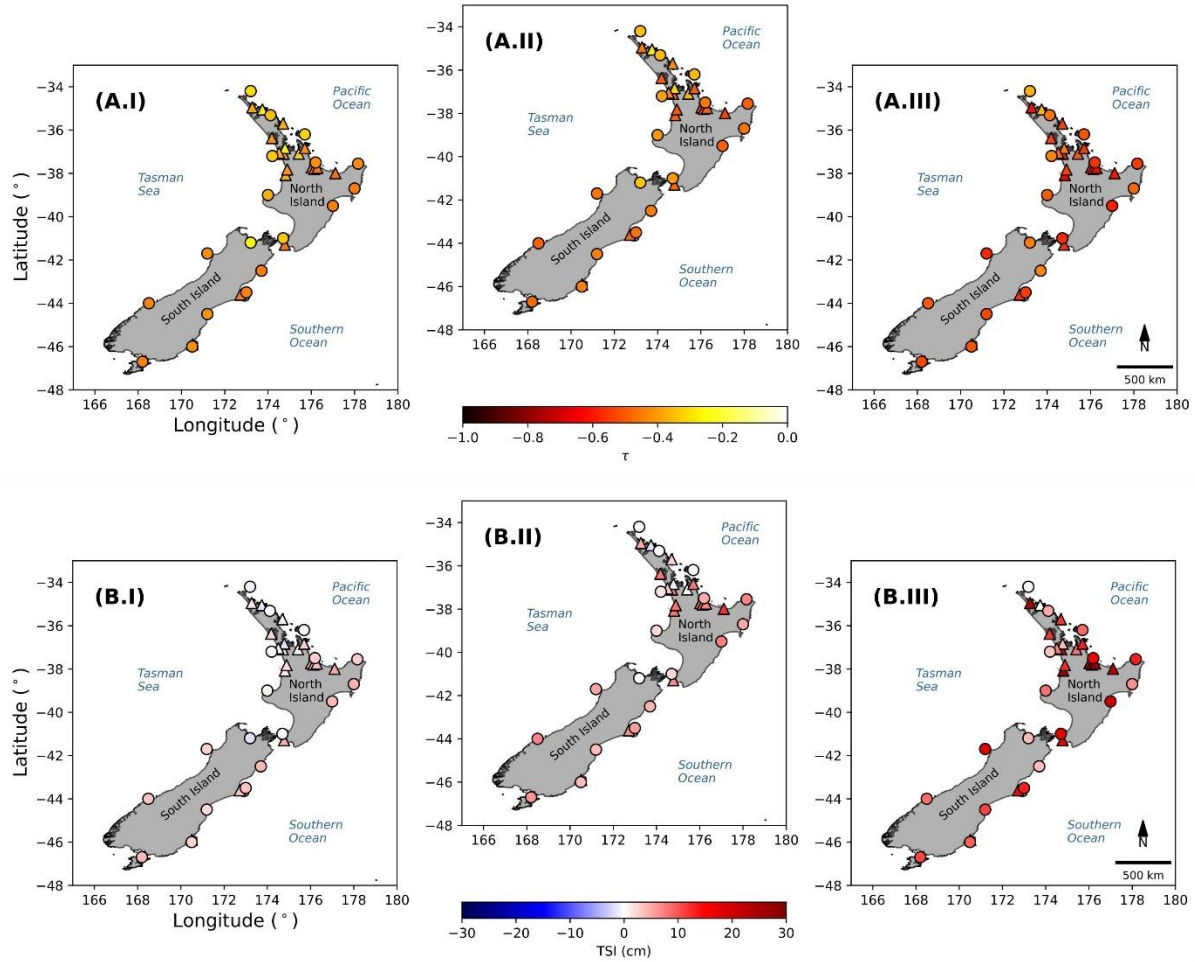

Figure 3.7. Kendall ranked coefficient (τ) (A) and TSI (B) calculated following Arns et al. (2020) (NTR x astronomical tide) corresponding to the storm events that produced an SWL ≥ 98th (I), 99th (II), and 99.8th (III) percentile. Triangles (circles) mark tide gauges located within estuaries (outside estuaries).

3.4.2 NTR and skew-surges in shallow and enclosed areas.

The only estuarine morphologic attribute (see Section 3.3.4.1) that showed any significant correlation ($p \leq 0.05$) with the coefficient τ calculated using the Arns et al. approach — dependence between NTR and astronomical tide at the 99.8th percentile of SWL — across all 26 sites was the intertidal zone area, which showed a correlation of τ = -0.46. This means that the larger the intertidal zone area is in relation to the estuarine total area, the strongest is the TSI (more negative).

In addition, the detailed analysis of Lyttelton, Otago, Manukau, and Tauranga harbours shows that estuarine bathymetry and geometry affect the SWL. The effects on SWL differ according

to the harbour, mainly driven by deformations that affect the tidal wave as it propagates within the estuary. They include tidal amplification, dampening, and asymmetry. The effects are observed to be stronger in Manukau and Tauranga Harbour, which are places with the largest intertidal areas.

Tidal amplification occurs in Manukau, Lyttelton, and Otago Harbours. The probability distribution and quantile-quantile plots of SWL, astronomical tide, and NTR for these locations are shown in Figure 3.8 and 3.9. For instance, the largest amplification occurs in Manukau Harbour. Figure 3.8 (C.I, C.IV) shows that the distribution of the SWL and astronomical tide (resp.) are wider at Onehunga (ranging from <-2m to >+2m) than at Anawhata (ranging from >-2m to <+2m). The amplification can be equal to 32 cm for the upper tail of the distribution (95^{th} –99.8^{th} percentiles) and 18 cm on average considering all quantiles, Figure 3.9 (C.I, C.IV). For Otago and Lyttelton Harbours, the amplification is lower, reaching a maximum of 13 and 4 cm in the upper tail, respectively, Figure 3.9 (A.IV, B.IV).

Tidal dampening is observed in Tauranga Harbour. Figure 3.8 shows a slight shortening of the distribution of SWL (D.I) and astronomical tide (D.IV), which ranges from around -1m to +1m. Indeed, the quantile-quantile plot (Figure 3.9) shows that the dampening is about 3 cm on average and a maximum of 6 cm considering all quantiles, Figure 3.9 (D.IV). For the upper tail (99^{th} percentile), the dampening is about 2 cm.

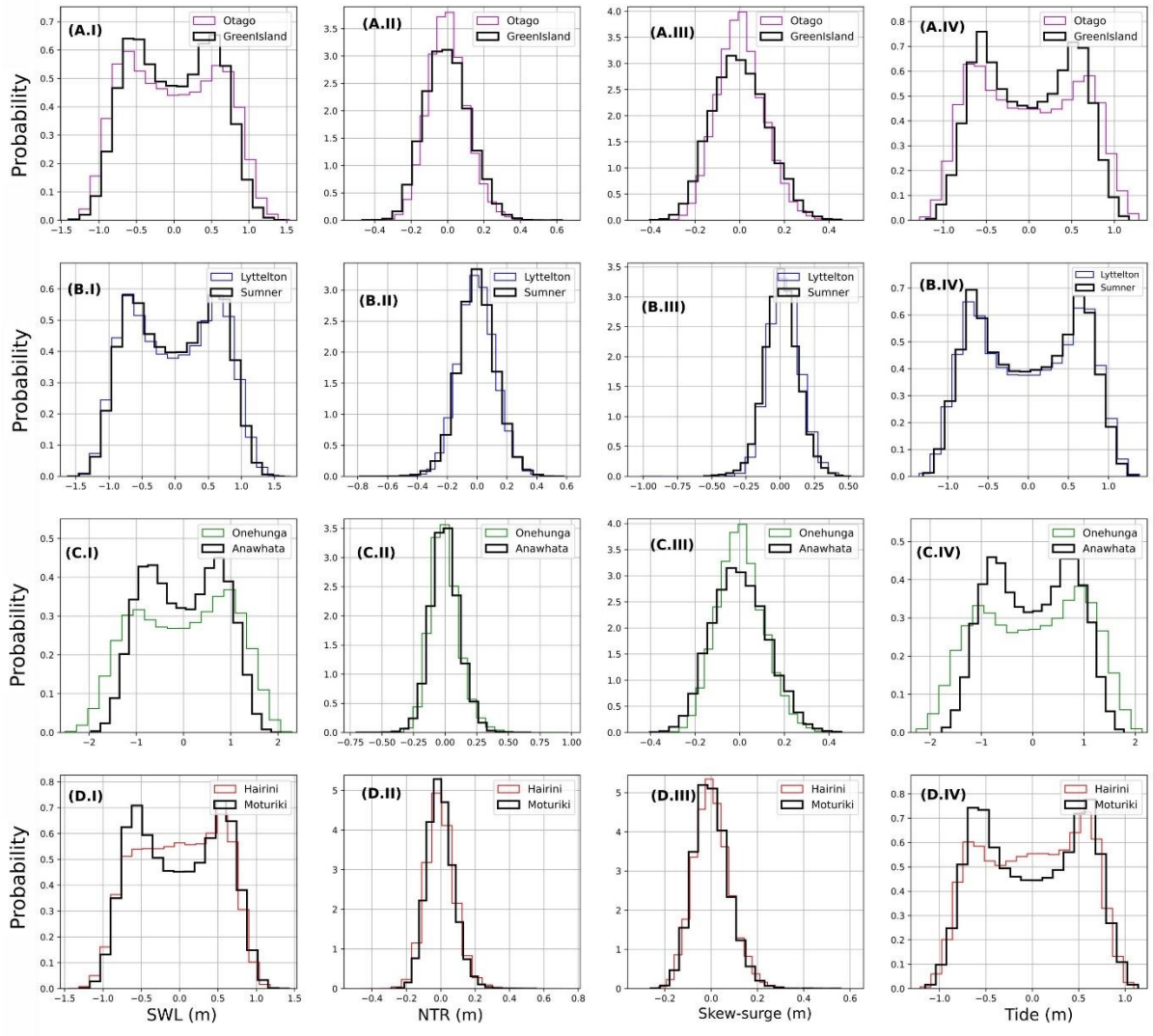

Figure 3.8. Probability distribution of SWL (I), NTR (II) and skew-surge(III) astronomical tide (IV) at Otago (A), Lyttelton (B), Manukau (C), and Tauranga (D) Harbour.

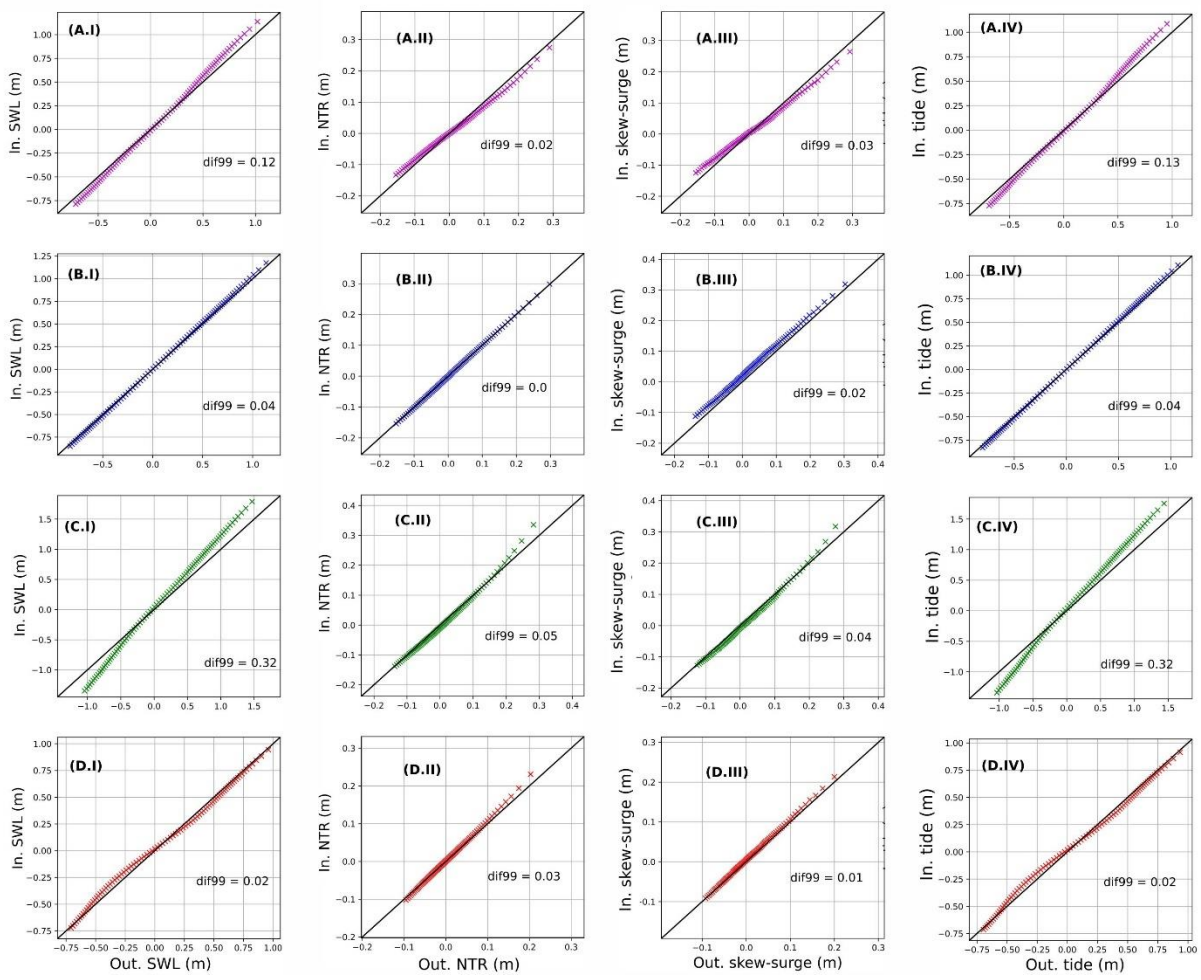

Figure 3.9. The quantile-quantile plot of SWL (I), astronomical tide (II), NTR (III) and skew-surge (IV) at Otago (A), Lyttelton (B), Manukau (C), and Tauranga (D) Harbour. For each panel, the absolute difference at the 99th percentile (dif99) between the measure variable inside and outside the harbour is shown.

Tidal asymmetry occurred in Manukau, Otago and Tauranga Harbours, shown in Figure 3.8 (A, C, and D rows). For instance, the positive and negative part of the bimodal tidal distribution at Anawhata, Figure 3.8 (C.IV), shows equally distributed values with a statistical mode of approximately -0.8m and +0.8m (resp.) and a probability of ~0.45. However, the distribution is positively skewed inside the estuary (i.e., Onehunga). Thus, positive values are more likely to happen than negative ones. For instance, the probability of the positive and negative modes is 0.38 and 0.33, respectively, Figure 3.8 (C.III). Similar positive skewness occurs in Tauranga Harbour, but with a larger difference between positive and negative mode probabilities, 0.7 and 0.6, respectively, Figure 3.8 (D.IV). Figure 3.8 (A.IV) shows a slight negative skewness in Otago Harbour.

NTR and skew-surge are modified when the waves propagate inside the estuary. This can be observed for all estuaries in Figure 3.9 (column II and III), but especially for Manukau Harbour (C.II and C.III), where an increment of 5 cm and 3 cm were observed at the 99th percentile for NTR and skew-surge, respectively.

Because of the effects of morphology on the tide (i.e. dampening, amplification, and asymmetry) and their influence on TSI, the extreme SWLs events inside and outside the estuary are not expected to always co-occur. Table 3.2 shows that for all four estuaries analysed, only a fraction of the extreme events related to the 99.8th percentile co-occur within a ± 6-hour time window, either inside and outside the estuaries or vice-versa. The lowest co-occurrence rate occurs in Manukau Harbour, which varies between 49–55%. The co-occurrence rates are the highest in Tauranga Harbour, with 84%–79%, followed by Lyttelton and Otago harbour, in this order. The co-occurrence rates of SWL annual maxima are even lower. The highest co-occurrence rates occur in Tauranga (43%) and Lyttelton (36%) Harbours. The lowest co-occurrence rates occur in Otago (20%) and Manukau (27%) Harbours.

Table 3.2. Co-occurrence rates between extremes of SWL (99.8th percentile) and annual maxima occurring inside (INNER) and outside (OUTER).

	POT selection		Annual maxima	
Estuary	Occurs OUTER and INNER	Occurs INNER And OUTER	Co-occurrence	Number of years
Manukau Harbour	55%	49%	27%	11
Tauranga Harbour	84%	79%	43%	16
Lyttelton Harbour	79%	68%	36%	25
Otago Harbour	70%	54%	20%	10

3.4.3 Harmonic analysis

Transformations in the astronomical tide (i.e., shoaling, dampening, and asymmetry) are the main contributors to the changes in the SWL observed in Section 3.4.2. Table A.7 compares

the amplitude and amplification factor of the principal astronomical (M_2, S_2, and N_2) and shallow water (M_4, MS_4, and MN_4) constituents inside and outside the four studied harbours (i.e., Otago, Lyttelton, Manukau, and Tauranga Harbour). The three principal tidal components amplify for all these estuaries, but the M_2 was affected the most. For instance, in Tauranga Harbour, M_2 is damped by 2 cm. In Otago, Lyttelton and Manukau Harbour, the M_2 is increased by 3 cm, 9 cm, and 28 cm, respectively.

The shallow-water harmonic constituents (e.g., M_4, MS_4, MN_4) have amplitudes ranging from <0.01 m up to 0.05 m through all tide gauges located inside or outside the estuaries. If compared to the principal constituents as M_2, S_2, and N_2, where the amplitudes range from 0.06 m (N_2 at Sumner) to 1.33 m (M_2, at Onehunga), the shallow-water constituents are a minor contribution to the astronomical tide. However, the shallow constituents are amplified more than the principal constituents within the harbours. Table A.7 shows that the amplification factor in Manukau and Tauranga Harbour for M_4 can increase by 1.22 and 1.64 times, respectively. Indeed, Table A.8 shows that the ratio M_4/M_2 increases when tide propagates inside Manukau and Tauranga harbours, which means that the constriction and bed friction effects are important in these sites for the tidal amplification. In Lyttelton and Otago harbours, a decrease of the M_4/M_2 is observed, which means that the effects of constriction and bed friction are not the main drivers for the tidal amplification, but the gradual changes in the bathymetry. The greatest ratio difference occurred in Manukau Harbour, where M_4/M_2 equals 0.027 in Anawhata and becomes 0.039 in Onehunga. Regarding the tide dominance, the difference of phase in $2gM_2$-gM_4 indicates that Manukau, Lyttelton and Tauranga Harbours are ebb dominant, while Otago is flood dominant. The M_4/M_2 was significantly correlated with the TSI ($\tau = 0.36$), considering all the 36 tide gauges in this study (see Section 3.3.4.3).

3.4.4 Hydrodynamic modelling results

3.4.4.1 TSI on extreme SWLs and the effect of the water depth and bed friction.

The results show that TSI occurs inside Manukau Harbour is spatially heterogeneous. TSI decreases the SWL when tide and NTR are modeled together (SC1) in comparison to the scenario where tide and surge are independent and so cannot interact (SC2+SC3). For instance, Figure 3.10A shows that TSI is the strongest in the inner estuarine region, reaching approximately -0.35 m, when considering the maximum TSI per grid cell for the entire period

of simulation. When the peaks over the 98th, 99th, and 99.8th percentiles of SWL are analysed (Table 3.3), a decrease is observed in the SWL of up to 16 cm at Onehunga and 9 cm at the harbour entrance (i.e., Paratutae). However, TSI was not important at the Anawhata tide gauge outside the Harbour. The TSI also varied according to the tidal cycle. For instance, Figure A.3 shows that the largest interactions occur during spring tide, particularly when the tide transitions between spring to neap tides and vice-versa.

Table 3.3. Mean absolute TSI from numerical model.

	Mean absolute TSI (cm)		
Location	**98th percentile peaks**	**99th percentile peaks**	**99.8th percentile peaks**
Anawhata	~ 0	~ 0	~ 0
Paratutae	7	9	7
Onehunga	15	16	16

In addition, the outputs of scenarios SC4, SC5, and SC6 (Figure 3.10 B, C, and D, respectively) show that the effects of bed friction and water depth are equally important to the TSI and are spatially heterogeneous through the Harbour. The scenarios agree that TSI gets stronger (+) in the inner estuarine regions when bed friction, channel and intertidal zone depths are changed. Most of the differences in TSI between scenarios vary between ± 0.05 m with some regions of the estuary showing larger values (up to ~ 0.2 m).

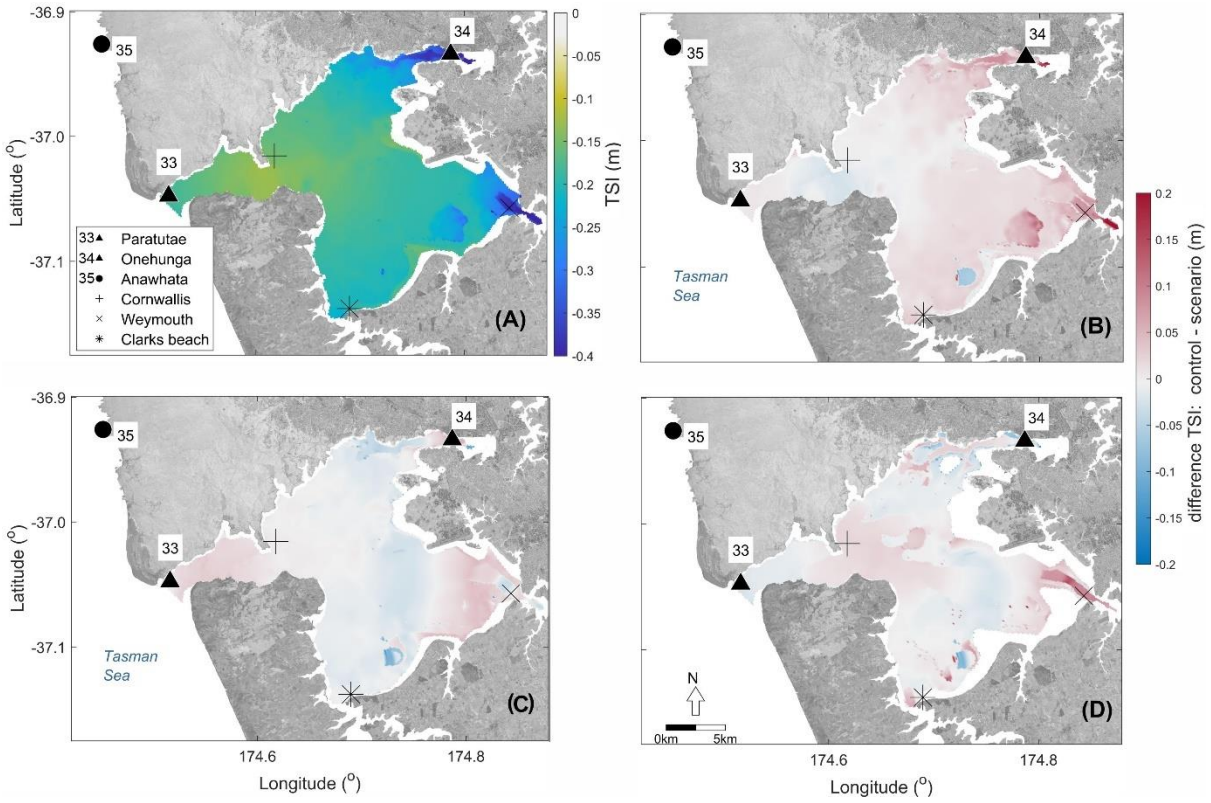

Figure 3.10. TSI in Manukau Harbour. TSI on the control scenario SC1 (A). Change in TSI in the model domain for SC4, when the Chézy coefficient for bed roughness is equal to 65 (B). Change in TSI for SC5, when the model was forced with the channel at the entrance of the harbour shallower (C). Change in TSI for SC7, when the model was forced with the tidal flats shallower (D). Note the ocean domain to the west has been removed to focus on the estuary. Background image: aerial photos from Land Information New Zealand (LINZ). Projection: WGS84.

3.4.4.2 The effects of TSI on the tidal amplification

The hydrodynamic modelling results show that TSI affects the amplification of SWL in Manukau Harbour. Figure 3.11 shows the amplification of the astronomical tide (A), NTR (B), astronomical tide and NTR when these two variables are independent (C), and SWL (D). Figure 3.11A (corresponding to SC2) shows that most of the tidal amplification in Manukau Harbour occurs at the entrance of the estuary, between Paratutae Island and the Cornwallis headland. This is easily observed in Figure 3.11A, where contour lines show that the gradient of amplification is stronger at the entrance of the estuary in comparison to the inner estuarine region. Amplification also occurs when NTR is modelled independently (SC3), which shows that the morphology of the Harbour can directly affect the NTR. For instance, Figure 3.11B shows that the NTR is amplified also near the entrance and in the intertidal zones. This

amplification can reach up to ~260% (Amp. Fac.≅ 1.6) at the upper estuarine region (e.g., Onehunga, Weymouth, and Clarks Beach).

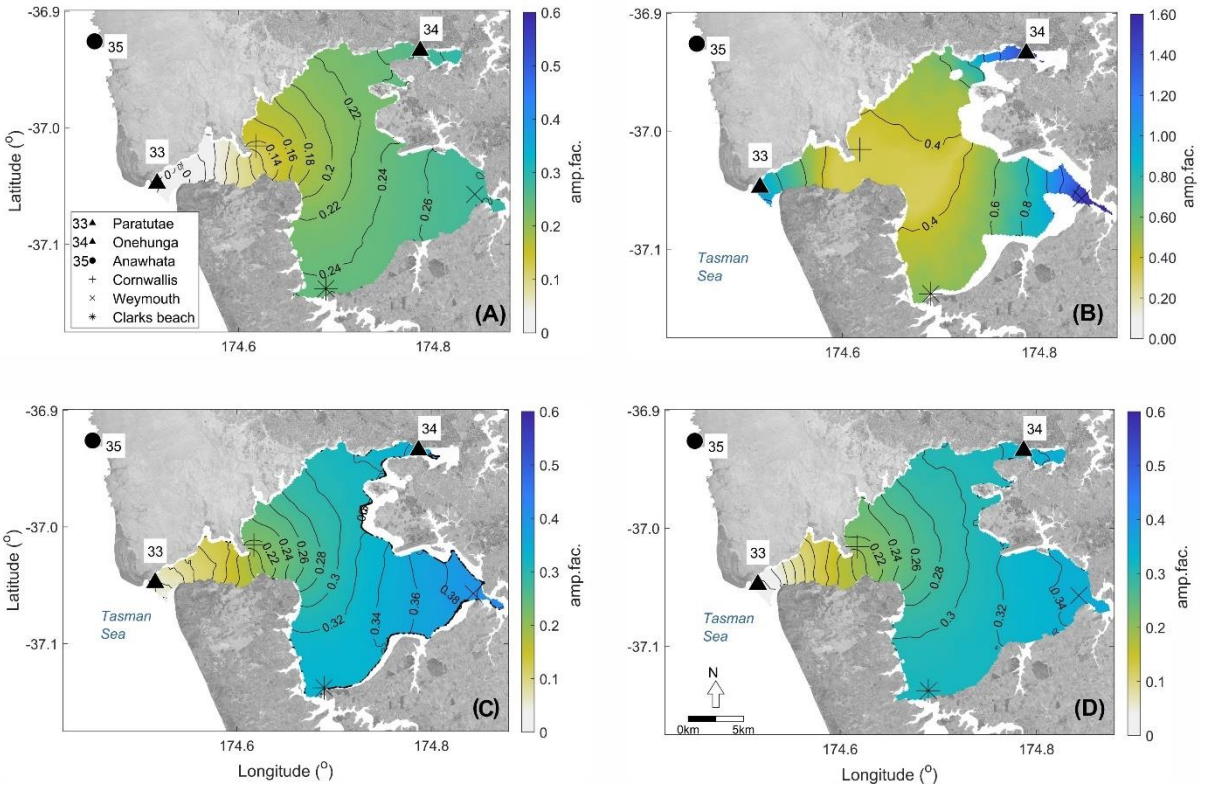

Figure 3.11. Co-amplification lines of the astronomical tide (A), NTR (B), astronomical tide + NTR (C), and SWL (D) according to the outputs of the simulation scenarios SC2, SC3, SC2+SC3, and SC1 respectively. Note the ocean domain to the west has been removed to focus on the estuary. Background image: aerial photos from Land Information New Zealand (LINZ). Projection: WGS84.

Hydrodynamic modelling also showed the amplification was greater or lower if the NTR and tide were allowed to interact (the model was forced with SWL, SC1) versus when they were modelled separately and added together (SC2+SC3). If the combined model provided a different result to the additive model, then the difference in water level inside and outside the estuary might be accounted for by the TSI (see Section 3.3.5.1). In fact, when SWL is simulated and tides and NTRs interact (SC1), the amplification is lower in comparison to the scenario when astronomical tide and NTR are considered independent (SC2+SC3). For instance, Figure 3.11C shows an amplification factor of 0.38 at Weymouth when tides and NTRs are simulated independently (SC2+SC3), while Figure 3.11D shows an amplification factor of 0.34 at the same location when astronomical tide and NTR interact (SC1). TSI decreases the amplification heterogeneously through the harbour and is more evident in the upper estuarine regions. For

instance, the SWL at Weymouth is decreased up to -0.04 (-4%) and at Onehunga is -0.02 (-2%). Considering a peak of SWL occurring at Anawhata of 1.64 m (i.e., the 99.8th percentile), the resulting dampening in the SWL because of the non-linear interactions between tide and NTR would be 6 cm and 3 cm for Weymouth and Onehunga, respectively. Note that these differences consider the maximum SWL at each grid cell over the entire period of simulation and that the differences at the peaks of SWL could be larger as shown in Table 3.3.

In addition, the NTR directly affects the tidal amplification. Figure 3.12 shows the effect of positive (A) and negative (B) NTRs on the tide. For instance, the outputs of SC7 and SC8 showed that positive NTR (SC7) decreases the tidal amplification by up to -5% (Figure 3.12A). Negative NTR (SC8) can increase the tidal amplification by +5% (Figure 3.12B). These differences in the tidal amplification are evident in the inner estuarine region (e.g., nearby Onehunga, Weymouth, and Clark beach).

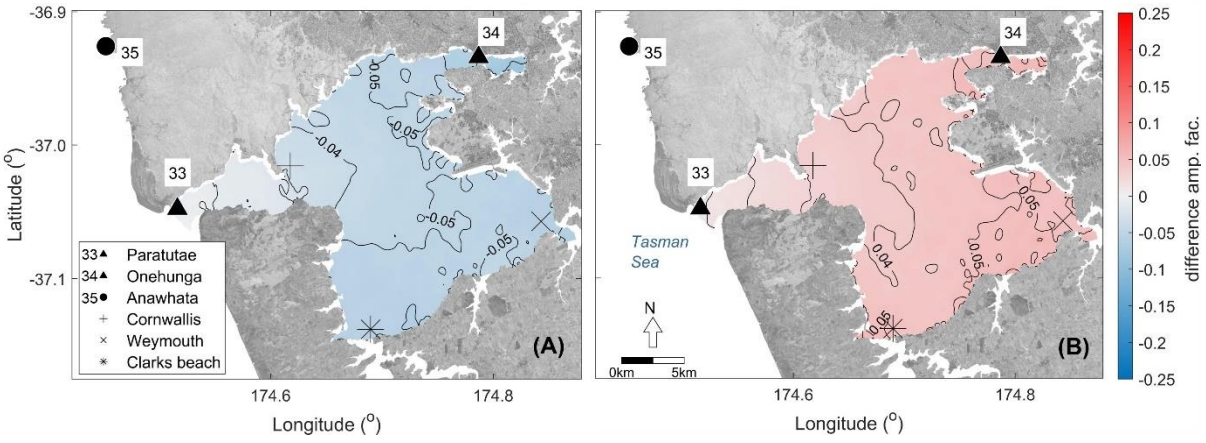

Figure 3.12. Effects of the NTR on the tidal amplification. The difference in the tidal amplification between a scenario forced by only astronomical tide (SC2) and another forced by astronomical constituents plus a positive (SC7) and a negative (SC8) NTR is shown in panels (A) and (B), respectively. Note the ocean domain to the west has been removed to focus on the estuary. Background image: aerial photos from Land Information New Zealand (LINZ). Projection: WGS84.

3.5 Discussion

The astronomical tide and NTR are statistically dependent at most locations of NZ, and the morphology of the coast or estuary can enhance the degree of dependence. This is shown in

multiple ways, by analysing the occurrence of the largest NTRs as a function of tide level (i.e., Dixon and Tawn et al., 1994), tidal phase (i.e., Haigh et al., 2010), and by analysing the dependence between NTRs and astronomical high tide that corresponds to extreme SWLs (i.e., the skew-surge in Arns et al., 2020). The largest NTRs occur at low tide and from 4 to 6 h after the peak of high tide in most of the study sites, especially in the ones located in the inner regions of estuaries.

The degree of dependence between NTR and astronomical tide varied according to the method applied for the analysis. Based on past work, the coasts with a narrow continental shelf, as in NZ, the NTR and astronomical tide were expected to be independent. This assumption is supported here by the results obtained by applying the Dixon and Tawn (1994) method, which showed that TSI did not occur in most of the records from tide gauges located outside estuaries. However, astronomical tide and NTR were shown to be dependent on almost all tide gauges at the coast when the tide phase was used as a basis for analysis (i.e., Haigh et al., 2010) or during extreme SWLs (Arns et al., 2020). There are three possible explanations for this. First, the Haigh et al. method has more degrees of freedom in the chi-squared test than the Dixon and Tawn method, 13 and 5, respectively. Second, the Dixon and Tawn method cannot identify interactions caused by phase alteration, which can be done by Haigh et al. Third, the dependence between NTR and astronomical high tides found during extreme SWLs (i.e., using Arns et al., 2020) may be explained by the lower number of samples (i.e., calculations were made here only using the NTR associated with the highest SWL) and the process of mutual phase alteration. Mutual phase alteration is when tide and surge interact to change each of their propagation celerities — e.g., larger tides (surges) would slow the surge (tide) and consequently decrease the surge (tide) amplitude (Rossiter, 1961; Proudman, 1955a; Proudman, 1955b), see Section 3.1.

Although a statistical dependence was found between astronomical tides and surges (i.e., for both the NTR and the skew-surge), the magnitude of these interactions can vary widely. For instance, the TSI estimated by applying Arns et al. (2020) showed that the TSI is mostly positive and vary between >+10 cm up to +27 cm. However, these values are averaged for a specific quantile, as TSI for single storms can vary between negative to positive values at the same location (Arns et al., 2020). For instance, the results of our numerical modelling showed that TSI occurs in Manukau Harbour (e.g., Paratutae and Onehunga tidal gauges) and is negative (≅ -16 cm) for a single extreme SWL. That means the SWL would be overestimated

if tide and surge were assumed to be independent. In addition, when the difference between the quantiles of skew-surges and NTRs were analysed at the same site (Section 3.4.1 and 3.4.2), these differences are close to zero or negative, with the largest of -4 cm and with the skew-surge quantile lower than the respective NTR quantile.

The positive TSI estimated for tide gauges in NZ using the NTR is not what has been observed in most locations globally, using the same methodology (Arns et al., 2020). For instance, Arns et al (2020) have only observed positive TSI in the Northern Sea. Positive (negative) values of TSI mean that if TSI is not considered, the predictions can be underestimated (overestimated). The positive TSI obtained when applying Arns et al. can be explained by the limitation of statistical models in representing local physical processes, which the author also highlights. For instance, when tide and surges propagate inside an estuary, they interact not just with each other (i.e., mutual phase alteration (Rossiter, 1961)) but also with the geometry, bathymetry, bed friction of the estuary, and local processes that can affect the NTR inside the estuary (as shown with our numerical modelling scenarios). All these factors potentially increase the non-linear response between surges and tides within a harbour, especially in NZ, where the complex morphology and extensive intertidal zones are commonly found in estuaries and are different from the funnel-shaped estuarine settings in pioneering studies of TSI. Another factor which might explain the difference is the lower accuracy of the Arns et al. model on fitting TSI where the astronomical tides represent more than 80% of the SWL during extreme events. Positive TSI was found by the same study for some Pacific islands where the astronomical tide represents >80% of the SWL during extreme events, which is the case of NZ (see Table A.9). For instance, at Anawhata, Paratutae, and Onehunga tide gauges, the astronomical tide represents ~90% of the SWL during extremes over the 99.8^{th} percentile.

The complex morphology of the estuaries (e.g., extensive intertidal flats) can enhance the TSI because of tide and surge transformations (e.g., asymmetry, amplification, dampening). Usually, the process of mutual phase alteration between astronomical tide and the NTR results in the largest NTRs being unlikely to occur at high tide, but rather within a few hours of high tide, during the rising or falling tide. We show multiple lines of evidence that for NZ's estuaries with extensive intertidal zones, the largest NTR occurs near the low tide. Firstly, Dixon and Tawn and Haigh et al. methods showed a strong tendency of the largest NTRs to occur close to the low tide and around 4–6 hours after the high tide in estuaries with large intertidal zones (e.g., Onehunga, see Figure 3.6B). Secondly, a significant correlation that was found between

the coefficient τ (NTR × astronomical tide during extreme SWLs) and the area of the intertidal zone throughout the fourteen different estuaries (see Section 3.4.2). Thirdly, the significant correlation between τ and the M_4/M_2 was calculated for all 36 tide gauges in this study. Fourthly, our hydrodynamic modelling results showed that water depth and bed friction are equally important for TSI at Manukau Harbour (Section 3.4.4.1) and can increase or decrease the TSI heterogeneously within the harbour (see Figure 3.10). Ultimately, the tidal asymmetry and the amplification of shallow-water harmonics result from the effects of bed friction and morphology on the tidal wave propagation, which are the same elements of the shallow-water equations that contribute the most to the TSI. The contribution of bed friction and shallow water effects have been shown as the most important for TSI in previous studies (e.g., Idier et al 2012, Antony et al., 2020).

In contrast to the relationship between NTR and tides, skew-surges and tides were generally shown to be independent in NZ. In this respect, the Williams et al. and the Arns et al. method (both of which were applied to skew-surge) provide conflicting results, which demonstrates the sensitivity to small differences in how the analysis is performed. Williams et al. method showed that the skew-surges and astronomical tides are independent whereas the Arns et al. method showed that they are dependent. Williams et al. method analyses the dependence between the highest skew-surges and the water level at the nearest astronomical high tide, which can include peaks of SWL occurring during neap and spring tides and results in a larger dataset. The Arns et al. method analyses only the skew-surge and nearest astronomical high tide associated with the highest SWLs (also time-declustered), which results in a much shorter dataset. Williams et al. method was validated for North Atlantic and widely applied globally. Although these regions experience larger NTR than NZ, they also experience larger tides, which makes the contributions of tide and surges to the SWL similar and they are both tide dominant (i.e., NZ and UK) (Stephens et al., 2020; Williams et al., 2016). Most of the coastal flooding studies performed in NZ applied the skew-surge joint probability model (SSJPM), which assumes independence between skew-surge and astronomical tides. Stephens et al. (2020) have compared different methods of extreme value analysis in NZ. In this work, the authors calculated the return period of extreme SWL fitting peaks over threshold using both General-Pareto distribution (GPD) — which theoretically considers the TSI — and the SSJPM. The SSJPM was similar to the GPD or overestimated the return periods of 1 year to 25 years and better fit the return periods >50 years. The overestimation in the lower return periods (i.e., <50 years) for some of the sites analysed by Stephens et al. (2020) may potentially indicate that the

assumption of independence is not always valid — as shown by the tide-skew-surge dependence shown here by the application of Arns et al. method using the highest SWLs. Other studies, such as Santamaria-Aguilar and Vafeidis (2018), have shown that skew-surge and astronomical tide can be dependent, especially in shallow seas (which can apply to estuaries) with mixed semidiurnal tides. In mixed semidiurnal regimes, two high tides occur over a day, but one high tide is lower than the other, which may allow the largest skew-surge to preferably occur at the lower or higher high tide. Although Santamaria-Aguilar and Vafeidis (2018) show convincing evidence that skew-surge and astronomical tide can be dependent, they do state that further numerical modelling should be done to properly prove the dependence. The Santamaria-Aguilar and Vafeidis procedure was also applied to the datasets presented here and no dependence between extreme skew-surge and tides were found (not shown).

The TSI explains the differences in the co-occurrence of extremes inside and outside harbours, which is also supported by the results of the hydrodynamic modelling (Figure 3.11 and 3.12). First, the model outputs showed that surges can be amplified within the harbour when considering a scenario where NTR are simulated independently and interacting only with the morphology (shallow water effects, bed friction). The NTR amplification is relatively higher than for astronomical tides. Second, TSI was shown to affect the amplification of the astronomical tide. For instance, during an extreme SWL occurring outside the harbour —with an equinoctial high tide and a strong positive NTR (99.8^{th} percentile) — tide and surge would add to each other linearly because the TSI outside the harbour was proven to be weak. However, when the same tide and NTR propagate into the harbour, the tide will be amplified less or more according to the local mean water level, which will vary according to the NTR. In the case of a positive NTR (scenario SC7), the mean water level will be higher, and the tide will propagate more quickly within the estuary. Consequently, the amplification caused by funnelling (due to gradual change of entrance width and bottom friction) or shoaling (due to gradual change of bathymetry) is more likely to decrease, and the corresponding SWL inside the estuary (e.g., at Onehunga tidal gauge) may no longer be considered an extreme event. A practical outcome of these results is that interactions between tide, NTR and morphology would have equal or more impact on the NTR than wind set-up and wind generated waves, which have been shown to increase the water level by few centimetres in Manukau Harbour (Smith et al., 2001).

Although the present study is focused on NZ, the main findings are relevant globally. Although the statistical analyses used here are commonly employed to assess TSI, it can be difficult to

interpret the results, particularly when different tests give different outcomes; only a robust numerical study can provide a full physical interpretation of the processes involving tide, NTR, and skew-surge, as highlighted in previous studies (Santamaria-Aguilar and Vafeidis, 2018; Arns et al., 2020). In general, TSI becomes stronger the shallower the bathymetry becomes — e.g., extensive and shallow continental shelf, shallow seas, shallow estuary — and the coastal geometry becomes more complex — e.g., coastal embayment, coastal lagoons — because the shallow water effects, bed friction, and advection enhance non-linear interactions between NTR and tides (Flather, 2001; Zhang et al., 2010). Therefore, the results are applicable to similarly complex sites such as the English Channel (Idier et al., 2012), the Southwestern Atlantic coast (Santamaria-Aguilar and Vafeidis, 2018), the Bay of Bengal (Antony et al., 2020), or even the Pacific Islands where Arns et al. have shown that TSI can be positive (as previously discussed). Where TSI is likely to be strong, and in situ water level records are scarce and short, the use of skew-surge joint probability methods is a better approach for robust extreme value analysis (since the skew-surge is less likely to be influenced by TSI). Although in general, extreme skew-surges have been shown to be independent of astronomical tide in most of the locations around the world (Williams et al. 2016), exceptions have been reported (Santamaria-Aguilar and Vafeidis, 2018; Arns et al., 2020). Further validation could use the numerical modelling approach outlined here. Finally, it is generally impractical to adequately monitor a complex coastal setting, and the results here show the limitations on our ability to extrapolate between settings (such as from outside an estuary to inside an estuary). Understanding and being able to isolate morphological effects would help to eventually improve the prediction of non-linear effects and consequently the prediction of extreme water levels inside harbours or in locations with complex geometry. An extreme outside a harbour may not cause extreme event inside the harbour.

A number of processes which may have important effects on tides, NTR, and their dependence on estuarine morphology, have been neglected in this study, such as multiple flooding drivers like wind-generated waves, wind set-up, fluvial discharge, and infragravity waves. For instance, previous studies have shown that wind can generate waves in Manukau Harbour, which can affect the NTR (Smith et al., 2001), especially in estuaries with extensive shallow areas, because the wind stress component of the storm surge is inversely proportional to the water depth (Pugh and Woodworth, 2014). The wind can also induce vertical flows; for instance, return flow in channels, which would be considered by forcing with wind in a 3D hydrodynamic model. The simulation scenarios performed here considered a homogeneous bed

friction coefficient over the model domain, which is not realistic; bed materials are not constant throughout the estuary and water depth and current speed can affect them (Sternberg, 1968; Nihoul, 1977; Kagan et al., 2010). However, the model approximated well to the observed amplification in Onehunga, and the general patterns of amplification throughout the estuary corroborates previous studies (Bell et al., 1998). In addition, infragravity and short waves can increase NTR inside estuaries (Bertin et al., 2019). The powerful swells that reach NZ (Godoi et al., 2017; Albuquerque et al., 2021) could produce infragravity waves propagating to inner estuarine regions.

Ultimately, one of the biggest challenges is determining how sea level rise (SLR) is and will affect the TSI in NZ's estuaries. Although just a few strong trends in skew-surge/SLR and TSI/SLR have been found globally (Mawdsley and Haigh, 2016; Arns et al. 2020), the response of the tidal range and asymmetry to SLR is strongly affected by the estuarine morphology, especially in locations where the tides are the main driver for flooding (Du et al., 2018; Khojasteh et al., 2020, 2021). For instance, Du et al. (2018) have shown that the response of the tidal range to SLR is nonlinear, spatially heterogeneous within the estuary, and highly affected by the length and bathymetry of an estuary, with tidal range decreasing in short estuaries with broad intertidal zones. Khojasteh et al. (2020) have shown that the entrance restriction drives the estuarine response to SLR; the smaller the cross-sectional area of the estuary mouth, the smaller the tidal range within the estuary. Khojasteh et al. (2021), in a broad review on the subject of SLR and its effects on the tidal range in estuaries, concluded that the tidal range is more likely to increase in estuaries where fixed structures (e.g., sea-walls) are established, while in estuaries with preserved intertidal zones and flood-plains, where these areas have space to migrate landward in case of SLR, the tidal range is more likely to decrease.

3.6 Conclusion

The TSI in observations from 36 tidal gauges around NZ was analysed and a numerical study, focused on a single location (Manukau Harbour), was performed aiming to explain some of the patterns. TSI occurs at most of the sites in NZ and mainly affects the time when the largest surges occur relative to high tide. Furthermore, TSI did not show any regional patterns linked to the distribution of tide, NTR, or skew-surge regimes around NZ. However, the strongest TSI

occurs at tide gauges located in inner estuarine locations and are correlated with the intertidal areas within these estuaries. Data analysis, statistical and numerical models were used to quantify the magnitude of the TSI. The values vary according to the method applied, and they are larger for individual events than for quantiles, and range from -16 cm to +27 cm, which means that the water level can decrease (-) or increase (+) if TSI is not accounted for.

In addition, the highest skew-surges and associated astronomical tides were shown to be statistically independent in most cases. This is important because the current return periods of extreme SWL are calculated by using SSJPM which assumes independence between these two variables. In fact, the greater likelihood of independence of the skew-surge (compared to the NTR) is why the skew-surge was used as a basis for the SSJPM. In some cases, skew-surges and astronomical tides were dependent when associated with the highest extreme SWLs (used in the Arns et al. method), which may explain some of the inconsistencies in previous research found in the fitting of extreme value for the lower return period SWLs (up to the 50-year return). Further work is needed to determine the conditions under which skew-surge can be considered unilaterally independent.

Numerical and observational data were used to provide strong evidence that TSI modulates the co-occurrence rate of extreme SWL in estuaries of NZ by affecting tidal amplification. An understanding of the co-occurrence of extreme events is important to develop localised hazard assessment for regional planning. For instance, if observations are available only outside a harbour, the schematisation of the boundary conditions (i.e., waves, tides, surges) being used to drive a hydrodynamic model, may not correspond appropriately to the hydrodynamic response that generates the extreme events inside the harbour. Such an approach would limit understanding of the full range of possible storms affecting the water levels inside estuaries when extreme water levels are estimated using only observations made outside a harbour.

The estuarine morphology has been shown to affect astronomical tide, the NTR and the TSI, as shown by the significant correlation found with the intertidal area. In addition, the ratio between the principal astronomical and the shallow constituent of the astronomical tide and the τ coefficient shows that the importance of the TSI in enclosed sites is likely caused by non-linear effects (which is also supported by the numerical modelling study in Manukau Harbour); however, determining which non-linear term contributes the most to the TSI was not possible (e.g., shallow-water effects, bed friction, or advection terms).

Ultimately, the present manuscript highlights the urgency of investment into tide gauge networks, to provide longer-duration observations inside estuaries and in locations with high morphological complexity. This is particularly important in Aotearoa New Zealand, which has a complex coast in terms of geometry, so tide transformations and their interaction with NTR can generate different local responses to storms than in the open ocean. Ultimately, a better understanding of tide-surge interactions will improve the quality of projections of damage and costs caused by sea level rise and coastal flooding.

Chapter 4

Comprehensive Assessment of Compound Flooding Potential and Storm Clustering in Coastal Areas: Insights from Aotearoa New Zealand

Wagner L. L. Costa[1], Karin R. Bryan[1], Scott A. Stephens [2], Giovanni Coco [3] (to be submitted)

[1]Coastal Marine Group, School of Science, The University of Waikato, Hamilton, New Zealand

[2] National Institute for Water and Atmospheric Research Ltd, Hamilton, New Zealand.

[3] School of Environment, University of Auckland, Auckland, New Zealand.

Contribution of Authors: The main conception and design of the study were given by Wagner L.L. Costa with important contributions given by Karin Bryan, Scott Stephens, and Giovanni Coco. The statistical analysis and numerical modelling were performed by Wagner L.L. Costa and supervised by Karin Bryan and Scott Stephens. The hydrodynamic modelling was elaborated and performed by Wagner L.L. Costa under supervision of Karin Bryan. The database was organised by Scott Stephens and Wagner L.L. Costa. The first draft of the manuscript was written by Wagner Costa. All authors contributed to manuscript revision, read, and approved the current version.

Code availability: the main codes used in this chapter are available at https://github.com/CostaAndCoasts/

Abstract

This study investigates the potential of compound flooding and the dynamics of storm clustering in coastal and estuarine regions with a focus on waves and storm surges. Although waves can enhance storm surges, especially inside estuaries, their effect is often assumed to be minimal and neglected. Intense low-pressure atmospheric systems can generate extreme storm surge and wave events simultaneously and in close succession, exacerbating flooding impacts. Here, 36 tide gauges across Aotearoa New Zealand and wave hindcast data at 14 locations were used to analyse the regional patterns of the compound flooding and clustering of extreme events. If extreme events occur close to each other in time, originate from the same weather systems and show statistical dependence, compound flooding is hypothesized to be more likely. Three different analyses were performed: analysis of temporal clustering and seasonality of extreme events of wave height, storm surges and water level; analysis of the dependence structure of swell and wind wave heights and skew-surge during extreme water level events; and weather type classification for the most severe events. Wave height and skew-surge were found to be significantly correlated, where tide gauges located on the North Island and close to the estuarine entrance have a stronger correlation. Event clusters and individual extreme events tend to occur with similar time intervals and seasonality. On average, at least 30% of the extreme events occur in clusters (from 3 to 15 days of time interval) across all tide gauges and wave hindcast points. Wave height, skew-surge, and water level event clusters occur mostly in winter months, and on average, comprise 2–5 extreme events, although clusters containing up to 11 and 12 events were identified for skew-surge and water level through all tide gauges. The highest skew surges and wave height corresponding to extreme events of water level are related to the same weather types, where the degree of exposure to strong westerly and southerly winds explains the relationship between the different drivers. The study's findings highlight the potential impact of combined wave and storm surge effects on extreme sea levels and coastal flooding, with far-reaching implications for coastal planning and resilience.

4.1 Introduction

Flooding and erosion risks are predicted to increase in coastal areas worldwide due to sea level rise and intensification of storm strength and frequency caused by climate change

(Oppenheimer et al., 2019). Economic costs due to coastal storms are predicted to increase severely by 2050 (Hallegatte et al., 2013) and strongly affect coastal populations (Hinkel et al., 2014). Specifically for estuaries, studies have highlighted the importance of considering multiple physical factors in flooding assessments (e.g., storm surge, waves, fluvial and pluvial discharge) as the compound effect of these variables during storms events can be greater than the effects expected when considering each one of them individually (Bevacqua et al., 2021; Jafarzadegan et al., 2023).

The variations in the sea level caused by the action of storm surges and waves can be represented as non-tidal residuals (NTR). The NTR is the difference between the predicted astronomical tide and the observed water level record, composed of the tide, variations in the sea level associated with storm surges — driven by sea level pressure gradient and wind friction on the sea surface — and waves. Waves generated by a storm can travel to the coast and directly affect the water level through three different mechanisms (Flather, 2001). First, wind waves can enhance sea surface stress, which increases the storm surge. Second, wave orbital velocities in shallow waters reach the seabed and increase bottom stress, which acts on surge (i.e., NTR). Third, at the beach, non-linear interactions can induce changes in the mean water depth (wave set-up and set-down), primarily through wave breaking. Studies commonly describe the physical process of waves affecting storm surges by analysing the radiation stress and wave age. Radiation stress is the excess momentum flux due to the presence of waves, which is particularly important in coastal areas — where depth-induced changes cause shoaling or breaking, which control wave set-up. Wave age is a measure of the wave's development state. Young waves (i.e., wind sea) can affect the sea-surface stress more — and potentially increase the NTR — than fully developed waves (i.e., swell) because young waves are steeper and propagate more slowly (relative to the wind speed), which makes them aerodynamically rougher than fully developed waves.

Waves can also exacerbate coastal flooding by eroding beaches. Severe beach erosion can be produced by one rare storm (with a high return period), but equally can be caused by a combination of storms (with a lower return period) that occur in close succession, also called storm clusters (Senechal et al., 2017). Past studies have highlighted that the impact of storm clusters on the beach morphology can be equal to or greater than the impact of one rare storm (e.g., Ferreira, 2005).

In enclosed estuaries and tidal lagoons, the coast and constrained entrance geometry are expected to limit the action of waves. However, studies have shown that waves can still affect sea levels inside enclosed estuaries (e.g., Pugh, 1981; Bertin et al., 2015; Rahbani et al., 2022). Usually, wind seas affect the NTR more than swell waves because they can increase sea surface roughness and radiation stress (Pugg 1981; Flather 2001). However, swell and infragravity waves have also been shown to be potential contributors to NTR and erosion inside estuaries (Bertin et al., 2019; Gallop et al., 2020; Rahbani et al., 2022). For instance, Bertin et al. (2015) have shown through a numerical modelling study that wind waves contributed to the surge peak by 0.1 m to 0.2 m inside enclosed harbours during the storm Xynthia in the Bay of Biscay, France. The study showed how wind waves increase the sea-surface roughness, affecting the surge's peak. In Australia, Rahbani et al. (2022) used field measurements to show that wind seas, swells, and infragravity waves can act inside enclosed estuaries up to ~8km from the estuarine mouth, showing that spectral analysis would be a valuable tool to study the morphodynamic of beaches inside estuaries, including storm response and subsequent recovery. Gallop et al. (2020) showed that erosional processes in beaches inside bays and estuaries have long recovery time, due to the lack of low-frequency, beach-building waves and, in some cases, limited sediment supply from adjacent sediment reservoirs. Moreover, this makes estuarine beaches highly sensitive to shifts in wave direction because the propagation of waves inside estuaries depends on the angle of incidence of waves regarding the orientation of the estuarine mouth. Because of the non-linear interactions between tides, surges and morphology of the estuary, the skew-surge parameter is often used to describe surge levels inside estuaries instead of NTR (Stephens et al., 2020; Costa et al., 2023). The skew surge is the difference between the peak of the observed tide and the closest peak of the predicted astronomical tide. The advantage of using skew-surge instead of NTR is that the over- or under-estimation of the surge levels due to non-linear effects is removed.

A detailed analysis of compound flooding and storm clustering impacts at the coast often requires field measurement combined with robust numerical modelling, which are not always cost-effective. Alternatively, data-driven or statistical models have low computational costs; however, they depend on data availability and are limited in representing local physical processes (e.g., wave distortion due to the morphology of the estuary and water level set-up caused by wave and wind). Regional data analysis can optimise the selection of forcing dynamics (e.g., waves, tides, surges) and the appropriate modelling techniques (e.g., numerical or statistical modelling) by identifying the most susceptible areas to compound flooding and

storm clustering. For instance, in compound flooding, the statistical dependence between different flooding drivers is often assessed by calculating correlation coefficients (e.g., Kendall coefficient,τ) of their extreme values (Kumbier et al., 2018; Orton et al., 2020; Nasr et al., 2021), which gives a first assessment of the independence of different drivers during extreme events. In addition, correlation coefficients can be used to validate joint probability and Gaussian methods, often used to address stochasticity in coastal flooding (Aikaterini et al., 2023). Similarly, a regional storm clustering analysis can identify which areas are more exposed to severe coastal erosion due to storms occurring in close succession. This type of analysis has been primarily focused on coastal erosion (e.g., Coco et al., 2014; Vousdoukas et al., 2011; Splinter et al., 2014). However, it has also been applied to analyse the wave climate in isolation (Santos et al., 2007, Godoi et al., 2017), surges (storm surge and skew-surge) and sea levels (Haigh et al., 2016, Stephens et al., 2020) and wave, surges, and sea level (Jenkins et al., 2023) for the coast of the United Kingdom and Aotearoa New Zealand.

Compound flooding and storm clustering analysis require the identification of storm events, which is made by identifying peaks in a time series that represent extreme values and applying time declustering schemes. Peaks over the threshold (POT) and block maxima selection are commonly used. Block maxima require a long time series (~30 years) to properly identify extreme values, which makes POT selection appropriate for shorter records. Consequently, models and statistical techniques that use POT are highly sensitive to the threshold value (Collins, 2001). Threshold values with this purpose are often chosen based on quantiles belonging to the upper tail distribution (e.g., 0.95, 0.99)

The meteorological systems are important to consider in regional analysis because they generate waves and storm surges that impact the coast. Clusters of storms are common in temperate climates because of the types of weather patterns that characterise these climates. Techniques combining principal component analysis (PCA) and data clustering (e.g., K-means), such as weather types classification (e.g., Kidson, 2000), have been used to provide a general understanding of the main physical processes involved in storm events (e.g., Coggins et al. 2015). Statistical downscaling methods based on weather types are widely used to predict the climate of waves and storm surges at the coast (e.g., Camus et al., 2016, Rueda et al., 2019, Costa et al., 2020).

Storm clusters can produce coastal flooding either by directly influencing wind and atmospheric pressure, or indirectly, though also generating wave induced effects (or both). Therefore, interactions between waves and surges can amplify the hazards associated with storms. Current modelling methods applied to NZ and other regions worldwide do not consider wave and storm surge interaction because of computational costs or lack of data for model input or validation. Specifically for estuaries, wave contribution is sometimes neglected because waves are not considered an important driver of sea level in such environments. Also, projected return periods of extreme sea levels often consider only astronomical tides and surges (e.g., skew-surge or non-tidal residual). Although in Aotearoa New Zealand (hereafter NZ), the climate of waves, storm surges, and sea levels has been well documented independently, their compound and clustering effects still need to be assessed, especially in estuaries.

Here we use water records and wave hindcast data from NZ to study the potential storm clustering and compound effects of waves and surges on the extreme water level variations. For that, we aimed to answer the following questions:

- Do wave events explain a fraction of variation in skew-surge and sea levels?

- Do wave and surge events cluster (either independently or not), and do such clusters vary on intra-annual and seasonal scales?

- What kind of weather patterns are storm events associated with?

4.2 Marine and atmospheric climate around Aotearoa New Zealand

The marine climate of NZ is marked by a wide range of wave directions (Godoi et al., 2017; Rueda et al., 2019; Albuquerque et al., 2021), relatively small storm surges (Stephens et al., 2020) — if compared to other locations in the world —, and microtidal to mesotidal regimes. Coastal flooding in NZ is tide dominant, where high perigean spring tides combined with severe storm surges are the main contributors to flooding events (Rueda et al., 2019; Cagigal et al., 2020; Stephens et al., 2020). Extreme skew-surges and storm surges usually do not exceed 50 cm, but rare events with larger surges have occasionally been observed (Stephens et

al., 2020). Extremes in sea level tend to be separated by more than 4 to 10 days (Stephens et al., 2020). The seasonal pattern of extreme sea levels and skew-surge events closely follows the seasonal pattern of mean sea-level anomaly (Stephens et al., 2020). However, they do not follow any climate pattern (e.g., southern annular mode and southern oscillation index).

The largest waves occur in southern NZ, and the smallest ones are observed in areas sheltered from south-westerly swells (Godoi et al., 2016, 2017; Albuquerque et al., 2021). The number of extreme events varies substantially throughout the year, while the differences in intensity are more consistent. Events occur more/less frequently in winter/summer months. The greatest mean annual variability of extreme wave height is found on the north coasts of the North and South Islands, where more locally-generated storms drive the extremes (Godoi et al. 2017). The interannual variability is largest along the country's north coast and South Island's east coast, suggesting relationships with La Niña-like effects and the Southern Annular Mode, respectively (Godoi et al. 2016). In addition, Albuquerque et al. (2021) have shown that both wind-sea and swells — when analysed separately — show even more robust correlations with the southern annular mode and southern oscillation index than the integrated wave hindcast data.

The weather climate in NZ can be categorised into 12 weather types, which are divided into three main groups (Through, Blocking, and Zonal) (Kidson, 2000). Extreme sea level events are more likely to impact the east coast of the North Island of NZ during Blocking weather types and the South Island and west coast of the North Island during Through weather types. Coggins et al. (2016) have shown that high waves in the south of the country coincide with local strong south-westerly winds — which can occur during Through, Zonal, and Blocking weather types — while those in the north are dominated by distantly generated swells (Through), punctuated by strong local events (Blocking and Through).

The geometry of the coast and the shallow bathymetry of the estuaries and harbours of NZ affect extreme sea levels through non-linear interactions between surge and tide (Costa et al., 2023; Tausía et al., 2023). Costa et al. (2023) showed that extreme NTR generally occurs 4–6 h after the peak of high tide, close to the peak of low tide, and provided strong statistical and numerical evidence that this happens because the shallow water effects and bed friction imposed by the extensive and shallow intertidal areas. In NZ, most of the estuaries can have

more than 80% of the total surface area of the estuary covered by the intertidal zone (Hume et al., 2016).

4.3 Methods

The methods are organised as illustrated in Figure 4.1. Firstly, the database is presented and divided into water level and wave data. Secondly, the water level data processing is detailed. Thirdly, the procedure to identify the storm events of wave height, skew-surges, and water level is described. Fourthly, the clustering, the weather types, and the statistical dependence analysis are explained.

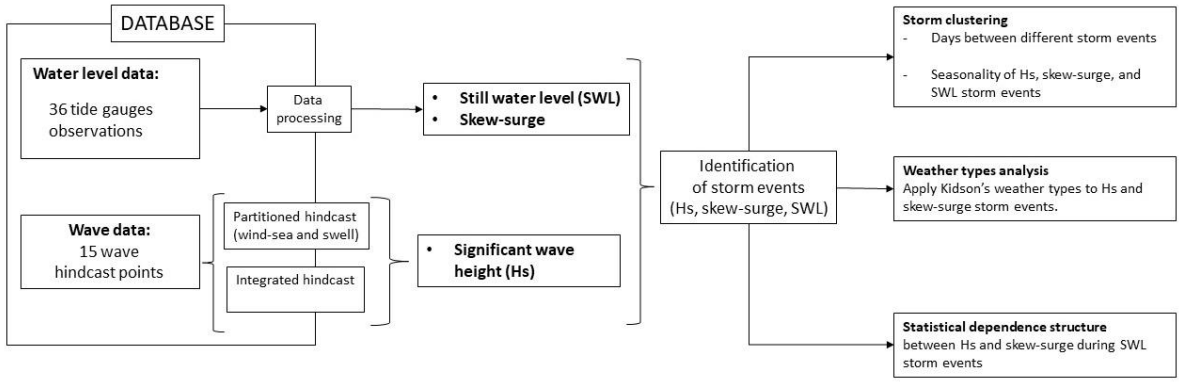

Figure 4.1. Method's pipeline.

4.3.1 Database

Figure 4.2 shows the main NZ geographical features and all water level and wave data locations. Observations from 36 tide gauges around NZ were used to analyse the water level and nontidal residual. The degree of exposure of each tide station to waves varies widely; stations are located at the coast, on islands, inside port wharves, and in estuaries (close to the mouth and in the upper estuarine region). The tide gauges have different owners and sensor types; detailed information can be found in the Table A.1. For each observation point, the data were processed as described in Section 4.3.2.

To examine the wave influence on the NTR and water level, output from a wave hindcast at 15 locations (Albuquerque et al., 2021) were used, available at https://coastalhub.science. This

wave hindcast has been created by first calibrating the results of a 26-year (1993-2019) global wave model (Rascle and Ardhuin, 2013) and then downscaling the multimodal wave spectra using a SWAN model (Booij et al., 1999) that covers the whole NZ area.

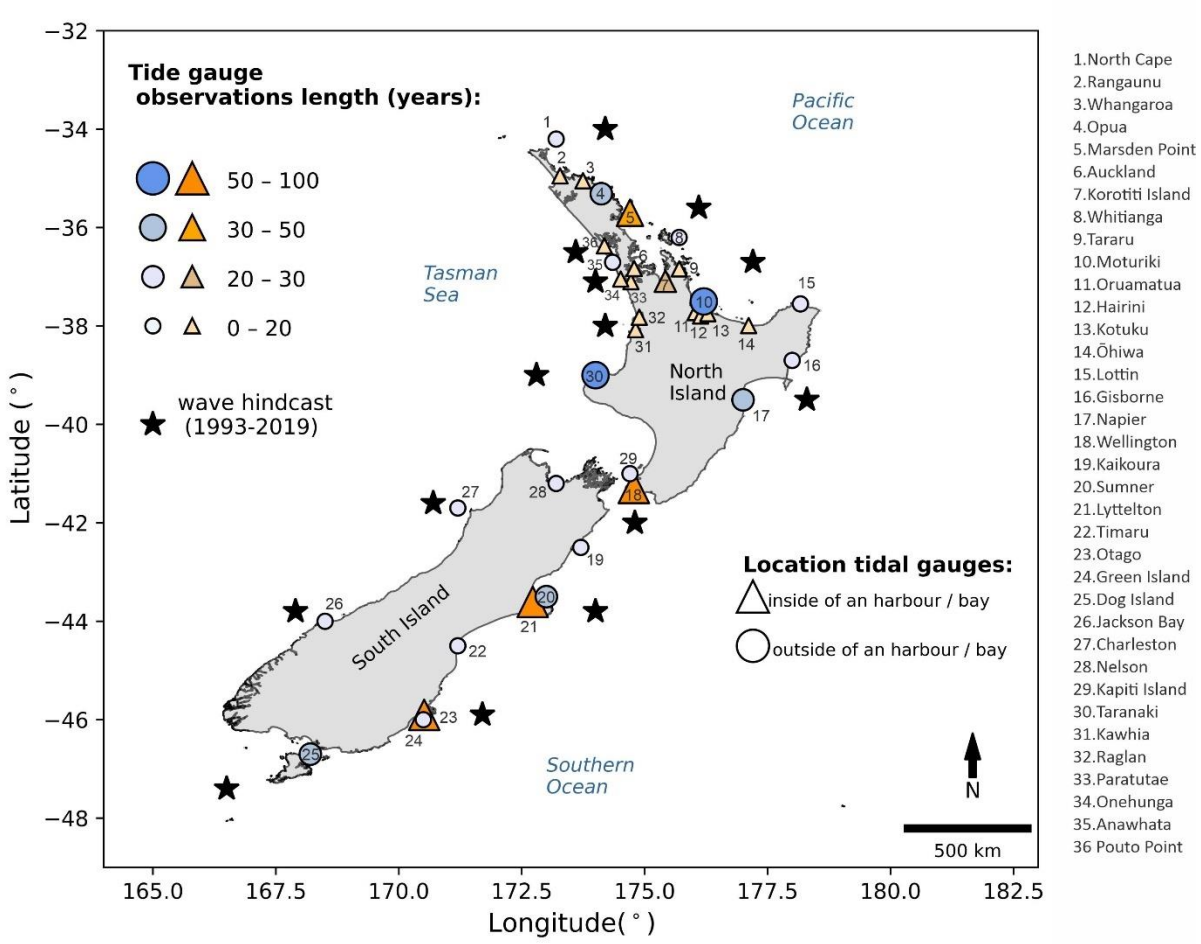

Figure 4.2. Study site. Location of tide gauges and wave hindcast data points.

The Albuquerque et al. (2021) wave hindcast consists of integrated or partitioned data with a temporal resolution of 3h. In this manuscript, both integrated and partitioned hindcast data were used. A sea state can have one direction (unimodal) or several components (multimodal). Hindcasts with integrated wave data means that wave parameters are calculated by integrating over spectral frequencies, regardless of how many wave systems are present. Partitioned hindcasts are estimated using an algorithm that can recognise the different wave systems in a multi-modal sea state (i.e., wind-sea and swell waves), calculate their parameters and store them in different partitions. The Albuquerque et al. (2021) wave hindcast comprises 12 different sea states, and here we use the significant wave height (H_s) and the most energetic swell and the sea-wind state (Hm0 and Hm1, computed with the spectral zero-order moment).

4.3.2 Data processing and extreme event definition

Data processing is required to eliminate signals present in the water level observations that are not relevant for the study, for instance, sea-level rise trends or any human or natural activity that might move the tidal sensors, inducing a change in the mean level recorded and the noise caused by infragravity and tsunami waves. The data pre-processing was applied for each of the 36 water level records following the Stephens et al. (2020) approach. Firstly, the effect of infragravity and tsunami waves was reduced by applying a 15 min running average filter. Secondly, all data were subsampled to 1 h intervals to homogenise all the time series. Thirdly, a 1-year-running average filter was applied to remove the effects of historical sea-level rise from the water level records. As a result of the third step, a filtered water level record — hereafter called still water level (SWL) — is obtained, where the data vary relative to mean sea level = 0 m. Fourthly, a harmonic analysis was performed using the SWL, with 67 standard astronomical components of the tide using the Unified Tidal Analysis package (Codiga, 2011). As a result, the astronomical tide prediction for each tide gauge was obtained. Fifthly, the skew-surge component of each SWL time series was determined by subtracting the SWL peak and the astronomical tide's closest peak. The non-tidal residual was not used because tide-surge interactions were strong in NZ.

The extreme events of SWL, skew-surge, and significant wave height (H_s) were identified using the Stephens et al. (2020) approach. Note that for H_s and skew-surge, extreme events are related to meteorological storms that generated them, while the SWL extreme events can be related to high perigean tides and low storm surge, which means that they are not necessarily related to meteorological storms. The H_s is the highest third part of the wave height in an observational record, calculated over a time period (Holthuijsen, 2007). The extreme events for each variable (SWL, skew-surge, H_s) were selected independently by applying peaks over threshold (POT) using the 99th and the 95th percentile with a declustering scheme of 3 days between events (to ensure that events are independent of each other). Declustering schemes are required for a statistically robust calculation of extreme values using maxima techniques like POT (Coles, 2001). The storm events determined using POT 95th were used in the weather types analysis (Section 4.3.5); the events determined using POT 99th were used in the time clustering (Section 4.3.4) and dependence structure analysis (Section 4.3.3). Although Stephens et al. (2020) use a threshold equal to the 99.8th percentile for SWL, a sensitivity test

showed that using the 99th and 95th percentile give a more robust analysis (greater degrees of freedom), especially for shorter observation records (e.g., < 10 years).

4.3.3 Statistical dependence

Waves, storm surges, and tides have their non-linear interactions enhanced in shallow water due to bed friction, water depth and radiation stress. One method to obtain statistical evidence that this interaction occurs is by calculating the dependence structure of multiple variables. The Kendall-ranked correlation coefficient (τ) is the statistical correlation parameter used here. Kendall's correlation method has been widely applied to study non-linear statistical relationships in coastal science because it does not depend on assumptions of linearity between the variables and is less sensitive to outliers and skewed distribution than Pearson's correlation. The value of τ ranges between -1 and 1, where 0 indicates no correlation and 1 (-1) is a perfect relationship (disagreement). In this manuscript, a confidence interval of 95% was used, which means that the correlation is significant (insignificant) if the $p \leq 0.05$ ($p \geq 0.05$). The statistical dependence between SWL, skew-surge, and waves — H_s *(integrated hindcast* wave data), and Hm0 (partitioned wave data, swell and sea-wind) — were calculated between skew-surge and the wave height parameter associated with each SWL extreme event (POT = 99th percentile).

4.3.4 Clustering analysis

As noted above, storm events occurring in close succession exacerbate coastal erosion and potentially increase the flooding vulnerability of coastal areas. If storm clusters of waves and storm surges occur in close succession, they can potentially enhance SWL extreme events. The clustering analysis aims determine the proximity in time of these events.

The time interval between different extreme events was independently calculated for each variable (SWL, skew-surge, H_s). Note that extreme events of skew-surge and waves can be considered as storm events, while SWL extreme events do not necessarily are originated in meteorological storms, as elucidate in Section 4.3.2. For the seasonality analysis, the number of clusters and independent extreme events for each variable (H_s, skew-surge, and SWL) occurring in each month of the year was counted. The index of dispersion (*Id*) of time intervals between extreme peaks was applied following Godoi et al. (2018) to identify if different extreme events belong to the same cluster or are isolated events. The *Id* is the ratio of the variance $(\Delta T - \langle \Delta T \rangle)^2$ of the time interval ΔT between extreme peaks to the mean interval

$\langle \Delta T \rangle$. Consecutive events were part of the same cluster if the time interval was < 0.5*Id*. The reasoning behind this threshold is that for two or more storms to be considered part of the same cluster, the time difference between their peaks should be lower than the Id and the mean interval of each location analysed. This approach has been used for wave climate in NZ (Godoi et al., 2018) and studies focusing on the beach recovering times for storm erosion (Birkemeier et al., 1999; Ferreira, 2005; Almeida et al., 2012; Karunarathna et al., 2014). Here, the Id was also calculated for extreme events detected in the skew-surge and SWL records. Using this criterion, the average maximum time interval between events where clusters were identified was equal to 15 days for H_s, 25 days (skew-surge), and 7 days (SWL) through all tide gauges or wave hindcast points. To homogenise and ease the analysis' interpretation and minimise the effects of data gaps in the observation records of water level, an interval time between extreme peaks of 15 days was applied as a cut-off for all data (H_s, skew-surge and SWL). Thus, events with a time difference of <15 days were considered part of the same cluster, while time intervals >15 days indicate independent events.

4.3.5 Weather types

Synoptic weather systems generate storm surges and waves. The waves can develop into swells if the weather system is relatively far from the coast. If not, they propagate as wind seas. The weather-type analysis aims to investigate if the weather systems that generate upper tail values of SWL (above the 95th percentile, see Section 4.3.2) at the coast are also associated with storms of skew-surge and H_s. This manuscript has used the Kidson (2000) weather types classification. Figure 4.3 shows the 12 weather types that compose Kidson's classification, which can be aggregated into three different groups: the *Through* (*T, SW*, *TNW*; *TSW*), Zonal (*H*, *HNW*, *W*), and the Blocking (*HSE*, *HE*, *NE*, *HW*, *R*). The first group represents the through meteorological systems that cross the country and generates westerly fluxes (*T*) that can be deviated to the north (*TNW*) or the south — *TSW* and *SW*; the first, if the low centre is in the land, and the second if it is far in the ocean. The Zonal group is marked by intense anticyclones (*H*) above latitude 40 S located over the North Island. The centre of the anticyclone can be located further west or north, causing a northwestern (*HNW*) or western (*HW*) flux, respectively. The *Blocking* group has high centres lying to the southeast, northeast and west of the South Island (*HSE*, *NE*, *HW*, respectively), east of the North Island (HE) and simultaneously at the west and east coast of the South Island (*R*). Kidson (2000) applied a k-means clustering algorithm to characterise the main atmospheric patterns for NZ. The algorithm was applied to

the normalised principal components of the first five empirical orthogonal functions of 1000 hPa geopotential height anomalies of the NCEP-NCAR reanalysis. Each SWL extreme event was associated with one of the 12 weather types. Thus, the magnitude of the skew-surge and H_s that corresponds to the event of SWL were analysed to see if there is any relationship between synoptic weather systems, skew-surge, and H_s during storm events of SWL (using POT = 95th percentile).

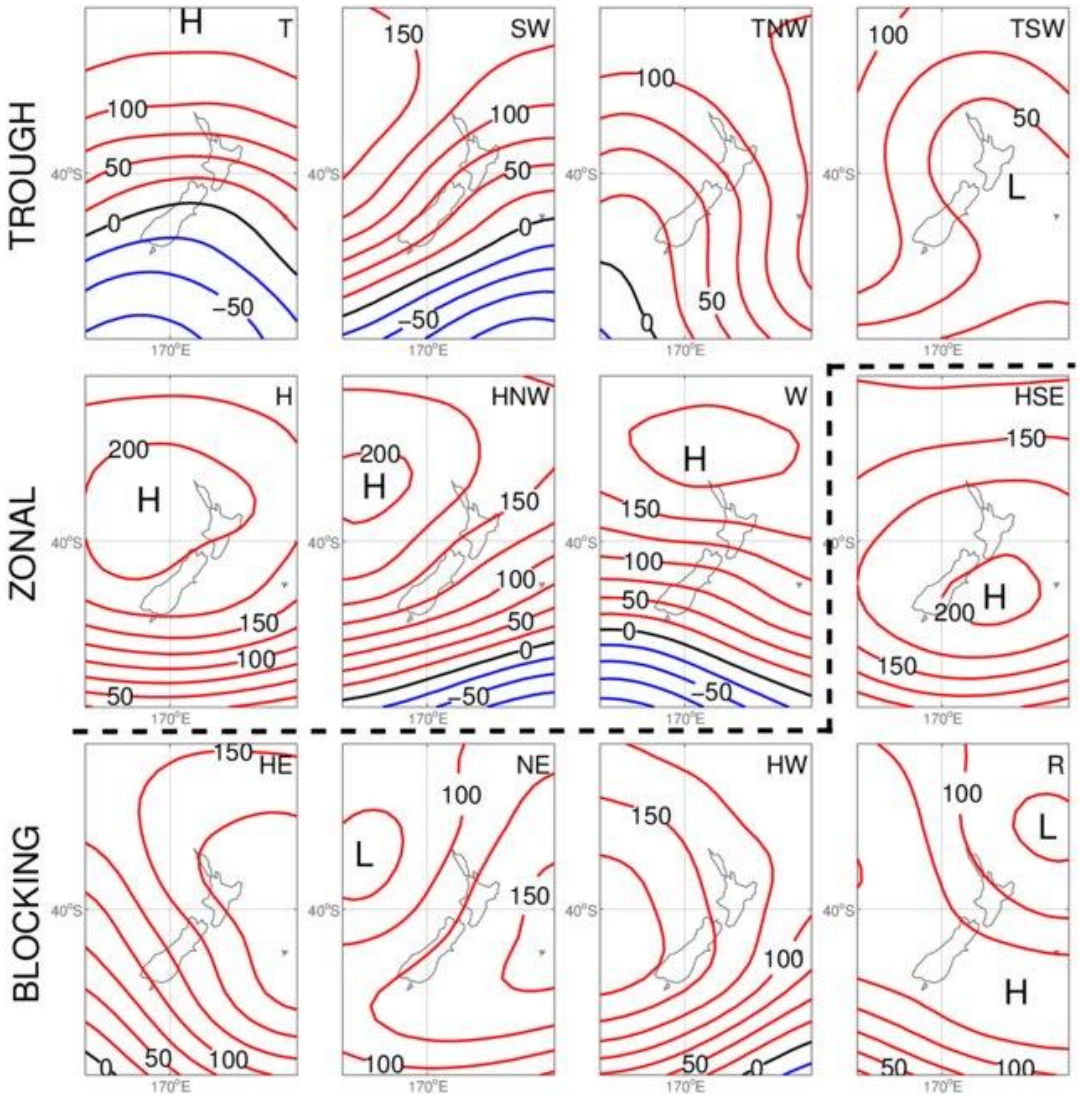

Figure 4.3. Kidson (2000) weather types classification. The maps show the centre of low (L) and high (H) atmospheric pressure and the isolines representing sea level pressure gradient relative to the isoline of 1000 hPa. Red isolines represent positive, while blue isolines have negative sea level pressure gradients. The figure was taken from Ackerley et al. (2011).

4.4 Results

4.4.1 Statistical dependence

Wave and skew-surge are strongly correlated, evidenced by the significant correlation between skew-surge and H_s associated with storm events of SWL. Figure 4.4 shows that the τ ranked coefficient ranges from 0.1 to 0.6, and locations on the North Island showed a stronger correlation (e.g., Kawhia, Raglan, Pouto Point, Ōhiwa and all the Northland locations), while sites on the South Island showed a lower correlation (Kaikoroa, Jackson Bay, Otago Habour). Surprisingly, the sites where tide gauges are located inside estuaries and close to the estuarine mouth showed higher correlation coefficients than other locations at exposed sites (i.e., Kawhia, Raglan, Ōhiwa, Pouto Point). Regarding the contribution of wind waves (Figure 4.4B) and swells (Figure 4.4C), skew-surge on the North Island's west coast correlates better with wind-sea H_s, while on the east coast, the correlation is stronger for swell H_s.

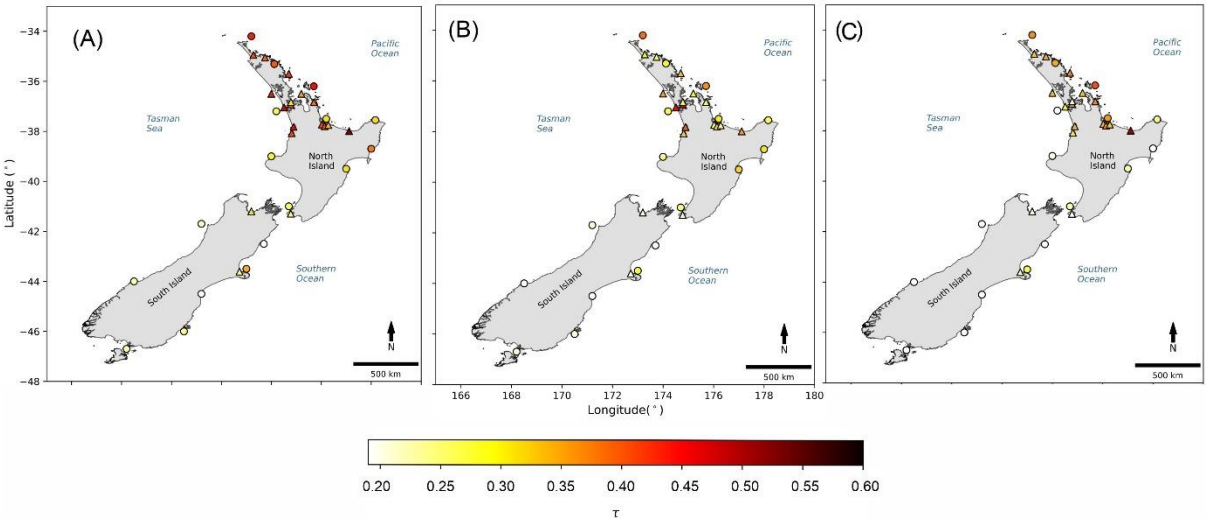

Figure 4.4. The correlation coefficient τ between skew-surge and H_s during SWL storm events: (A) H_s integrated, (B) H_s wind waves, and (C) H_s swell waves.

4.4.2 Extreme event clustering

Extreme events clusters and individual events patterns of skew-surge and H_s are similar. Figures 4.5 and 4.6 show the probability of consecutive events of H_s and skew-surge, respectively, to occur in different time intervals. On average, at least 30% of the extreme events occur in clusters (from 3 to 15 days of time interval) across all tide gauges and wave hindcast

points. However, most events (~50%) of H_s occur between 20 to 60 days from each other, while events of skew-surges occur within 40–90 days. As illustrated by Figure 4.7, consecutive SWL events are more likely to occur with time intervals of 3–5 days (which represents clustering events) with up to 30% of probability and 20–30 days with a probability >30%. On average, H_s, skew-surge, and SWL event clusters comprise 2–5 extreme events, although clusters containing up to 11 and 12 events were identified for skew-surge and SWL through all tide gauges.

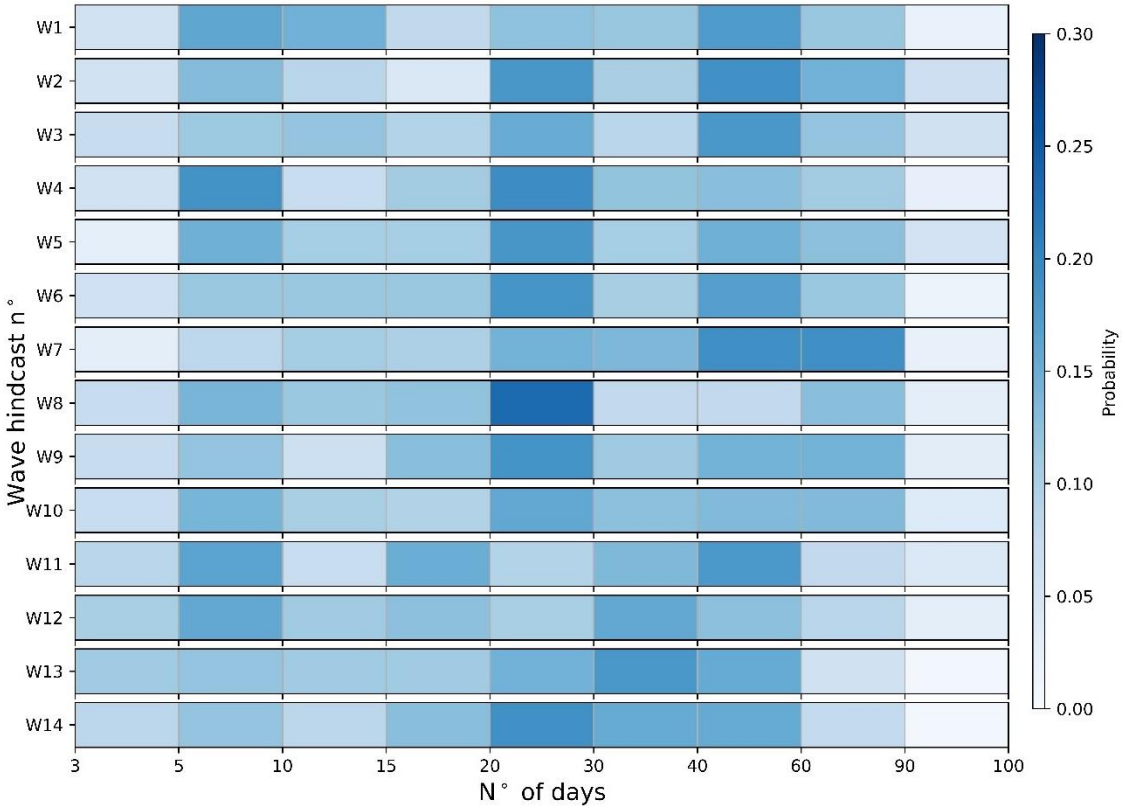

Figure 4.5. The time interval between two consecutive extreme events of H_s in 14 wave hindcast data points (W1–14). Stronger colours represent time intervals more likely to occur between two storms.

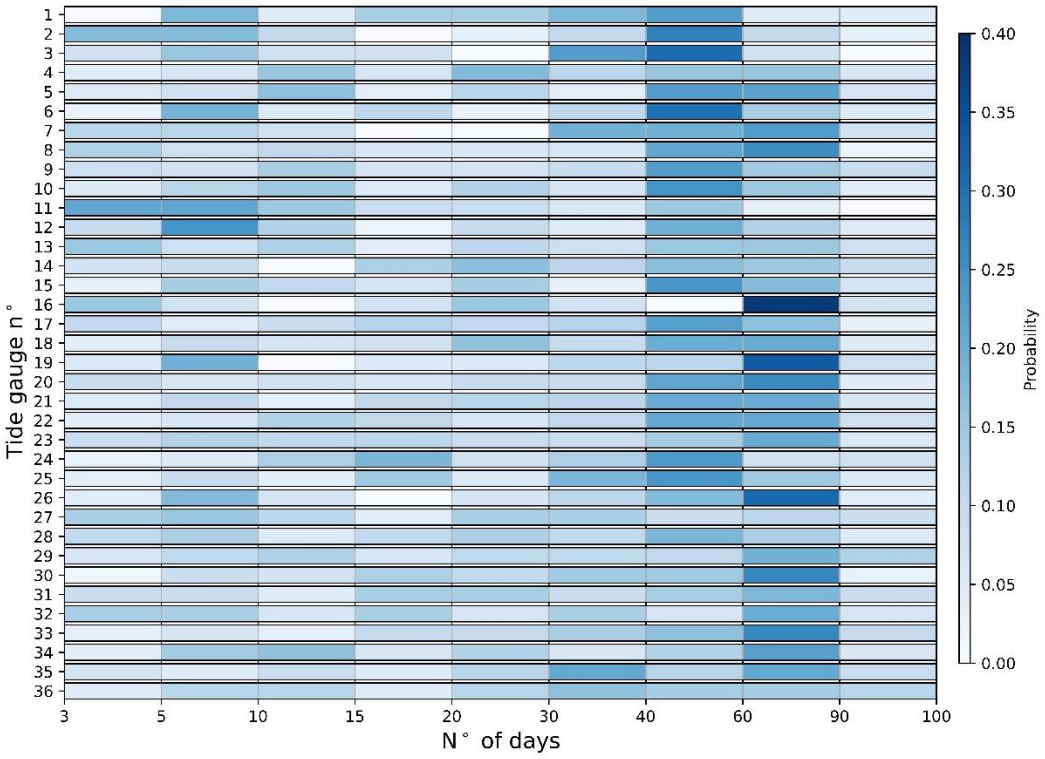

Figure 4.6. Probability of the time interval between two consecutive extreme events of skew-surge in 36 tide gauge observations. Stronger colours represent time intervals more likely to occur between two storms.

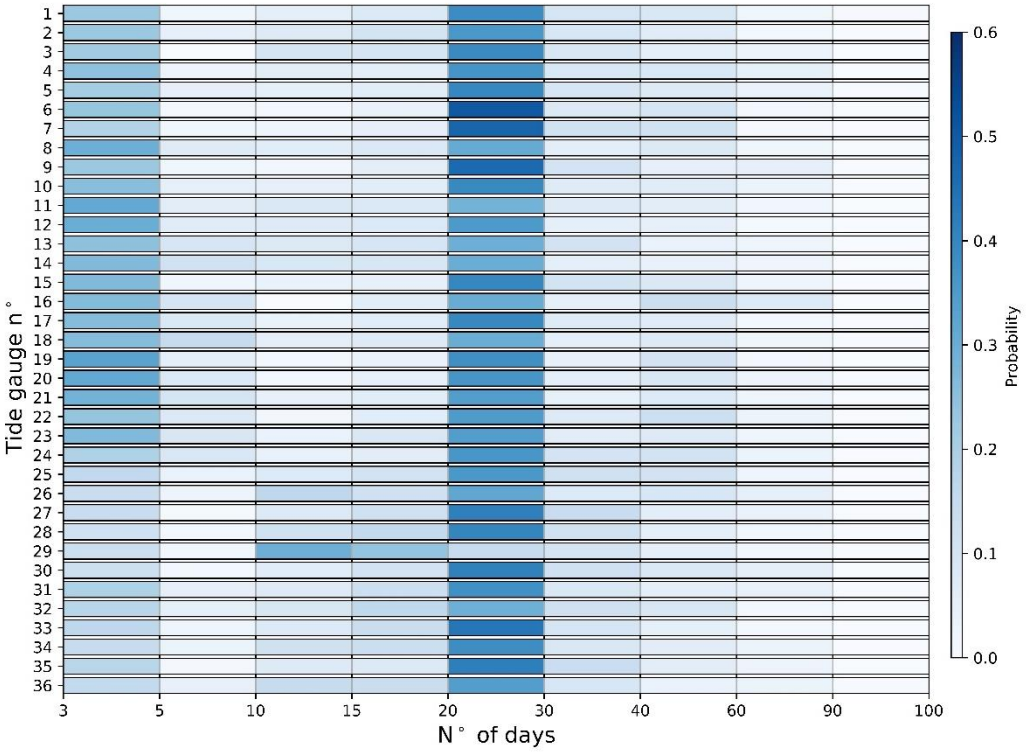

Figure 4.7. Probability of the time interval between two consecutive extreme events of SWL in 36 tide gauge observations. Stronger colours represent time intervals more likely to occur between two storms.

The seasonality of H_s and skew-surge event clusters follow close patterns, with a higher probability of occurrence in the winter months (from May to August) in most studied locations. For example, Figure 4.8 shows the likelihood of event cluster occurrence distributed over the months of the year for Ōhiwa (A), Pouto Point (B), Paratutae (C), and Kawhia (D), where the darker the shade of green, the higher is the probability of extreme events to occur in close succession (<15-days interval) in each month. Similarly, for individual events (occurring > 15-day intervals from each other), Figure 4.9 shows that they are more likely to occur in winter months. However, the probabilities of occurrence are more equally distributed throughout the year than the probability of event cluster occurrence. Of all sites, Ōhiwa (A) is the one that shows the most similar seasonality between H_s, skew-surges and SWL, especially for event clusters.

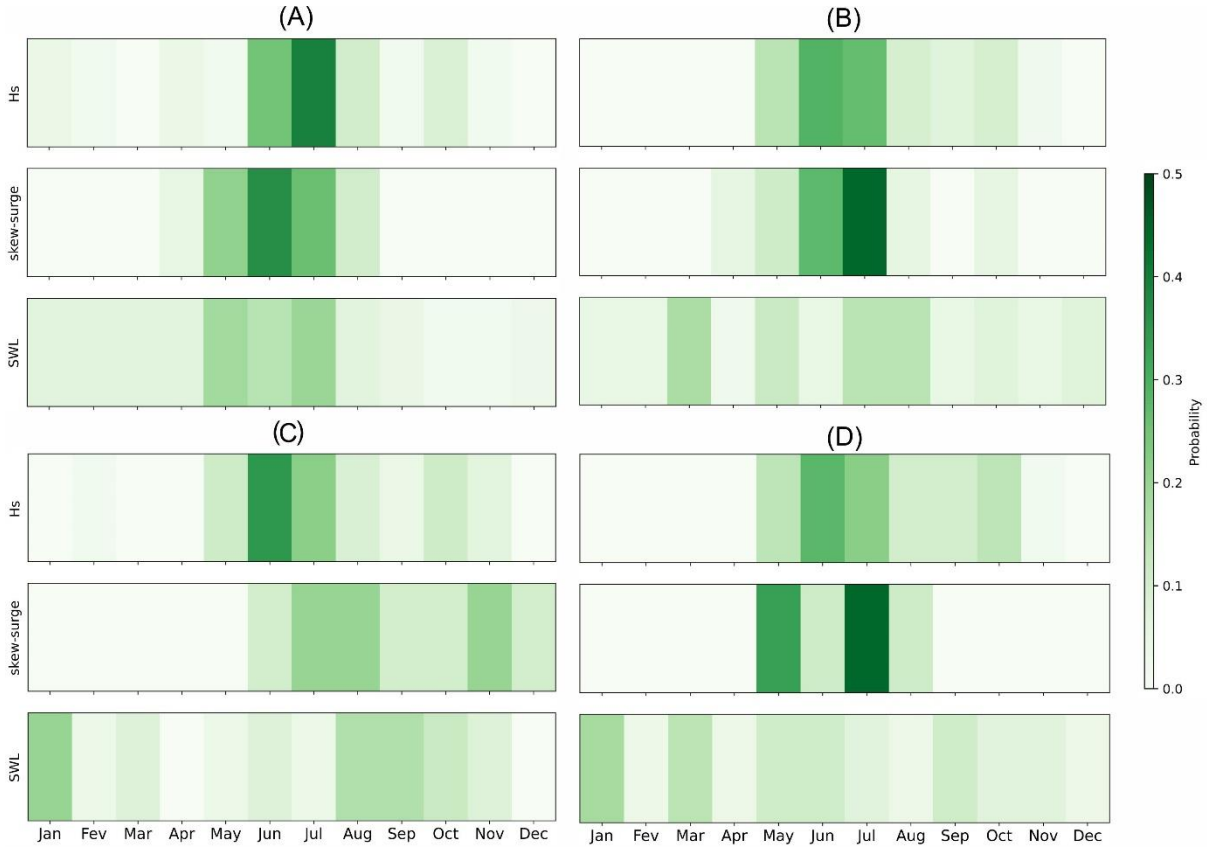

Figure 4.8. Seasonality of extreme events clustering of H_s, skew-surge, and SWL for Ohiwa (A), Pouto Point (B), Paratutae (C), and Kawhia (D). Stronger colours represent a higher number of events occurring in that period.

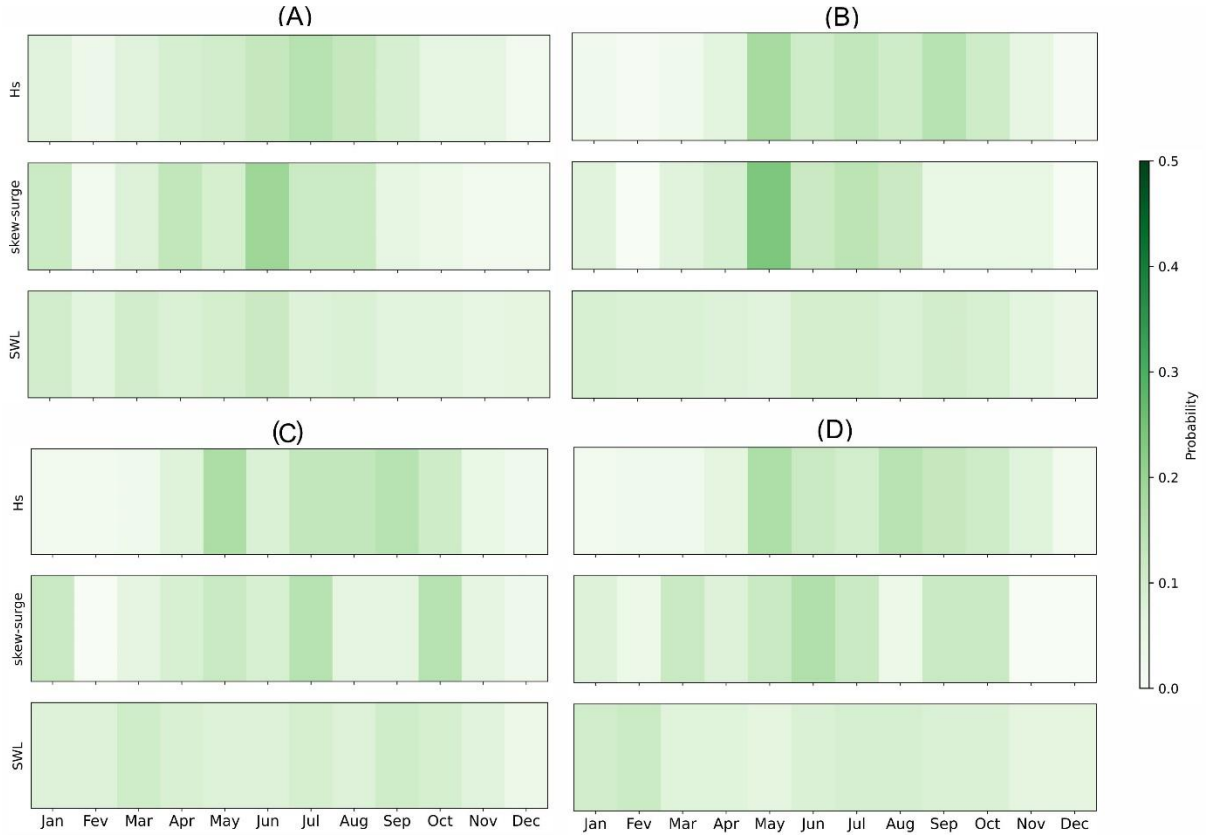

Figure 4.9. Seasonality of individual extreme events of H_s, skew-surge, and SWL for Ohiwa (A), Pouto Point (B), Paratutae (C), and Kawhia (D). Stronger colours represent a higher number of events occurring in that period.

4.4.3 Weather Types

The highest skew surges and H_s occur during the same weather types. On the west coast of North Island, the highest skew-surges and H_s are related to the Through weather type. For the east coast of the North Island, the highest skew surges and H_s are related to both Through and Blocking weather types; for the South Island, Through, Blocking and Zonal weather types are related to the highest skew-surges and H_s. For instance, Figures 4.10 and 4.11 show the distribution of H_s and skew-surge associated with the extreme events of SWL over the threshold of the 95th percentile at Onehunga (A) — located at the west coast of the North Island —, Hairini (B) — located at the east coast of the North Island —, Lyttelton (C), and Otago (D) — both located at the east coast of the South Island —. For Onehunga, weather types Through (T and SW) are responsible for the highest skew surge (~0.6 m) and H_s (~9 m). For Hairini, similarly, the Through weather types (T, TNW, TSW) are responsible for higher H_s and skew-surge responses. However, higher values of skew-surge can also occur during Blocking

weather types. For the sites located at the South Island (Lyttelton and Otago Harbour), Through (e.g., SW) and Blocking (e.g., HW) weather types produce higher skew-surges and H_s; however, the Zonal weather type HNW can also be associated to stronger skew-surge and H_s responses.

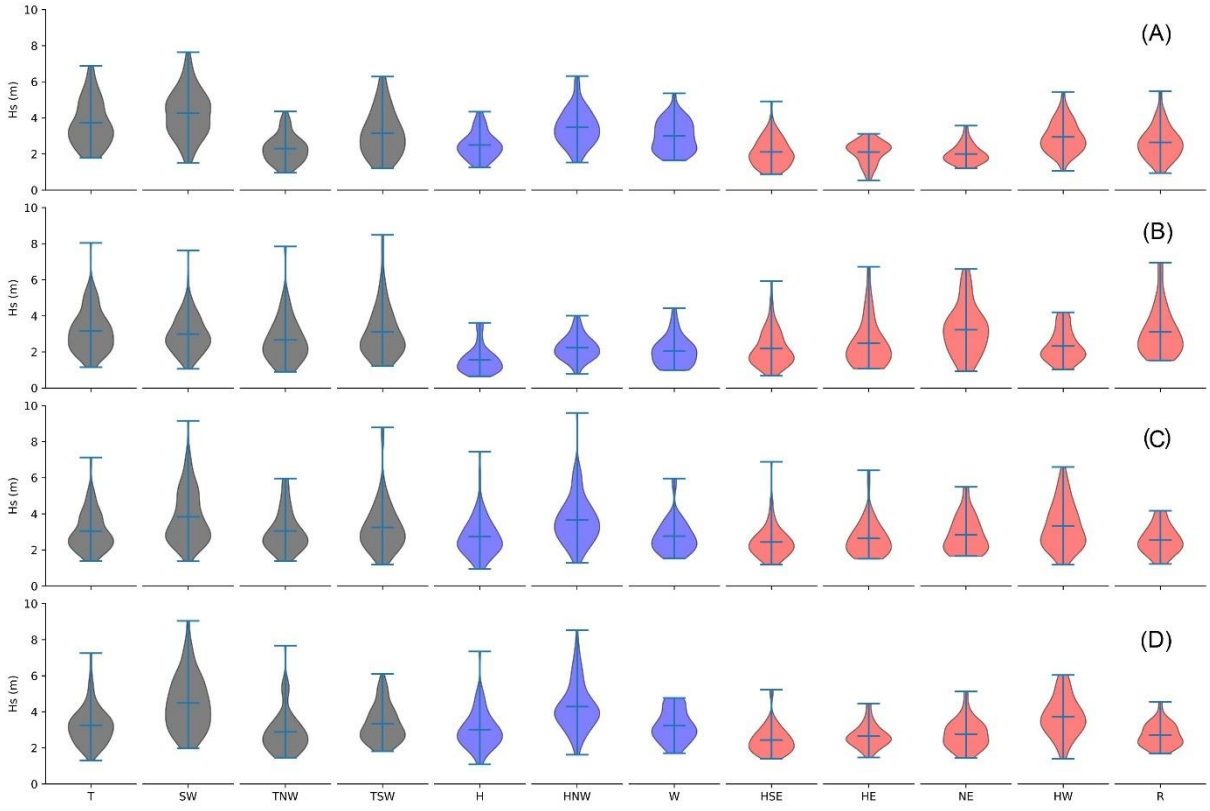

Figure 4.10. Distribution of Hs (integrated) corresponding to SWL storm events (POT=95th percentile) through 12 Kidson et al weather types for (A) Onehunga, (B) Hairini, (C) Lyttelton, and (D) Otago Harbour. Black violin distribution represents *Trough*; blue represents *Zonal* group; red represents *Blocking* weather types.

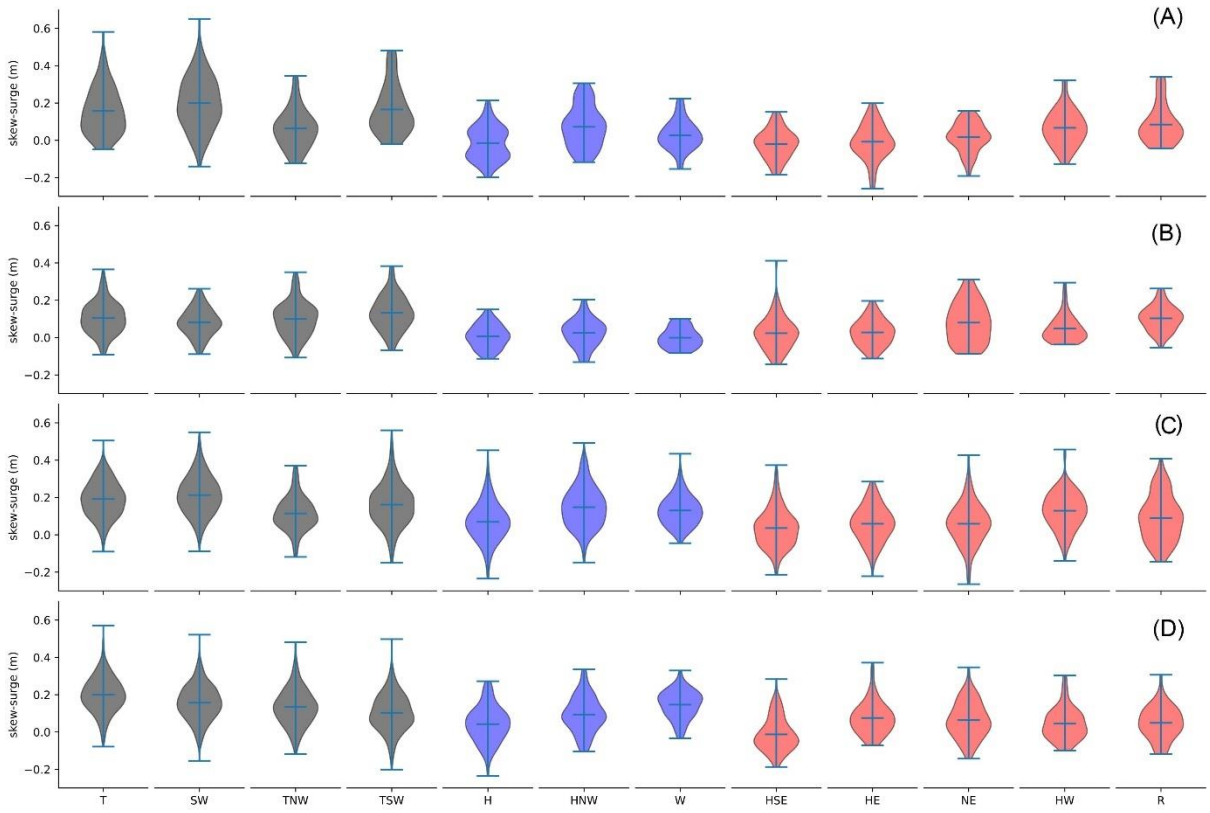

Figure 4.11. Distribution of skew-surge corresponding to SWL storm events (POT=95th percentile) through 12 Kidson et al. weather types for (A) Onehunga, (B) Hairini, (C) Lyttelton, (D) Otago. Black violin distribution represents *Trough*; blue represents *Zonal* group; red represents *Blocking* weather types.

4.5 Discussion

The statistical evidence presented here shows the importance of the compound effect of waves and skew surges on extreme sea levels and coastal flooding, which has practical implications for coastal planning. For instance, current projections for return periods of extreme SWL worldwide are commonly predicted using only astronomical tides and surges (i.e., storm surge or skew-surge), which partially ignores the potential contribution of waves. In the specific case of NZ, extreme events of waves have been shown to intensify over time (Godoi et al., 2016), and current projections show that on the east coast, wave heights are more likely to increase (Albuquerque et al., 2022). Given that we have shown that waves can directly affect the water levels by showing that they co-occur and are correlated, they should be accounted for in SWL storm return periods calculations. In addition, the results found here show that event clusters of waves, skew-surge and SWL have similar seasonality. Event clusters are known to be equal

to or more energetic than individual extreme events (e.g., Ferreira, 2005, Senechal et al., 2017). In that case, our findings show that event clusters of waves and skew-surges can impact the coast at the same time, exacerbating coastal flooding risk through beach erosion and increased sea levels.

The strong correlation — between H_s and skew-surge corresponding to SWL extreme events — found at tide gauges inside estuarine regions is unexpected. Theoretically, tide gauges located at exposed areas by the coast should be more affected by waves because of the release of energy in the breaking-wave zone, generating wave set-up. However, the tide gauges used in this work at exposed sites are not placed on the beach. Instead, they are in embayment and port wharves (e.g., Taranaki, Gisborne, Napier), protecting the sensors from breaking waves. The influence of waves inside the estuary has been the focus of different studies (Bertin et al., 2012, 2015, 2019; Khan et al., 2021). For instance, Bertin et al. (2015) have shown that short waves caused an increment of 0.2 m on the water level in Arcachon Estuary (an enclosed tidal lagoon), France, during cyclone Xynthia. Bertin et al. (2019) showed that, through field measurements, infragravity waves of up to 0.4 m could propagate inside Albufeira Lagoon, Portugal, during flood tide and are fundamental for the closure dynamics of the estuarine inlet. Costa et al. (2019) demonstrated that wave-tide interactions modulate the sediment flux on headland by-passing and sand spit in the tidal inlet of the Babitonga Bay, a complex estuarine system on the southern coast of Brazil. Most of these studies have shown that waves can strongly affect the hydro- and sediment dynamics nearby the estuarine or enclosed embayment mouth, but just a few of them have investigated how far in the upper estuarine areas this influence can reach (Gallop et al., 2020; Rahbani et al., 2022). For instance, in Australia, Rahbani et al. (2022) used wave spectra analysis to show that the wave signature in four different beaches located at bays and estuaries are dominated by swell (>53%), followed by locally generated wind waves (<43%) and infragravity waves (<35%). In the most sheltered beaches (e.g., in the upper estuarine region), infragravity waves were dominant; at mid-distance from the estuarine mouth (~8km), wind-sea and swells alternated the dominance of the spectral energy; close to the estuarine mouth, swells were dominant. In addition, the strong winds caused by storms generate local waves, which can substantially increase the water level inside large estuaries, where there is a large fetch for wind-waves to develop. Local wind-generated waves have been studied in NZ, especially in Manukau Harbour — an extensive shallow estuary with wide intertidal area — where the large fetch area inside the estuary (10–15 km)

allow wind waves of 0.12–0.40 m to develop, although they are strongly attenuated by the tidal regime (Smith et al., 2001).

The H_s, skew-surge, and SWL event clusters and individual extreme events tend to occur with similar time intervals and seasonality, which reveals the potential of the compound effect on extreme water level events. However, H_s and skew-surge events are more strongly linked to each other than SWL events. In addition, H_s and skew-surge have shown a strong correlation during extreme events of SWL. The weaker link between SWL and the other variables (i.e., H_s and skew-surge) can be explained by the tide cycles and the shallow water effects inside estuaries. As shown in Figure 4.7, the consecutive extreme events of SWL occur mainly during time intervals of 3–5 days and 20–30 days, which would match with the high SWLs occurring during the same spring tide cycle (within seven days) and with an entire tidal cycle of difference (~29 days). Regarding seasonality, perigean tides in the southern hemisphere occur in March–April, and the largest waves and skew-surges occur in the winter months in most locations (June, July, and August). Note that the surges (skew-surges and NTR) are relatively lower in NZ compared to other places globally, and the astronomical tide drives the extreme SWL events (Stephens et al., 2020). In addition, a recent study has shown that non-linear interactions between surges and tides are strong inside the estuaries of NZ (Costa et al., 2023). The shallow estuaries and complex geometry of the coast make the extreme surges (i.e., non-tidal residual) more likely to occur during low tides inside harbours, which would not affect the peak of the SWL. Thus, interactions between storm surges and waves would only substantially increase the peak of the SWL when rare extreme surges coincide with high tide.

Similar clustering and compound analysis have been performed in the northern hemisphere; however, they are focused on temporal clustering (Jenkins et al., 2023) or compound flooding (Camus et al., 2021; Nasr et al., 2021) only, not bringing a combined interpretation. Jenkins et al. (2023) have shown strong intra-annual and interannual variability for NTR, H_s and SWL extreme events in the United Kingdom. For instance, events with < 50 days of time interval form each other account for ~ 35–44% and ~ 15–22% of all exceedances at the 1 in 1- and 5-year return levels, respectively. For wave climate, Godoi et al. (2017) have calculated the intensity of storm clusters and estimated temporal trends and variations according to climate indexes (e.g., Southern Ocean Oscillation Index). Although surge (non-tidal residual, storm surge, skew-surge) climate does not vary according to climate indexes, they were shown to be linked to anomalies in the sea level (Stephens et al., 2020). Thus, further studies comparing

sea-level rise and temporal trends of storm intensity would be of fundamental importance to predict future skew-surge, H_s and SWL climate. Compared to previous studies on storm clustering, the analyses shown here give a broader interpretation of the combined action of waves and skew-surges by considering the dependence structure of waves and skew-surges during extreme water level events. Some compound flooding studies use a two-way validation method to assess the dependence structure of multiple variables (e.g., Camus et al., 2021; Nasr et al., 2021). For example, the correlation coefficient is calculated between the storm events of H_s and the corresponding SWL and surge (i.e., NTR, storm surge, or skew-surge). The same process is done for each other variable independently, totalling six interactions. This procedure was tested here and returned no significant correlations (with a confidence interval ≥ 95%).

The highest skew surges and H_s corresponding to extreme events of SWL are related to the same weather types. The link between anomalies of H_s and Kidson's weather types has been shown in (Coggins et al., 2015), and our findings corroborate it. Weather types that induce strong westerly and southerly winds are linked to the highest H_s observed in NZ's west, south, and southeast coast during storm events. This is because the wind blowing from these directions can locally generate sea winds, which is especially noted during Through and Zonal weather types — for the west coast of North and South Islands — and during Blocking weather types — for south and east coasts of the South Island. For the north-eastern coast of the North Island, the Through weather types (subclass TSW) and Blocking (subclass R) are linked to higher values of H_s because they are related to extra-tropical cyclones that commonly impacted the region during Austral summer—for example, the recent Cyclone Gabrielle (2023).

Similarly, the degree of exposure to strong westerly and southern winds explains the relationship between weather types and skew-surge during extreme events of SWL, corroborating Stephens et al. (2020). This is because the wind is one of the components of the storm surge, and its importance increases as the coastal/ estuarine area becomes shallower. Furthermore, weather types representing strong sea level pressure gradients can increase the hydrostatic pressure component of the storm surges. For instance, Through and Blocking weather types are related to extratropical cyclones (low sea level pressure centres) crossing or passing near NZ, which causes the increase of the sea level through the hydrostatic pressure approximation and surface stress because of strong westerly and southerly winds. Conversely, Zonal weather types usually do not represent strong positive skew-surges because they are

associated with high sea level pressure centres crossing NZ, which generally causes a decrease in the sea level according to the hydrostatic pressure approximation.

The contribution of swells should be further investigated as NZ has been proven to be impacted by a broad range of swell directions (Coggins et al., 2015; Godoi et al., 2016). Our analysis of dependence structure reveals that the swell component holds greater importance for the northeast coast of the North Island, while wind-sea waves dominate on the west coast. However, integrated wave data demonstrated a strong relationship between skew-surge and waves during extreme events of SWL around the entire North Island, highlighting the importance of considering the compound effects of wind-sea and swell waves. This regional variation happens because the origin region of the swells impacting NZ is wide. Storms in the Indian and Southern Oceans originate the southerly and westerly swells that affect the west and south coasts. In contrast, the northern swells, originating in the Southern Pacific Ocean, impact the North Island east, west, and north coasts (Rueda et al., 2019). Therefore, Kidson's weather types are limited in assessing weather patterns contributing to distant swell generation because they are restricted to analysing an area close to Aotearoa New Zealand. To address this limitation, weather types that encompass a wider area (e.g., including South Pacific and Indian Ocean) (Rueda et al., 2019) could be optimal to fully understand the dynamics of swells impacting the water levels at the coast and inside estuaries.

A strong regional variability between North and South Island regarding dependence structure between skew-surge and waves during extreme SWL was also found, which can be explained by the geographical setting. The tide gauges in the east and southeast coast of Aotearoa New Zealand (located at the open coast and inside harbours) are oriented toward north and northeast (e.g., Sumner, Lyttelton, Otago Harbour), therefore, being sheltered from the southern waves. The incident angle of the wave is a limiting factor for swell wave signature, even in locations nearby the estuarine mouth (Rahbani et al., 2022). However, the weak relationship between skew-surge and waves in these places does not necessarily mean that wave and storm surge interactions are unimportant. The wave climate of the South Island experience higher surges (storm surge and skew-surge) (Cagigal et al., 2018; Stephens et al., 2020) and waves (Godoi et al., 2016; Godoi et al., 2017; Albuquerque et al., 2021) than North Island, which represents a potential for wave-surge interactions.

4.6 Conclusion

A regional data analysis showed which areas in NZ and at which times of the year the compound effects of wave and storm surge (here studied through skew-surge) are important both to individual storms and to storm clusters (i.e., storms occurring in close succession). To support this finding, several statistical analyses were applied. Firstly, during the extreme events of SWL, the corresponding skew-surge and H_s are significantly correlated, and their correlation is stronger in locations inside estuaries and close to the entrance of estuaries. Wave and skew-surge were particularly important for sea level variations on the northeastern and northwestern coasts of North Island, especially during the Austral winter. Furthermore, the seasonality of individual extreme events and clusters (H_s, skew-surge and SWL) were similar, although the tidal component modulates extreme events of SWL. In addition, waves and skew-surge events generally originated from the same meteorological systems (especially *Through* and *Blocking* weather types, varying on the analysis region). Ultimately, our findings help build knowledge on the compound effects of waves and surges during coastal flooding.

Chapter 5

Modelling extreme water levels using intertidal topography and bathymetry derived from multispectral satellite images

Wagner L.L. Costa[1*], Karin R. Bryan[1], Giovanni Coco [2] (published in Natural Hazards and Earth Sciences (2023). DOI 10.5194/nhess-2021-387)

[1]Coastal Marine Group, School of Science, The University of Waikato, Hamilton, New Zealand

[2] School of Environment, University of Auckland, Auckland, New Zealand.

Contribution of Authors: Wagner L.L. Costa: methodology, numerical modelling, data analysis, writing – original draft, visualisation. Karin R. Bryan: conceptualisation, supervision, writing – review & editing, resources, funding acquisition. Giovanni Coco: Writing – review & editing, supervision.

Code availability: the main codes used in this chapter are available at https://github.com/CostaAndCoasts/

Conference presentation and scientific promotion: the developments of this chapter were presented in the Australasian Coasts and Ports Conference, Chirstchurch and online, New Zealand, April, 2022. In addition, a conference paper about this chapter was published and it is available at https://www.coastsandports.org/all-conference-papers/. A short article for scientific promotion was also published by The New Zealand Coastal Society at Coastal News journal (https://www.coastalsociety.org.nz/media/view/publications/storm-surge-satellite-bathymetry/).

International collaboration: The codes developed in this chapter are being used and adapted to integrate the Coastal Analyst System from Space Imagery Engine (CASSIE). More information can be accessed at: https://cassiengine.org/

Abstract

Topographic and bathymetric data are essential for accurate predictions of flooding in estuaries because water depth and elevation data are fundamental components of the shallow-water hydrodynamic equations used in models for storm surges and tides. Where LiDAR or in-situ acoustic surveys are unavailable, recent efforts have centred on using satellite images to derive bathymetry (SDB) and topography (SDT). This work is aimed at (1) determining the accuracy of SDT and (2) assessing the suitability of the SDT and SDB for surge/tidal modelling of estuaries. The SDT was created by extracting the waterline as it tracks over the topography with changing tides. The method was applied to four different estuaries in Aotearoa New Zealand: Whitianga, Maketū, Ōhiwa and Tauranga Harbours. Results show that the waterline method provides similar topography to the LiDAR with a root-mean-squared error equal to 0.2 m, and it is slightly improved when two correction methods are applied to the topography derivations: the removal of statistical bias (0.02 m improvement) and hydrodynamic modelling correction of waterline elevation (0.01 m improvement). The use of SDT in numerical simulations of surge levels was assessed for Tauranga Harbour in eight different simulation scenarios. Each scenario explored different ways of incorporating the SDT to replace the topographic data collected using non-satellite survey methods. In addition, one of these scenarios combined SDT (for intertidal zones) and SDB (for subtidal bathymetry), so only satellite information is used in surge modelling. The latter SDB is derived using the well-known ratio-log method. For Tauranga Harbour, using SDT and SDB in hydrodynamic models does not result in significant differences in predicting high water levels when compared with the scenario modelled using surveyed bathymetry.

5.1 Introduction

Coastal flooding has become increasingly concerning because of growing storm intensity (Emanuel, 2005; Webster et al., 2005; Sobel et al., 2016) and sea-level rise, which will potentially increase the risk exposure of coastal communities (Nicholls and Cazenave, 2010; Oppenheimer et al., 2019). In practice, predicting flooding depends on understanding the contribution from the astronomical tide, storm surge, wave run-up, changes in the sea level and, in some cases, the fluvial discharge and vertical land motion. In coastal zones, these processes can interfere with each other, for example, in tide-surge interactions (Spicer et al., 2019; Wankang et al., 2019). In the case of estuaries, bathymetric and topographic data are essential for coastal risk assessment (Parodi et al., 2020) because they influence the accuracy of water level predictions (Cea and French, 2012; Pedrozo-Acuña et al., 2012; Falcão et al., 2013; Mohammadian et al., 2022). Water depth is a fundamental component in the shallow-water hydrodynamic equations used in extreme water level modelling. Together with the estuary's geometry and length — which can cause shoaling and choking — and bed-shear stress — which reduces energy due to its effect on friction — bathymetry and topography control the amplitude and phase (timing) of the propagating tide. The estuary's morphology is also fundamental for studying the tidal response to sea-level rise (Du et al., 2018; Khojasteh et al., 2020, 2021).

The methods used to measure bathymetry and topography in coastal zones have evolved rapidly. In estuaries, there are permanently inundated areas and intertidal zones, which are flooded and exposed to the tide. Here we define the terms bathymetry and topography to reflect permanently-inundated and intertidal areas, respectively. Currently, there are four types of systems for measuring these: ship-based systems (e.g., single-beam and multibeam echosounders); non-imaging active remote sensing (e.g. LiDAR); imaging active remote sensing (e.g. synthetic aperture radar — SAR); and, imaging passive remote sensing (e.g. optical systems) (Jawak et al., 2015; Salameh et al., 2019; Ashphaq et al., 2021). Traditionally, the most commonly-used systems are echosounders and LiDAR. Both produce highly accurate data; however, several factors constrain their application, such as cost, labour, inaccessibility of remote areas, and environmental conditions (e.g., low tide navigational restrictions). Consequently, according to IHO (2020), approximately 70% of the world's coastal areas have

bathymetric surveys that need updating or are insufficiently detailed (e.g., are of large scale 1:100).

Space-borne remote sensing techniques overcome the limitations of traditional techniques and can provide topographic and bathymetric data for a wide range of environments, including areas that are more difficult to measure, such as remote shallow coastal waters (Lyzenga, 1985; Ehses and Rooney, 2015; Caballero and Stumpf, 2019) and extensive intertidal areas (Bishop-Taylor et al., 2019; Fitton et al., 2021). Several methods are used to derive bathymetric data — hereafter called satellite-derived bathymetry (SDB) — in shallow waters (i.e., between 0–15 m depth) using imaging passive remote sensing of reflectance (Ashphaq et al., 2021). Most methods are developed around the process of light attenuation through the water column and can be categorised into two approaches. Empirical methods — which use direct observations of water depth in the study area to calibrate the reflectance-to-depth relationship (e.g., Stumpf et al., 2003; Caballero and Stumpf, 2019) — and physics-based inversion algorithms — which use physical processes/models to solve for water depth (e.g., radiative transfer models) without the need for in situ calibration data (e.g., Lee et al., 1998; Kerr and Purkis, 2018).

The present manuscript focuses on empirical methods to obtain the SDB, including the ratio-log method proposed by Stumpf et al. (2003). The main limitations of the Stumpf method are the requirement of in situ bathymetric data for calibration and its sensitivity to environmental conditions that can change bottom and water reflectance — e.g., high water turbidity and variation in the benthic substrates — both of which often occur in enclosed seas, bays and estuaries (Morris et al., 2007). Some studies have proposed techniques to tackle these empirical issues (e.g., Geyman and Maloof, 2019; Caballero and Stumpf, 2020). For example, Geyman and Maloof (2019) implemented the cluster-based regression algorithm to deal with different bottom substrates, first segmenting the satellite image into zones of spectral homogeneity and then calibrating the log-linear colour-to-depth relationship separately for each class. Caballero and Stumpf (2020) adjusted reflectance ratios to reduce the effects of water turbidity and calculated the maximum chlorophyll index prior to analysis to identify pixels containing floating and submerged vegetation, allowing them to remove these pixels before further implementation of the ratio-log formula.

In intertidal regions, remote sensing can also be used to obtain satellite-derived topography (SDT) — and the waterline method is the most commonly applied. The method was first

applied to SAR images (Mason and Davenport, 1996) and recently also to multispectral space-borne images (Khan et al., 2019; Salameh et al., 2020; Fitton et al., 2021). The technique functions by detecting the edge between the flooded and exposed intertidal zone in multiple images (i.e., the waterline) and assigning a height to each waterline by using the local tidal level at the time of image acquisition. The tidal level can be acquired by a numerical tide model (e.g., Khan et al., 2019; Kang et al., 2020; Salameh et al., 2020) or from a local tide gauge (Mason and Davenport, 1996; Salameh et al., 2020). The resulting collection of waterlines is interpolated over the intertidal domain, generating a digital elevation model (DEM). The approach assumes that estuary morphology does not change between images and has a gentle slope. The main disadvantages of this method are the dependence of accuracy on the number of images used in the processing and the reduced performance when applied to sites with complex morphology, i.e., variable terrain slopes within the intertidal zone (Liu et al., 2013; Salameh et al., 2019, 2020). Other methods used to derive topography in intertidal zones are the interferometric SAR (Li and Goldstein, 1990), satellite radar altimetry (Salameh et al., 2018) and near-infrared logistic approach (Bué et al., 2020).

As remote-sensing techniques have developed, cloud computation and storage systems such as Google Earth Engine (Gorelick et al., 2017) have also advanced considerably. Consequently, scientists now have an enhanced capacity to quickly manage large geographical datasets, allowing global-scale studies in coastal science to evolve rapidly (e.g., Murray et al., 2019; Vos et al., 2019; Bishop-Taylor et al., 2019). For instance, databases now exist on the distribution of and changes to global tidal flats (Murray et al., 2019), as well as a global estimate of coastline position (Almeida et al., 2021; Vos et al., 2019). Satellite-derived bathymetry (SDB) and topography (SDT) techniques are now routinely applied over extensive areas (e.g., Traganos et al., 2018; Bishop-Taylor et al., 2019; Fitton et al., 2021). Despite the vast and growing application of SDB and SDT methods to coastal science and engineering (Turner et al., 2021), it is not yet clear whether the accuracy of the resulting bathymetry/topography is suitable for modelling extreme water levels in coastal areas (e.g., estuaries and bays). Only limited studies exist on SDB, SDT and numerical modelling — generally aimed at using the model to assign the waterline height (Khan et al., 2019; Salameh et al., 2020; Fitton et al., 2021). For instance, Mason et al. (2010) used SDT to calibrate a morphodynamical model.

The present study aims to evaluate whether SDT and SDB can replace surveyed data as a boundary condition in hydrodynamic modelling — focusing on predicting high water levels

(surges and extreme high tides) in estuaries with complex morphology. The study has three specific objectives:

1. To determine whether satellite imagery can be used to extract accurate SDT;

2. To investigate the main source of errors in the satellite-derived techniques; and,

3. To assess the use of SDT and SDB for hydrodynamic modelling of estuaries as an alternative to data derived from traditional methods.

This manuscript is divided into two main parts, as illustrated by the two grey panels in Figure 5.1: (a) the SDT and SDB framework and (b) the hydrodynamic modelling assessment. The chart flow follows the numbered sections within the text, with the two small left-side panels contributing to Parts (a) and (b). The methods section begins with a description of the study sites and database (blue box in Figure 5.1). Following this, the optical waterline (black box) and ratio-log (light-yellow box) methods for generating SDT (waterline and ratio-log) and SDB (ratio-log) are described. The hydrodynamic modelling description is given in Section 5.2.4 (left side box in Figure 5.1). Following, the two correction methods are explained: the dynamical correction (green box, Figure 5.1) and the statistical correction (red box, Figure 5.1). The main workflow for the modelling assessment of SDT/SDB is illustrated in Part (b) (Figure 5.1) and consists of running simulation scenarios using different combinations of topo-bathymetry datasets and hydrodynamic forcing conditions. Results for Parts a and b are shown in Section 5.3, including the waterline-derived and the ratio-log-derived intertidal elevation, the proposed correction techniques, and the modelling assessment. In Section 5.4, the main findings are discussed: the advantages and limitations of our proposed SDT and SDB framework and correction approaches; and the hydrodynamic modelling assessment. The conclusion is in Section 5.5 (not shown in Figure 5.1).

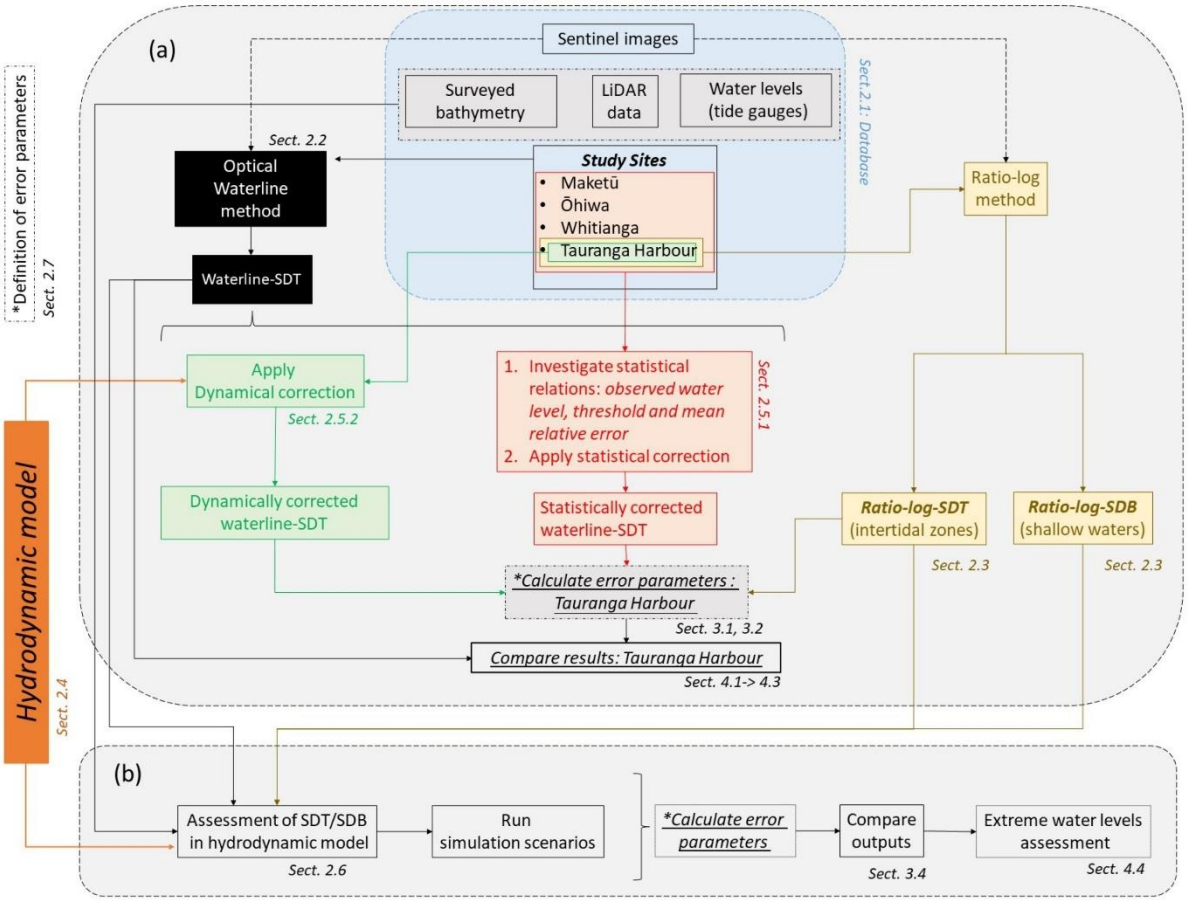

Figure 5.1. A flow chart showing the main structure of the manuscript. Please note that the number of the sections are omitting the number of the current thesis' chapter (5) for simplification. Panel (a) shows the steps taken to derive the SDT/SDB and how the statistical relationships and source of errors were investigated. Panel (b) summarises the framework to test the utility of SDT/SDB in modelling high water levels.

5.2 Methods

5.2.1 Study site and database

The study areas are four estuaries on the east coast of Aotearoa New Zealand's North Island. Three are in the Bay of Plenty region: Tauranga, Ōhiwa and Maketū Harbours and one in the Coromandel: Whitianga Harbour, Figure 5.2 (a). The sites consist of barrier-enclosed sandy estuaries, which are common in Aotearoa New Zealand (Hume et al., 2007, 2016) and all have micro-tidal regimes — the spring tidal range varies between 1.4 m to 1.9 m — and spring tides combined with severe storm surges drive the extreme sea levels (Rueda et al., 2019; Stephens

et al., 2020). In Aotearoa New Zealand, the storm surges usually add ≤ 0.5 m to the water level; however, larger storm surges can occur occasionally (Stephens et al., 2020). The extensive intertidal zones and vegetation (e.g., seagrass and mangrove) that are present in the majority of the estuaries in Aotearoa New Zealand can attenuate tides (Tay et al., 2013) and storm surges (Montgomery et al., 2019). The water level inside the estuaries is not considered to be substantially affected by waves (i.e., wave set-up) because all of them are enclosed coastal lagoons with restricted entrances. All four estuaries have large intertidal areas covering 58% to 84% of the estuaries' total area (Hume et al., 2007, 2016); see Table 5.1. The extent of the tidal flats is evident in Tauranga Harbour by comparing low and high tide satellite images, Figure 5.2 (b) and (c), respectively. Mangrove forests can be observed in all the estuaries, and seagrass banks are visible in Maketū, Ōhiwa and Tauranga Harbours. Detailed images of the intertidal zones in Tauranga Harbour, showing seagrass banks and mangroves, can be seen in Figure S3.

Imagery, tidal levels and topography data (e.g., LiDAR) were acquired to implement and validate the SDT techniques. For the Bay of Plenty region, historical tide levels were downloaded from the Bay of Plenty Council data portal (https://envdata.boprc.govt.nz/); the topography data consisted of the LiDAR survey, with a spatial resolution of 1 x 1 m, available on the Land Information New Zealand (LINZ) data portal (https://data.linz.govt.nz/). For Whitianga, water level time series and elevation data (LiDAR) were acquired through the Thames-Coromandel District Council's website (http://www.tcdc.govt.nz/). The LiDAR data have an accuracy of ± 0.2 m in the vertical and ± 0.6 m in the horizontal with 95% confidence for the Bay of Plenty. All LiDAR data were converted to the local vertical datum (i.e., Moturiki 1953), which is 0.13 m below mean sea level (MSL), using the GEOID elevation grids available in the LINZ data portal.

Satellite images from European Space Agency (ESA) Copernicus Sentinel were accessed through Google Earth Engine (Gorelick et al., 2017) and consisted of spacecraft Sentinel 2A and B, product type level-2A. The Sentinel-2 products are composed of elementary tiles, which are 100 x 100 km^2 ortho-images in the UTM/WGS84 projection, with a revisit frequency of 5 days in the Aotearoa New Zealand region. The level-2A product type provides bottom-of-atmosphere (BOA) images, which are already corrected for the effects of the top-atmosphere, terrain and cirrus cloud using the Sen2Cor processing tool (ESA). Each image has the spectral resolution of 12 bands with spatial resolution differing between 10, 20 and 60 m depending on

the band. The green (band 3, 560 nm), blue (band 2, 490 nm) and near-infrared (band 8, 842 nm) bands were used for this analysis, all of them with 10 m spatial resolution.

In summary, a complete set of LiDAR, tidal gauge observations and a satellite image was obtained for each estuary. For example, the Tauranga Harbour dataset is shown in Figure 5.2, including the location of the tide gauges (Ōmokoroa, Hairini, Ōruamatua, and Moturiki) and the intertidal exposure during low tide (Figure 5.2b) and high tide (Figure 5.2c). In Figure 5.2 (d), the corresponding water level records for the acquisition period of the satellite images are shown. (Moturiki time series is not shown).

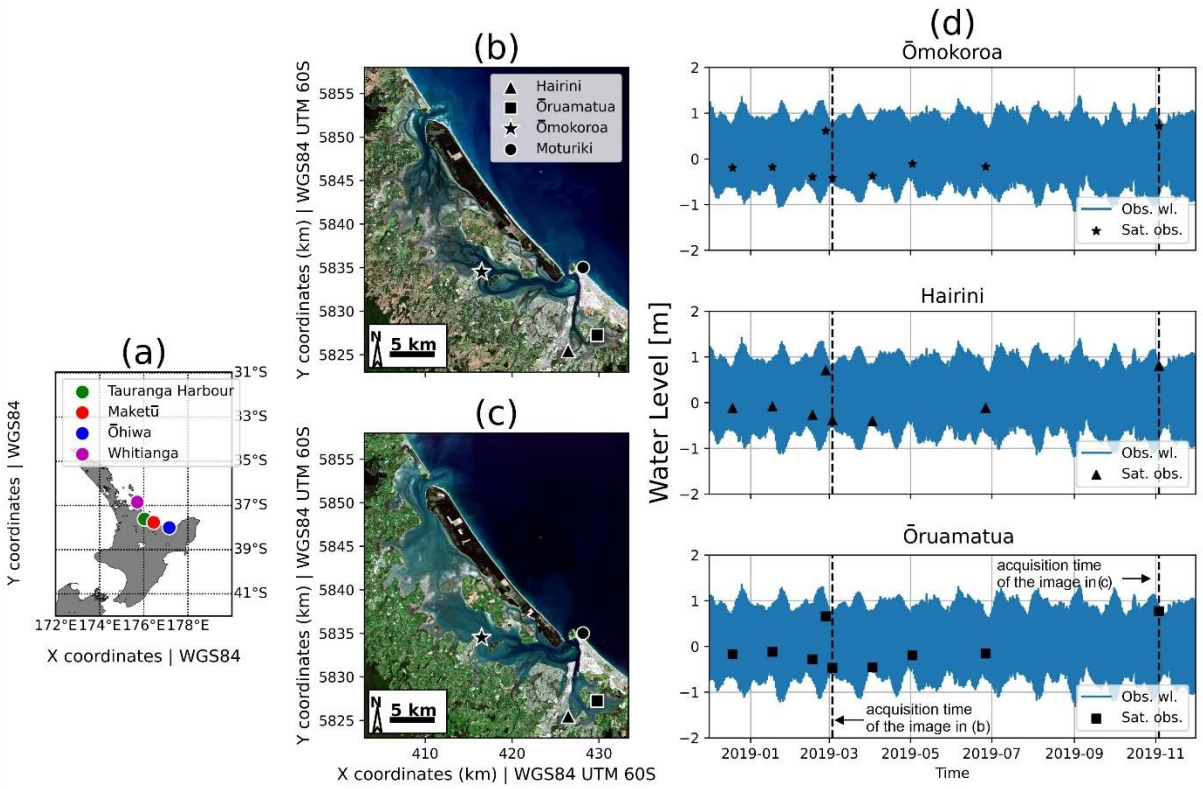

Figure 5.2. The four estuaries where the SDT method was tested (a). Tauranga Harbour and tide gauge locations during low tide (b) and high tide (c) with the background image from ESA Sentinel 2A. Water level time series from the three of local tide gauges shown in panels b and c during the period over which satellite images were acquired (d). The water levels associated with images shown in panels b and c are marked with a vertical dashed black line in (d) (Vertical Datum: MSL).

5.2.2 Satellite-derived topography: the waterline method.

The framework to generate the SDT in intertidal zones using the waterline method (hereafter called waterline-SDT) was composed of three stages, as illustrated in Figure 5.3: Stage 1 was

to query an image collection; Stage 2 was to identify the intertidal zone; and Stage 3 was to determine the waterline position and height. First, an image collection was acquired for each estuary through the Google Earth Engine application (Gorelick et al., 2017) using the Google Colaboratory environment. Each image collection has images from the satellite Sentinel 2A and B, product type level-2A, covering the estuary domain, in which fewer than 5% of the pixels are covered by clouds. A small number of images with low cloud coverage were included because of the restricted number of available images; however, any irregularities from the small areas of clouds and their shadows were removed manually in post-processing quality control. The number of images corresponding to the collection and environmental properties for each estuary (e.g., coverage of intertidal zone in the estuary; spring tidal range) is shown in Table 5.1.

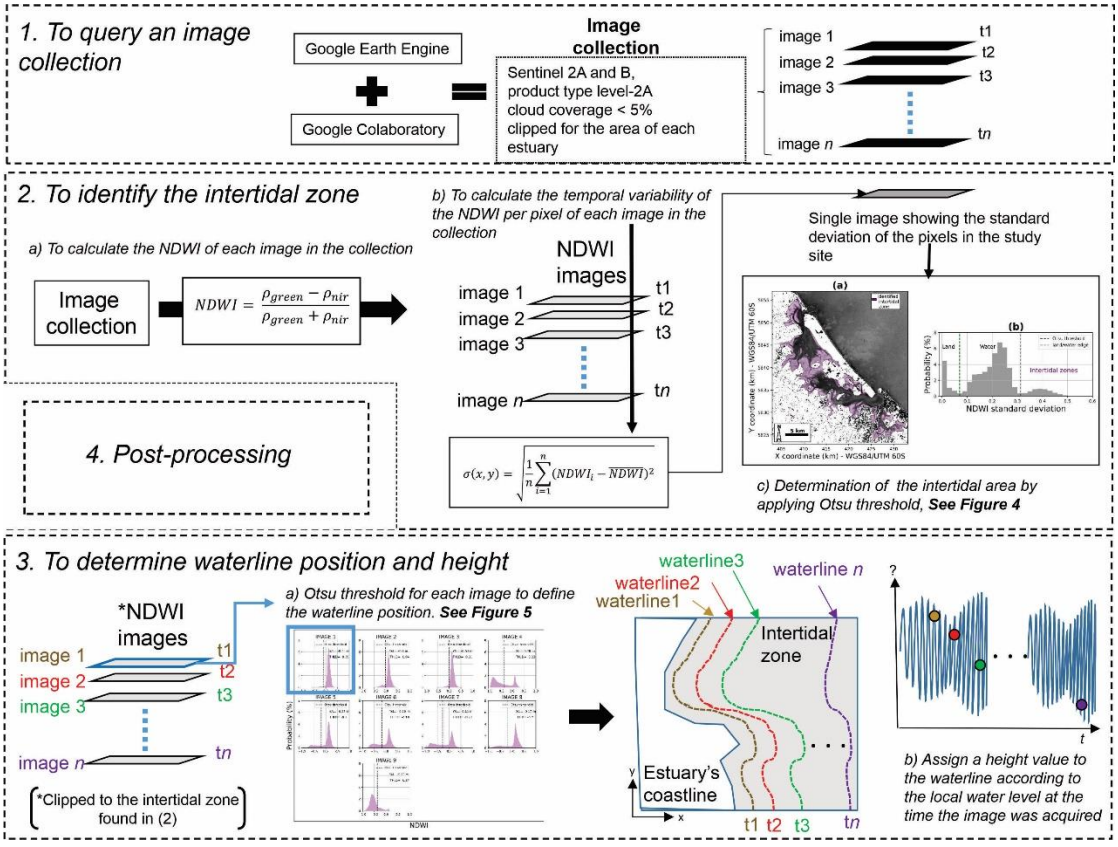

Figure 5.3. The framework for the application of the waterline method to derive topographic data in intertidal zones. First (1) an image collection was acquired. Second (2), the intertidal zone was identified by calculating the temporal of NDWI. Note that NDWI is the index used to detect the existence of water from satellite reflectance (see text). Third (3), the waterline position and height were determined. This was done by identifying the boundary between wet and dry cells within the intertidal zone (i.e., waterline) and assigning a height value for the waterline obtained from the local tide gauge observation at the time of the image acquisition.

Table 5.1. Number of images in the collection and for estuary's characteristics.

Estuary	Nº of images in the collection	Total intertidal area (Hume et al., 2016)	Surface area (Hume et al., 2016)	Spring tidal range
Tauranga Harbour	9	77%	~200 km^2	1.75 m
Ōhiwa	6	84%	~27 km^2	1.9 m
Maketū	12	58%	~ 2.6 km^2	1.4 m
Whitianga	8	72%	~ 15.5 km^2	1.7 m

In the second stage (Figure 5.3), the intertidal zone was identified. The aim was to eliminate pixels that are not in the intertidal area — thus avoiding needless image processing. For that, the approach based on Bué et al. (2020) was used, in which the intertidal extent was determined by calculating the temporal variability of the Normalized Difference Water Index (NDWI) (McFeeters, 1996) at each pixel over the entire image collection, using Equation 5.1 and 5.2:

$$\sigma(x,y) = \sqrt{\frac{1}{n}\sum_{i=1}^{n}(NDWI_i - \overline{NDWI})^2}; \quad (5.1)$$

where

$$NDWI = \frac{\rho_{green} - \rho_{nir}}{\rho_{green} + \rho_{nir}}; \quad (5.2)$$

and where x and y are the pixel coordinates, and n is the number of images in the collection. NDWI is determined as a normalised difference between ρgreen and ρnir, which are the reflectance of the green and near-infrared bands of Sentinel-2 images, respectively. As a result, one single greyscale image was generated representing the NDWI temporal standard deviation (σ), Figure 5.4 (a) because of the consistent change between exposed (low tide) and inundated (high tide) conditions, the highest standard deviation values were assumed to occur in the intertidal zones. Thus, the pixels representing the intertidal zone were the ones with an σ greater than the threshold value. For instance, Figure 5.4 (b) shows that for Tauranga Harbour, the

threshold is > 0.32. The threshold was set using the Otsu (1979) approach, where its value depends on the probability distribution of σ, as illustrated in Figure 5.4 (b). The Otsu method identifies the optimum threshold between two data classes in the image distribution that maximises the value of the within-class variance. The advantage of using an adaptive threshold is that it can be objectively tailored to each image collection and estuary.

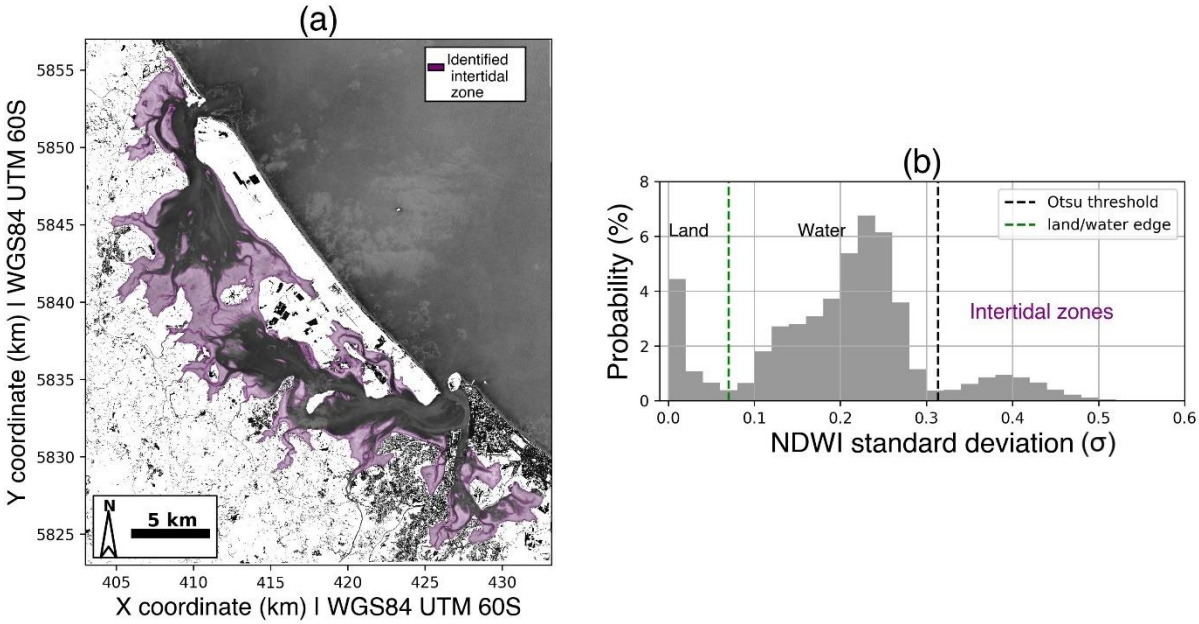

Figure 5.4. (a) Intertidal areas identified using the temporal variability of NDWI (σ) of the Tauranga Harbour image collection. Determination of the Otsu threshold for the identification of the intertidal zone (b).

In the third stage (Figure 5.3), for each image in the collection, the corresponding NDWI maps were clipped into the intertidal zone (which was defined using the whole image collection in stage two). From the intertidal NDWI maps, the waterline position in that image was extracted by applying the algorithm "Finding_Contours" from the scikit.measure (Van Der Walt et al., 2014) Python library. This contour extraction method searches for a given value (i.e., threshold) in a two-dimensional array of pixels, using the 'marching squares' algorithm (Lorensen and Cline, 1987) to identify contour boundaries precisely by linearly interpolating between adjacent pixel values; therefore, the method is able to define waterline with a subpixel resolution. The Otsu method was used to determine the threshold that should be applied to each image. Figure 5.5 illustrates the different thresholds applied to each image in the Tauranga collection according to the corresponding distribution of NDWI. Once the waterline position was identified for a given image, a height value was assigned to the waterline by finding the

corresponding observed tide level at the local tide gauge (Ōmokoroa for the Tauranga Harbour case study, Figure 5.2d). After all images in the collection were processed, a collection of waterlines with different height values was created (see Figure 5.3, Stage 3b), which was gridded to create an SDT (i.e., waterline-SDT). The accuracy of the waterline-SDT was assessed against the LiDAR data by comparing the LIDAR at each point along the waterline and by comparing the corresponding digital elevation model (DEM). The module DELFT-QUICKIN was used to create DEMs for each estuary. The triangular interpolation method was applied in a grid with a spatial resolution of 10 m.

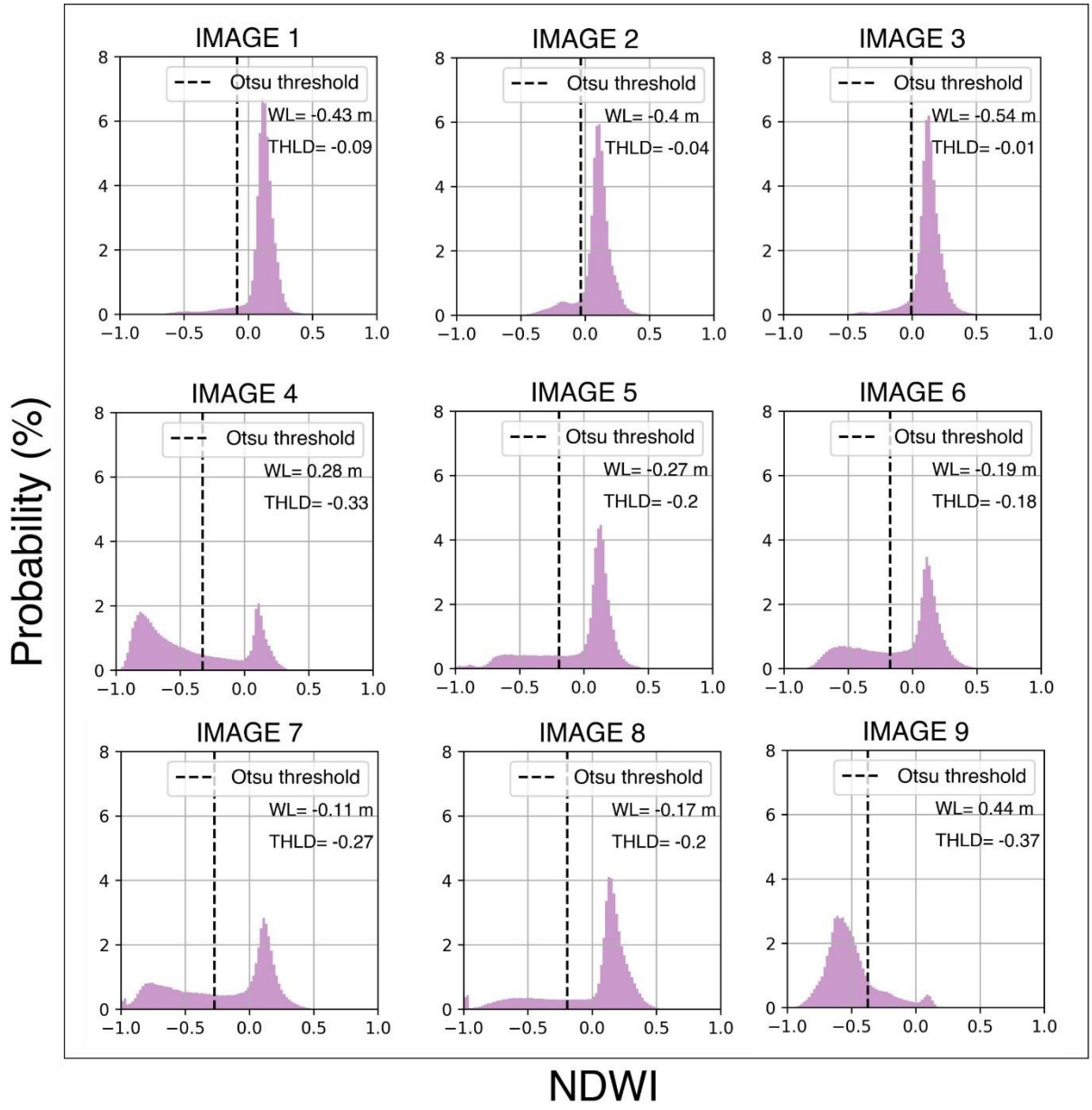

Figure 5.5. Otsu threshold (THLD) applied to identify the waterline position for each image in the Tauranga Harbour collection. The observed water level from the Ōmokoroa tide gauge at the moment of the image acquisition (i.e., waterline height relative to mean sea level) is also shown in each panel (marked WL).

5.2.3 Satellite-derived bathymetry: the ratio-log method.

Additionally, the ratio-log method (Stumpf et al., 2003) was applied in Tauranga Harbour separately for intertidal zones (ratio-log-SDT) and shallow water (ratio-log-SDB). The ratio-log and waterline methods were assessed in two different ways: first, to compare their approximation of topographic data in intertidal zones (Figure 5.1a) and second, to compare their use in hydrodynamic models (Figure 5.1b). The ratio-log method is not limited by the number of satellite images available covering the estuarine area and can be applied to extract

the SDT from a single image. In its original application, the ratio-log empirical approach was used to derive shallow water bathymetry (SDB). However, because of the relatively low turbidity of intertidal water in Tauranga Harbour, the method may also be suitable for deriving topography (SDT) within intertidal zones. To compare, the ratio-log method was applied to an image acquired at high tide, where the intertidal zone was completely flooded. The numerical assessment was built on a pilot study by Costa et al. (2021), where the method was trialled in a small region within the Tauranga Harbour. Detailed information about the application of the ratio-log method and the results for tidal flats and shallow water are provided in Appendix B, Figure B.1 and Figure B.2. Because the ratio-log method is based on an empirical fit, additional bathymetric data were needed to implement the ratio-log method for shallow water. For this, multiple-source bathymetric data were used, which is detailed in Section 5.2.4.

5.2.4 Hydrodynamic modelling: the baseline model

A baseline hydrodynamic model was set up for Tauranga Harbour. The modelling study was only undertaken in this estuary (rather than all four sites) because a calibrated and validated DELFT3D-FLOW model was already available (Stewart, 2021). The baseline model was first used to account for the tidal propagation within the estuary as a way of improving the waterline SDT (Section 5.2.5.2) and, second, was used as a base-case against which to assess the use of SDT and SDB as the bathymetry/topography for modelling extreme water levels in estuaries (Section 5.2.6). The grid domain and interpolated bathymetry are shown in Figure C.1 (Appendix C), and they cover the central to the southern part of the Harbour with a 20 × 20 m resolution grid. The north and south boundaries were set as open boundaries (free Neuman), and the model was forced with water level along the seaward boundary with the astronomical components of the tide. For the latter, harmonic astronomical tidal analysis was undertaken on the Moturiki Island tide gauge using U_tide (Codiga, 2011). The topographic and bathymetric data used in the baseline hydrodynamic model were assembled using a combination of data from multiple sources: Multibeam survey (Port of Tauranga, 2017), LiDAR (2008 from AAM HATCH and 2016 from LINZ) and LINZ hydrological charts NZ 5411, 2016. These data were all converted to mean sea level (MSL) vertical reference.

The model was validated to ensure the bed roughness parameters were appropriate by simulating an equinoctial tidal period from 01/03/2019 to 31/03/2019. The details of the model setup, calibration and validation are presented in Appendix C. The vertical datum in the

simulation was the MSL, and the time step was 0.5 min; the advection scheme for calculating the flooded and dried cells is cyclic, using the water level averaged on the grid cells. The model was calibrated against three tide gauge observation points (Ōmokoroa, Hairini and Ōruamatua).

5.2.5 The SDT correction approaches

5.2.5.1 Correcting SDT using the bias between LiDAR data and SDT: the statistical correction

The first method to correct the waterline-SDT trialled was to remove the statistical bias—potentially caused by conditions that can interfere with the pixel reflectance and, as a consequence, the waterline position at different tide levels within the tidal flats. Conditions that can interfere with detection include complex intertidal zone morphology, water turbidity, variation of the benthic substrates (sand, seagrass), and groundwater seepage. Specifically, groundwater seepage leaves a film of moisture on the exposed intertidal detectable in images (Huisman et al., 2011). Because the studied estuaries have similar characteristics — i.e., morphology complexity (extensive intertidal zones and channelisation), tidal range, white sand, and presence of seagrass — a statistical correction was developed for all four estuaries on the basis that the detected waterline is consistently further seaward or landward than the actual waterline across all sites. For the statistical correction, a linear equation was fitted to the relationship between the value of the Otsu threshold — used to position the waterline within the intertidal zone (see Section 5.2.2) — and the bias between the waterline-SDT and the LiDAR data in all the estuaries (i.e., Tauranga, Maketū, Ōhiwa, and Whitianga Harbours).

5.2.5.2 Correcting SDT using the hydrodynamic model: the dynamical correction

The second method to correct the waterline SDT was using the hydrodynamic model (Section 5.2.4); this correction approach is hereafter called the dynamical correction. The water level is not homogeneous throughout a large estuary at one instant in time because of the time it takes for the tide to propagate around the estuary and the potential tidal wave deformations induced by the estuarine morphology, such as shoaling, reflection and dampening. Thus, for every image processed by the waterline method, the detected waterline height might vary spatially, and assigning a waterline height using information from one tide gauge (as in Section 5.2.2) may not be appropriate. The dynamical correction uses the hydrodynamic model to assign a spatially-varying height to each waterline.

The dynamical correction was implemented as follows. First, the model bathymetry was replaced in the intertidal zones with the waterline-SDT (with the original bathymetry retained in the shallow water areas), and a new depth file was created. Using this new depth file, nine independent simulation cases were performed corresponding to the acquisition times of the nine images in the Tauranga Harbour image collection. Each case had a simulation period starting ten days prior to the date and time that the satellite image was acquired to allow for model spin-up. The spatially-varying water level model output was extracted along each of the corresponding waterlines (one waterline is detected in each image, Section 5.2.2). The waterline height was assigned by interpolating the position of each waterline onto the gridded model output.

5.2.6 Assessing extreme water level simulations with SDB and SDT

To properly assess the use of satellite-derived topo-bathymetric data in hydrodynamic modelling, scenarios were designed with different combinations of SDB, SDT, and hydrodynamic forcing conditions. Table 5.2 shows the specifications of the eight simulation scenarios: the source of elevation data, the physical forcing, and the simulation period. Note that the "surveyed topo-bathymetry" data refers to the multiple-source data described in Section 5.2.4.

The four first scenarios (i.e., S1–S4) test different combinations of topo-bathymetric data to be used in hydrodynamic modelling. Here, the model was forced with the astronomical constituents extracted from the Moturiki tide gauge record, as described in Section 5.2.4, varying only the topo-bathymetric data. For instance, our baseline model (S1) represents the condition when the modeller depends only on the in situ measured elevation. In the S2 and S3 scenarios, the intertidal zone bathymetry was replaced with the SDT generated by using the waterline (waterline-SDT) and the ratio-log (ratio-log-SDT) methods, respectively. The S4 scenario was developed to assess the use of only SDB and SDT in the entire model domain (so only satellite-derived data). Thus, the waterline-SDT was used for the tidal flat and the ratio-log-SDB for the shallow areas within the harbour.

The simulation scenarios S5–S8 were designed to investigate the potential of SDT and SDB as a replacement for the surveyed topo-bathymetry in modelling more extreme water level events, where the interactions between storm surge and astronomical tides are important. For that, two extreme events were selected based on the water level observations at the Moturiki tide gauge

in the period ranging from the years 2002 to 2018, see Figure E.2. Trends of sea-level rise were first filtered from the water level observations by applying a 1-year-running average, which resulted in a filtered time series hereafter called total water level. Both extreme events represented the highest water levels for the period and consisted of peaks of a total water level of ~1.4 m. However, the contribution of the storm surge is different for each event. The definition of storm surge used here is the difference between astronomical tide and the detrended water level for a given time series. The first event occurred on 16/04/2003 and consisted of a storm surge = 0.55 m, which represents ~ 40% of the observed total water level. The second event occurred on 05/01/2018 and consisted of a storm surge = 0.32 m, which represents ~ 22% of the observed total water level. Ultimately, these two events were modelled using only surveyed topo-bathymetry (S5 and S7) and only satellite-derived data (S6 and S8).

To assess the simulations, the tide levels extracted from each scenario were compared to the astronomic tide at three points for S1–S4 (Ōmokoroa, Hairini, and Ōruamatua), the total water level at two points for S5–S8 (Hairini, and Ōruamatua), and the tide and total water level output maps from each simulated scenario. Note that the Ōmokoroa tide gauge was not used to assess S5–S8 because its records do not cover the period of the first storm event.

Table 5.2. Simulation scenarios to assess the use of SDT and SDB in hydrodynamic modelling.

Scenarios	Source intertidal zone	Source shallow waters	Forcing	Contribution of storm surge at the peak of water level	Simulation start time	Simulation end time
S1	surveyed topo-bathymetry	surveyed topo-bathymetry	Astronomical constituents	-	01/03/2019	31/03/2019
S2	waterline-SDT	surveyed topo-bathymetry	"	-	"	"
S3	ratio-log-SDT	surveyed topo-bathymetry	"	-	"	"
S4	waterline-SDT	Ratio-log-SDB	"	-	"	"
S5	surveyed topo-bathymetry	surveyed topo-bathymetry	Total water level	22%	02/01/2018	10/01/2018
S6	waterline-SDT	Ratio-log-SDB	"	"	"	"
S7	surveyed topo-bathymetry	surveyed topo-bathymetry	Total water level	40%	10/04/2003	19/04/2003
S8	waterline-SDT	Ratio-log-SDB	"	"	"	"

5.2.7 Assessment of framework performance

The accuracy of the SDB, SDT, the hydrodynamic model, and the dynamical and statistical corrections was assessed by calculating the following error metrics: root mean square error (RMSE), maximum absolute error (MAXE), relative error (RE), coefficient correlation (R2), and bias (BIAS) (Equations 5.3–5.7 respectively). In the corresponding equations, h_{est} is the estimated value (e.g., SDT, SDB, hydrodynamic model output), and h_{obs} is the observed value (e.g., LiDAR data, tide gauge measurements).

In the case of SDB and SDT evaluation, the RE can be either negative or positive. For the results derived from the ratio-log method (SDT and SDB), the RE reflects only the vertical difference between the estimate and the in-situ data (i.e., LiDAR data for SDT and surveyed bathymetry for SDB). For the waterline-SDT, the RE reflects both vertical and horizontal accuracies. For instance, Figure 5.6 shows a schematic topo-bathymetric profile illustrating the error calculation for the waterline-SDT. Although the error is evaluated as a height difference, it can originate from either horizontal (δx) or vertical (δz) inaccuracies. Thus, negative (positive) RE means that the estimate is shallower (deeper) or located further landward (seaward) than the LiDAR data.

$$RMSE = \sqrt{\sum_{i=1}^{n} \frac{(h_{est} - h_{obs})^2}{n}}; \qquad (5.3)$$

$$MAXE = \max_{i=1\ldots n} |h_{est}\mathrm{i} - h_{obs}\mathrm{i}|; \qquad (5.4)$$

$$RE = h_{obs} - h_{est}; \qquad (5.5)$$

$$R^2 = \frac{\sum_{i=1}^{n} (h_{est}i - \overline{h_{obs}})^2}{\sum_{i=1}^{n} (h_{obs_i} - h_{est_i})^2 + (h_{est_i} - \overline{h_{obs}})^2}; \qquad (5.6)$$

$$\mathrm{BIAS} = \overline{h_{obs}} - \overline{h_{est}}; \qquad (5.7)$$

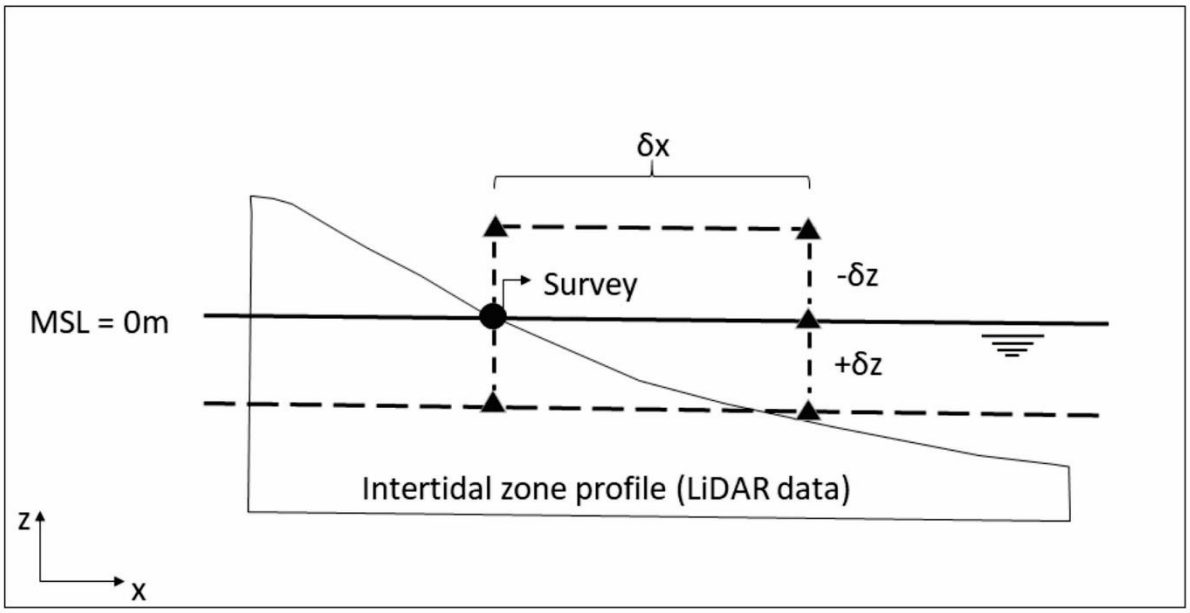

Figure 5.6. Schematic showing the error calculation. The circle shows the actual location of the water line, and triangles show the location of the remotely sensed shoreline. There are two ways that an error can be caused. The waterline can be detected landward or seaward of its actual location (δx), or the waterline is assigned an elevation that is too high or too low (δz).

5.3 Results

5.3.1 The waterline satellite-derived topography (waterline-SDT)

The waterline-SDT accuracy, compared to the LiDAR data, for all the studied estuaries is shown in Table 5.3; the average RMSE across all estuaries was 0.33 m, and the average MAXE was 1.74 m. The technique's worst performance was in the Maketū Estuary (RMSE =0.41 m and MAXE= 2.38 m), Figure D.1. Ōhiwa and Whitianga Estuary have similar performance, Figures S5 and S7. Tauranga Harbour was associated with the best estimates with RMSE = 0.20 m. Note that the error parameters calculated for the corresponding DEMs are lower, especially in terms of MAXE. The detail of the images that were acquired and the corresponding water level for each estuary is shown in Appendix D.

Table 5.3. Waterline-SDT errors for every studied estuary. DEM is the digital elevation model obtained by interpolating the corresponding waterline-SDT in the intertidal zone with a spatial resolution of 20m and triangulation method. The elevation range in the LiDAR data within the intertidal zone is also shown. Vertical Datum: MSL.

	SDT		DEM		LiDAR
Estuary	**RMSE (m)**	**MAXE (m)**	**RMSE (m)**	**MAXE (m)**	**elevation range (m)**
Maketū	0.41	2.38	0.47	2.19	-0.63 | +1.90
Ōhiwa	0.35	2.00	0.34	1.61	-0.98 | +2.98
Tauranga Harbour	0.20	1.60	0.23	1.14	-1.11 | +1.44
Whitianga	0.35	1.00	0.28	1.17	-1.12 | +1.92
Average	0.33	1.74	0.33	1.53	

Although the SDT accuracy differed depending on the estuary, the BIAS increased at high and low tide for all estuaries, and the lowest errors occurred at mid-tide. Figure 5.7 shows the linear correlation found between the bias (BIAS), the waterline height (Z), and the Otsu adaptive threshold (THLD), which also demonstrates the aforementioned dependence on the tide level. For instance, the THLD and the BIAS have a goodness of fit of $R^2 = 0.58$ (Figure 5.7b); the THLD and the Z have a goodness of fit of $R^2 = 0.83$ (Figure 5.7a), and BIAS and Z have a goodness of fit of $R^2 = 0.68$ (Figure 5.7c). However, whether a waterline is extracted on the flooding or the ebbing tide cycles does not affect the waterline-SDT accuracy. Equation 5.8 (also shown in Figure 5.7c) was used as the basis of the statistical correction (where the statistical bias was removed from the waterline-SDT for Tauranga Harbour (Section 5.2.5.1)).

$$\mathrm{BIAS} = -0.49 * \mathrm{Z} - 0.088 \qquad (5.8)$$

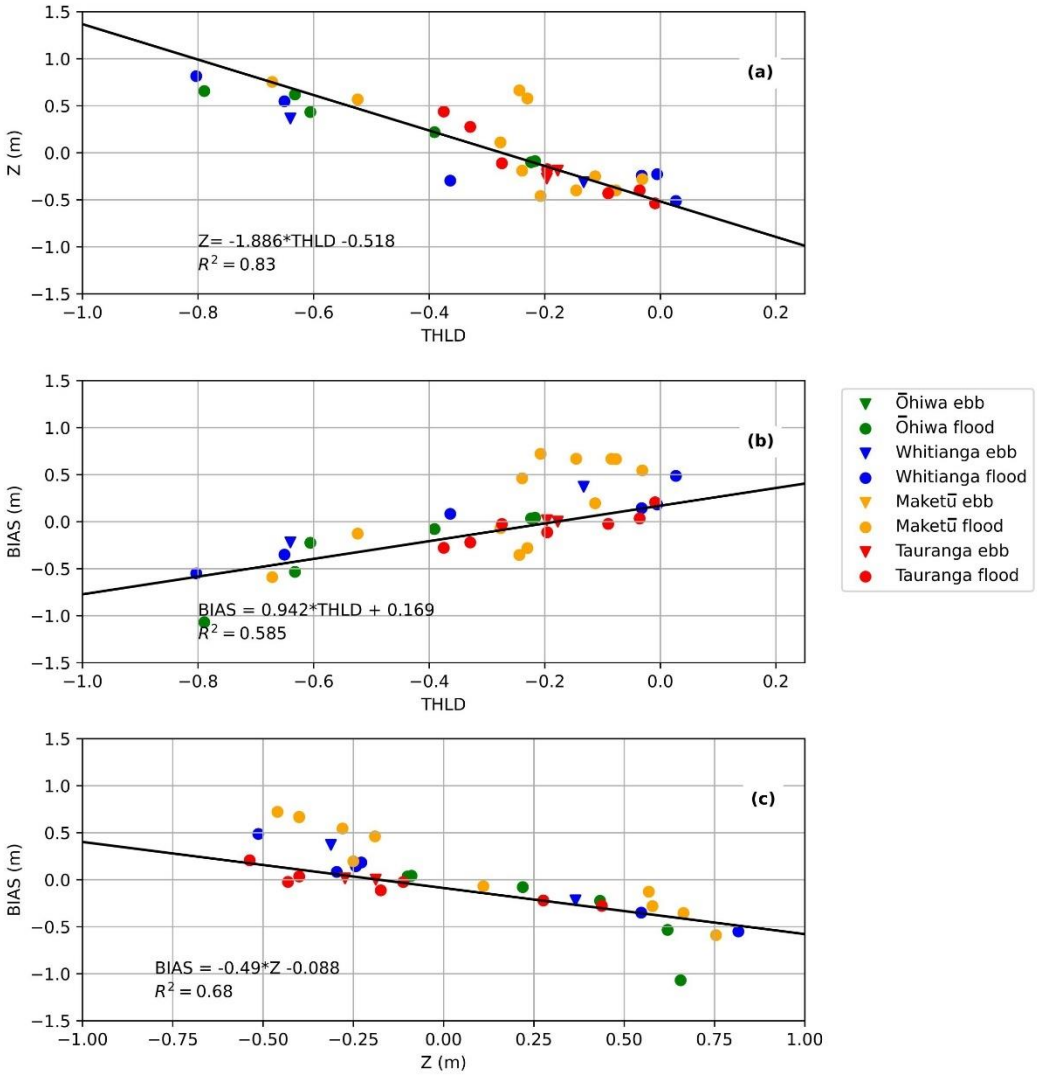

Figure 5.7. Statistical relationships at all estuaries (Ōhiwa, Whitianga, Tauranga, Maketū): (a) water level Otsu threshold (THLD) and observed water level (Z); (b) THLD and the SDB mean error (bias); (c) Z and the SDB mean relative error (bias). The relationship shown in (c) was used in the statistical correction (see Section 5.3.2).

5.3.2 The statistical and dynamical corrections

The waterline-SDT (Section 5.2.2), the statistically (Section 5.2.5.1 and 5.3.1), and the dynamically (Section 5.2.5.2) corrected waterline-SDT showed an overall RMSE equal to 0.20, 0.18 and 0.19 m, respectively (Figure 5.8). The statistical correction was effective where the SDT was strongly biased (e.g., Figure 5.8, images 4 and 9). However, for the cases where the uncorrected SDT showed good results (Figure 5.8, images 1–3), the statistical correction causes bathymetry estimates to be less accurate by increasing the corresponding bias. The dynamical correction was more effective when the waterline was extracted from images collected at mid

to high tides Figure 5.8; images 4–9) compared to at low tides (Figure 5.8; images 1–3), improving the RMSE values by 0.05 m on average. However, the estimates during low tides are less accurate (a reduction of 0.10 m on average)

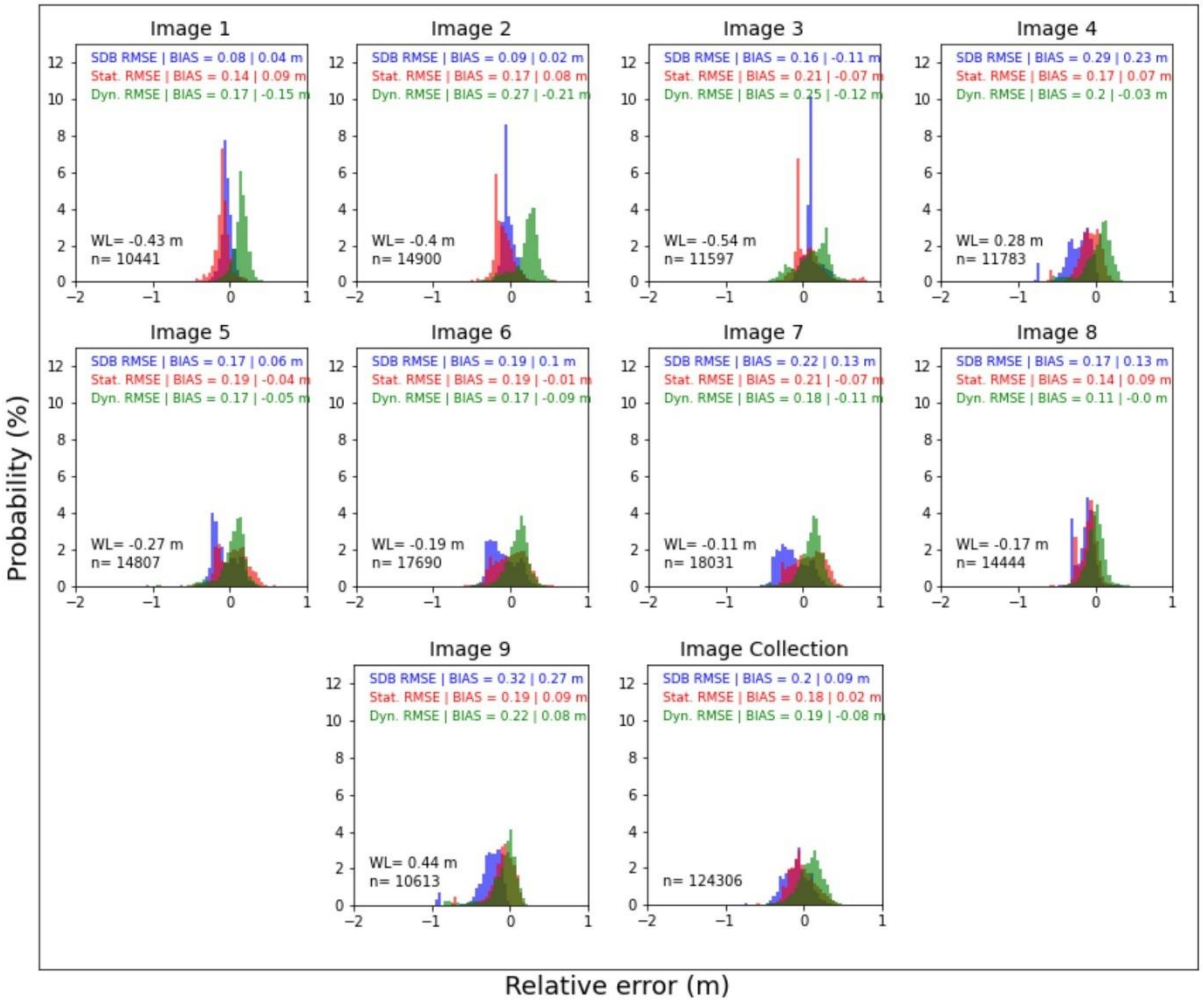

Figure 5.8. Histograms of the waterline-derived SDT relative error (RE) for each image in the collection for Tauranga Harbour: waterline-SDT (blue), statistically corrected waterline-SDT (red) and dynamically corrected waterline-SDT (green). RMSE, BIAS, waterline height (WL), and number of waterline samples (n) are shown.

5.3.3 Prediction of extreme water level using the SDB

The simulation scenarios showed that the combined use of SDB and SDT can be used to obtain water level predictions of similar accuracy to those predicted using only surveyed bathymetry (although the log-ratio method requires some in situ calibration data). To simplify the interpretation of the results, Figure 5.9 illustrates the average error parameters calculated when comparing the model output with the record of the three tide gauges. A detailed assessment of

each of the gauges is provided in Appendix E. In S4, the waterline-SDT for intertidal zones combined with the ratio-log-SDB for shallow waters can predict the astronomical tide more accurately (RMSE ~ 0.07 m). In the S1 results, the model uses surveyed bathymetry (S1) with poorer performance (RMSE ~ 0.09 m). S4 also performs better than S1 when assessed with the maximum absolute error (MAXE), ~ 0.25 m and ~ 0.31 m, respectively. In addition, Figure E.1 (Appendix E) shows that at the location of the Ōruamatua tide gauge, the predictions were improved in the S4 scenario (RMSE = 0.05 m) compared to S1 (RMSE = 0.13 m). Regarding the scenarios where SDTs replace only the intertidal topography (S2 and S3), the waterline-SDT (S2) provided superior performance (RMSE ~ 0.07 m). The model that uses ratio-log-SDT (S3) showed poorer performance (RMSE ~ 0.09 m).

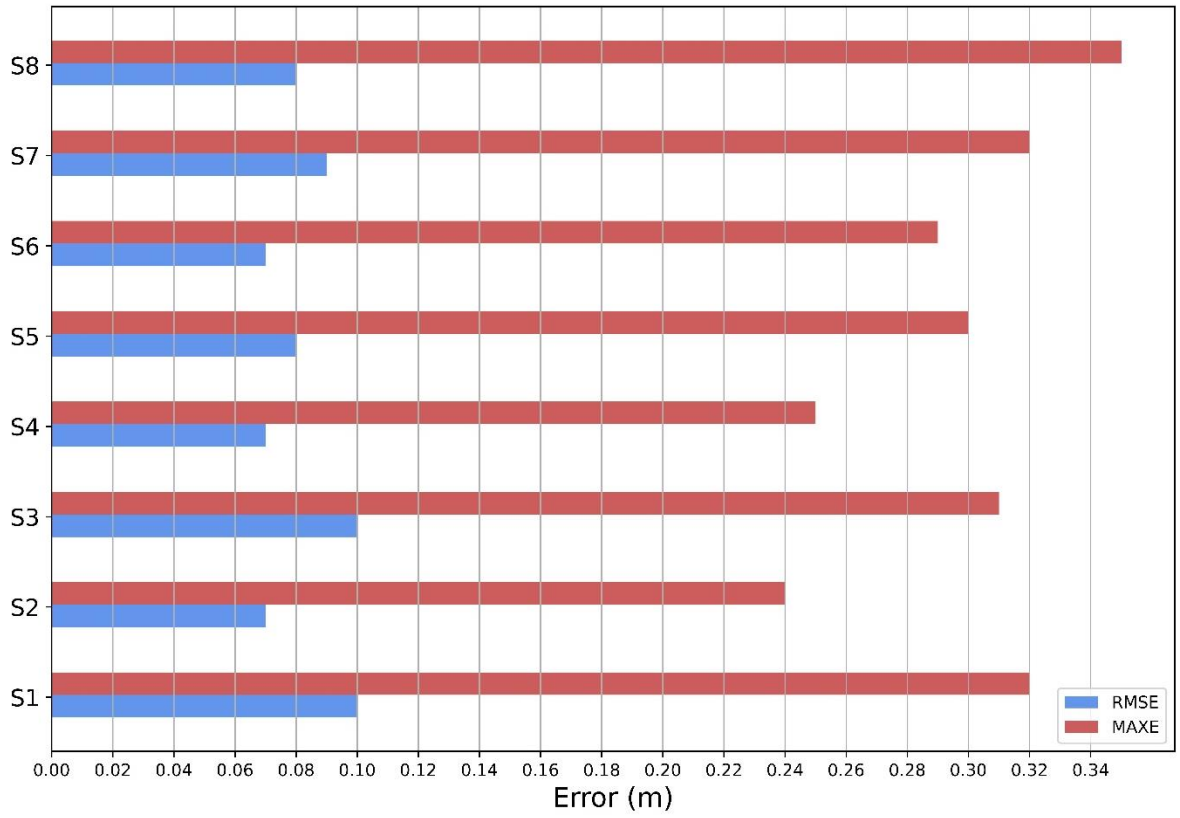

Figure 5.9. The average parameter errors calculated considering the results at the three tide gauge locations (Ōmokoroa, Hairini, Ōruamatua) for each simulation scenario (S1, S2, S3, and S4) — RMSE (blue bar), MAXE (red bar).

Similar accuracies were shown in the simulation tests using two distinct extreme events (scenarios S5–S8); see Figure E.3. The averaged error parameters for the scenarios using satellite-derived data (i.e., S6 and S8) are close to the ones for scenarios using only surveyed

topo-bathymetry (i.e., S5 and S7), as shown in Figure 5.9. The RMSE of these scenarios range from 0.07 m to 0.09 m, and the MAXE from 0.29 m to 0.35 m. At the time of the most extreme total water level, the scenarios using surveyed topo-bathymetry and satellite-derived data showed agreement on their accuracy, with some differences depending on which extreme event and the location analysed (i.e., Hairini and Ōruamatua). For the first event, scenarios S5 and S6 underestimated the total water level at Harini by -0.05 m and -0.07 m and at Ōrumatua by -0.33 m and -0.23 m, respectively (Figure E.3). For the second event, the scenarios S7 and S8 overestimated the total water level by 0.27 m and 0.21 m at Hairini, and by 0.07 m and 0.12 m at Ōruamatua, respectively. Note that the assessment here is not aimed at assessing whether the model accurately predicted the total water level but rather whether the satellite-derived topo-bathymetry prediction accuracy is similar to that of the surveyed topo-bathymetry.

The good agreement between scenarios using surveyed topo-bathymetry and satellite-derived data is also shown over the entire model domain. For example, Figure 5.10 shows the difference at the maximum (a) and minimum (b) astronomical tide/ total water level at each grid cell over the entire simulation between the scenarios S1 x S4 (I), S5 x S6 (II), and S7 x S8 (III). The differences are > -0.10 m and < +0.10 m at the maximum astronomical tide/ total water level (a). Figure 5.10 (a. II and III) shows that these differences intensify across the estuary when storm surge is considered in the model forcing. The north-western (i.e., above Ōmokoroa) and the south-eastern (i.e., Hairini and Ōruamatua) estuarine regions are the most affected, showing slightly stronger red colours for S5 x S6 (a.II) and S7 x S8 (a.III) than in S1 x S4 (a.I) comparisons. Major differences (≤ -0.10 m and ≥+0.10 m) in the astronomical tide/ total water level predictions occur in the estuary's inner channels at the minimum (low tide) total water level at each grid cell (b).

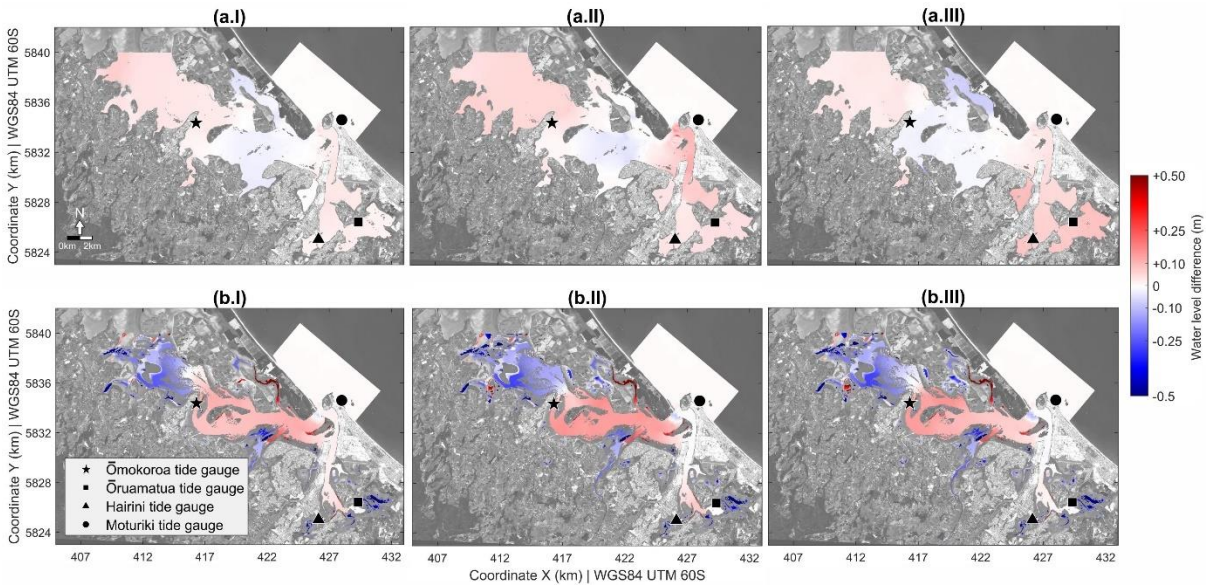

Figure 5.10. Spatial difference between the hydrodynamic model output using surveyed topo-bathymetry (S1, S5, S7) and the waterline-derived plus ratio-log derived SDB (S4, S6, S8). The differences in the maximum (a) and minimum (b) astronomical tide/ total water level per grid cell over the simulation period are compared for S1 x S4 (I), S5 x S6 (II) and S7 x S8 (III). Red (blue) colours represent positive (negative) differences, which means that the resulting water level from scenarios using only topo-bathymetric surveyed data (i.e., S1, S5, S7) is higher (lower) than the resulting water levels from the scenarios using only satellite-derived topo-bathymetric data. Background image: ESA Sentinel 2A. Date and time of the image acquisition: 18/12/2018 10:15 h (UTC+12h).

5.4 Discussion

5.4.1 The proposed waterline method for deriving topography from space-borne images and its limitations.

Topography estimated using the waterline method compares well to LiDAR data in our study sites — considering that the topography in the intertidal zone ranges between -1.12 m to +2.98 m relative to MSL (see Table 5.3) and the vertical and horizontal accuracy of the LiDAR data are 0.20 m and 0.60 m, respectively. Although it is hard to directly compare studies conducted in different coastal areas, our results show a similar bias to other studies performed in similar estuarine environments. For example, Salameh et al. (2020) applied the waterline method to Arcachon Bay in France, with the estimated DEM accuracy of RMSE = 0.27 m; Bué et al.

(2020) generated SDTs for Azinheira Estuary (Portugal) based on logistic regression with an RMSE = 0.6 m.

Despite the encouraging results of waterline-SDT in Aotearoa New Zealand's estuaries, the method is sensitive to the correct positioning and height-assigning of the waterline. Environmental conditions such as the complex morphology, varied bed substrates, and groundwater seepage could reduce the accuracy of the waterline position. Also, the location of the tide gauge used to assign the waterline height is important. For instance, Maketū Estuary is a small estuary with complex morphology, and the tide gauge of Moturiki is located approximately 27 km from the estuarine entrance, which likely explains the low accuracy of SDT for that location. Furthermore, using just one tide gauge to assign the waterline height can add vertical error to the estimates because it does not account for the tide deformation and propagation in such a complex environment. Maketū is currently undergoing staged engineering works to remove former flood protection, which could have caused changes to the bathymetry between images and after the LiDAR survey was undertaken.

Complex morphology affects the estimates differently over different parts of the topographic profile — waterlines closer to the MSL (water level ~0 m) are more accurate, and waterlines closer to the peak of the high and low tides are less accurate (see Section 5.3.2). Our results corroborate those of Liu et al. (2013), who quantitatively analysed the waterline method in Dongsha Sandbank, China (an exposed coastal area). In their study, the authors have found that the main error source in the waterline method is linearly correlated to the slope and area of the intertidal zone. These can be directly linked to the tidal range (micro, meso and macro regimes). Assuming the same intertidal slope, the area of the tidal flats would increase with the tidal range, which would, in turn, require more images to adequately represent the topographic profile. Furthermore, having enough images to characterise the morphology of the study site is a commonly limiting factor in the waterline method, as highlighted by previous studies (e.g., Liu et al., 2013; Salameh et al., 2019). Our results are also clearly affected by the number of images in our collection. For example, gaps where no topographic data could be derived, can be seen between waterlines, shown in Figure 7 (Section 5.3.2). Although the Sentinel-2 images are acquired every five days, they are often not useable due to cloud coverage.

The bed substrate can directly affect the waterline positioning, especially in Aotearoa New Zealand's estuaries, where clear water is common. For example, in Tauranga Harbour, the

seagrass banks (Ha et al., 2020) and the groundwater seepage (shown to cause an error in water line detection in Huisman et al., 2011) can abruptly change the reflectance of the pixels around the waterline, especially in the centre part of the estuary, where the seagrass banks occur (Figure S3). The adaptive Otsu method (Nobuyuki Otsu, 1979) was used to detect the edges between water and intertidal zones. The method showed good performance in determining the waterline location in estuaries, corroborating studies on lakes, rivers, water reservoirs (Donchyts et al., 2016), and coastlines (Vos et al., 2019). Other edge detection techniques were also tested in the present study, such as by calculating the mean or the median of NDWI distribution following approaches in previous studies (Sagar et al., 2017; Bishop-Taylor et al., 2019). However, these did not perform as well (not shown). The Otsu method defines a threshold by detecting the value that maximises the within-class variance between two classes of a grey-scale distribution, which has two limitations: first, the inability to correctly detect waterlines in images with complex conditions (i.e., where the water is clear, and the bed substrates reflectance can be seen in the satellite images); and, second, the Otsu threshold method will detect waterlines even when all intertidal pixels are flooded (at high tide) or exposed (at low tide), adding bias in the extremes of the topographical profiles.

There are currently several methods for edge detection that have been implemented in waterline-SDT that can potentially overcome the issues highlighted above. One practical solution would be the manual identification of the waterline; however, it is subjective and labour-intensive when applied over a large area and in multiple study sites. Another way would be to apply image segmentation techniques, for instance, K-means clustering techniques applied to edge detection (Salameh et al., 2020). Alternatively, the identification of sea-grass banks could be used to remove areas where the waterline is poorly detected prior to analysis. Simple algorithms could be used for this, such as Ha et al. (2020), who identified seagrass using ensemble-based machine learning algorithms. Caballero and Stumpf (2020) identified algae and seagrass by using an empirical formula to calculate the maximum chlorophyll index, which uses three different optical bands to explain the radiance peak at the red-edge band.

5.4.2 The proposed correction methods for waterline-SDTs.

Our proposed correction methods (i.e., statistical and dynamic) for the SDT only resulted in a 1–2 cm improvement across the case-study estuary. However, our insights into why and where the correction resulted in improvements provide the basis for further work (e.g., when more

imagery becomes available to test error sources more thoroughly). The statistical relationship between the error and the waterline height, the elevation on the tidal flat (LiDAR) and the waterline detection threshold in all four studied estuaries allowed us to set a semi-independent framework to correct the vertical level in the waterline-derived SDT. For example, the relation between THLD and BIAS could be learned in similar estuaries and subsequently used to correct to an entirely different study area with similar intertidal zone properties, such as estuaries with similar sediment colour, water turbidity, spring tidal range and intertidal area coverage.

The dynamical correction should give more realistic waterline heights because it accounts for the tide propagation within the estuary. However, the approach did not significantly improve the SDT as expected. There are four possible reasons for the limited improvement. First, inaccuracies in horizontal waterline position may be more important than inaccuracies in the waterline height. This can be demonstrated by examining the location of waterlines on LIDAR-derived profiles. Figure 5.11 (m1) shows three different waterline positions (red, blue, and green lines) and three different LIDAR-derived profiles that intersect these waterlines (p1, p2, and p3) in Tauranga Harbour. In panels p1, p2, and p3, the three profiles are shown in detail. The horizontal location of the three uncorrected waterline-SDTs is represented on the profiles by the coloured circles (red, green, blue) with their corresponding tide-gauge-derived heights (solid line). The corresponding dynamically-corrected waterline heights are also plotted, represented by the dashed lines. Note that in the dynamical correction, just the waterline height is corrected, and the observed waterline position remains unchanged. Because the numerical model is expected to give more realistic water levels — that account for the tidal propagation within the estuary— the correct position of the waterline should be where the dynamically corrected waterline height (dashed lines) intersects the topographic profile (continuous black line) in the Figure 5.11 (panels p1, p2, and p3). Thus, all the waterlines in p1 would need to be further seaward than they are to intersect with the profile at the correct location. In p2, waterline 3 (blue circle) should be slightly landwards, and waterline 1 (green circle) and 2 (red circle), further seaward. In p3, all corrected waterlines should be further seaward. However, when the waterline is well positioned, waterline heights are similar to the LiDAR data; for instance, in p2 for all waterlines (all dashed lines).

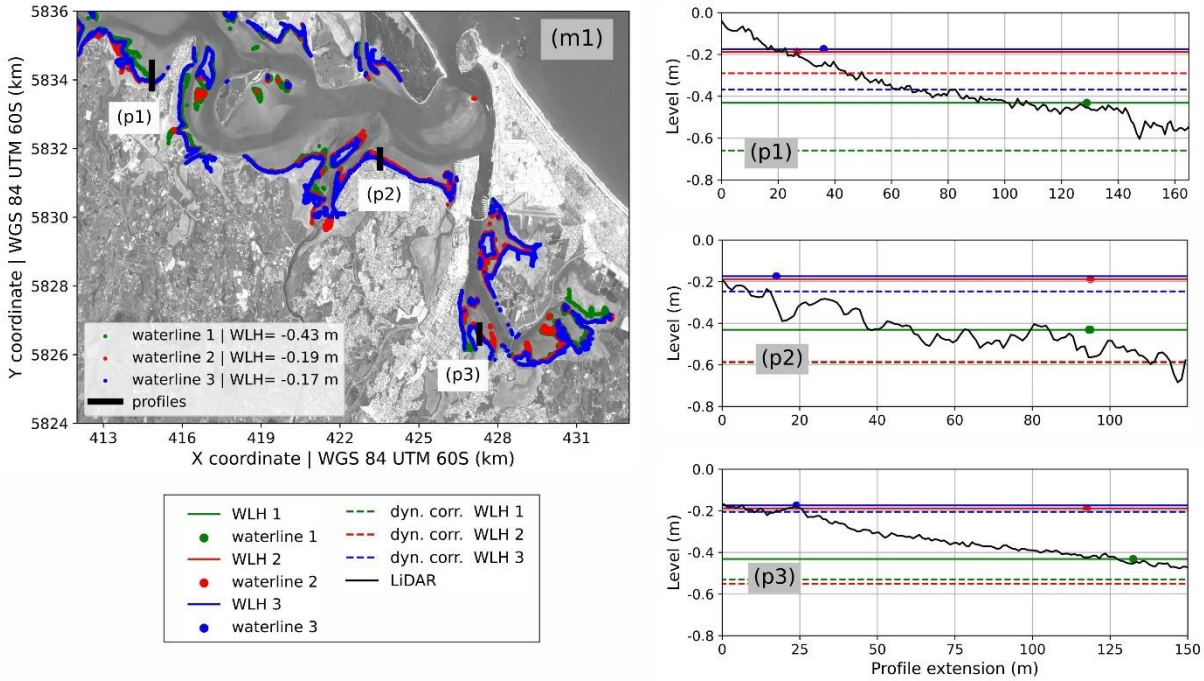

Figure 5.11. Analysis of the dynamical correction in three different profiles (p1, p2, p3). [m1] shows the location of the LIDAR-derived profiles in Tauranga Harbour. The panels (p1), (p2), and (p3) show the location of the three waterlines along the three profiles (black line). Each panel highlights the waterline height (WLH) extracted from the tide gauges and the horizontal position of three different waterlines (green (waterline 1), red (waterline 2), and blue (waterline 3)). The corresponding dynamically corrected waterline height (dyn. corr. WLH) is also shown (dashed lines). Considering that the hydrodynamical model should give more accurate water levels, the correct waterline positioning should be where the dyn. corr. WLH intersects the LiDAR profile. Background image: ESA Sentinel 2A. Date and time of the background image acquisition: 18/12/2018 10:15 h (UTC+12h).

The second factor that can influence the performance of the dynamical correction is the hydrodynamic model accuracy — especially at low tide, as can be seen in Figure 5.10. The spatial resolution of the numerical grid (20 m) can limit the model's ability to correctly solve the flooding and drying within grid cells around narrow channels, potentially adding horizontal bias to the waterline heights. Furthermore, the tidal wavelength is hundreds of kilometres, which means that the water level should not be affected significantly by smaller-scale bathymetric features. Moreover, the fourth limiting factor is the LiDAR data horizontal and vertical accuracy, which limits the potential correction. The use of hydrodynamic modelling to assign the waterline heights is a common practice when generating SDTs (e.g., Liu et al., 2013; Khan et al., 2019; Salameh et al., 2020; Fitton et al., 2021). However, in most cases, the studies cover extensive areas with exposed coastlines or sand banks, in which regional tide models are used where there are not enough tide gauges to provide tide levels (Liu et al., 2013; Khan et

al., 2019; Fitton et al., 2021). In just a few of these studies, enclosed estuaries were studied by setting up local-scale hydrodynamic modelling (e.g., Liu et al., 2013; Salameh et al., 2020). In Arcachon Bay (France), Salameh et al. (2020) compared the waterline-SDTs that were generated by assigning waterline heights according to single-location tide gauges, single-location model point output, and grid hydrodynamic model output. Similar to our results, they found that the waterline heights assigned by using grid model output did not improve the SDTs compared with using a single-location tide gauge within the estuary. They explained the unexpected result as due to the slope of the tidal flat and the model's inability to provide accurate sea level heights over the intertidal area. Similarly, Liu et al. (2013) used a regional tide model for the South Yellow Sea (China) to assign waterline heights to a local-scale study in Dongsha Sandbank (an exposed tidal flat), which limited the vertical accuracy of the SDT up to 30 cm (corresponding to the model's accuracy).

5.4.3 Comparison between the waterline method and ratio-log for intertidal zones.

The results show that, for Tauranga Harbour, the waterline and the ratio-log techniques performed similarly for the task of deriving topography over intertidal zones using satellite images. Thus, for estuaries with low water column turbidity, pre-existing surveyed topo-bathymetric data, and low numbers of available satellite images covering its area — as is the case of Tauranga Harbour — the ratio-log method could potentially replace the waterline method for deriving elevation data for intertidal zones. Although the waterline method shows better performance when considering the RMSE — either evaluated on a point-to-point basis (0.20 m) or evaluated using the DEM (0.23 m), see Table 5.3 — than the ratio-log method (0.25 m). Evaluating RMSE using the DEM provides more information for comparison. Figure 5.12 shows the density SDT points and distribution of the relative vertical error (RE) for Tauranga Harbour's waterline-SDT and ratio-log-SDT for intertidal zones, where the colour represents positive (red) or negative (blue) errors. Positive (negative) errors indicate that SDT estimates are deeper (shallower) or further landward (seaward) than the LiDAR data (see Section 5.2.7). The waterline-SDT (Figure 5.12: a1, b1, c1, d1) provides estimates that are generally shallower or further seaward than the LiDAR — as the negative RE indicates — with the worst estimates in the tidal flat's upper region (bluer colour dots). The positive RE values (redder colour dots) are concentrated in the estuary's wide flat centre region (Figure 5.12 b1) and indicate that the estimates are deeper or further landward than the LiDAR data. As

discussed in Section 5.4.1, the waterline method is mainly limited by the number of images required to properly define the morphology of the study site. In the case of Tauranga Harbour, as a consequence of the high complexity of its morphology, the SDT provided by the present framework could be substantially improved with more images, making the waterline method even more accurate than the ratio-log method.

The ratio-log-SDT (Figure 5.12: a2, b2, c2, d2) allows the water depth to be assessed on a pixel-by-pixel basis, with a resolution of 10 m in the case of Sentinel Copernicus data. However, the application of this method has several limitations. In our application, the intertidal topography was flattened; the positive and negative errors are in the upper and lower parts of the tidal flats, respectively. In the middle of the topographic profile, the estimates are more accurate (whiter colour dots). The low data variability (pixels reflectance) probably causes the lower accuracy of the ratio-log-SDT in comparison to the waterline-SDT (the ratio-log method depends on calibration data covering the range of conditions). The ratio-log (green/blue band ratio) poorly explains the depth (LiDAR data), which leads to a low correlation coefficient (R2=0.12). This assumption is confirmed by the higher correlation coefficient (R2=0.24) obtained when the same method is applied to the shallow waters within Tauranga Harbour. In addition, the presence of seagrass in the intertidal zones and shallow water (Figure S3) can potentially worsen the ratio-log-SDT and SDB by affecting the reflectance (Geyman and Maloof, 2019; Caballero and Stumpf, 2020).

Many estuaries have turbid water, which would reduce the quality of SDBs and SDTs derived from both ratio-log and waterline methods. The ratio-log derivations would be affected by the interference of the suspended material on the light absorption rate through the water column — which could be improved by using methods that adjust the ratio-log method for turbid water (e.g., Caballero and Stumpf, 2020). The waterline derivations would be affected by intertidal zone identification. The NDWI of the pixels in shallow water with a high concentration of suspended materials could have similar values to those in the intertidal zone. Consequently, determining the intertidal areas would be less accurate in environments with high concentrations of suspended material.

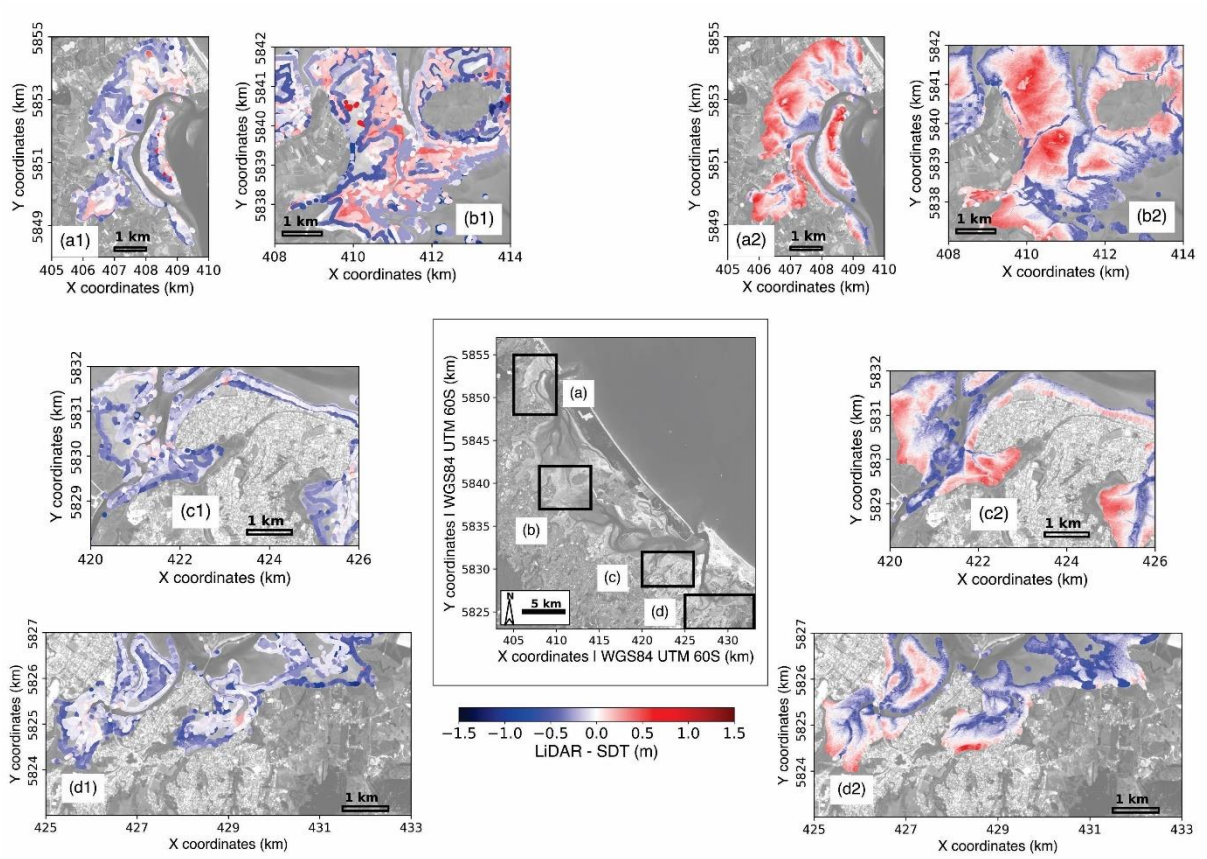

Figure 5.12. Estimated SDT and corresponding relative vertical error (LiDAR-SDT) for the intertidal zone in Tauranga Harbour using waterline-derived (a1, b1, c1, and d1) and ratio-log (a2, b2, c2, and d2) methods. The root-mean-squared error for the waterline method is 0.20 m, and for the ratio-log method is 0.25 m (not shown in the figure). However, the waterline method results in less density of estimates (due to imagery constraints), while the ratio-log method results in a pixel-by-pixel estimate density. Background image: ESA Sentinel 2A. Date and time of the background image acquisition: 18/12/2018 10:15 h (UTC+12h).

In addition, image pre- and post-processing are other factors that may improve the accuracy of the SDT and SDB of waterline and ratio-log methods. In the present manuscript, available Sentinel images were used, which are already pre-processed by using Sen2Cor, which creates surface-reflectance images (see Section 5.2.1). However, several pre-processing tools are available (Pereira-Sandoval et al., 2019). Some of these are designed specifically for use in coastal areas — where water is often turbid, containing a high concentration of suspended sediments and other materials. For instance, the ACOLITE tool (Vanhellemont and Ruddick, 2018) has been widely applied in estuaries (e.g., Bué et al., 2020; Salameh et al., 2020; Fitton et al., 2021). In the case of exposed coastal areas or where local wind waves can increase the rugosity of the water surface, filters to eliminate sun glint can be applied (Hedley et al., 2005).

5.4.4 Hydrodynamic modelling assessment

The bathymetric and topographic data quality is fundamental for reliable hydrodynamic modelling. Despite the limited accuracy of the SDT and SDB (see Section 5.4.1–5.4.3), our results show that hydrodynamic models using satellite-derived elevation can predict water level with similar accuracy to models using only surveyed data (see Section 5.3.3, Figures 5.9 and 5.10). Thus, water level modelling may not be sensitive to small uncertainties in the bathymetric data but rather to the larger scale characteristics of the estuary, such as the width of entrances and overall geometry. Bathymetric uncertainties can arise from the interpolation technique used to create the DEMs (Hare et al., 2011; Kang et al., 2017, 2020; Salameh et al., 2020) — e.g., spline, kriging, inverse distance weighting, nearest neighbour, triangulation. However, previous studies have found that uncertainties in the elevation data lead to minor differences in the water level predictions (Cea and French, 2012; Falcão et al., 2013). For instance, Cea and French (2012) showed that water level predictions do not significantly change with vertical uncertainties of up to 1 m in the bathymetry. Similarly, Falcão et al. (2013) have shown that the DEMs created with the same interpolation technique (i.e., kriging) but with a different spatial resolution (i.e., 5 and 50m) did not significantly affect the water level prediction. Corroborating our results, Falcão et al. (2013) also found that the worst predictions are for grid cells where the water level is at a minimum when comparing these two scenarios. The stream current magnitude and direction predictions are affected the most by the uncertainties in the bathymetric and topographic data (Cea and French, 2012; Falcão et al., 2013).

Despite the uncertainties in the estimates, SDT and SDB can generate a fair approximation of estuary relief, which can be helpful in long-term predictions for coastal management applications. In idealistic numerical studies, the extension and slope of the intertidal zone, the estuary's length, and the width of the mouth are the main factors causing changes in the tidal range within harbours (Du et al., 2018; Khojasteh et al., 2020; Khojasteh et al., 2021). For instance, Du et al. (2018) show that the length of an estuary and intertidal zone slope strongly influences the tidal range. However, the entrance restriction drives the estuarine response to sea-level rise (Khojasteh et al., 2020); the smaller the cross-sectional area of the estuary mouth, the smaller would be the tidal range within the estuary. Moreover, SDT and SDB could be used for data assimilation in numerical modelling, as in Mason et al. (2010), who used the SDT to calibrate a morphodynamic model. Ultimately, the SDTs and SDBs can decrease the

uncertainties of flood-risk management in the present and future scenarios of sea-level rise where studies are limited due to a lack of elevation data in remote areas such as small islands in developing states (Parodi et al., 2020) and coastal lagoons in developing countries (Pedrozo-Acuña et al., 2012).

Although the differences in the resulting water level between the SDT, SDB, and surveyed bathymetry simulation scenarios show that satellite techniques compare well, our simulations were only conducted in one estuary, albeit a large and relatively complex estuary — where the astronomical spring tides are the main driver for estuarine flooding. Therefore, studies are required in sites with different physical conditions would be useful to validate the use of SDT and SDB more broadly. For example, estuaries where the storm surge is the main driver for flooding; or/and exposed estuaries where the wave forces can increase the water level (i.e., wave set-up); e.g., Bertin et al. (2019). Many such effects can be strongly dependent on the topography, for example, the wind effect on the storm surge (wind surface stress) and generation of local waves (e.g., Smith et al., 2001; Bertin et al., 2015) and tide-surge interactions (Spicer et al., 2019; Wankang et al., 2019; Zheng et al., 2020).

5.5 Conclusions

A waterline technique for deriving topography from multispectral satellite images was developed, and its use in hydrodynamic modelling was assessed. The simple pre-processing required for the satellite images combined with the use of cloud computing and storage make the present framework highly applicable to regional-scale studies. Our main findings show that the accuracy of the waterline SDT is similar or even superior to other techniques applied in previous studies to comparable sites and similar to the vertical error in the LiDAR dataset used to assess accuracy. In addition, optical empiric methods such as the ratio-log could potentially replace the waterline-SDT in case of imagery constraints and when applied to an estuary with low water turbidity. The main source of error for the waterline-SDT is whether the number of satellite images is adequate to cover the intertidal zone and the accuracy of the waterline positioning. Statistical and dynamical corrections were trailed but provided limited improvements. The hydrodynamic modelling assessment was encouraging and showed that SDT and SDB techniques have the potential for use in predictions for extreme water levels

(such as those associated with spring tides and severe storm surges). Scenarios using different applications of the SDT and SDB did not show major high water level differences over most of the numerical domains for Tauranga Harbour. The use of SDT and SDB for hydrodynamic modelling in estuaries can make flooding assessment for remote coastal areas feasible and provides a pathway around the need for expensive surveys for economically depressed vulnerable areas.

Chapter 6

General discussion and conclusions

Predicting coastal flooding is highly complex because it requires understanding several physical drivers that mutually interact, especially in estuarine environments, where marine (e.g., astronomical tides, storm surges, waves) meet land forcings (e.g., river discharge, sediment influx). Moreover, climate change modifies the frequency and magnitude of storm events related to these forcings. For instance, a warming climate results in more severe meteorological systems, potentially increasing wave height and the frequency of wave storms and higher and more persistent storm surges. On the land forcings, it can be expected that increased rain volume will result in an increased fluvial discharge. This is especially threatening for estuaries and, consequently, to coastal communities. In addition, rising mean sea levels would directly modify astronomical and gravity wave propagation, impacting sediment transport magnitude and direction and, therefore, coastal and estuarine morphology. In the Thesis, I have focused on marine forcings of estuarine flooding.

My main findings rely on identifying regional patterns of extreme water levels due to storm events of wave and storm surges and how important the coastal and estuarine morphology is in modulating these patterns. In summary, estuarine morphology around Aotearoa New Zealand affects the time between the maximum storm surge and the peak of the astronomical tides inside estuaries and the co-occurrence of extreme events inside and outside a given estuary. Waves contribute to non-tidal residuals, and compound and storm cluster effects between storm surge and waves are expected to be strong, especially in North Island, even inside estuaries. Thus, coastal morphology should be monitored, and a framework for deriving topographic and bathymetric data based on satellite images was developed. The derived elevation data were tested in hydrodynamic modelling of extreme water levels, showing to be a good replacement when surveyed data is scarce. A detailed summary of the findings is given in Section 6.1.

Despite all the complexity involving the scientific and technical aspects of estuarine flooding presented in this thesis, its outcomes are also useful for the general public. In my understanding, the ultimate question that a common citizen would like to know regarding coastal flooding

would be if their houses or places they frequently go will be flooded — if yes, when? How often and how severe would that happen? Although the investigation of non-linear interactions between different flooding drivers and the estuarine morphology cannot promptly answer these questions, the main findings of the thesis can be useful to improve current modelling methods that are applied worldwide to assess the risk of coastal areas regarding climate change. In the specific case of Aotearoa New Zealand, the most recent National Adaptation Plan (Ministry of the Environment, 2022) indicates that coastal flooding is the main threat related to climate change. As an island nation with a diverse coastal environment and a culture intimately related to the sea, its population depends on it for diverse purposes. The sea and coastal environments are where thousands of Aotearoa New Zealanders spend most of their lifetime, whether for living and working or recreational activities (e.g., fishing, camping, hiking, surfing). Especially for Māori culture, the sea has an intimate relationship with their gods and beliefs. In addition, many Maraes (Māori communities) are in coastal zones, which makes coastal flooding a cultural threat for tangata whenua (literally "people of the land"). Furthermore, the economy and financial system of Aotearoa New Zealand depend on the good maintenance of national infrastructure such as roads, ports, and airports, often located near the coast and inside estuaries. Storm events often damage these structures, imposing restrictions or temporally suspending their functions and services. For instance, the recent storm Gabrielle (2023) flooded the biggest airport in Aotearoa New Zealand (Auckland Airport), stopping its functioning for a few days. The same storm caused landslides, damaged houses, buildings, and roads and inundated one of the country's most crucial agricultural zone production (Gisborne). In terms of the natural environment, estuaries have great ecological importance by serving as a wildlife sanctuary where several species of fauna (e.g., birds, fish) can develop, which is crucial for maintaining sustainable fishing stocks, for example. Ultimately, coastal retreat plans are based on inundation maps generated by modelling methods that benefit from the further understanding of non-linear processes occurring between different drivers in estuarine environments.

6.1 Summary of Findings

This thesis aimed to increase the knowledge of drivers for estuarine flooding, focusing on the interaction between astronomical tides, storm surges, waves, and morphology. The main findings are summarised below:

1- Estuarine morphology enhances tide-surge interactions, which has two main consequences:

a) The highest non-tidal residuals occur close to low tide.

b) Tide-surge interactions modulate the co-occurrence of extreme water levels inside and outside an estuary.

2 - Skew-surges and astronomical tides were shown to be independent, which validated the current joint-probability methods used in Aotearoa New Zealand to project future extreme water levels.

3 - Skew-surge and wave height storm events are statistically correlated during extreme water levels, and their correlation is stronger in locations inside and close to the entrance of estuaries. This provides evidence of the direct effect of waves on the variations of water levels inside estuaries and the potential for compound effects during flooding.

4 - Individual storms and storm clusters of wave height and skew-surge follow similar intra-annual patterns and seasonality, which means that highly energetic events occurring in close succession are likely to co-occur, exacerbating flooding damages.

5 - Satellite-derived topography and bathymetry were efficient in modelling extreme water levels inside estuaries with complex morphology.

The main questions posed in the introduction of this thesis are revisited and discussed below:

How does estuarine morphology affect tide and surge in NZ?

Chapter 3 has explained the critical role of Tide-Surge Interaction (TSI) in modulating extreme water levels within shallow coastal systems, specifically focusing on estuaries and harbours. The presence and implications of TSI have been elucidated through a comprehensive analysis of water level data derived from 36 tide gauges spanning the diverse Aotearoa New Zealand coastline. Notably, TSI emerges as a prevalent phenomenon, predominantly impacting the phase of major storm surges relative to high tide. Inner estuarine locations with extensive intertidal features experience the most pronounced TSI effects. The findings further underscore the variability in TSI magnitude, ranging from -16 cm to +27 cm, depending on the assessment

method employed. The modulation of co-occurrence rates of extreme water levels, both within and outside the same estuary, emphasises TSI's role in affecting tidal amplification and thereby influencing flooding risks. These outcomes accentuate the urgency of expanding the tide gauge network, particularly in densely populated estuarine regions, to enable more comprehensive and accurate observations, thus enhancing the incorporation of TSI into flooding hazard projections. This research contributes essential insights into the coastal vulnerability landscape of Aotearoa New Zealand, necessitating continued investment and vigilance for effective flood risk management strategies.

What are the main drivers of spatial variation in storm surges?

Chapter 4 investigated the significance of compound effects involving waves and skew surges in influencing extreme sea levels. Existing predictions of extreme water levels worldwide primarily consider astronomical tides and surges, partially neglecting the contribution of waves. In the context of Aotearoa New Zealand, where wave intensity during storm events has shown an increasing trend and projected wave heights are anticipated to rise, this research reveals the direct influence of waves on water levels, urging their inclusion in extreme water levels return period calculations. The synchronisation of storm clusters involving wave heights (H_s), skew surges, and still-water level (SWL) with similar temporal intervals and seasonality accentuates the potential for compound effects during flooding events. Notably, the strong correlation between H_s and skew surges during SWL extreme events within estuarine regions challenges conventional expectations and necessitates a reconsideration of wave impacts, even in sheltered locations. The findings highlight the importance of nuanced considerations of compound effects in flood risk assessments, specifically in complex estuarine morphology and regional variability. Furthermore, the study unveils a connection between H_s, skew surges, and specific weather patterns, emphasising their interaction in shaping extreme events. Regional disparities and dependencies between wave activity and skew-surges are observed, indicating the need for a comprehensive understanding of their interactions across diverse coastal zones. Ultimately, this research expands the knowledge of compound effects, underlining the necessity of a holistic approach to coastal management and hazard mitigation strategies, particularly in regions characterised by intricate estuarine systems and diverse wave-climate dynamics.

How well can we predict estuarine flooding events in areas where we do not have good topo-bathymetric data?

Chapter 5 investigated how satellite-derived elevation techniques — specifically waterline and ratio-log methods — perform in estuaries of Aotearoa New Zealand and if their use in hydrodynamic modelling could effectively replace surveyed data (e.g., when acquired by echosounders). The waterline method for estimating topography demonstrated good accuracy (~0.2 m) with LiDAR data within Aotearoa New Zealand's estuarine sites, considering the intertidal zone's varied topography relative to the mean sea level. While similar biases to analogous estuarine studies were observed, the method's accuracy was sensitive to precise waterline positioning and height assignment, influenced by factors like complex morphology, bed substrates, tide gauge location, and the number of images available for analysis. The study revealed a stronger accuracy in the derived elevation data closer to mean sea level, with errors increasing towards high and low tide peaks. In addition, correction techniques were developed to be implemented in the waterline-derived topography — one by using hydrodynamic modelling and the other by removing statistical bias; however, they led to minor enhancements (1–2cm).

Furthermore, Chapter 5 compares the performance of waterline and ratio-log techniques for deriving intertidal zone topography from satellite images in Tauranga Harbour. Both methods yielded similar results, with the ratio-log method potentially replacing the waterline method in estuaries characterised by low water column turbidity, pre-existing topo-bathymetric data, and limited satellite images. While the waterline method showed better root mean square error (RMSE) performance, the ratio-log method allows pixel-level water depth assessment. Seagrass presence and turbid water can further affect the accuracy of both methods. Turbid water in estuaries could interfere with the ratio-log method due to suspended materials affecting light absorption, while intertidal zone identification using the waterline method might be less accurate in turbid environments.

Despite the inherent uncertainties in satellite-derived topographic data (SDT) and satellite-derived bathymetric data (SDB), it was demonstrated in Chapter 5 that hydrodynamic models using these datasets have similar accuracy in predicting extreme water levels to models relying only on surveyed data. Although bathymetric uncertainties may arise from interpolation methods, previous research indicates that small vertical uncertainties have minimal effects on water level predictions. While stream current predictions are more susceptible to data uncertainties, SDT and SDB remain valuable for approximating estuary relief and enhancing

flood-risk management, especially in sea-level rise scenarios and remote areas lacking elevation data.

6.2 Conclusions

This thesis has provided significant insights into the interactions between different flooding drivers and estuarine morphology for coastal flooding modelling, which has useful outcomes for predicting extreme water levels inside estuaries and flooding risk management. The present research contributes to the body of knowledge by investigating how non-linear interactions affect extreme water level events, a subject of particular interest in the scientific community because regional models usually have the worse accuracy in shallow coastal areas with complex morphology as estuaries, where interactions between tides, storm surge, and waves become stronger. If non-linear interactions are not considered in modelling extreme water levels, it could lead to inaccurate predictions. Furthermore, the thesis explores techniques to acquire elevation data, which is fundamental for good modelling of extreme water levels and, ideally, should be updated routinely because the shallow-water effects are sensitive to the water depth. However, shallow estuaries can have their navigation restricted at low tide, and the devices used to survey their topo-bathymetry are expensive, which makes the survey campaigns often prohibitive. In this thesis, I have developed a framework to apply existing Satellite-derived topography (SDT) and bathymetry (SDB) techniques that could be applied to estimate topo-bathymetric data in inaccessible areas.

Chapter 3 investigated tidal surge interaction (TSI) using observations from multiple tidal gauges around Aotearoa New Zealand and a focused numerical study in Manukau Harbour. It revealed that TSI affects the phase of the largest surges relative to high tide and is most pronounced in inner estuarine locations correlated with intertidal areas. Furthermore, the chapter established the independence between skew-surges and astronomical tides, vital for extreme sea-level return period calculations widely applied in Aotearoa New Zealand and worldwide. The chapter also explores the interplay of TSI and tidal amplification in modulating the co-occurrence of extreme sea levels inside and outside NZ estuaries. This is important for modelling practitioners, highlighting the significance of accurate boundary conditions for hydrodynamic models, especially when predicting extreme events within harbours. Estuarine

morphology's influence on the astronomical tide, non-tidal residuals, and TSI were also demonstrated, stressing the need for comprehensive tide gauge networks within estuaries and coasts with complex geometry. Furthermore, in Chapter 4, a regional data analysis elucidated the importance of wave and storm surge (skew-surge) compound effects during coastal flooding, particularly on the northeastern and northwestern coasts of the North Island, with seasonal similarities in individual storm and cluster dynamics.

Ultimately, Chapter 5 tested if the non-linear interactions between drivers investigated in Chapters 3 and 4 could be properly modelled using satellite-derived topo-bathymetry. The satellite-derived elevation demonstrated its suitability for hydrodynamic modelling with accuracy comparable to other methods. Optical empiric methods like the ratio-log show promise, especially in low-water turbidity estuaries. While statistical and dynamic corrections offered limited improvements, hydrodynamic modelling indicated that SDT and SDB techniques could predict extreme water levels and flood assessment in remote and economically vulnerable coastal areas. Ultimately, this research shows the importance of investing in extensive tide gauge networks and advancing satellite-derived methods, contributing to a better understanding of complex coastal interactions, flood risk management, and projections of sea-level rise impacts.

The mutual effects of flooding drivers and estuarine morphology connect the chapters. Chapter 2 described the non-linear effects involving tides, surges, and gravity waves when propagating inside estuaries as shallow water waves, mainly by altering their phase. In addition, they are deformed by the effects of friction and constriction imposed by the estuarine morphology. Thus, estuarine morphology modulates these deformations. On the other hand, the dynamics of tides, surges, waves and their residual currents will govern the transport of sediments inside the harbour, which will affect the estuarine morphology. In summary, it is necessary to properly predict flooding events to understand the main mechanisms of non-linear interactions between flooding drivers and morphology (investigated in Chapters 3 and 4). However, estuarine morphology constantly changes, needing constant monitoring and data updates (subject investigated in Chapter 4). With respect to risk assessment and implementation of climate adaptation plans, understanding non-linear physical processes would enhance the water level prediction inside estuaries where a great part of Aotearoa New Zealand’s population lives, which is of fundamental importance for planning coastal retreatment policies. The physical processes and topographic data must be highly accurate to properly estimate the inundation

maps. For instance, uncertainties in flooding modelling and topographic data could result in coastal retreat plans that would move thousands of people from coastal areas needlessly or have the value of their land decreased erroneously. In contrast, some other regions could be mistakenly classified as safe zones, exposing those people to danger. In addition, a high-frequency monitoring system for topographic data combined with hydrodynamic modelling could model the future behaviour of intertidal zones and their related ecosystems, such as mangrove and saltmarsh forests in the context of climate changes and sea level rise, which has fundamental importance to coastal defense and adaptation, since these environments serve as natural protection from storms, attenuating erosion and flooding.

6.3 Suggestions for future work

Although this thesis presents several useful findings on non-linear processes between different flooding drivers, there are still many options for future work. Suggestions for future work can be divided into extreme water level modelling, temporal trends of flooding drivers, and satellite-derived techniques.

On the application for extreme water level modelling, further investigations should consider regional patterns of other flooding drivers, such as rainfall, river discharge and level. Although pluvial and fluvial contributions may not directly impact the observed water level recorded in tide gauges, the compound effect of these drivers can potentially exacerbate flooding events. Moreover, the findings shown here indicate the main temporal and spatial patterns of flooding drivers inside estuaries, which could help to enhance the regional models of storm surges and extreme water levels in these complex environments. Dynamic and data-driven approaches could be applied further to investigate the non-linear processes along Aotearoa New Zealand. Numerical models are powerful tools for local scale studies to understand underlying physical processes. Statistical models and deep learning techniques could be used to reconstruct water level time series inside estuaries on a regional scale. Hindcasts of water level could be useful to make the extreme value analysis more robust for estuaries with short observation periods. Novel data-driven techniques such as physical process algorithm deep learning could also be a strong tool to predict historical water levels once they can generate results quickly while obeying physical assumptions. The findings presented here could assist in properly choosing

the predictors and forcing inputs for those models and their validation. Furthermore, understanding the stochasticity of flooding drivers is one of the biggest challenges in predicting future coastal flooding. Then, studies analysing the combined regional trends of sea levels, storm surges, waves, and vertical land motion can be fundamental for predicting long-term coastal flooding.

Regarding satellite-derived techniques, Chapter 5 proposed and applied statistical and dynamic correction methods for improving the accuracy of waterline-derived topography. While these methods were capable of only minor enhancements of 1-2 cm in the case-study estuary, the insights obtained provide valuable foundations for future research. The statistical approach, driven by relationships between error sources, waterline height, and tidal flat elevation, offers the potential for semi-independent correction frameworks across similar estuaries. These could be highly applicable when more images become available and the tide gauge network increases in the number of stations and observation period. Another alternative for correction techniques would be to develop techniques to pre-select or eliminate pixels, avoiding bias caused by environmental characteristics like bed substrates (e.g., seagrass banks and groundwater seepage) and improving edge detection algorithms. Furthermore, using satellite-derived topography (SDT) and bathymetry (SDB) for extreme water level modelling needs broader validation. For instance, applying a similar approach in storm surge-driven or exposed estuaries would extend the utility of SDT and SDB in diverse physical conditions, accounting for factors like wind effects, local wave generation, and tide-surge interactions.

References

Abbaszadeh, P., Muñoz, D. F., Moftakhari, H., Jafarzadegan, K., & Moradkhani, H. (2022). Perspective on uncertainty quantification and reduction in compound flood modelling and forecasting. IScience, 25, 10, 105201. doi: 10.1016/j.isci.2022.105201

Ackerley, D., Lorrey, A., Renwick, J.A., Phipps, S.J., Wagner, S., Dean, S., Singarayer, J., Valdes, P., Abe-Ouchi, A., Ohgaito, R., Jones, J.M. (2011). Using synoptic type analysis to understand New Zealand climate during the Mid-Holocene. Climate of the Past, 7, 4, 1189–1207. doi: 10.5194/cp-7-1189-2011.

Albuquerque, J., Antolínez, J. A. A., Gorman, R. M., Méndez, F. J., and Coco, G. (2021). Seas and swells throughout New Zealand: A new partitioned hindcast. Ocean Modelling, 168, 101897, 1–21. doi: 10.1016/j.ocemod.2021.101897.

Albuquerque, J., Antolínez, J.A.A., Méndez, F.J., and Coco, G. (2022). On the projected changes in New Zealand's wave climate and its main drivers. New Zealand Journal of Marine Freshwater Research, 1–38. doi: 10.1080/00288330.2022.2135116.

Almar, R., Bergsma, E.W.J., Maisongrande, P., Almeida, L.P.M. (2019). Wave-derived coastal bathymetry from satellite video imagery: a showcase with Pleiades persistent mode. Remote Sensing Environment. 231, 111263, 1–8. doi: 10.1016/j.rse.2019.111263

Almeida L.P., de Oliveira, I.E., Lyra, R., Dazzi, R. L. S., Martins, V. G., Klein, A. H. F. (2021). Coastal Analyst System from Space Imagery Engine (CASSIE): Shoreline management module, Environmental Modelling & Software, 140, 105033, 1–11. doi: 10.1016/j.envsoft.2021.105033.

Almeida, L.P., Vousdoukas, M.V., Ferreira, Ó., Rodrigues, B.A., Matias, A. (2012). Thresholds for storm impacts on an exposed sandy coastal area in southern Portugal. Geomorphology, 143–144, 3–12. doi: 10.1016/j.geomorph.2011.04.047.

Anderson, D. L., Ruggiero, P., Mendez, F. J., Barnard, P. L., Erikson, L. H., O'Neill, A. C., et al. (2021). Projecting climate dependent coastal flood risk with a hybrid statistical dynamical model. Earth's Future, 9, e2021EF002285, 1–24. doi: 10.1029/2021EF002285

Antony, C., Unnikrishnan, A. S., Krien, Y., Murty, P. L. N., Samiksha, S. V., and Islam, A. K. M. S. (2020). Tide–surge interaction at the head of the Bay of Bengal during cyclone Aila. Regional Studies in Marine Science, 35, 101133, 1–10. doi: 10.1016/j.rsma.2020.101133

Arns, A., Wahl, T., Wolff, C., Vafeidis, A. T., Haigh, I. D., Woodworth, P., et al. (2020). Non-linear interaction modulates global extreme sea levels, coastal flood exposure, and impacts. Nature Communications, 11, 1918, 1–9. doi: 10.1038/s41467-020-15752-5

Ashphaq, M., Srivastava, P. K., and Mitra, D. (2021). Review of near-shore satellite-derived bathymetry: Classification and account of five decades of coastal bathymetry research. Journal of Ocean Engineering and Science, 6, 340–359. doi: 10.1016/j.joes.2021.02.006.

Barnard, P.L., Erikson, L.H., Foxgrover, A.C., Hart, J.A.F., Limber, P., O`Neil, A.C., van Ormondt, M., Vitousek, S., Wood, N., Hayden, M.K., and Jones, J.M. (2019). Dynamic flood modeling essential to assess the coastal impacts of climate change. Scientific Reports, 9, 4309, 1–9. doi: 10.1038/s41598-019-40742-z

Bass, B., and Bedient, P. (2018). Surrogate modeling of joint flood risk across coastal watersheds. Journal of Hydrology, 558, 159–173. doi: 10.1016/j.jhydrol.2018.01.014

Batstone, C., Lawless, M., Tawn, J., Horsburgh, K., Blackman, D., McMillan, A., Worth, D., Laeger, S., Hunt, T. (2013). A UK best- practice approach for extreme sea-level analysis along complex topographic coastlines. Ocean Engineering, 71, 28–39. doi: 10.1016/j.oceaneng.2013.02.003

Beavan, R. J., and Litchfield, N. J. (2012) Vertical land movement around the New Zealand coastline: implications for sea-level rise, GNS science report 2012/29. Available at: https://www.hbrc.govt.nz/assets/Hazards-Database/Sea-level-rise-projections-adjusted-for-vertical-tectonic-land-movement-along-the-Hawkes-Bay-coastline.pdf.

Bell, R. G., Dumnov, S.V., Williams, B. L., and Greig, M. J. N. (1998). Hydrodynamics of Manukau Harbour, New Zealand. New Zealand Journal of Marine Freshwater Research, 32, 81–100. doi: 10.1080/00288330.1998.9516807.

Bell, R., Goring, D., de Lange, W. (2000). Sea-level change and storm surges in the context of climate change. The Institute of Professional Engineers of New Zealand Transactions, 27, 1–10.

Bell, R., Hannah, J., and Andrews, C. (2022). Update to 2020 of the annual mean sea level series and trends around New Zealand. Prepared Ministry Environ. August 2022 (NIWA Client Rep. No: 2021236HN) (New Zealand: NIWA). Available at: https://environment.govt.nz/publications/update-to-2020-of-the-annual-mean-sea-level-series-and-trends-around-new-zealand

Bernier, N.B., Thompson, K.R. (2007). Tide-surge interaction off the east coast of Canada and the northeastern United States. Journal of Geophysical Research: Oceans, 112, C06008, 1–12. doi: 10.1029/2006JC003793.

Bertin, X., Bruneau, N., Breilh, J., Fortunato, A. B., and Karpytchev, M. (2012). Importance of wave age and resonance in storm surges : The case Xynthia, Bay of Biscay. Ocean Modelling, 42, 16–30. doi: 10.1016/j.ocemod.2011.11.001.

Bertin, X., Li, K., Roland, A., and Bidlot, J. (2015). The contribution of short-waves in storm surges: Two case studies in the Bay of Biscay. Continental Shelf Research, 96, 1–15. doi: 10.1016/j.csr.2015.01.005.

Bertin, X., Mendes, D., Martins, K., Fortunato, A. B., and Lavaud, L. (2019). The Closure of a Shallow Tidal Inlet Promoted by Infragravity Waves. Geophysical Research Letters, 46, 6804–6810. doi: 10.1029/2019GL083527.

Bevacqua, E., De Michele, C., Manning, C., Couasnon, A., Ribeiro, A. F. S., Ramos, A. M., et al. (2021). Guidelines for studying diverse types of compound weather and climate events. Earth's Future, 9, 1–23. doi: 10.1029/2021EF002340

Bevacqua, E., Maraun, D., Hobæk Haff, I., Widmann, M., & Vrac, M. (2017). Multivariate statistical modelling of compound events via pair-copula constructions: Analysis of floods in Ravenna (Italy). Hydrology and Earth System Sciences, 21, 6, 2701–2723. doi: 10.5194/hess-21-2701-2017

Bevacqua, E., Vousdoukas, M. I., Shepherd, T. G., and Vrac, M. (2020b). Brief communication: The role of using precipitation or river discharge data when assessing global coastal compound flooding, Natural Hazards Earth System Sciences, 20, 1765–1782. doi: 10.5194/nhess-20-1765-2020.

Bevacqua, E., Vousdoukas, M.I., Zappa, G., Hodges, K., Shepherd, T.G., Maraun, D., Mentaschi, L., Feyen, L. (2020a). More meteorological events that drive compound coastal flooding are projected under climate change. Communications Earth Environment, 1, 47, 1–11. doi: 10.1038/s43247-020-00044-z

Bilskie, M. V., & Hagen, S. C. (2018). Defining flood zone transitions in low-gradient coastal regions. Geophysical Research Letters, 45, 6, 2761–2770. doi: 10.1002/2018GL077524

Bilskie, M. V., Angel, D., Yoskowitz, D., & Hagen, S. C. (2022a). Future flood risk exacerbated by the dynamic impacts of sea level rise along the northern Gulf of Mexico. Earth's Future, 10, 4, 1–14. doi: 10.1029/2021EF002414

Bilskie, M. V., Asher, T. G., Miller, P. W., Fleming, J. G., Hagen, S. C., & Luettich, R. A., Jr. (2022b). Real-time simulated storm surge predictions during Hurricane Michael (2018). Weather and Forecasting, 37, 7, 1085–1102. doi: 10.1175/waf-d-21-0132.1

Birkemeier WA, Nicholls RJ, Lee G. 1999. “Storms, storm groups and nearshore morphologic change” in Coastal Sediments ’99, International symposium; 4th, Coastal engineering and science of coastal sediment processes, Vol. 1–3, Kraus NC, McDougal W (eds). ASCE: Hauppauge, NY, 1109–1122.

Bishop-Taylor, R., Sagar, S., Lymburner, L., and Beaman, R. J. (2019) Between the tides: Modelling the elevation of Australia’s exposed intertidal zone at continental scale, Estuarine Coastal Shelf Science, 223, 115–128. doi: 10.1016/j.ecss.2019.03.006.

Booij, N., Ris, R. C., and Holthuijsen, L. H. (1999). A third-generation wave model for coastal regions: 1. Model description and validation. Journal of Geophysical Research: Oceans, 104, 7649–7666. doi: 10.1029/98JC02622

Brenstrum, E. (2000). The cyclone of 1936: the most destructive storm of the twentieth century? Weather and Climate, 20, 23–27. doi: 10.2307/44279931

Brown, J., Bolanos-Sanchez, M., Rodolfo, X.X., Wolf, J. (2011). Impact assessment of advanced coupling features in a tide–surge–wave model, POLCOMS-WAM, in a shallow water application. Journal of Marine Systems, 87, 1, 13–24. doi: 10.1016/j.jmarsys.2011.02.006

Bruneau, N., Polton, J., Williams, J., Holt, J. (2020). Estimation of global coastal sea level extremes using neural networks. Environmental Research Letters, 15, 7, 1–11. doi: 10.1088/1748-9326/ab89d6.

Brunton, S.L., Proctor, J.L., Kutz, J.N. (2016). Discovering governing equations from data by sparse identification of nonlinear dynamical systems. Proceedings of the National Academy of Sciences, 113, 15, 3932–3937. doi: 10.1073/pnas.1517384113.

Bué, I., Catalão, J., and Semedo, Á. (2020). Intertidal bathymetry extraction with multispectral images: A logistic regression approach. Remote Sensing, 12, 8, 1311, 1–24. doi: 10.3390/RS12081311

Caballero, I. and Stumpf, R. P. (2019). Retrieval of nearshore bathymetry from Sentinel-2A and 2B satellites in South Florida coastal waters. Estuarine, Coastal, and Shelf Science, 226, 106277, 1–12. doi: 10.1016/j.ecss.2019.106277.

Caballero, I. and Stumpf, R. P. (2020). Towards routine mapping of shallow bathymetry in environments with variable turbidity: Contribution of sentinel-2A/B satellites mission. Remote Sensing, 12, 1451, 1–23. doi: 10.3390/rs12030451

Cagigal, L., Rueda, A., Castanedo, S., Cid, A., Perez, J., Stephens, S. A., et al. (2020). Historical and future storm surge around New Zealand: From the 19th century to the end of the 21st century. Int. J. Climatol. 40, 1512–1525. doi: 10.1002/joc.6283.

Calafat, F.M., Wahl, T., Tadesse, M.G., Sparrow, S. N. (2022). Trends in Europe storm surge extremes match the rate of sea-level rise. Nature, 603, 841–845. doi: 10.1038/s41586-022-04426-5

Camus, P., Haigh, I. D., Nasr, A. A., Wahl, T., Darby, S. E., & Nicholls, R. J. (2021). Regional analysis of multivariate compound coastal flooding potential around Europe and environs: Sensitivity analysis and spatial patterns. Natural Hazards and Earth System Sciences, 21, 7, 2021–2040. doi: 10.5194/nhess-21-2021-2021

Camus, P., Rueda, A., Méndez, F.J., Losada, I.J. (2016). An atmospheric-to-marine synoptic classification for statistical downscaling marine climate. Ocean Dynamics, 66, 1589–1601. doi: 10.1007/s10236-016-1004-5

Cea, L. and French, J. R. (2012). Bathymetric error estimation for the calibration and validation of estuarine hydrodynamic models, Estuarine, Coastal and Shelf Science, 100, 124–132. doi: 10.1016/j.ecss.2012.01.004.

Chadenas, C., Creach, A. & Mercier, D (2014). The impact of storm Xynthia in 2010 on coastal flood prevention policy in France. Journal of Coastal Conservation, 18, 529–538. doi: 10.1007/s11852-013-0299-3

Coco, G., Senechal, N., Rejas, A., Bryan, K.R., Capo, S., Parisot, J.P., Brown, J.A., MacMahan, J.H.M. (2014). Beach response to a sequence of extreme storms. Geomorphology, 204, 493–501. doi: 10.1016/j.geomorph.2013.08.028.

Codiga (2011). Unified tidal analysis and prediction using the UTide Matlab functions. The University of Rhode Island Technical report no: URI/GSO Technical Report 2011-01. The University of Rhode Island. doi: 10.13140/RG.2.1.3761.2008.

Coggins, J. H. J., Parsons, S., and Schiel, D. (2016). An assessment of the ocean wave climate of New Zealand as represented in Kidson's synoptic types. International Journal of Climatology, 36, 2481–2496. doi: 10.1002/joc.4507.

Coles, S. (2001). An introduction to statistical modeling of extreme values. London, New York: Springer. doi:10.1007/978-1-4471-3675-0

Corbella, S., and Stretch, D. D. (2013). Simulating a multivariate sea storm using Archimedean copulas. Coastal Engineering, 76, 68–78. doi: 10.1016/j.coastaleng.2013.01.011

Costa, W.L.L., Bryan, K. R., Coco, G. (2021). Assessing the use of satellite derived bathymetry in estuarine storm surge models – study case: Tauranga Harbour, Proceedings of The Australasian Coasts and Ports, Christchurch, New Zealand. Available at: https://www.coastsandports.org/papers/2021/106_costa_finalpaper.pdf, last access: 08 March 2023.

Costa, W.L.L., Bryan, K. R., Stephens, S. A., and Coco, G. (2023). A regional analysis of tide-surge interactions during extreme water levels in complex coastal systems of Aotearoa New Zealand. Frontiers in Marine Science, 10, 1–21. doi: 10.3389/fmars.2023.1170756.

Costa, W.L.L., Silveira, L.F., and Klein, A.H.F. (2019). Influence of wave climate and tidal regime on Headland Bypassing - study case: northern São Francisco Do Sul Island, SC, Brazil. Coastal Sediments 2019, 488-501. doi:10.1142/9789811204487_0044.

Dangendorf, S., Calafat, F. M., Arns, A., Wahl, T., Haigh, I. D., and Jensen, J. (2014), Mean sea level variability in the North Sea: Processes and implications, Journal of Geophysical Research: Oceans, 119, 6820–6841. doi: 10.1002/2014JC009901

d'Anna, M., Castelle, B., Idier, D., Rohmer, J., Le Cozannet, G., Thieblemont, R., & Bricheno, L. (2021). Uncertainties in shoreline projections to 2100 at Truc Vert beach (France): Role of

sea-level rise and equilibrium model assumptions. Journal of Geophysical Research: Earth Surface, 126, e2021JF006160, 1–26. doi: 10.1029/2021JF006160

de Lange, W., Gibb, J. (2000). Seasonal, interannual, and decadal variability of storm surges at Tauranga, New Zealand. New Zealand Journal of Marine Freshwater Research, 34, 419–434. doi: 10.1080/00288330.2000.9516945.

Dietrich, J.C., Bunya, S., Westerink, J.J., Ebersole, B.A., Smith, J.M., Atkinson, J.H., et al. (2010). A high resolution coupled riverine flow, tide, wind, wind wave and storm surge model for southern Louisiana and Mississippi: part II — synoptic description and analyses of Hurricanes Katrina and Rita. Monthly Weather Review, 138, 378–404. doi: 10.1175/2009MWR2906.1

Ding, Y., Ding, T., Rusdin, A., Zhang,Y., & Jia, Y. (2020). Simulation and prediction of storm surges and waves using a fully integrated process model and a parametric cyclonic wind model. Journal of Geophysical Research: Oceans, 125, 1–35. doi: 10.1029/2019JC015793

Dixon, M.J., and Tawn, J.A. (1994). Extreme Sea-levels at the UK A-class Sites: Site–by-site Analysis. POL Internal Document no 65. Available at: http://www.pol.ac.uk/ntslf/pdf/id65.pdf.

Dodet, G., Melet, A., Ardhuin, F., Bertin, X., Idier, D., Almar, R. (2019). The Contribution of Wind-Generated Waves to Coastal Sea-Level Changes. Surveys in Geophysics, 40, 1563–1601. doi: 10.1007/s10712-019-09557-5

Donchyts, G., Schellekens, J., Winsemius, H., Eisemann, E., and van de Giesen, N. (2016). A 30 m resolution surfacewater mask including estimation of positional and thematic differences using landsat 8, SRTM and OPenStreetMap: A case study in the Murray-Darling basin, Australia, Remote Sens., 8, 5, 386, 1–22. doi: 10.3390/rs8050386.

Doodson, A.T. (1929). Report on Thames floods. Geophysical Memoirs London, 47, 1–26. Available at: https://searchworks.stanford.edu/view/133937

Du, J., Shen, J., Zhang, Y. J., Ye, F., Liu, Z., Wang, Z., et al. (2018). Tidal response to Sea-level rise in different types of estuaries: the importance of length, bathymetry, and geometry. Geophysical Research Letters, 45, 227–235. doi: 10.1002/2017GL075963

Durante, F., & Sempi, C. (2015). Principles of Copula Theory (1st ed.). Chapman and Hall/CRC, New York, 332 p. doi: 10.1201/b18674

Ehses, J. S. and Rooney, J. J. (2015). Depth Derivation Using Multispectral WorldView-2 Satellite Imagery, NOAA Technical Memoir, NMFS-PIFSC-46, 24. doi: 10.7289/V5668B40.

Emanuel, K. (2005). Increasing destructiveness of tropical cyclones over the past 30 years. Nature, 436, 686–688. doi: 10.1038/nature03906.

Falcão, A. P., Mazzolari, A., Gonçalves, A. B., Araújo, M. A. V. C., and Trigo-Teixeira, A. (2013). Influence of elevation modelling on hydrodynamic simulations of a tidally- dominated estuary. Journal of Hydrology, 497, 152–164. doi: 10.1016/j.jhydrol.2013.05.045.

Fernández-Montblanc, T., Vousdoukas, M.I., Ciavola, P., Voukouvalas, E., Mentaschi, L., Breyiannis, G., Feyen, L., Salamon, P. (2019). Towards robust pan-European storm surge forecasting. Ocean Modelling, 133, 129-144. doi: 10.1016/j.ocemod.2018.12.001.

Ferreira Ó. (2005). Storm groups versus extreme single storms: predicted erosion and management consequences. Journal of Coastal Research, 42, 221–227. Available at: https://www.jstor.org/stable/25736987

Fitton, J. M., Rennie, A. F., Hansom, J. D., and Muir, F. M. E. (2021). Remotely sensed mapping of the intertidal zone: A Sentinel-2 and Google Earth Engine methodology. Remote Sensing Applications: Society and Environment, 22, 100499. doi: 10.1016/j.rsase.2021.100499.

Flather, R. A. (2001). "Storm surges", in Encyclopedia of Ocean Sciences, ed. Steele, J. H., Thorpe, S. A., and Turekian, K. K. (Academic Press: San Diego, California), 2882–2892. doi: 10.1006/rwos.2001.0124.

French, J., Mawdsley, R., Fujiyama, T., and Achuthan, K. (2017). Combining machine learning with computational hydrodynamics for prediction of tidal surge inundation at estuarine ports. Procedia IUTAM, 25, 28–35. doi: 10.1016/j.piutam.2017.09.005

Gallop, S. L., Concejo, A. V., Fellowes, T. E., Harley, M. D., and Laurier, J. L. (2020). Wave direction shift triggered severe erosion of beaches in estuaries and bays with limited post-storm recovery. 3868, 3854–3868. doi 10.1002/esp.5005.

Gesch Dean B. (2018). Best Practices for Elevation-Based Assessments of Sea-Level Rise and Coastal Flooding Exposure. Frontiers in Earth Science, 6, 1–18. doi:10.3389/feart.2018.00230

Geyman, E. C. and Maloof, A. C. (2019). A simple method for extracting water depth from multispectral satellite imagery in regions of variable bottom type. Earth and Space Science, 6, 527–537. doi: 10.1029/2018EA000539.

Godoi V.A., Bryan K.R., Gorman R.M. (2018) Storm wave clustering around New Zealand and its connection to climatic patterns. International Journal of Climatology, 38, 401–417. doi: 10. 1002/joc. 5380

Godoi, V. A., Bryan, K. R., Stephens, S. A., and Gorman, R. M. (2017). Extreme waves in New Zealand waters. Ocean Model. 117, 97–110. doi: 10.1016/j.ocemod.2017.08.004.

Godoi, V.A., Bryan, K.R., and Gorman, R.M. (2016). Journal of Geophysical Research : Oceans. Regional influence of climate patterns on the wave climate of the southwestern Pacific: The New Zealand region. Journal Geophysical Research: Oceans, 121, 4056–4076. doi: 10.1002/2015JC011572.

Gorelick, N., Hancher, M., Dixon, M., Ilyushchenko, S., Thau, D., Moore, R. (2017). Google Earth engine: planetary-scale geospatial analysis for everyone. Remote Sensing of Environment, 202, 18–27. doi: 10.1016/j.rse.2017.06.031.

Gori, A., Lin, N., & Smith, J. (2020a). Assessing compound flooding from landfalling tropical cyclones on the North Carolina coast. Water Resources Research, 56, 1–21. doi: 10.1029/2019WR026788

Gori, A., Lin, N., and Xi, D. (2020b). Tropical cyclone compound flood hazard assessment: From investigating drivers to quantifying extreme water levels. Earth's Future, 8, 1–18. doi: 10.1029/2020EF001660

Guillou, N. and Chapalain, G. (2021). Machine learning methods applied to sea level predictions in the upper part of a tidal estuary. Oceanologia, 63, 4, 531–544. doi: 10.1016/j.oceano.2021.07.003.

Ha, N. T., Manley-Harris, M., Pham, T. D., and Hawes, I. (2020). A comparative assessment of ensemble-based machine learning and maximum likelihood methods for mapping seagrass using sentinel-2 imagery in Tauranga Harbor, New Zealand, Remote Sensing, 12, 3, 355, 1–16. doi: 10.3390/rs12030355.

Haigh, I. D., Pickering, M. D., Green, J. A. M., Arbic, B. K., Arns, A., Dangendorf, S., et al. (2019). The tides they are a-changin': A comprehensive review of past and future nonastronomical changes in tides, their driving mechanisms and future implications. Reviews of Geophysics, 57, 1–39. doi: 10.1029/2018RG000636

Haigh, I., Nicholls, R., Wells, N. (2010). Assessing changes in extreme sea levels: application to the English Channel, 1900-2006. Continental Shelf Research, 9, 1042–1055. doi: 10.1016/J.CSR.2010.02.002.

Haigh, I.D., Wadey, M.P., Wahl, T., et al. (2016) Spatial and temporal analysis of extreme sea level and storm surge events around the coastline of the UK. Scientific Data, 3, 160107, 1–14. doi: 10. 1038/ sdata. 2016.107

Hallegatte, S., Green, C., Nicholls, R. J., and Corfee-morlot, J. (2013). Future flood losses in major coastal cities. Nature Climate Change, 3, 802–806. doi: 10.1038/nclimate1979.

Hare, R.; Eakins, B.W.; Amante, C.J. (2011). Modelling bathymetric uncertainty. The International Hydrographic Review, 6, 455–462. Available at: https://journals.lib.unb.ca/index.php/ihr/article/view/20888

Heath, R.A., 1979. Significance of storm surges on the New Zealand coast. New Zealand Journal of Geology and Geophysics, 22, 259–266. doi: 10.1080/00288306.1979.10424224.

Hedley, J. D., Harborne, A. R., and Mumby, P. J. (2005). Simple and robust removal of sun glint for mapping shallow-water benthos. International Journal of Remote Sensing, 26, 2107–2112. doi: 10.1080/01431160500034086.

Heimhuber, V., Vos, K., Fu, W., Glamore, W. (2021). InletTracker: An open-source Python toolkit for historic and near real-time monitoring of coastal inlets from Landsat and Sentinel-2. Geomorphology, 389, 107830, 1–19. doi: 10.1016/j.geomorph.2021.107830.

Hinkel, J., Lincke, D., Vafeidis, A. T., Perrette, M., Nicholls, R. J., Tol, R. S. J., Marzeion, B., Fettweis, X., Ionescu, C., and Levermann, A. (2014). Coastal flood damage and adaptation costs under 21st century sea-level rise, Proceedings of National Academy of Science USA, 111, 3292–3297. doi: 10.1073/pnas.1222469111

Holthuijsen, L.H. (2007). Waves in Oceanic and Coastal Waters. Cambridge: Cambridge University Press. ISBN 978-0521860284.

Horsburgh, K.J., and Wilson, C. (2007). Tide-surge interaction and its role in the distribution of surge residuals in the North Sea. J. Geophys. Res. 112, C08003. doi: 10.1029/2006JC004033.

Horstman, E. M., Lundquist, C. J., Bryan, K. R., Bulmer, R. H., Mullarney, J. C., and Stokes, D. J. (2018). "The Dynamics of Expanding Mangroves in New Zealand," in Threats to Mangrove Forests. Coastal Research Library, 25, 23–51, eds C. Makowski and C. Finkl (Cham: Springer). doi: 10.1007/978-3-319-73016-5_2

Huisman, C. E., Bryan, K.R., Coco, G., and Ruessink, B. G. (2011). The use of video imagery to analyse groundwater and shoreline dynamics on a dissipative beach. Continental Shelf Research, 31, 1728–1738. doi: 10.1016/J.CSR.2011.07.013.

Hume, T., Gerbeaux, P., Hart, D., Kettles, H., Neale, D. (2016). A classification of New Zealand's coastal hydrosystems. Prepared for Ministry of the Environment. October (NIWA Client Report No: HAM2016-062). NIWA. New Zealand. Available at: https://environment.govt.nz/publications/a-classification-of-new-zealands-coastal-hydrosystems/.

Hume, T., Snelder, T., Weatherhead, M., and Liefting, R. (2007). A controlling factor approach to estuary classification. Ocean & Coastal Management, 50, 905–929. doi: 10.1016/j.ocecoaman.2007.05.009.

Idier, D., Dumas, F., and Muller, H. (2012). Tide-surge interaction in the English channel. Natural Hazards Earth System Science, 12, 3709–3718. doi: 10.5194/nhess-12-3709-2012

Idier, D., Paris, F., Le Cozannet, G., Boulahya, F., Dumas, F. (2017). Sea-level rise impacts on the tides of the European Shelf. Continental Shelf Research, 137, 56–71. doi: 10.1016/j.csr.2017.01.007.

International Hydrographic Organization (2020). IHO C-55 Publication Status of Hydrographic Surveying and Charting Worldwide, Monaco. Available at: https://iho.int/uploads/user/pubs/cb/c-55/c55.pdf

Jafarzadegan, K., Moradkhani, H., Pappenberger, F., Moftakhari, H., Bates, P., Abbaszadeh, P., Marsooli, R., Ferreira, C., Cloke, H.L., Ogden, F, and Duan Q. (2023). Recent advances

and new frontiers in riverine and coastal flood modeling. Reviews of Geophysics, 61, e2022RG000788, 1–52. doi: 10.1029/2022RG000788

Jane, R., Wahl, T., Santos, V. M., Misra, S. K., White, K. D. (2022). Assessing the Potential for Compound Storm Surge and Extreme River Discharge Events at the Catchment Scale with Statistical Models: Sensitivity Analysis and Recommendations for Best Practice. Journal of Hydrologic Engineering, 27, 3, 1–16. doi: 10.1061/(asce)he.1943-5584.0002154.

Jawak, S. D., Vadlamani, S. S., and Luis, A. J. (2015). A Synoptic Review on Deriving Bathymetry Information Using Remote Sensing Technologies: Models, Methods and Comparisons. Advances in Remote Sensing, 4, 147–162. doi: 10.4236/ars.2015.42013.

Jenkins, L. J., Haigh, I. D., Camus, P., and Pender, D. (2023). The temporal clustering of storm surge, wave height, and high sea level exceedances around the UK coastline. Natural Hazards, 115, 1761–1797. doi: 10.1007/s11069-022-05617-z.

Kagan, B.A., Sofina, E.V., and Rashidi, E. (2012). The impact of the spatial variability in bottom roughness on tidal dynamics and energetics, a case study: the M2 surface tide in the North European Basin. Ocean Dynamics, 62, 1425–1442. doi: 10.1007/s10236-012-0571-3.

Kang, Y., Ding, X., Xu, F., Zhang, C., and Ge, X. (2017). Topographic mapping on large-scale tidal flats with an iterative approach on the waterline method. Estuarine Coastal and Shelf Science, 190, 11–22. doi: 10.1016/j.ecss.2017.03.024.

Kang, Y., Lv, W., He, J., and Ding, X. (2020). Remote sensing of time-varying tidal flat topography, Jiangsu Coast, China, based on the waterline method and an artificial neural network model. Applied Sciences,10, 10, 3645, 1–17. doi: 10.3390/app10103645

Karim, M. F. and Mimura, N. (2008). Impacts of climate change and sea-level rise on cyclonic storm surge floods in Bangladesh. Global Environmental Change, 18, 3, 490–500. doi: 10.1016/j.gloenvcha.2008.05.002.

Karunarathna, H., Pender, D., Ranasinghe, R., Short, A.D., Reeve, D.E. (2014). The effects of storm clustering on beach profile variability. Marine Geology, 348, 103–112. doi:10.1016/j.margeo.2013.12.007.

Kashinath, K., Mustafa, M., Albert, A., Wu, J.-L., Jiang, C., Esmaeilzadeh, S., Aziz-zadenesheli, K., Wang, R., Chattopadhyay, A., Singh, A., Manepalli, A., Chirila, D., Yu, R., Walters, R., White, B., Xiao, H., Tchelepi, H.A., Marcus, P., Anandkumar, A., Hassanzadeh, P., Prabhat, n., (2021). Physics-informed machine learning: case studies for weather and climate modelling. Phil. Trans. R. Soc. A 379, 1–36. doi: 10.1098/rsta.2020.0093.

Kendall, M. G. (1938). A new measure of rank correlation. Biometrika, 30, 1–2, 81–93. doi:10.1093/biomet/30.1-2.81.

Kennedy, A.B., Gravois, U., Zachry, B.C., Westerink, J.J., Hope, M.E., Dietrich, J.C., Powell, M.D., Cox, A.T., Luettich Jr., R.A., Dean, R.G. (2011). Origin of the Hurricane Ike forerunner surge. Geophysical Research Letter 28, 1–5. doi:10.1029/2011GL047090

Kerr, J. M. and Purkis, S. (2018). An algorithm for optically-deriving water depth from multispectral imagery in coral reef landscapes in the absence of ground-truth data, Remote Sensing of Environment, 210, 307–324. doi: 10.1016/j.rse.2018.03.024.

Khan, M. J. U., Ansary, M. N., Durand, F., Testut, L., Ishaque, M., Calmant, S., Krien, Y., Saifu, A. K. M., and Papa, F. (2019). High-resolution intertidal topography from sentinel-2 multi-spectral imagery: Synergy between remote sensing and numerical modeling. Remote Sensing, 11, 1–20. doi: 10.3390/rs11242888.

Khan, M. J. U., Durand, F., Bertin, X., Testut, L., Krien, Y., Islam, A. K. M. S., et al. (2021). Towards an efficient storm surge and inundation forecasting system over the Bengal delta: Chasing the Supercyclone Amphan. Nat. Hazards Earth Syst. Sci. 21, 2523–2541. doi: 10.5194/nhess-21-2523-2021.

Khojasteh, D., Glamore, W., Heimhuber, V., Felder, S. (2021). Sea level rise impacts on estuarine dynamics: A review. Science of The Total Environment, 780, 146470, 1–16. doi: 10.1016/j.scitotenv.2021.146470.

Khojasteh, D., Hottinger, S., Felder, S., De Cesare, G., Heimhuber, V., Hanslow, D. J., et al. (2020). Estuarine tidal response to sea level rise: the significance of entrance restriction. Estuarine Coastal Shelf Science, 244, 106941, 1–11. doi: 10.1016/j.ecss.2020.106941

Kidson, J.W. (2000). An analysis of New Zealand synoptic types and their use in defining weather regimes. International Journal of Climatology, 20, 299–316. doi: 10.1002/(SICI)1097-0088(20000315)20:3<299::AID-JOC474>3.0.CO;2-B.

Kirezci, E., Young, I.R., Ranasinghe, R. et al (2020). Projections of global-scale extreme sea levels and resulting episodic coastal flooding over the 21st Century. Scientific Reports, 10, 11629, 1–12. doi: 10.1038/s41598-020-67736-6

Kumbier, K., Carvalho, R.C., Vafeidis, A.T., and Woodroffe, C.D. (2018). Investigating compound flooding in an estuary using hydrodynamic modelling: A case study from the Shoalhaven River, Australia. Nat. Hazards Earth Syst. Sci. 18, 463–477. doi: 10.5194/nhess-18-463-2018.

Kyprioti, A. P., Irwin, C., Taflanidis A. A., Nadal-Caraballo, N. C., Yawn, M. C., Aucoin, L. A. (2023). Spatio-temporal storm surge emulation using Gaussian Process techniques. Coastal Engineering, 180, 104231, 1–23. doi: 10.1016/j.coastaleng.2022.104231

Lee, Z., Carder, K. L., Mobley, C. D., Steward, R. G., and Patch, J. S. (1998). Hyperspectral remote sensing for shallow waters I A semianalytical model. Applied Optics, 37,27, 6329–6338. doi: 10.1364/ao.37.006329.

Li, F. K. and Goldstein, R. M. (1990). Studies of Multibaseline Spaceborne Interferometric Synthetic Aperture Radars. IEEE Transactions on Geosciences and Remote Sensing, 28, 1, 88–97. doi: 10.1109/36.45749.

Liu, W.C., Huang, W.C., Chen, W.B. (2016). Modeling the interaction between tides and storm surges for the Taiwan coast. Environmental Fluid Mechanics, 16, 721. doi: 10.1007/s10652-015-9441-0.

Liu, Y., Li, M., Zhou, M., Yang, K., and Mao, L. (2013). Quantitative analysis of the waterline method for topographical mapping of tidal flats: A case study in the Dongsha Sandbank, China. Remote Sensing, 5, 6138–6158. doi: 10.3390/rs5116138

Longuet-Higgins, M.S., and Stewart, R.W. (1964). Radiation stresses in water waves; a physical discussion, with applications, Deep Sea Research and Oceanographic Abstracts, 11, 4, 529–562. doi: 10.1016/0011-7471(64)90001-4.

Lorensen, W. E. and Cline, H. E. (1987). Marching cubes: A high resolution 3D surface construction algorithm. Proceedings of the 14th Annual Conference on Computational Graphics and Interactive Technologies, 21, 163–169. doi: 10.1145/37401.37422.

Luijendijk, A., Hagenaars, G., Ranasinghe, R., et al. (2018). The State of the World's Beaches. Scientific Reports, 8, 6641, 1–11. doi: 10.1038/s41598-018-24630-6

Lyzenga, D. R. (1985). Shallow-water bathymetry using combined lidar and passive multispectral scanner data. International Journal of Remote Sensing, 6, 115–125. doi: 10.1080/01431168508948428

Marcos, M., Rohmer, J., Vousdoukas, M. I., Mentaschi, L., Le Cozannet, G., and Amores, A. (2019). Increased extreme coastal water levels due to the combined action of storm surges and wind waves. Geophysical Research Letters, 46, 4356–4364. doi: 10.1029/2019GL082599

Mason, D. C. and Davenport, L. J. (1996). Accurate and efficient determination of the shoreline in ERS-1 SAR images. IEEE Transactions on Geosciences and Remote Sensing, 34, 1243–1253. doi: 10.1109/36.536540.

Mason, D. C., Scott, T. R., and Dance, S. L. (2010). Remote sensing of intertidal morphological change in Morecambe Bay, U.K., between 1991 and 2007. Estuarine, Coastal and Shelf Sciences, 87, 487–496. doi: 10.1016/j.ecss.2010.01.015.

Mawdsley, R. J., and Haigh, I. D. (2016). Spatial and temporal variability and long-term trends in skew surges globally. Frontiers of Marine Science, 3, 1–17. doi: 10.3389/fmars.2016.00029.

McFeeters, S. K. (1996). The use of the Normalized Difference Water Index (NDWI) in the delineation of open water features. International Journal of Remote Sensing, 17, 1425–1432. doi:10.1080/01431169608948714.

Ministry for the Environment (2022). Aotearoa New Zealand's first national adaptation plan. Wellington. Ministry for the Environment. 196 p. ISBN: 978-1-99-102549-4. Available at: https://environment.govt.nz/

Moftakhari, H., Schubert, J. E., AghaKouchak, A., Matthew, R. A., & Sanders, B. F. (2019). Linking statistical and hydrodynamic modeling for compound flood hazard assessment in tidal channels and estuaries. Advances in Water Resources, 128, 28–38. doi: 10.1016/j.advwatres.2019.04.009

Mohammadian, A., Morse, B., and Robert, J. L. (2022). Calibration of a 3D hydrodynamic model for a hypertidal estuary with complex irregular bathymetry using adaptive parametrization of bottom roughness and eddy viscosity. Estuarine, Coastal and Shelf Sciences, 265, 107655, 1–17. doi: 10.1016/j.ecss.2021.107655.

Montgomery, J.M., Bryan, K.R., Mullarney, J.C. and Horstman, E.M. (2019). Attenuation of storms by coastal mangroves. Journal of Geophysical Research Letters, 46, 5, 2680-2689. doi:10.1029/2018GL081636

Morim, J., Hemer, M., Wang, X.L. et al (2019). Robustness and uncertainties in global multivariate wind-wave climate projections. Nature Climate Changes, 9, 711–718. doi: 10.1038/s41558-019-0542-5

Morris, A. B. D., Coco, G., Bryan, K. R., Turner, I. L., Street, K., and Vale, M. (2007). Video-derived mapping of estuarine evolution. Journal of Coastal Research, Proceedings of the 9th International Coastal Symposium, 50, 410–414. Available at: https://www.jstor.org/stable/26481623, date of last access: 18/09/2023. ISSN 0749.0208.

Murray, N. J., Phinn, S. R., DeWitt, M., Ferrari, R., Johnston, R., Lyons, M. B., Clinton, N., Thau, D., & Fuller, R. A. (2019). The global distribution and trajectory of tidal flats. Nature, 565, 222–225. doi: 10.1038/s41586-018-0805-8

Naderi A., and Siadatmousavi S.M. (2023). Extreme value analysis for waves in the Persian Gulf: Skill assessment of different methods for a fetch-limited basin. Regional Studies in Marine Science, 59, 102812, 1–11. doi: 10.1016/j.rsma.2023.102812.

Nasr, A. A., Wahl, T., Rashid, M. M., Camus, P., & Haigh, I. D. (2021). Assessing the dependence structure between oceanographic, fluvial, and pluvial flooding drivers along the United States coastline. Hydrology Earth System Sciences, 25, 6203–6222. doi: 10.5194/hess-25-6203-2021

Nerem, R.S., Beckley, B.D., Fasullo, J.T., Hamlington, BD, Masters, D, Mitchum, G.T. (2018). Climate-change-driven accelerated sea-level rise detected in the altimeter era. Proceedings of the National Academy of Science U S A., 115, 2022–2025. doi: 10.1073/pnas.1717312115.

Nicholls, R. J. and Cazenave. A. (2010). Sea-level rise and its impact on coastal zones. Science, 328, 1517–1520. doi:10.1126/science.1185782.

Nihoul, J.C.J. (1977). Three-dimensional model of tides and storm surges in a shallow well-mixed continental sea. Dynamics of Atmosphere and Oceans, 2, 29–47. doi: 10.1016/0377-0265(77)90014-8.

Oppenheimer, M., B.C. Glavovic , J. Hinkel, R. van de Wal, A.K. Magnan, A. Abd-Elgawad, R. Cai, M. Cifuentes-Jara, R.M. De Conto, T. Ghosh, J. Hay, F. Isla, B. Marzeion, B. Meyssignac, and Z. Sebesvari, (2019). "Sea Level Rise and Implications for Low-Lying Islands, Coasts and Communities" in IPCC Special Report on the Ocean and Cryosphere in a Changing Climate, eds. H.-O. Pörtner, D.C. Roberts, V. Masson-Delmotte, P. Zhai, M. Tignor, E. Poloczanska, K. Mintenbeck, A. Alegría, M. Nicolai, A. Okem, J. Petzold, B. Rama, N.M. Weyer (Cambridge, UK and New York, NY, USA: Cambridge University Press), 321-445. doi:10.1017/9781009157964.006.

Orton, P., Georgas, N., Blumberg, A., Pullen, J. (2012). Detailed modeling of recent severe storm tides in estuaries of the New York City region, Journal of Geophysical Research: Oceans, 117, C09030, 1–17. doi:10.1029/2012jc008220.

Orton, P.M., Conticello, F.R., Cioffi, F., Hall, T.M., Georgas, N., Lall, U., et al. (2020). Flood hazard assessment from storm tides, rain and sea level rise for a tidal river estuary. Nat. Hazards 102, 729–757. doi: 10.1007/s11069-018-3251-x.

Otsu, N. (1979). A Threshold Selection Method from Gray-Level Histograms. IEEE Transactions on Systems, Man, and Cybernetics, 9, 1, 62–66. doi: 10.1109/TSMC.1979.4310076

Park, Y.H., and Suh, K. (2012). Variations of storm surge caused by shallow water depths and extreme tidal ranges. Ocean Engineering, 55, 44–51. doi: 10.1016/ j.oceaneng.2012.07.032.

Parodi, M. U., Giardino, A., Van Dongeren, A., Pearson, S. G., Bricker, J. D., and Reniers, A. J. H. M. (2020). Uncertainties in coastal flood risk assessments in small island developing states. Natural Hazards and Earth System Sciences, 20, 2397–2414, doi: 10.5194/nhess-20-2397-2020.

Paulik, R., Stephens, S. A., Bell, R. G., Wadhwa, S., and Popovich, B. (2020). National-Scale Built-Environment Exposure to 100-Year Extreme Sea Levels and Sea-Level Rise. Sustainability 12, 1–16. doi: 10.3390/su12041513

Pedrozo-Acuña, A., Ruiz de Alegria-Arzaburu, A., Mariño-Tapia, I., Enriquez, C., and González Villareal, F. J. (2012). Factors controlling flooding at the Tonalá river mouth (Mexico). Journal of Flood Risk Management, 5, 226–244. doi: 10.1111/j.1753-318X.2012.01142.x.

Pereira-Sandoval, M., Ruescas, A., Urrego, P., Ruiz-Verdú, A., Delegido, J., Tenjo, C., Soria-Perpinyà, X., Vicente, E., Soria, J., Moreno, J. (2019). Evaluation of Atmospheric Correction Algorithms over Spanish Inland Waters for Sentinel-2 Multi Spectral Imagery Data. Remote Sens., 11,12,1469. doi: 10.3390/rs11121469.

Plüß, A., Rudolph, E., Schrodter, D. (2001). Characteristics of storm surges in German estuaries. Climate Research, 18, 71–76. doi: 10.3354/cr018071.

Proudman, J. (1955a). The effect of friction on a progressive wave of tide and surge in an estuary. Proc. R. Soc Lond. A 233, 407–418.

Proudman, J. (1955b). The propagation of tide and surge in an estuary. Proc. R. Soc Lond. A. 231, 8–24.

Pugh, D. (1987). Tides, Surges and Mean Sea Level: A Handbook for Engineers and Scientists. John Wiley & Sons, Chichester, 472 p.

Pugh, D., and Woodworth, P. (2014). Sea-level Science: Understanding Tides, Surges, Tsunamis and Mean Sea-level Changes. Cambridge: Cambridge University Press.

Rahbani, M., Vila-concejo, A., Fellowes, T. E., Gallop, S. L., Winkler-prins, L., and Largier, J. L. (2022). Geomorphology Spatial patterns in wave signatures on beaches in estuaries and bays. Geomorphology, 398, 108070, 1–12. doi: 10.1016/j.geomorph.2021.108070.

Ralston, D. K., Talke, S., Geyer, W. R., Al-Zubaidi, H. A. M., & Sommerfield, C. K. (2019). Bigger tides, less flooding: Effects of dredging on barotropic dynamics in a highly modified estuary. Journal of Geophysical Research: Oceans, 124, 196–211. doi: 10.1029/2018JC014313

Rascle, N., and Ardhuin, F. (2013). A global wave parameter database for geophysical applications. Part 2 : Model validation with improved source term parameterisation. Ocean Model. 70, 174–188. doi: 10.1016/j.ocemod.2012.12.001.

Rego, J. L., and Li, C. (2010). Storm surge propagation in Galveston bay during hurricane Ike. Journal of Marine Systems, 82, 265–279. doi: 10.1016/j.jmarsys.2010.06.001

Rossiter, J. R. (1961). Interaction between tide and surge in the Thames. Geophysical Journal of the Royal Astronomical Society, 6, 29–53. doi: 10.1111/j.1365-246X.1961.tb02960.x

Rueda, A., Cagigal, L., Antolínez, J.A.A., Albuquerque, J.C., Castanedo, S., Coco, G., Méndez, F.J. (2019). Marine climate variability based on weather patterns for a complicated island setting: The New Zealand case. International Journal of Climatology, 39, 1777–1786. doi: 10.1002/joc.5912.

Sagar, S., Roberts, D., Bala, B., and Lymburner, L. (2017). Extracting the intertidal extent and topography of the Australian coastline from a 28-year time series of Landsat observations. Remote Sensing of Environment, 195, 153–169. doi: 10.1016/j.rse.2017.04.009.

Saintilan, N., Khan, N., Ashe, E., Kelleway, J., Rogers, K., Woodroffe, C.D., et al. (2020). Thresholds of mangrove survival under rapid sea level rise. Science, 368, 1118–1121. doi: 10.1126/science.aba2656

Salameh, E., Frappart, F., Almar, R., Baptista, P., Heygster, G., Lubac, B., Raucoules, D., Almeida, L. P., Bergsma, E. W. J., Capo, S., De Michele, M. D., Idier, D., Li, Z., Marieu, V., Poupardin, A., Silva, P. A., Turki, I., and Laignel, B. (2019). Monitoring Beach Topography and Nearshore Bathymetry Using Spaceborne Remote Sensing: A Review. Remote Sensing, 11, 19, 2212, 1–32. doi:10.3390/rs11192212.

Salameh, E., Frappart, F., Marieu, V., Spodar, A., Parisot, J. P., Hanquiez, V., Turki, I., and Laignel, B. (2018). Monitoring sea level and topography of coastal lagoons using satellite radar altimetry: The example of the Arcachon Bay in the Bay of Biscay. Remote Sensing, 10, 1–22. doi:10.3390/rs10020297.

Salameh, E., Frappart, F., Turki, I., and Laignel, B.: Intertidal topography mapping using the waterline method from Sentinel-1 & -2 images (2020). The examples of Arcachon and Veys Bays in France, ISPRS Journal of Photogrammetry and Remote Sensing, 163, 98–120. doi: 10.1016/j.isprsjprs.2020.03.003

Salvadori, G., and De Michele, C. (2007). On the use of copulas in hydrology: Theory and practice. Journal of Hydrologic Engineering, 12, 369–380. doi: 10.1061/(ASCE)1084-0699(2007)12:4(369)

Salvadori, G., Durante, F., Tomasicchio, G. R., & D'Alessandro, F. (2015). Practical guidelines for the multivariate assessment of the structural risk in coastal and off-shore engineering. Coastal Engineering, 95, 77–83. doi: 10.1016/j.coastaleng.2014.09.007

Santamaria-Aguilar, S., and Vafeidis, A.T. (2018). Are Extreme Skew Surges Independent of High Water Levels in a Mixed Semidiurnal Tidal Regime? Journal of Geophysical Research: Oceans, 123, 8877–8886. doi: 10.1029/2018JC014282.

Santiago-Collazo, F. L., Bilskie, M. V., & Hagen, S. C. (2019). A comprehensive review of compound inundation models in low-gradient coastal watersheds. Environmental Modelling & Software, 119, 166–181. doi: 10.1016/j.envsoft.2019.06.002

Santos, V.M., Haigh, I.D., and Wahl, T. (2017). Spatial and Temporal Clustering Analysis of Extreme Wave Events around the UK Coastline. doi: 10.3390/jmse5030028.

Santos, V.M., Wahl, T., Jane, R., Misra, S.K., White, K.D. (2021). Assessing compound flooding potential with multivariate statistical models in a complex estuarine system under data constraints. Journal of Flood Risk Management, 14, 1–16. doi: 10.1111/jfr3.12749.

Scarrott C., and MacDonald A. (2012). A review of extreme value threshold estimation and uncertainty quantification. REVSTAT Statistical Journal, 10, 1, 33 – 60. doi: 10.57805/revstat.v10i1.110.

Schumann Guy J-P., Bates Paul D. (2018). The Need for a High-Accuracy, Open-Access Global DEM. Frontiers in Earth Science, 6, 1–5. doi: 10.3389/feart.2018.00225

Schwanenberg, D., Natschke, M., Todini, E., & Reggiani, P. (2018). Scientific, technical and institutional challenges towards next-generation operational flood risk management decision support systems. International Journal of River Basin Management, 16, 345–352. doi: 10.1080/15715124.2017.1411924

Senechal, N., Castelle, B., Bryan, K.R. (2017). “Storm clustering and beach response” in Coastal Storms: Processes and Impacts. Wiley-Blackwell: New York, NY.

Serafin, K. A., Ruggiero, P., & Stockdon, H. F. (2017). The relative contribution of waves, tides, and non-tidal residuals to extreme total water levels on US West Coast sandy beaches. Geophysical Research Letters, 44, 1839–1847. doi: 10.1002/2016GL071020

Shen, J., Gong, W., (2009). Influence of model domain size, wind directions and Ekman transport on storm surge development inside the Chesapeake Bay: a case study of extratropical cyclone Ernesto. Journal of Marine Systems 75, 198–215. doi:10.1016/j.jmarsys.2008.09.001

Sheng Y. P., Paramygin, V.A., Yang, K., Rivera-Nieves, A. A. (2022). A sensitivity study of rising compound coastal inundation over large flood plains in a changing climate. Scientific Reports, 12, 1–14. https://doi.org/10.1038/s41598-022-07010-z

Sheng, Y. P., Alymov, V., and Paramygin, V. A. (2010), Simulation of storm surge, wave, currents, and inundation in the Outer Banks and Chesapeake Bay during Hurricane Isabel in 2003: The importance of waves. Journal of Geophysical Research, 115, 1–27. doi:10.1029/2009JC005402.

Shope, J. B., Erikson, L. H., Barnard, P. L., Storlazzi, C. D., Serafin, K., Doran, K., et al. (2022). Characterizing storm-induced coastal change hazards along the United States West Coast. Scientific Data, 9, 1–20. doi: 10.1038/s41597-022-01313-6

Smith, M. J., Stevens, C. L., Gorman, R. M., McGregor, J. A., and Neilson, C. G. (2001). Wind-wave development across a large shallow intertidal estuary: a case study of Manukau Harbour, New Zealand. New Zealand Journal of Marine Freshwater Research, 35, 985–1000. doi: 10.1080/00288330.2001.9517058

Sobel, A. H., Camargo, S. J., Hall, T. M., Lee, C., Tippett, M. K., & Wing, A. A. (2016). Human influence on tropical cyclone intensity. Science, 353, 6296, 242–246. doi:10.1126/science.aaf6574

Speer, P. E., and Aubrey, D. G. (1985). A study of non-linear tidal propagation in shallow inlet-estuarine systems. part II: theory. Estuarine Coastal Shelf Science, 21, 207–224. doi: 10.1016/0272-7714(85)90097-6

Speer, P. E., Aubrey, D. G. (1985). A study of non-linear tidal propagation in shallow inlet-estuarine systems. Part II: Theory. Est. Coast. Shelf Sci. 21, 207-224. doi: 10.1016/0272-7714(85)90097-6

Spencer, T., Schuerch, M., Nicholls, R. J., Hinkel, J., Lincke, D., Vafeidis, A. T., Reef, R., McFadden, L., & Brown, S. (2016). Global coastal wetland change under sea-level rise and related stresses: The DIVA Wetland Change Model. Global and Planetary Change, 139, 15–30. doi: 10.1016/j.gloplacha.2015.12.018

Spicer, P., Huguenard, K., Ross, L., and Rickard, L. N. (2019). High-Frequency Tide-Surge-River Interaction in Estuaries: Causes and Implications for Coastal Flooding. Journal of Geophysical Research: Oceans, 124, 9517–9530. doi: 10.1029/2019JC015466.

Splinter, K.D., Carley, J.T., Golshani, A., Tomlinson, R. (2014). A relationship to describe the cumulative impact of storm clusters on beach erosion. Coastal Engineering 83, 49–55. doi: 10.1016/j.coastaleng.2013.10.001.

Stephens, S. A., Bell, R. G., and Haigh, I. D. (2020). Spatial and temporal analysis of extreme storm-tide and skew-surge events around the coastline of New Zealand. Natural Hazards Earth System Science, 20, 783–796. doi: 10.5194/nhess-20-783-2020

Sternberg, R.W. (1968). Friction factors in tidal channels with differing bed roughness, Marine Geology, 6, 243–260. doi: 10.1016/0025-3227(68)90033-9.

Stewart, B. (2021). Investigating groundwater derived nutrient fluxes within Tauranga harbour. Doctoral dissertation. The University of Waikato, Hamilton, Waikato, New Zealand. 180 p. Available at https://hdl.handle.net/10289/14405, date of last access: 18/09/2023, 2021.

Stumpf, R. P., Holderied, K., and Sinclair, M. (2003). Determination of water depth with high-resolution satellite imagery over variable bottom types. Limnology and Oceanography, 48, 547–556. doi:10.4319/lo.2003.48.1_part_2.0547

Svensson, C., & Jones, D. A. (2004). Dependence between sea surge, river flow and precipitation in south and west Britain. Hydrology and Earth System Sciences, 8, 973–992. doi:10.5194/hess-8-973-2004

Tadesse, M. G., and Wahl, T. (2021). A database of global storm surge reconstructions. Scientific Data, 8, 1–10. doi: 10.1038/s41597-021-00906-x.

Tadesse, M., Wahl, T., Cid, A. (2020). Data-driven modeling of global storm surges. Frontiers in Marine Science, 7, 260,1–19. doi: 10.3389/fmars.2020.00260.

Taherkhani, M., Vitousek, S., Barnard, P.L. et al. (2020). Sea-level rise exponentially increases coastal flood frequency. Scientific Reports, 10, 6466, 1–17. doi: 10.1038/s41598-020-62188-4

Talke, S. A. and Jay, D. A. (2020). Changing Tides: The Role of Natural and Anthropogenic Factors. Annual Review of Marine Science, 1, 12, 121–151. doi:10.1146/annurev-marine-010419-010727

Tang, Y.M., Grimshaw, R., Sanderson, B., Holland, G. (1996). A numerical study of storm surges and tides with application to the North Queensland coast. Journal of Physical Oceanography, 26, 2700–2711. doi:10.1175/1520-0485.

Tausía, J., Delaux, S., Camus, P., Rueda, A., Méndez, F., Bryan, K. R., et al. (2023). Rapid response data-driven reconstructions for storm surge around New Zealand. Appl. Ocean Research, 133, 103496, 1–12. doi: 10.1016/j.apor.2023.103496.

Tay, H.W., Bryan, K.R., De Lange, W.P., and Pilditch, C.A. (2013). The hydrodynamics of the southern basin of Tauranga Harbour, New Zealand Journal Marine Freshwater Research, 47, 249–274. doi: 10.1080/00288330.2013.778300.

Thompson, P. R., Mitchum, G. T., Vonesch, C., and Li, J. (2013). Variability of winter storminess in the Eastern United States during the Twentieth Century from tide gauges. Journal of Climate, 26, 9713–9726. doi: 10.1175/JCLI-D-12-00561.1

Thompson, R., and Hamon, B. V. (1980). Wave setup of harbor water levels. Journal of Geophysical Research, 85, 1151–1152. doi: 10.1029/JC085iC02p01151

Tiggeloven, T., Couasnon, A., van Straaten, C., Muis, S., Ward, P.J. (2021). Exploring deep learning capabilities for surge predictions in coastal areas. Scientific Reports, 11, 1, 17224, 1–15. doi: 10.1038/s41598-021-96674-0.

Traganos, D., Poursanidis, D., Aggarwal, B., Chrysoulakis, N., and Reinartz, P. (2018). Estimating satellite-derived bathymetry (SDB) with the Google Earth Engine and sentinel-2. Remote Sensing, 10, 6, 859, 1–18. doi: 10.3390/rs10060859.

Turner, I. L., Mitchell, D. H., Almar, R., Bergsma, E.W.J. (2021). Satellite optical imagery in Coastal Engineering. Coastal Engineering, 167, 1–8, doi: 10.1016/j.coastaleng.2021.103919.

van den Hurk, B., van Meijgaard, E., de Valk, P., van Heeringen, K.-J., & Gooijer, J. (2015). Analysis of a compounding surge and precipitation event in The Netherlands. Environmental Research Letters, 10, 3, 035001, 1–9. doi: 10.1088/1748-9326/10/3/035001

Van Der Walt, S., Schönberger, J. L., Nunez-Iglesias, J., Boulogne, F., Warner, J. D., Yager, N., Gouillart, E., and Yu, T. (2014). Scikit-image: image processing in Python. PeerJ, 453, 1–18. doi:10.7717/peerj.453.

van Rijn, L. C. (2011). Analytical and numerical analysis of tides and salinities in estuaries; part I: tidal wave propagation in convergent estuaries. Ocean Dynamics, 61, 1719–1741. doi: 10.1007/s10236-011-0453-0

Vanhellemont, Q. and Ruddick, K. (2018). Atmospheric correction of metre-scale optical satellite data for inland and coastal water applications. Remote Sensing of Environment, 216, 586–597. doi: 10.1016/j.rse.2018.07.015.

Vitousek S., Buscombe D., Vos K., Barnard P.L., Ritchie A. C., and Warrick, J.A. (2022). The future of coastal monitoring through satellite remote sensing. Cambridge Prisms: Coastal Futures, 1, 10, 1–18. doi: 10.1017/cft.2022.4

Vos, K., Splinter, K. D., Harley, M. D., Simmons, J. A., Turner, I. L. (2019). CoastSat: A Google Earth Engine-enabled Python toolkit to extract shorelines from publicly available satellite imagery, Environmental Modelling & Software, 122, 104528, 1–7. doi: 10.1016/j.envsoft.2019.104528.

Vousdoukas M.I., Almeida, L.P., Ferreira, Ó. (2011). Modelling storm-induced beach morphological change in a meso-tidal, reflective beach using XBeach. Journal of Coastal Research, SI64, 1916–1920. Available at: https://www.jstor.org/stable/26482510

Vousdoukas, M. I., Voukouvalas, E., Annunziato, A., Giardino, A., Feyen, L. (2016). Projections of extreme storm surge levels along Europe. Climate Dynamics, 47, 3171–3190. doi: 10.1007/s00382-016-3019-5

Wahl, T., Jain, S., Bender, J., Meyers, S. D., & Luther, M. E. (2015). Increasing risk of compound flooding from storm surge and rainfall for major US cities. Nature Climate Change, 5, 12, 1093–1097. doi: 10.1038/nclimate2736

Wahl, T., Plant, N. G., & Long, J. W. (2016). Probabilistic assessment of erosion and flooding risk in the northern Gulf of Mexico. Journal of Geophysical Research: Oceans, 121, 5, 3029–3043. doi: 10.1002/2015JC011482

Wankang, Y., Baoshu, Y., Xingru, F., Dezhou, Y., Guandong, G., and Haiying, C. (2019). The effect of nonlinear factors on tide-surge interaction: a case study of Typhoon Rammasun in Tieshan Bay, China. Estuarine Coastal Shelf Science, 219, 420–428. doi: 10.1016/j.ecss.2019.01.024.

Webster, P. J., Holland, G. J., Curry, J. A., and Chang, H. R. (2005). Atmospheric science: changes in tropical cyclone number, duration, and intensity in a warming environment. Science, 309, 1844–1846. doi: 10.1126/science.1116448.

Willard, J., Jia, X., Xu, S., Steinbach, M., Kumar, V., (2020). Integrating scientific knowledge with machine learning for engineering and environmental systems. Association for Computing Machinery, 1, 1, 1–35. doi: 10.48550/ARXIV.2003.04919.

Williams, J., Horsburgh, K. J., and Proctor, R. N. F. (2016). Tide and skew surge independence: New insights for flood risk, Geophysical Research Letters, 43, 6410–6417. doi:10.1002/2016GL069522.

Wolf, J. (1981). “Surge-tide interaction in the North Sea and river Thames” in Floods Due to High Winds Tides (New York, NY: Elsevier) 75–94.

Wolf, J. (2009). Coastal flooding: impacts of coupled wave-surge-tide models. Natural Hazards, 49, 241–260. doi: 10.1007/s11069-008-9316-5

Zhang, H., Cheng,W., Qiu, X., Feng, X.,and Gong,W.(2017). Tide-surge interaction along the east coast of the Leizhou peninsula, south China Sea. Continental Shelf Research, 142, 32–49. doi: 10.1016/j.csr.2017.05.015

Zhang, W.Z., Shi, F., Hong, H.-S., Shang, S.-P., Kirby, J. T. (2010). Tide-surge interaction intensified by the Taiwan Strait. Journal of Geophysical Research, 115, C06012. doi:10.1029/2009JC005762.

Zheng, F., Westra, S., Leonard, M., & Sisson, S. A. (2014). Modeling dependence between extreme rainfall and storm surge to estimate coastal flooding risk. Water Resources Research, 50, 3, 2050–2071. doi: 10.1002/2013WR014616

Zheng, P., Li, M., Wang, C., Wolf, J., Chen, X., De Dominicis, M., Yao, P., Hu, Z. (2020). Tide-Surge Interaction in the Pearl River Estuary: A Case Study of Typhoon Hato. Frontiers of Marine Science, 7, 236. doi: 10.3389/fmars.2020.00236.

Zscheischler, J., Martius, O., Westra, S., Bevacqua, E., Raymond, C., Horton, R. M., et al. (2020). A typology of compound weather and climate events. Nature Reviews Earth & Environment, 1, 7, 333–347. doi: 10.1038/s43017-020-0060-z

Appendices

Appendix A

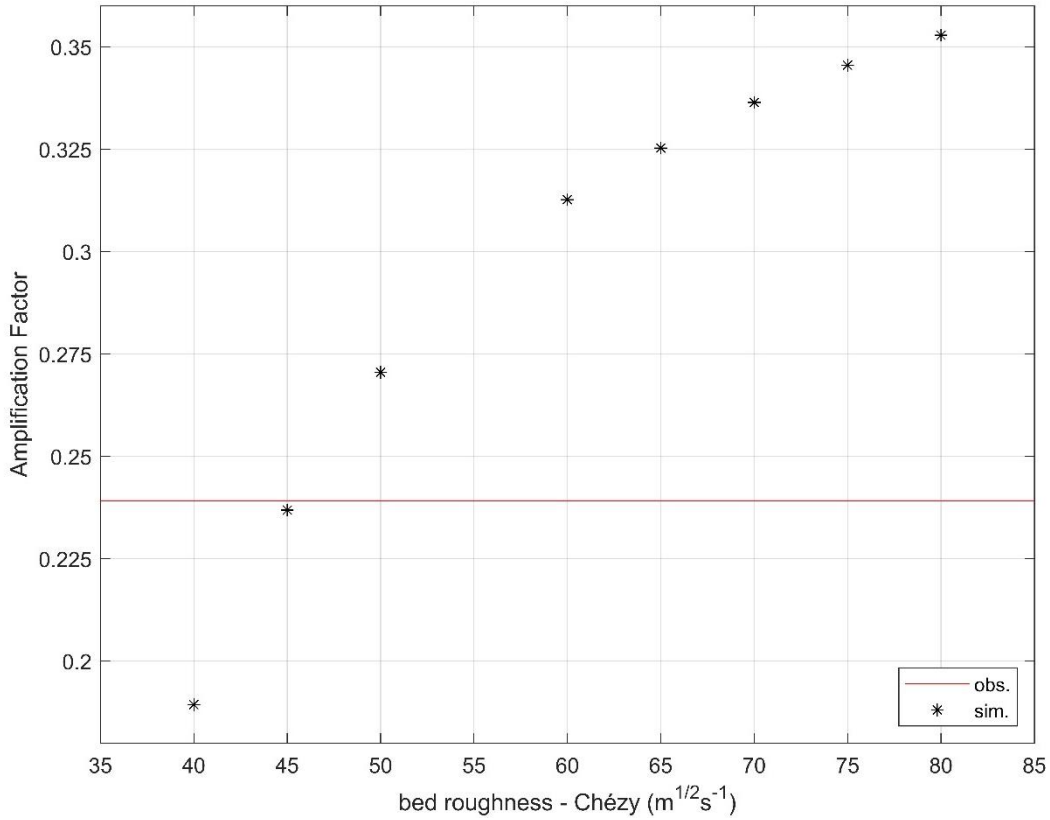

Figure A.1. Model calibration. The amplification factor between Anawhata and Onehunga tide gauges according to the Chézy coefficient used for bed roughness in the hydrodynamic model (sim.). The red line is the amplification factor calculated using observed data (the value of the 99.8th percentile) at the Onehunga and Anawhata tide gauges (obs.).

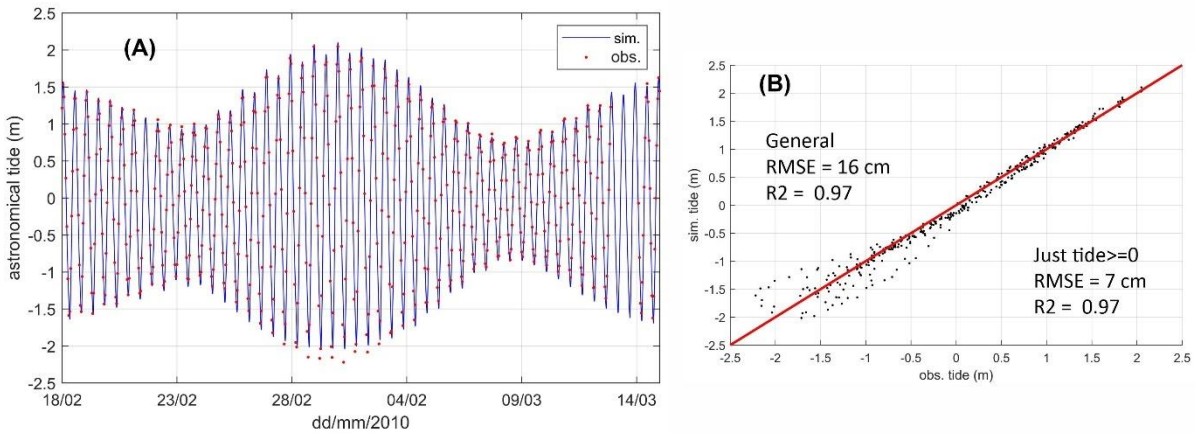

Figure A.2. Model calibration. Time series of the model result (sim.) in blue line and the observed astronomical tide (obs.) in red dots (A). Scatter plot of the simulated astronomical tide (sim. tide) and observed astronomical tide (obs. tide) (B).

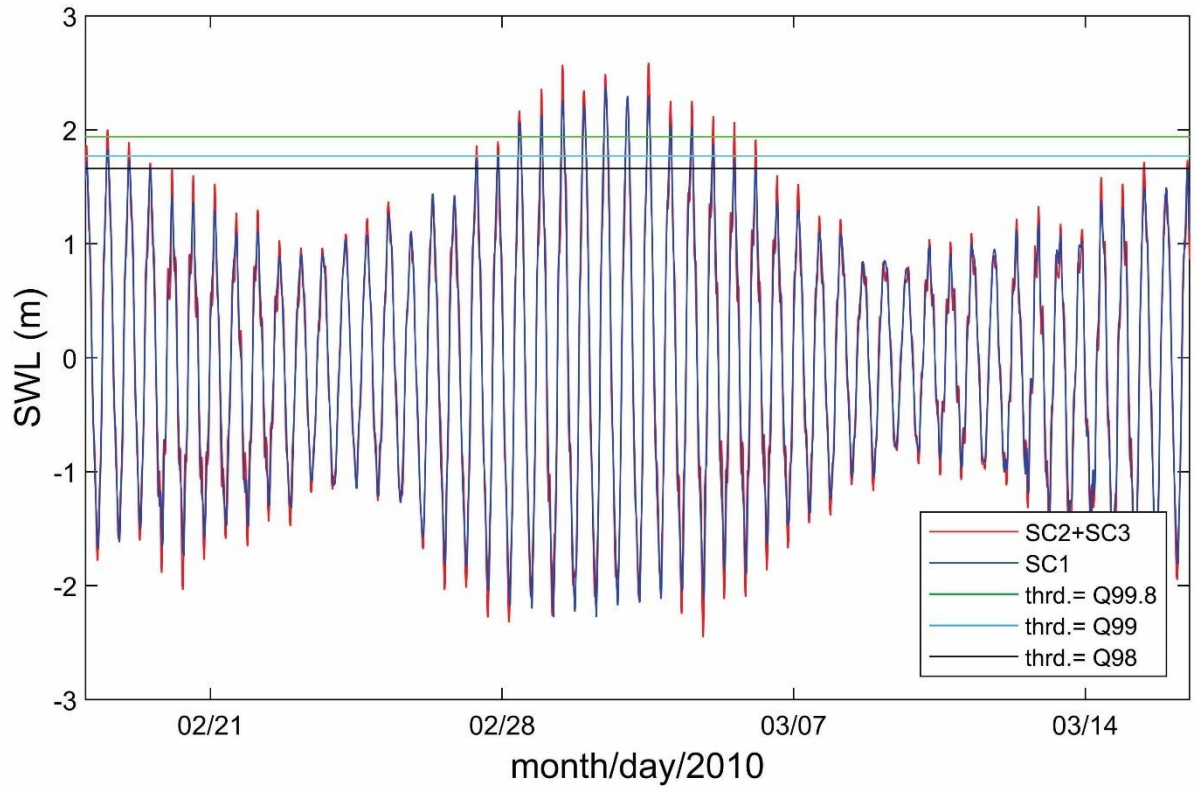

Figure A.3. Model calibration. Time series of the model result (sim.) in blue line and the observed astronomical tide (obs.) in red dots (A). Scatter plot of the simulated astronomical tide (sim. tide) and observed astronomical tide (obs. tide) (B).

Table A.1. Location and metadata of all tide gauges used in the study. "R.C." means Regional Council. "BoPRC" means Bay of Plenty Regional Council. Numeric values in this table were rounded.

Number ID	Station name	Long. (°)	Lat. (°)	Start year	End year	Owner	Gauge type	Tidal range (spring tide) (m)	Type of hydrosystem (Hume et al 2017*)	Coverage intertidal zones (when applied) (%)	Average Depth (m)	Surface area (Km^2)	Width mouth (Km)	M_2 (m)	M_4 (m)	M_4/M_2
1	North Cape	173.2	-34.2	2009	2020	LINZ/ GeoNet	Pressure transducer	2.06	Exposed coast	-	-	-	-	0.78	0.00	0.00
2	Rangaunu	173.28	-34.95	2004	2014	Northland R.C.	not informed	2.16	*Shallow drowned valley	78	2	102	1.6	0.83	0.04	0.05
3	Whangaroa	173.74	-35.05	2008	2014	Northland R.C.	not informed	2.16	*Deep drowned valley	32	4	25	0.3	0.80	0.00	0.00
4	Opua	174.12	-35.31	1991	2014	Northland R.C.	not informed	2.11	*Deep drowned valley	20	4	52	3.7	0.82	0.01	0.01
5	Marsden Point	174.7	-35.7	1964	2018	Northport	not informed	2.26	*Shallow drowned valley	58	4	103	2.4	0.88	0.01	0.01
6	Auckland	174.79	-36.83	2009	2020	LINZ/ GeoNet	Pressure transducer	2.80	*Shallow drowned valley	36	4	80	2.6	1.11	0.02	0.02

7	Korotiti Island	175.7	-36.2	2010	2020	LINZ/ GeoNet	Pressure transducer	1.95	Exposed coast	-	-	-	-	0.78	0.00	0.00
8	Whitianga	175.7	-36.84	1999	2018	Waikato R.C.	Radar	1.75	*Tidal lagoon	72	1	15	0.2	0.68	0.01	0.02
9	Tararu	175.42	-37.09	1990	2018	Waikato R.C.	Ultrasonic	3.20	*Deep drowned valley	15	9	729	21.0	0.01	1.28	0.01
10	Moturiki	176.2	-37.5	1974	2018	NIWA	Float gauge	1.80	Exposed coast	-	-	-	-	0.73	0.00	0.00
11	Oruamatua	176.28	-37.75	2002	2017	BoPRC	not informed	1.82	*Shallow drowned valley	77	2	200	1.1	0.73	0.04	0.05
12	Hairini	176.13	-37.8	2002	2017	BoPRC	not informed	“	“	“	“	“	“	0.70	0.02	0.03
13	Kotuku	176.02	-37.73	2001	2014	BoPRC	not informed	“	“	“	“	“	“	0.71	0.03	0.04
14	Ohiwa	177.11	-37.99	2006	2021	BoPRC	not informed	1.80	*Deep drowned valley	84	2	27	1.8	0.68	0.04	0.06
15	Lottin	178.17	-37.55	2009	2020	LINZ/ GeoNet	Pressure transducer	1.8	Exposed coast	-	-	-	-	0.69	0.00	0.00
16	Gisborne	178	-38.7	2004	2013	Eastland Port	Radar	2.08	Port	-	-	-	-	0.63	0.00	0.00
17	Napier	177	-39.5	1989	2018	Port of Napier	Ultrasonic	1.81	Port	-	-	-	-	0.68	0.00	0.01
18	Wellington	174.78	-41.29	1945	2018	Wellington R.C.	Float gauge	1.37	*Deep drowned valley	0	16	85	2.8	0.48	0.01	0.02
19	Kaikoura	173.7	-42.5	1994	2006	LINZ/ GeoNet	Pressure transducer	1.73	Exposed coast	-	-	-	-	0.66	0.00	0.00

20	Sumner	173	-43.5	1994	2018	Environment Canterbury	Bubbler	2.24	Exposed coast	-	-	-	-	0.83	0.00	0.00
21	Lyttelton	172.72	-43.61	1924	2018	Lyttelton Port	Ultrasonic	2.27	*Deep drowned valley	16	6	42	2.2	0.85	0.00	0.00
22	Timaru	171.2	-44.5	2002	2018	Prime Port	not informed	2.05	Exposed coast	-	-	-		0.78	0.01	0.01
23	Otago	170.51	-45.9	1900	2012	Port Otago	not informed	2.15	*Deep drowned valley	45	4	48	0.7	0.82	0.07	0.09
24	Green Island	170.5	-46	2003	2018	Otago R.C., NIWA	Bubbler	1.94	Exposed coast	-	-	-	-	0.73	0.00	0.00
25	Dog Island	168.2	-46.7	1997	2018	Otago R.C.	not informed	2.25	Exposed coast	-	-	-	-	0.91	0.04	0.04
26	Jackson Bay	168.5	-44	1998	2016	Bureau of Meteorology (Australia), NIWA	Seaframe acoustic	2.19	Exposed coast	-	-	-	-	0.83	0.00	0.00
27	Charleston	171.2	-41.7	1998	2016	LINZ/ GeoNet	Pressure transducer	2.79	Exposed coast	-	-	-	-	1.06	0.00	0.00
28	Nelson	173.2	-41.2	1984	2018	Port of Nelson	Radar	3.70	Port	-	-	-	-	1.32	0.02	0.02
29	Kapiti Island	174.7	-41	1997	2012	NIWA	not informed	1.90	Exposed coast	-	-	-	-	0.55	0.02	0.04
30	Taranaki	174	-39	1984	2018	Port Taranaki	Radar - VegaPuls PSWL61	3.22	Exposed coast	-	-	-	-	1.19	0.02	0.02

31	Kawhia	174.82	-38.08	2008	2018	Waikato R.C.	Bubbler	3.24	*Shallow drowned valley	69	2	53	0.7	1.17	0.06	0.05
32	Raglan	174.89	-37.82	2008	2018	Waikato R.C.	Radar	3.21	*Shallow drowned valley	46	2	9	0.4	1.12	0.05	0.05
33	Paratutae Island	174.51	-37.05	2010	2020	LINZ/ GeoNet	Pressure transducer	2.97	*Shallow drowned valley	62	6	366	2.3	1.09	0.02	0.01
34	Onehunga	174.72	-37.1	2002	2018	Auckland Council	Ultrasonic	3.68	“	“	“	“	“	1.33	0.05	0.04
35	Anawhata	174.2	-37.2	1999	2011	NIWA	not informed	2.87	“	“	“	“	“	1.06	0.01	0.01
36	Pouto Point	174.18	-36.37	2002	2018	Northland RC	Bubbler	3.03	*Shallow drowned valley	42	5	743	7	1.12	0.00	0.00

Table A.2. Model setup calibration.

Parameter	
Bed roughness	homogeneous = Chezy 50 $m^{1/2}.s^{-1}$
Forcing	astronomical constituents
Simulation period	14th February to 16th March 2010
Time step	0.5 min
Gravity	9.81 m/s^2
Water density	1000 kg/m^3
Horizontal eddy viscosity	1 m^2/s (uniform)
Drying and flooding check	at grid cell centres and faces
Depth at grid cell faces	minimum
Advection scheme for momentum	cyclic

Table A.3. The 99.8th percentile of the SWL, astronomical tide, NTR, and skew surge. The differences in the 99.8th percentile between NTR and skew-surge are shown in the last column of the table.

Number ID	Station name	SWL	Astronomical tide	NTR	Skew surge	Difference NTR x skew-surge)
1	North cape	1.24	1.19	0.28	0.25	0.03
2	Rangaunu	1.29	1.23	0.38	0.34	0.03
3	Whangaroa	1.23	1.18	0.28	0.29	-0.01
4	Opua	1.26	1.21	0.29	0.28	0.01
5	MarsdenPt	1.33	1.29	0.34	0.34	0
6	Auckland	1.67	1.64	0.29	0.27	0.02
7	Korotiti island	1.15	1.12	0.23	0.23	0.01
8	Whitianga	0.98	0.94	0.3	0.28	0.02
9	Tararu	1.81	1.76	0.37	0.35	0.02
10	Moturiki	1.08	1.04	0.27	0.26	0.01
11	Oruamatua	1.09	1.02	0.35	0.33	0.02
12	Hairini	1.05	1	0.33	0.29	0.04
13	Kotuku	1.02	0.96	0.33	0.32	0.02
14	Ohiwa	1.08	1	0.39	0.38	0.01
15	Lottin	1.04	1	0.24	0.24	0.01
16	Gisborne	0.96	0.89	0.3	0.29	0.01
17	Napier	1.02	0.96	0.29	0.3	-0.01
18	Wellington	0.82	0.72	0.31	0.31	0
19	Kaikoura	1.03	0.96	0.28	0.27	0.01
20	Sumner	1.28	1.18	0.38	0.38	0
21	Lyttelton	1.32	1.22	0.4	0.4	0
22	Timaru	1.21	1.12	0.37	0.36	0
23	Otago	1.27	1.16	0.39	0.37	0.02
24	GreenIsland	1.18	1.07	0.36	0.36	0
25	DogIsland	1.4	1.3	0.43	0.4	0.03
26	JacksonBay	1.36	1.25	0.4	0.41	-0.01
27	Charleston	1.67	1.61	0.4	0.38	0.02
28	Nelson	2.14	2.08	0.37	0.36	0.01
29	Kapiti island	1.06	0.98	0.36	0.35	0.01
30	Taranaki	1.83	1.78	0.35	0.35	0.01
31	Kawhia	1.86	1.77	0.53	0.52	0.01
32	Raglan	1.8	1.69	0.57	0.55	0.02
33	Paratutae island	1.69	1.63	0.37	0.36	0.01
34	Onehunga	1.97	1.92	0.48	0.44	0.04
35	Anawhata	1.64	1.58	0.35	0.34	0.01
36	Pouto Point	1.72	1.67	0.41	0.39	0.02

Table A.4. Values of χ^2 from Haigh et al. (2010) and Dixon and Tawn (1994) methods. The rows marked with a pastel blue colour indicate that TSI is most likely to happen ($\chi^2 \geq 21$ and $\chi^2 \geq 9$ for Haigh et al. (2010) and Dixon and Tawn (1994) methods, respectively).

Number ID	Station name	χ^2-Haigh et al. (2020)	χ^2 -Dixon and Tawn (1994)
1	North cape	14.56	4.11
2	Rangaunu	110.21	34.97
3	Whangaroa	8.16	4.02
4	Opua	91.22	13.22
5	MarsdenPt	67.83	6.67
6	Auckland	41.50	4.60
7	Korotiti island	7.66	1.15
8	Whitianga	115.13	42.85
9	Tararu	115.29	110.01
10	Moturiki	52.57	10.77
11	Oruamatua	840.23	154.47
12	Hairini	893.11	256.26
13	Kotuku	217.98	63.22
14	Ohiwa	593.04	150.04
15	Lottin	10.27	1.96
16	Gisborne	8.80	5.42
17	Napier	46.15	5.23
18	Wellington	120.06	6.41
19	Kaikoura	36.49	17.14
20	Sumner	21.67	8.11
21	Lyttelton	367.54	121.99
22	Timaru	36.42	19.34
23	Otago	3277.49	359.28
24	Green island	23.02	7.57
25	Dog island	144.31	101.17
26	JacksonBay	63.23	5.20
27	Charleston	19.37	13.42
28	Nelson	127.41	3360.87
29	Kapiti island	23.84	4.16
30	Taranaki	31.91	27.73
31	Kawhia	210.81	50.88
32	Raglan	59.51	1616.05
33	Paratutae island	46.55	11.23
34	Onehunga	324.65	98.74
35	Anawhata	40.91	43.25
36	Pouto Point	54.53	62.96

Table A.5. Kendall coefficient (τ) calculated according to the Arns et al. (2020) method for astronomical tide and NTR (skew surge) occurring at extreme events over 99.8th percentile of SWL. The result of tide-surge interaction using Arns et al. (2020) statistical model is shown in the column "TSI (cm)".

		99.8th percentile of SWL					
		astronomical tide x NTR		astronomical tide x Skew surge			
Number ID	Station name	τ	p-value	τ	p-value	number of samples	TSI (cm)
1	North cape	-0.37	0.0005	-0.36	0.0006	43	1
2	Rangaunu	-0.61	0.0000	-0.60	0.0000	65	23
3	Whangaroa	-0.36	0.0047	-0.35	0.0067	30	0
4	Opua	-0.46	0.0000	-0.45	0.0000	102	5
5	MarsdenPt	-0.53	0.0000	-0.53	0.0000	196	12
6	Auckland	-0.44	0.0000	-0.44	0.0000	64	4
7	Korotiti island	-0.51	0.0000	-0.51	0.0000	60	9
8	Whitianga	-0.55	0.0000	-0.53	0.0000	104	13
9	Tararu	-0.50	0.0000	-0.48	0.0000	151	8
10	Moturiki	-0.56	0.0000	-0.56	0.0000	224	15
11	Oruamatua	-0.63	0.0000	-0.62	0.0000	79	26
12	Hairini	-0.63	0.0000	-0.63	0.0000	89	27
13	Kotuku	-0.61	0.0000	-0.61	0.0000	90	23
14	Ohiwa	-0.60	0.0000	-0.58	0.0000	92	22
15	Lottin	-0.55	0.0000	-0.54	0.0000	57	13
16	Gisborne	-0.48	0.0004	-0.48	0.0004	26	6
17	Napier	-0.59	0.0000	-0.58	0.0000	134	20
18	Wellington	-0.56	0.0000	-0.55	0.0000	386	16
19	Kaikoura	-0.44	0.0000	-0.44	0.0000	59	4
20	Sumner	-0.55	0.0000	-0.53	0.0000	131	13
21	Lyttelton	-0.56	0.0000	-0.54	0.0000	468	15
22	Timaru	-0.53	0.0000	-0.53	0.0000	92	11
23	Otago	-0.53	0.0000	-0.51	0.0000	310	11
24	Green island	-0.51	0.0000	-0.50	0.0000	74	9
25	Dog island	-0.52	0.0000	-0.53	0.0000	103	11
26	JacksonBay	-0.50	0.0000	-0.50	0.0000	66	9
27	Charleston	-0.58	0.0000	-0.58	0.0000	73	18
28	Nelson	-0.44	0.0000	-0.46	0.0000	64	4
29	Kapiti island	-0.57	0.0000	-0.57	0.0000	96	17
30	Taranaki	-0.50	0.0000	-0.50	0.0000	147	8
31	Kawhia	-0.63	0.0000	-0.63	0.0000	64	27
32	Raglan	-0.54	0.0001	-0.54	0.0001	25	13
33	Paratutae island	-0.49	0.0000	-0.47	0.0000	57	7
34	Onehunga	-0.59	0.0000	-0.59	0.0000	101	20
35	Anawhata	-0.43	0.0000	-0.43	0.0000	67	3
36	Pouto Point	-0.53	0.0000	-0.54	0.0000	78	12

Table A.6. Kendall coefficient (τ) calculated according to the Williams et al. (2016) method for astronomical tide and the largest 1% skew surges. The rows in blue pastel colour indicate that the correlation is significant ($p \leq 0.05$).

		98th percentile		99th percentile		99.8th percentile	
Number ID	**Station name**	**τ**	**p-value**	**τ**	**p-value**	**τ**	**p-value**
1	North cape	-0.02	0.79	0.00	0.96	0.19	0.39
2	Rangaunu	-0.01	0.83	0.02	0.74	0.12	0.30
3	Whangaroa	-0.07	0.43	0.01	0.91	-0.21	0.38
4	Opua	0.00	0.94	0.06	0.22	0.07	0.43
5	MarsdenPt	0.02	0.56	0.01	0.82	-0.01	0.87
6	Auckland	-0.02	0.76	0.03	0.63	0.05	0.64
7	Korotiti island	0.02	0.70	-0.01	0.92	-0.02	0.91
8	Whitianga	0.00	0.97	-0.04	0.41	0.20	0.05
9	Tararu	-0.05	0.04	-0.03	0.27	0.03	0.52
10	Moturiki	-0.01	0.72	-0.05	0.18	0.07	0.29
11	Oruamatua	-0.09	0.05	-0.15	0.01	-0.11	0.24
12	Hairini	-0.10	0.02	-0.12	0.01	-0.16	0.05
13	Kotuku	-0.06	0.22	-0.08	0.16	-0.05	0.66
14	Ohiwa	-0.08	0.05	-0.07	0.17	-0.16	0.06
15	Lottin	0.00	0.93	-0.04	0.52	-0.02	0.88
16	Gisborne	-0.03	0.77	-0.19	0.08	0.24	0.38
17	Napier	-0.02	0.49	-0.03	0.52	-0.04	0.51
18	Wellington	-0.01	0.66	0.00	0.84	-0.01	0.77
19	Kaikoura	-0.08	0.15	-0.12	0.08	0.03	0.86
20	Sumner	-0.04	0.32	-0.03	0.54	0.06	0.46
21	Lyttelton	0.01	0.47	0.00	0.85	-0.02	0.53
22	Timaru	-0.03	0.41	-0.01	0.81	0.12	0.20
23	Otago	0.03	0.11	0.03	0.29	0.02	0.63
24	Green Island	-0.08	0.09	-0.10	0.09	-0.19	0.12
25	Dog Island	-0.09	0.01	-0.10	0.04	-0.02	0.84
26	Jackson Bay	0.01	0.86	0.01	0.92	-0.01	0.94
27	Charleston	-0.01	0.80	-0.04	0.43	-0.01	0.94
28	Nelson	-0.10	0.06	0.01	0.87	-0.28	0.17
29	Kapiti Island	0.01	0.83	-0.03	0.54	0.01	0.93
30	Taranaki	-0.06	0.09	-0.02	0.66	0.06	0.38
31	Kawhia	-0.01	0.92	0.01	0.88	0.04	0.79
32	Raglan	0.13	0.11	0.15	0.23	-0.24	0.56
33	Paratutae Island	0.01	0.91	-0.01	0.85	0.07	0.57
34	Onehunga	-0.02	0.64	0.01	0.85	0.00	1.00
35	Anawhata	-0.12	0.01	-0.16	0.00	-0.07	0.52
36	Pouto Point	-0.05	0.27	-0.01	0.91	0.05	0.66

Table A.7. Tidal amplification and differences in amplitude of the main astronomical and shallow water constituents.

	Manukau Harbour		Lyttelton Harbour		Otago Harbour		Tauranga Harbour	
	Onehunga/Anawhata		Lyttelton/Sumner		Otago/Green Island		Harini/Moturiki	
	Ampl.fac.	Difference Onehunga-Anawhata	Ampl.fac.	Difference Sumner-Lyttelton	Ampl. fac.	Difference Green Island - Otago	Ampl. fac.	Difference Moturiki-Hairini
M_2	0.26	0.28	0.04	0.03	0.12	0.09	-0.03	-0.02
S_2	0.19	0.05	0.03	0.01	0.06	0.01	-0.11	-0.02
N_2	0.19	0.04	-0.01	0	-0.03	0	-0.14	-0.01
M_4	0.83	0.02	-0.04	0	0.06	0	0.14	0
MS_4	0.57	0.01	-0.06	0	0.85	0.01	0.69	0.01
MN_4	1.22	0.01	0.16	0	0.95	0.01	1.64	0.01

Table A.8. Phase difference and amplification between M_4 and M_2 tidal constituents.

	Manukau Harbour		Lyttelton Harbour		Otago Harbour		Tauranga Harbour	
	Onehunga	Anawhata	Lyttelton	Sumner	Otago	Green Island	Hairini	Moturiki
M_4/M_2	0.039	0.027	0.03	0.032	0.034	0.036	0.035	0.03
$2gM_2\text{-}gM_4$	304.05	x	182.33	x	169.78	x	199.3	x

Table A.9. The contribution of the astronomical tide at the 99.8th percentile of SWL in each of the 36 tidal gauges in the study.

Number ID	Station name	Astronomical tide (%)
1	North cape	91
2	Rangaunu	87
3	Whangaroa	91
4	Opua	92
5	MarsdenPt	91
6	Auckland	94
7	Korotiti island	92
8	Whitianga	86
9	Tararu	92
10	Moturiki	89
11	Oruamatua	85
12	Hairini	87
13	Kotuku	84
14	Ohiwa	82
15	Lottin	90
16	Gisborne	82
17	Napier	84
18	Wellington	76
19	Kaikoura	86
20	Sumner	84
21	Lyttelton	83
22	Timaru	82
23	Otago	83
24	Green Island	83
25	Dog Island	85
26	Jackson Bay	82
27	Charleston	89
28	Nelson	92
29	Kapiti Island	82
30	Taranaki	93
31	Kawhia	88
32	Raglan	73
33	Paratutae Island	90
34	Onehunga	91
35	Anawhata	90
36	Pouto Point	90

Appendix B

The ratio-log method

The logarithm ratio band (Stumpf et al., 2003) is based on the assumption that the light attenuation increases with the water depth. This method estimates the bathymetry using the ratio of the natural logarithm between the reflectance of two different spectral bands. Assuming that these bands are affected similarly by the atmosphere and bottom albedo, the method works because the attenuation rate with depth is dependent on the wavelength. The SDB using the ratio-log method is calculated as follows:

$$Z_{sat} = m1\left(\frac{\ln nR_w(\lambda_i)}{\ln nR_w(\lambda_j)}\right) + m_0 \qquad \text{(B1)}$$

Where Z_{sat} is the satellite derived bathymetry, n is a constant used in order to assure that the ratio remains always positive and that the ratio will produce a linear response with depth, m_1 is a tunable constant to scale the ratio to depth, and m_0 is the offset for a depth of 0m (Z=0); $R_w(\lambda_i)$ is the reflectance on the surface of the band i and $R_w(\lambda_j)$ is the reflectance on the surface of the band j. Here we used the green and blue band from Sentinel Copernicus, product type 2A images, respectively. To calculate the derived bathymetry, a single image dated on 2019/04/06 22:16:09 UTC for Tauranga Harbour only, was used when the observed tide was 0.94 m above mean sea-level at the Ōmokoroa tide gauge (at high tide).

The ratio-log-SDB

The ratio-log method was applied for Tauranga Harbour separately for shallow and intertidal areas, and the results can be seen in Figure S1 (which is used in Part A, Figure 1) and S2 (used for the bathymetry in scenario 4 of modelling tests in Part B, Figure 2). The use of this approach generated a high density of estimated points because it provides a value of depth for every image pixel.

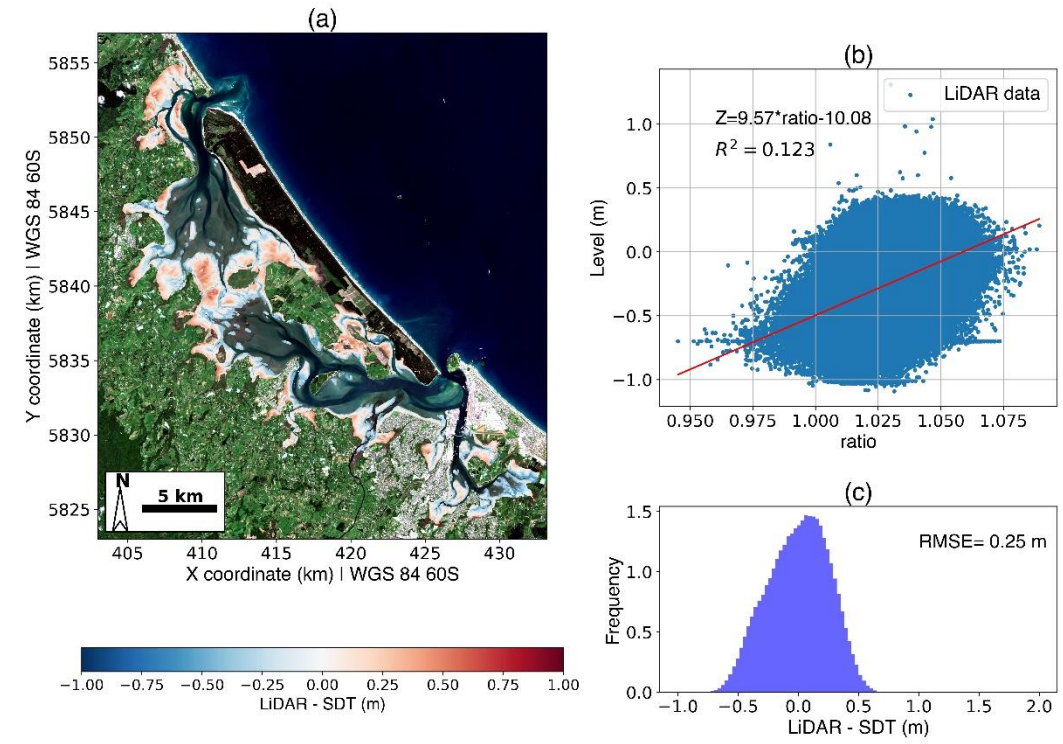

Figure B.1. Satellite-derived topography for Tauranga Harbour using the ratio-log method. (a) Map showing the estimated bathymetry samples and the spatial distribution of relative error. (b) Ratio-log method fitted using the LiDAR data ('ratio' is the ratio in Equation B1). (c) Relative error distribution of the SDT using ratio-log method. Background image: ESA Sentinel 2A. Image date and time (UTC+12): 18/12/2018 h. The water level at the moment of image acquisition: -0.41 m at Ōmokoroa tide gauge (MSL).

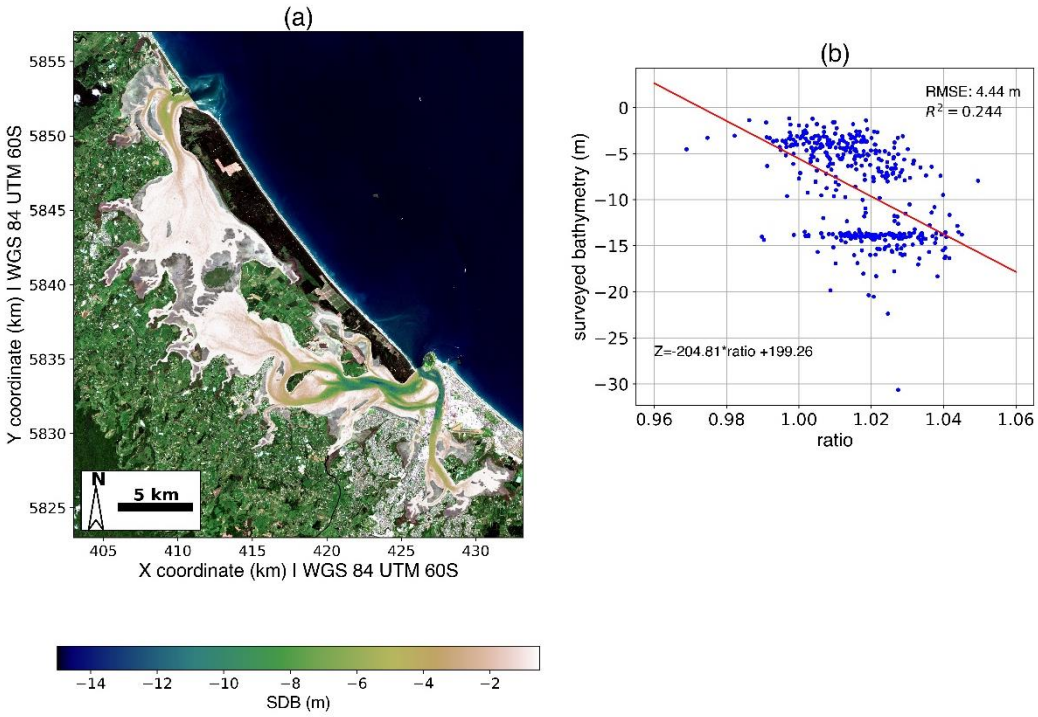

Figure B.2. Satellite derived bathymetry for Tauranga Harbour, shallow and channel areas, derived using ratio-log method. (a) Map showing the estimated bathymetry samples. (b) Ratio method fitted using the surveyed bathymetry ('ratio' is the ratio in Equation B1). Note the Harbour is dredged to -14m in some regions around the Port of Tauranga. Background image: ESA Sentinel 2A. Image date and time (UTC+12): 18/12/2018 h. The water level at the moment of image acquisition: -0.41 m at Ōmokoroa tide gauge (MSL).

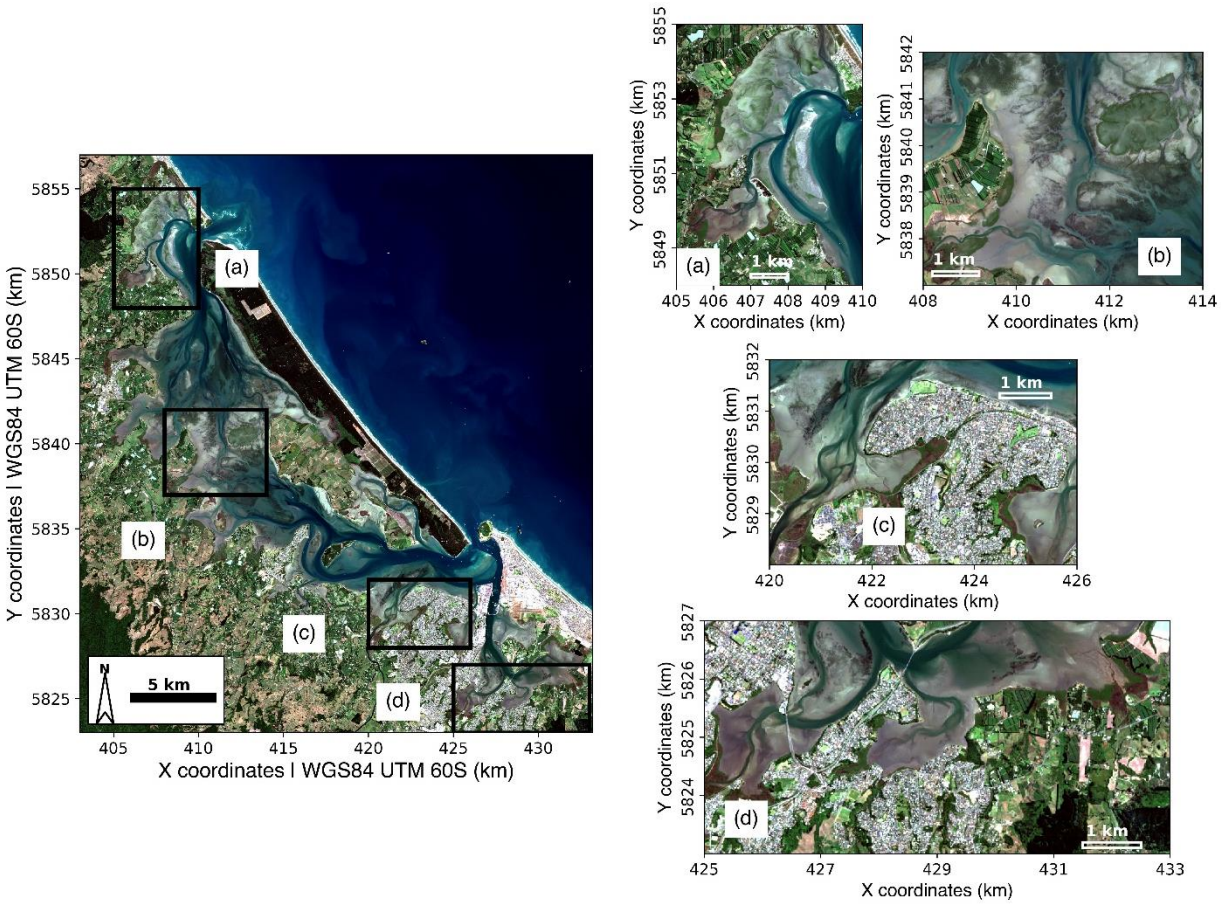

Figure B.3. An example of the effect of seagrass and complex morphology in Tauranga Harbour. Background image: ESA Sentinel 2A. Image date and time (UTC+12): 16/02/2019 10:15 h. The water level at the moment of image acquisition: -0.56 m at Ōmokoroa tide gauge (MSL). Note that the round vegetated feature at the top right of panel b is a mangrove 'island' located on the high intertidal.

Appendix C

Hydrodynamic settings and validation

The bed roughness used in our model was determined by Stewart (Stewart, 2021). The model was run 15 days for calibration to cover a complete spring-neap cycle over the period from 8th – 23rd of March 2017 and compared to the collected field data. The validation period was the following 15 days, which covers a neap-spring cycle between 24th of March – 8th April 2017. The best results were obtained with a variable bed roughness across the model domain, with values of Chézy coefficient of 35 m$^{1/2}$/s for the tidal flats, 45 and 55 m$^{1/2}$/s for intermediary-depth areas 65 and 75 m$^{1/2}$/s for the deepest channels. The model also validated for this study,

using the water level for the period that the images where acquired (year of 2019) as described in the main manuscript (Sect. 2.4).

Table C.1. Model parameters used in the calibration of the hydrodynamic modelling and determination of bed roughness. Extracted from Stewart (2021).

Parameter	Value	Units (if applicable)
Time step	0.5	minutes
Gravity	9.81	m/s^2
Water density	1000	kg/m^3
Roughness	75 - 35	Chézy ($m^{1/2}/s$). Spatial varying map used
Horizontal eddy viscosity	10	m^2/s
Threshold depth	0.1	m
Advection scheme for momentum	cyclic	-
Depth at grid cell faces	mean	-
Drying and flooding check at	grid cell centres and faces	-
Open boundary type	water level	-
Reflection parameter alpha	50	-
Forcing type	astronomic	-

Table C.2. Calibration and validation parameters for the hydrodynamic model of Tauranga Harbour. Extracted form Stewart (2021).

Period	Parameter	Statistics	
		Bias (m)	RMSE (m)
Calibration (08.03.2017 - 23.03.2017)	Water level (m)	0.04	0.15
	Current Velocity (m/s)	0.03	0.11
Validation (24.03.2017 - 08.04.2017)	Water level (m)	0.09	0.16
	Current Velocity (m/s)	0.03	0.13

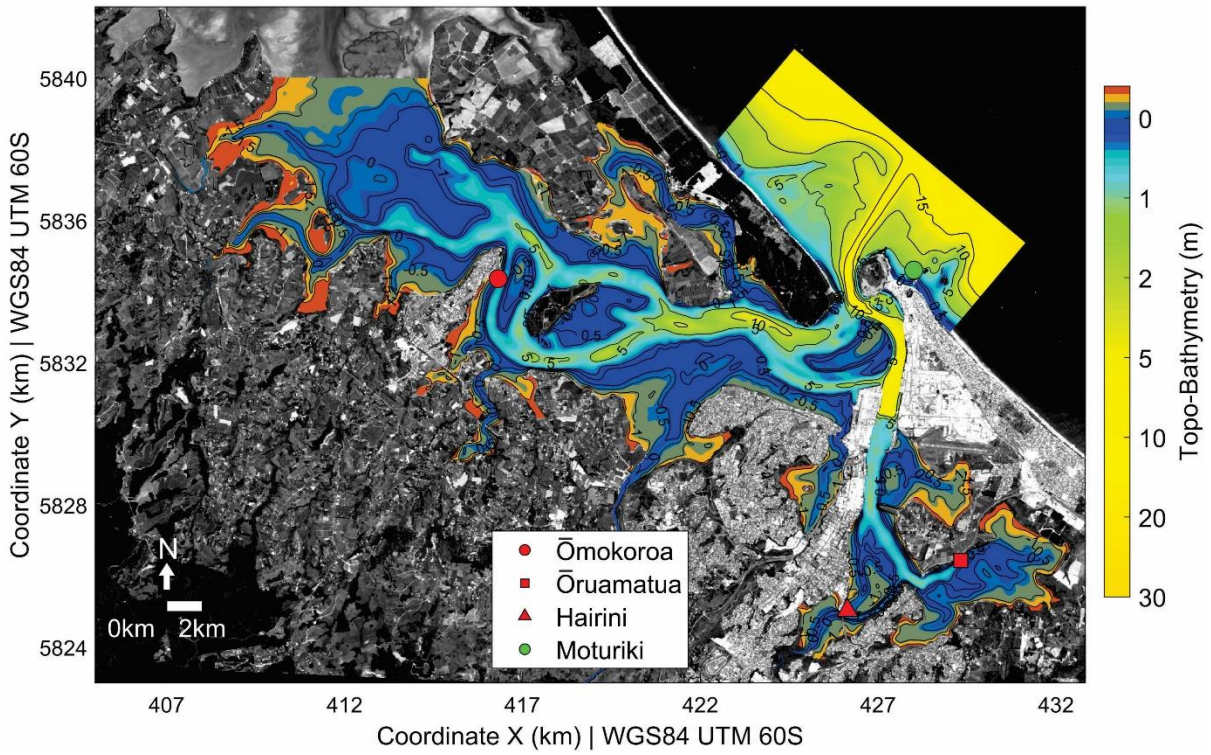

Figure C.1. Tauranga Harbour numerical model. Interpolated bathymetry in the model domain. The triangle, square and circle symbols locate the tide gauges used in the hydrodynamic model. Vertical reference level: MSL. Background image: ESA Sentinel 2A.

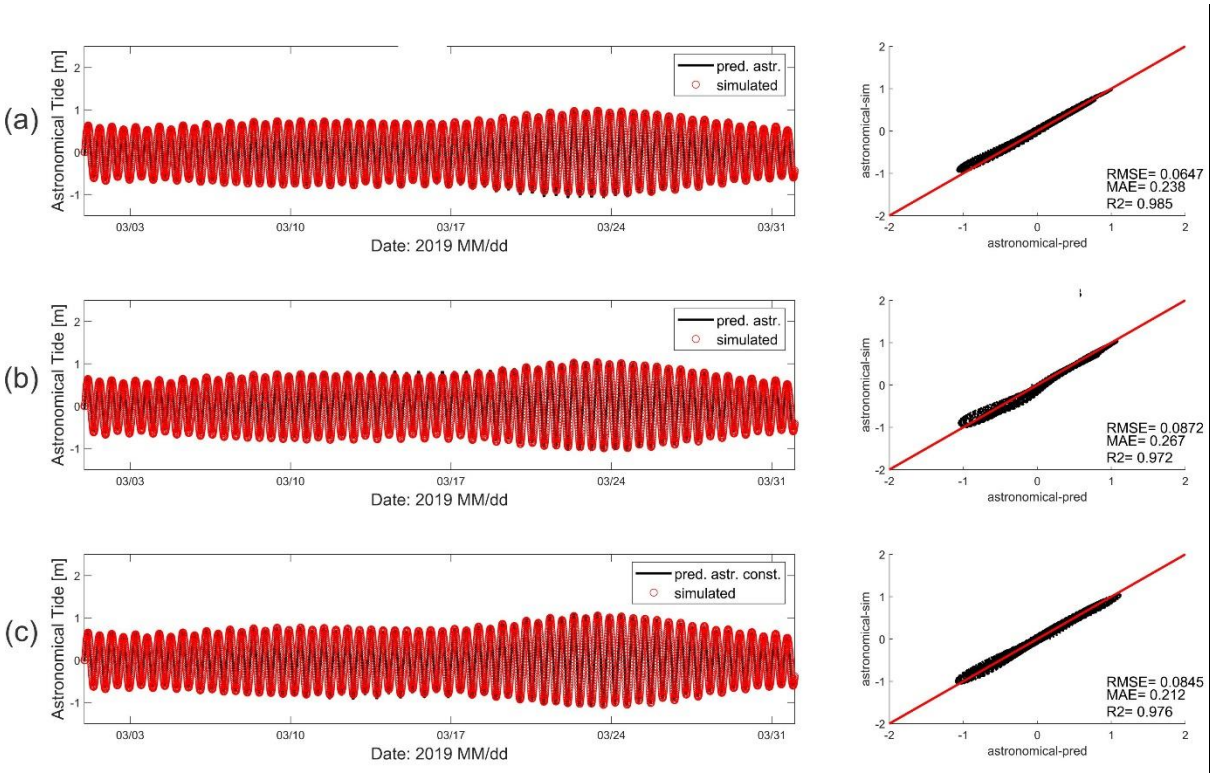

Figure C.2. Hydrodynamic model validation for Tauranga Harbour for an equinoctial tide cycle for the year of 2019 at three different observation points: the Ōmokoroa (a), Hairini (b) and Ōruamatua (c) tide gauges.

Appendix D

Table D.1. Details of each tide gauge used in the study.

Estuary	Tide gauge name	Latitude (WGS 84)	Longitude (WGS 84)	Easting (m) (UTM WGS 84)	Northing(m) (UTM WGS 84)	Manager
Maketū	Moturiki Island	-37°37'48"	176°11'9 "	428172.47 E	5834908.38 S	National Institute for Atmosphere and Water (NIWA)
Ōhiwa	Port Ōhope Wharf	-37° 59′ 2″	177° 6′ 28″	509464.67 E	5795967.06 S	Bay of Plenty Regional Council
Tauranga Harbour	Ōmokoroa	-37° 37′ 58″	176° 3′ 13″	416495.99 E	5834506.66 S	
	Hairini	-37° 42′ 54″	176° 9′ 56″	426454.73 E	5825477.93 S	
	Ōruamatua	-37° 41′ 58″	176° 12′ 13″	429794.21 E	5827233.01 S	
Whitianga	Whitianga Wharf	-36°49'58 "	175°42'32 "	384868.29 E	5922897.54 S	Waikato Regional Council

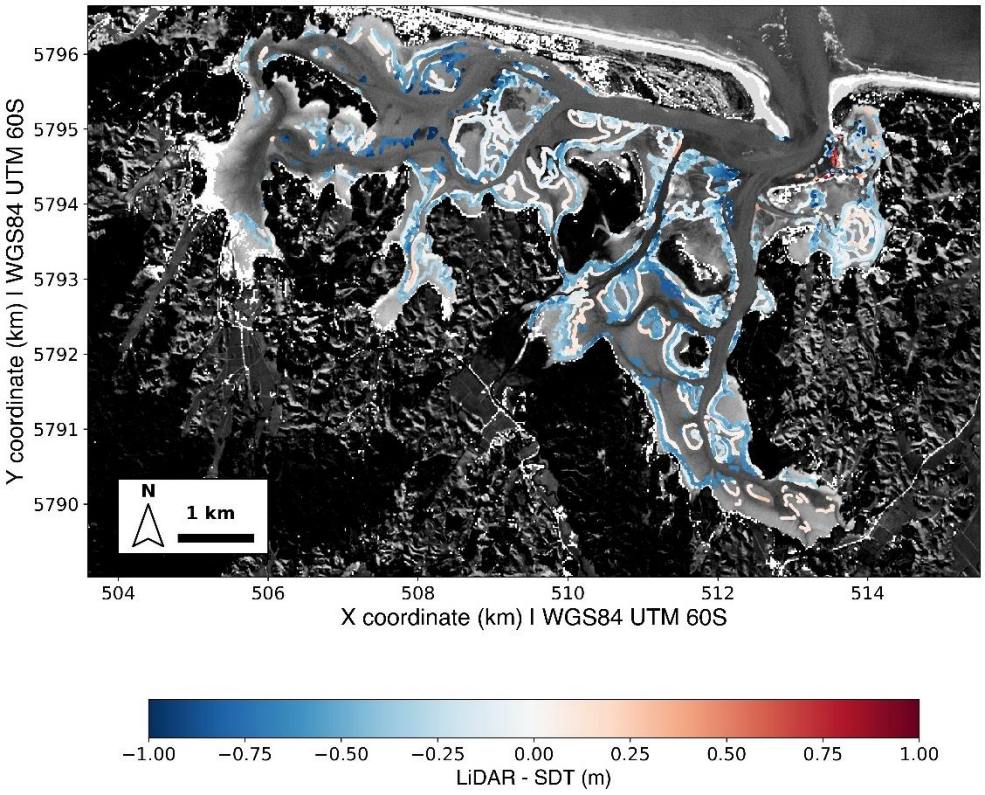

Figure D.1. Satellite derived bathymetry for Ōhiwa Harbour using waterline method. Map showing the estimated bathymetry samples and the spatial distribution of relative error. Background image: ESA Sentinel 2A. Image number 3 (see Table D.2).

Table D.2. Ōhiwa date, time, and observed water level at Port Ōhope Wharf tide gauge.

Image number	Date and Time (UTZ+12h)	Level (m) MSL
1	06/02/2019 10:16	0.656
2	26/02/2019 10:15	0.433
3	16/06/2019 10:16	-0.1
4	27/04/2019 10:16	0.219
5	30/08/2019 10:16	-0.089
6	03/11/2019 10:16	0.62

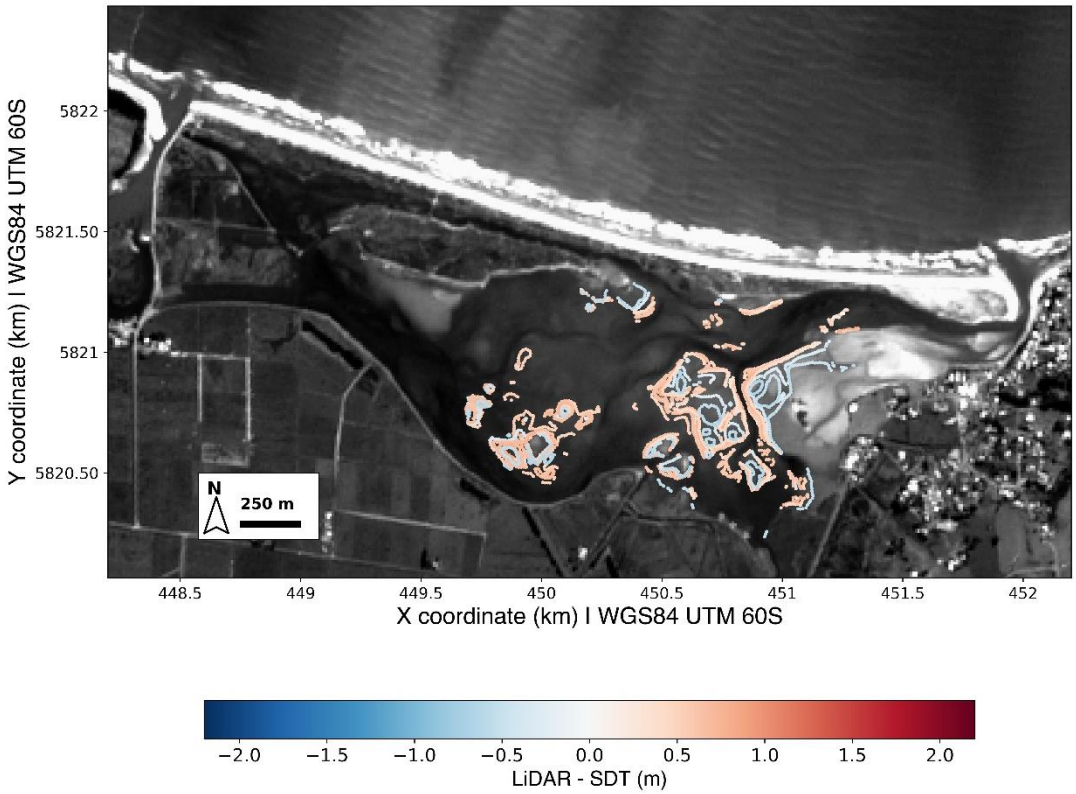

Figure D.2. Satellite derived topography for Maketū Harbour using waterline method. Map showing the estimated bathymetry samples and the spatial distribution of relative error. Background image: ESA Sentinel 2A. Image number 8 (see table D.3).

Table D.3. Maketu date, time, and observed water level at Moturiki Island tide gauge.

Image number	Date and Time (UTZ+12h)	Level (m) MSL
1	18/12/2018 10:15	-0.25
2	17/01/2019 10:15	-0.28
3	06/02/2019 10:16	0.41
4	16/02/2019 10:15	-0.4
5	26/02/2019 10:15	0.6
6	03/03/2019 10:15	-0.4
7	02/04/2019 10:16	-0.4
8	07/04/2019 10:16	0.46
9	02/05/2019 10:16	-0.46
10	26/06/2019 10:16	0.11
11	15/08/2019 10:16	-0.19
12	03/11/2019 10:16	0.84

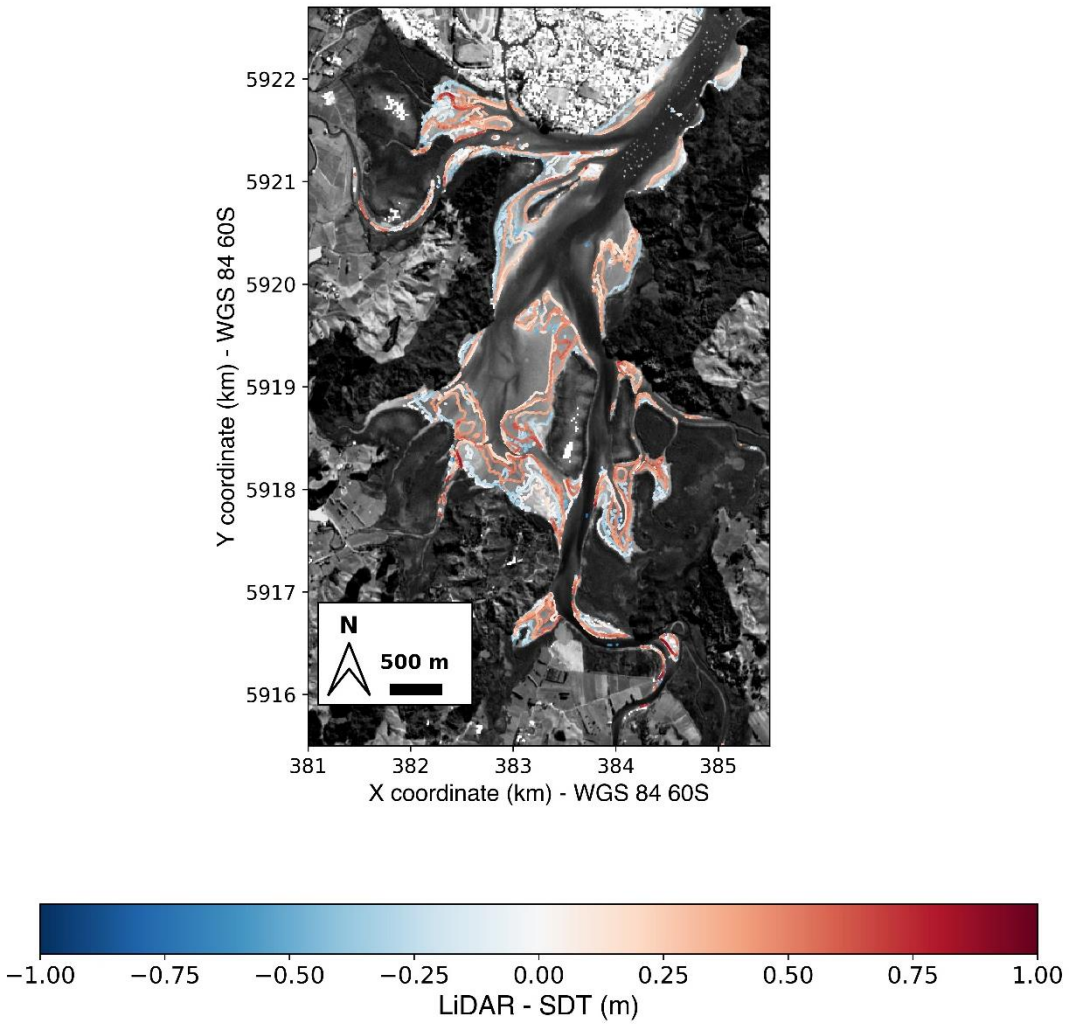

Figure D.3. Satellite derived bathymetry for Whitianga Harbour using waterline method. Map showing the estimated bathymetry samples and the spatial distribution of relative error. Background image: ESA Sentinel 2A. Image number 8 (see table D.4).

Table D.4. Whitianga date, time, and observed water level at Whitianga Wharf tide gauge.

Image number	Date and Time (UTZ+12h)	Level (m) MSL
1	18/12/2018 10:15h	-0.243
2	22/01/2019 10:15h	0.365
3	11/02/2019 10:15h	0.816
4	16/02/2019 10:15h	-0.296
5	26/02/2019 10:15h	0.547
6	30/04/2019 10:25h	-0.228
7	16/06/2019 10:16h	-0.312
8	27/10/2019 10:25h	-0.513

Appendix E

Satellite derived topography and bathymetry use in hydrodynamic modelling assessment.

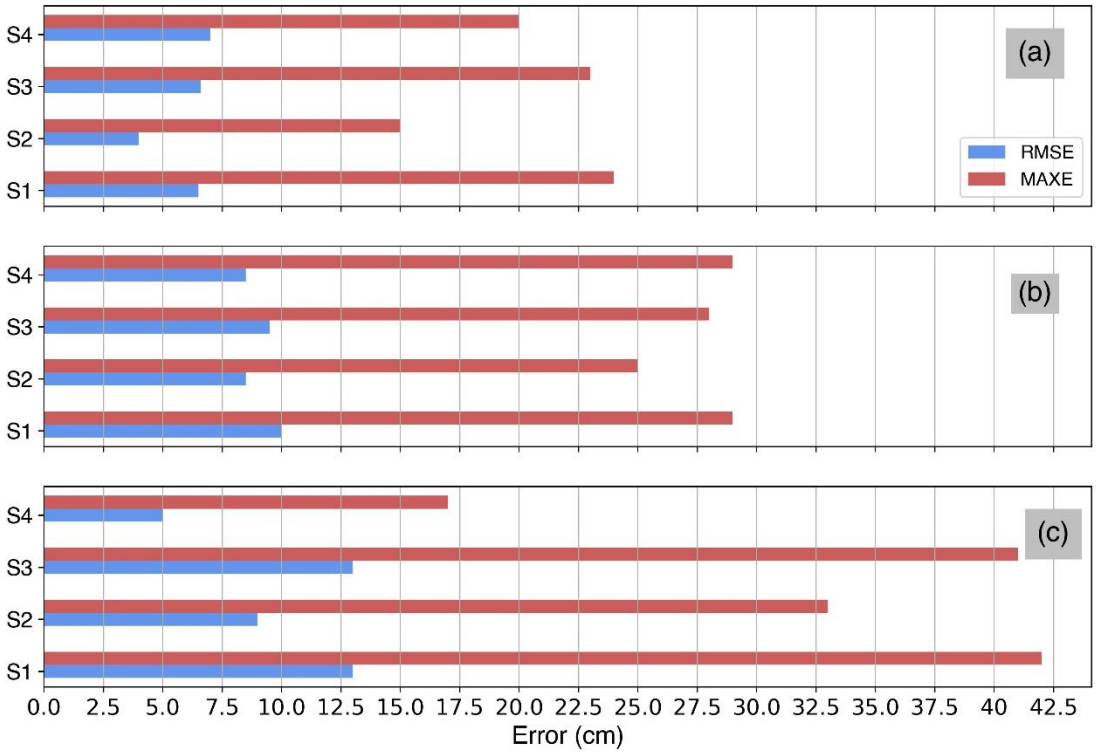

Figure E.1. The parameter errors of the four simulation scenarios (S1, S2, S3, and S4) – RMSE (blue bar), MAE (red bar) –at the 3 tide gauge locations: Ōmokoroa (a), Hairini (b), Oruamatua (c).

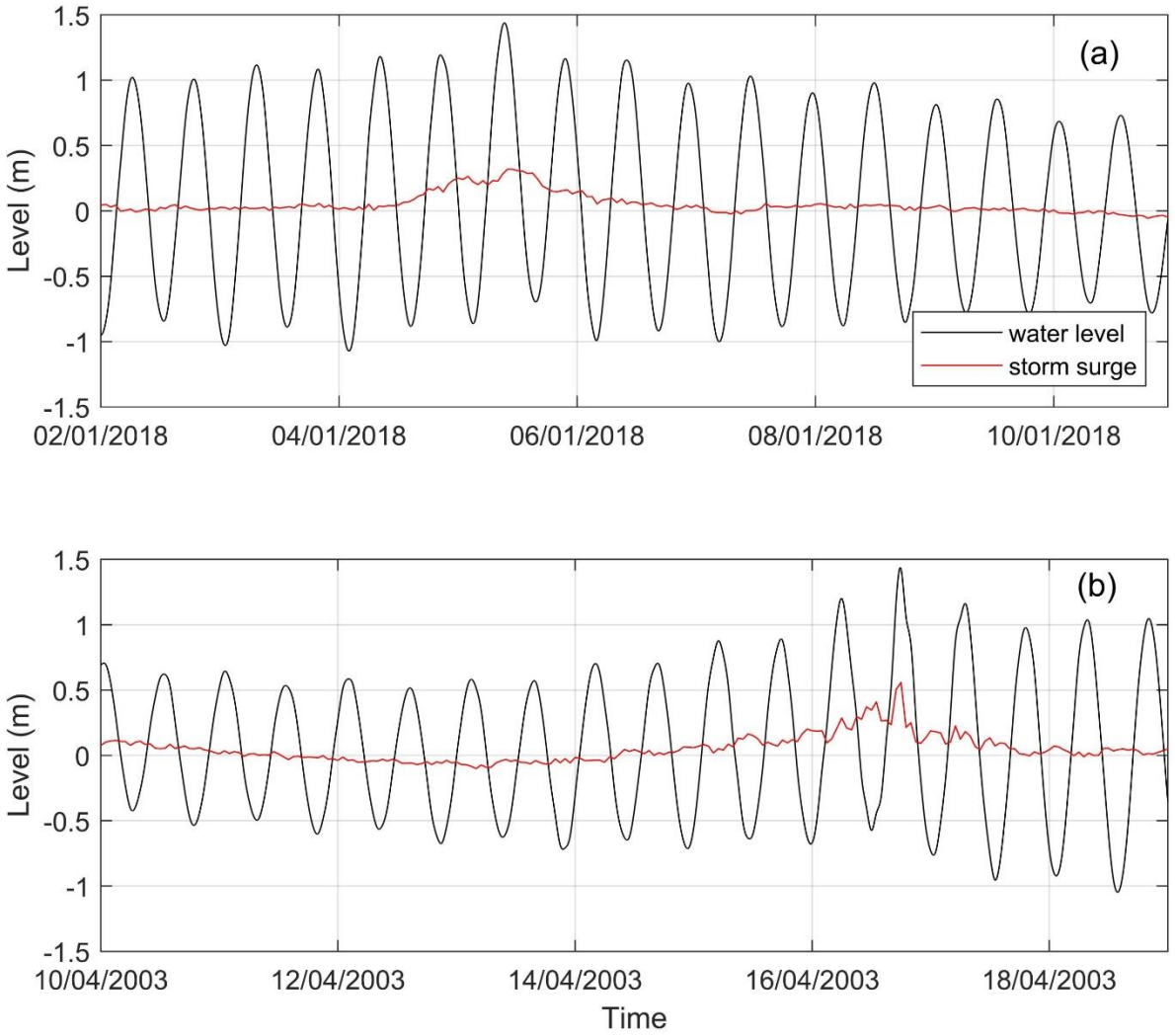

Figure E.2. Time series of water level forced in the model boundary of S5 and S6 (a), and S7 and S8 (b). Black line shows the water level record in Moturiki tide gauge at mean sea level. The red line refers to the storm surge contribution to the water level.

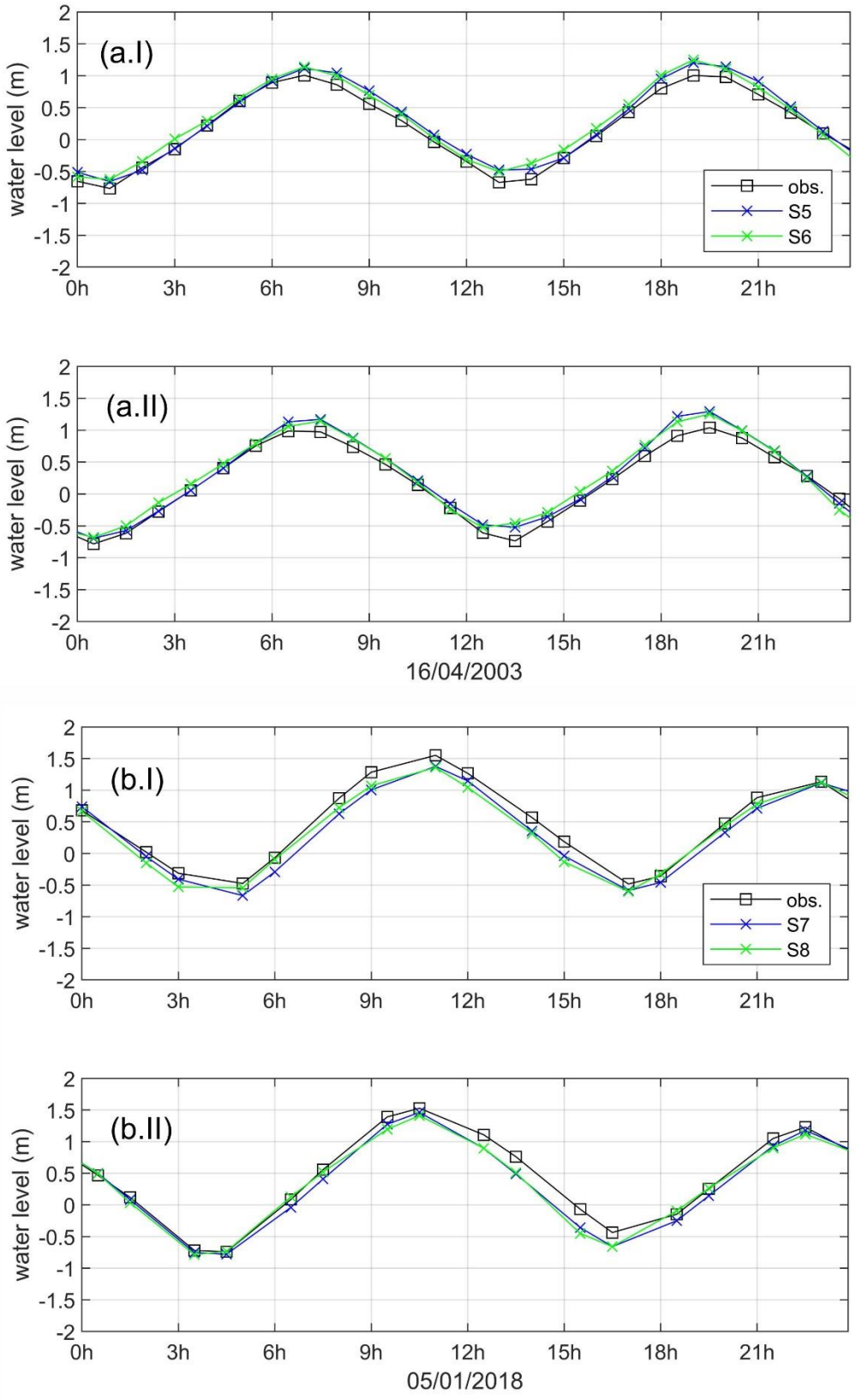

Figure E.3. Outputs of S5 and S6 (a), and S7 and S8 (b) for Harini (I) and Oruamatua (II). The observed water level for each time series is shown in black line with square markers.